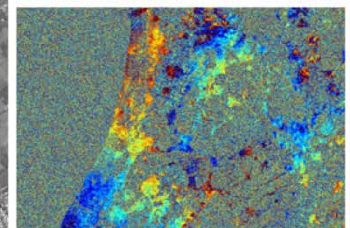
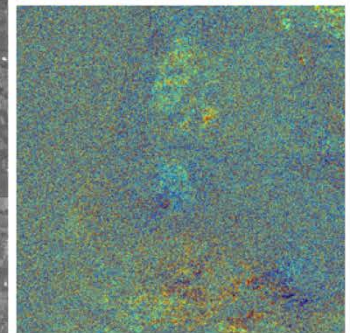
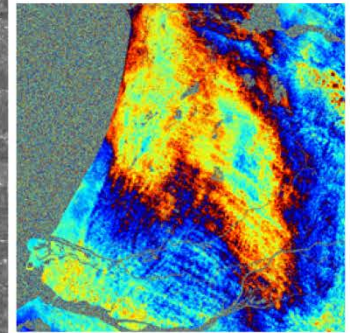
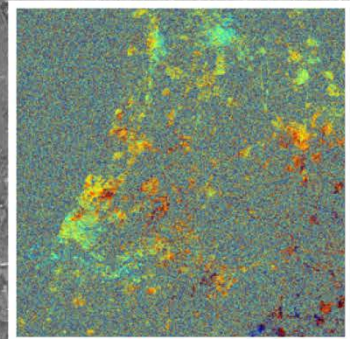


Persistent Scatterer Interferometry based on geodetic estimation theory

Freek van Leijen



Persistent Scatterer Interferometry based on geodetic estimation theory

Freek van Leijen

On the cover

Mean amplitude of a set of Envisat ASAR radar images of the western part of the Netherlands (background), together with a number of interferograms based on ERS-1/2 AMI radar images of the same region (in color).

Persistent Scatterer Interferometry based on geodetic estimation theory

PROEFSCHRIFT

ter verkrijging van de graad van doctor
aan de Technische Universiteit Delft,
op gezag van de Rector Magnificus prof. ir. K.C.A.M. Luyben,
voorzitter van het College voor Promoties,
in het openbaar te verdedigen op dinsdag 29 april 2014 om 15:00 uur
door

Frederik Johannes VAN LEIJEN

geodetisch ingenieur
geboren te Woerden.

Dit proefschrift is goedgekeurd door de promotoren:

Prof. dr. ir. R.F. Hanssen

Prof. dr. ir. P.J.G. Teunissen

Samenstelling promotiecommissie:

Rector Magnificus,	voorzitter
Prof. dr. ir. R.F. Hanssen,	Technische Universiteit Delft, promotor
Prof. dr. ir. P.J.G. Teunissen,	Technische Universiteit Delft, promotor
Prof. dr. A.J. Hooper,	University of Leeds
Prof. dr. ir. A. Stein,	Universiteit van Twente
Prof. ir. P. Hoozeboom,	Technische Universiteit Delft
PD Dr.-Ing. habil. X. Zhu,	Technische Universität München
Dr. ir. B.M. Kampes,	Royal Dutch Shell plc, Houston
Prof. dr. H.J.J. Jonker,	Technische Universiteit Delft, reservelid

van Leijen, Freek

Persistent Scatterer Interferometry based on geodetic estimation theory

Delft University of Technology

This research was financially supported by the dr. ir. Cornelis Lely Stichting.

Keywords: satellite radar interferometry, surface deformation, geodetic estimation and testing

ISBN 978-94-6186-299-0

Copyright © 2014 by Frederik Johannes van Leijen

All rights reserved. No part of the material protected by this copyright notice may be reproduced or utilized in any form or by any means, electronic or mechanical, including photocopying, recording or by any information storage and retrieval system, without the prior permission of the author.

Typeset by the author with the L^AT_EX Documentation System.

Published in the series: Publications on Geodesy, Nederlands Centrum voor Geodesie en Geo-informatie (NCG).

Preface

The idea of measuring millimetric motion of the Earth's surface from 800 kilometers altitude, without instruments on the ground, sounds crazy. Or at least I thought. However, from the nineties strong progress had been made in the field of satellite radar interferometry, which made it possible. I was eager to learn more about the technique. Lectures in Delft and a traineeship at the University of Cape Town, South Africa, gave me the first insights. However, the start of my PhD-research gave me the opportunity to focus completely on the topic.

Since then I analyzed many radar interferometric data sets from various places around the world. Each time I felt like an explorer, trying to discover new phenomena. What starts with a collection of billions of phase values between $-\pi$ and π , results in detailed knowledge of—possibly previously unknown—surface motion. By improving the algorithms, new surface motion features may become visible, even based on archived data. A great challenge to work on and I hope the research presented in this thesis forms a valuable contribution.

I am grateful to many people for their support during my research. Foremost, I would like to thank Ramon Hanssen for his supervision and overall guidance. I learned a lot from him, certainly not only about radar interferometry. His never ending enthusiasm and creativity have always been inspiring. Moreover, he enabled my participation in many interesting projects over the years. Furthermore, many thanks go to Peter Teunissen, who kept stimulating me to finish this thesis. I enjoyed the useful discussions we had.

A large part of the research presented in this thesis was performed in parallel with the research by my former colleagues Gini Ketelaar and Petar Marinkovic. Our close collaboration and team work resulted in a strong synergy, thereby significantly improving the results we obtained over the years. Many thanks for your contributions, the useful discussions, and the fun we had during conferences. Furthermore, the inputs from Miguel Caro Cuenca, Shizhuo Liu and Zbigniew Perski are highly appreciated. I also would like to thank Astrid Humme and Sami Samiei-Esfahany for their work and creativity during their MSc-projects and later on, which contributed to the content of this thesis. Also special thanks go to Petar Marinkovic, Mahmut Arikian and Prabu Dheenathayalan for their assistance in soft- and hardware related issues. Finally, I would like to thank the many other members of our radar group, who joined our group for shorter or longer terms over the years. I am sorry I cannot mention you all. It is great to work in such an international environment, with people from many different countries and cultures. I enjoyed the different food we tasted, the (political) discussions we had, but certainly also the beers we shared.

I am also grateful to my other colleagues within the MGP group for their support and providing a nice work environment. Especially, I would like to thank Ria Scholtes, Danko Roozmond, Lidwien de Jong, Rebeca Domingo, Rely van Wingaarden, Marjolein de Niet-de Jager, and File Koot-Stomp, for their administrative and project support. Also special thanks to Sandra Verhagen, who provided me with the latex-template for this thesis.

The content of this thesis benefited greatly from the critical reviews and valuable comments by my defense committee. This is highly appreciated. Furthermore, I would like to thank my paranymphs Bas Alberts and Lennard Huisman for their support in the final preparation of this manuscript.

This research was enabled by the financial support of the dr. ir. Cornelis Lely Stichting. A financial contribution from the Fulbright Program gave me the opportunity to perform a few months of my research at the University of Miami, USA. Falk Amelung and Tim Dixon, many thanks for having me.

The satellite radar data used in this thesis has been provided by the European Space Agency (ESA) and the German Space Agency (DLR). The SRTM data is made available by the National Aeronautics and Space Administration (NASA). The background imagery in some of the figures in this thesis is obtained from Google Maps.

Finally, I would like to thank my friends for providing the necessary amount of distraction from the never ending urge to improve one's research. And foremost, my father and mother, Tom and Nanda, and my sister, Anneloes, for their unconditional love and support.

Freek van Leijen
Delft, March 2014

Contents

Preface	i
Summary	vii
Samenvatting	ix
Nomenclature	xi
1 Introduction	1
1.1 Background	1
1.2 Research objective	3
1.3 Outline and methodology	4
2 Radar interferometry	7
2.1 Conventional interferometry	7
2.1.1 Imaging radar observations	7
2.1.2 The Single-Look Complex phase	9
2.1.3 The interferometric phase	10
2.2 Time series interferometry	20
2.2.1 Baseline configuration	23
2.2.2 Image resolution	24
2.2.3 Phase unwrapping	25
2.2.4 A-priori pixel selection	25
2.2.5 A-posteriori pixel selection	26
2.2.6 Atmospheric signal decomposition	26
2.2.7 Summary	27
3 PSI algorithm design and initialization	29
3.1 PSI algorithm design	29
3.2 Interferometric data stack creation	33
3.2.1 Master image selection	33
3.2.2 Image crop selection	35
3.2.3 Image oversampling and filtering	35
3.2.4 Image coregistration	36
3.2.5 Interferogram formation	38
3.3 Persistent Scatterer Candidate selection	40
3.3.1 PSC selection criteria	40
3.3.2 Amplitude calibration	43
3.3.3 PSC selection algorithm	43

3.4	Side lobe detection	45
3.4.1	Effect of side lobes	45
3.4.2	Side lobe detection procedure	49
3.5	Network formation	50
3.6	Summary	51
4	PSI temporal ambiguity resolution	53
4.1	Mathematical model	53
4.2	Functional model	54
4.2.1	Residual height	54
4.2.2	Deformation	56
4.2.3	Atmosphere and noise	58
4.2.4	Sub-pixel position	59
4.3	Stochastic model	61
4.4	Least-squares Variance Component Estimation (VCE)	65
4.5	Integer least-squares and integer bootstrapping	66
4.5.1	Integer least-squares in DePSI	67
4.5.2	Float solution	68
4.5.3	Ambiguity resolution	69
4.5.4	Fixed solution	75
4.5.5	Precision indicator: a-posteriori variance factor	75
4.6	Ambiguity function	76
4.7	Comparison of ambiguity resolution techniques	78
4.8	Summary	83
5	PSI spatial ambiguity resolution and phase screen estimation	85
5.1	Spatial ambiguity resolution	85
5.1.1	Testing of the ambiguities	86
5.1.2	Spatial ambiguity resolution algorithm	87
5.2	Orbital Phase Screen estimation	93
5.3	Atmospheric Phase Screen estimation	94
5.3.1	Atmospheric phase separation	94
5.3.2	Atmospheric phase prediction	95
5.4	PS densification	97
5.5	Summary	99
6	PS georeferencing and quality description	103
6.1	Georeferencing	103
6.1.1	Georeferencing procedure	103
6.1.2	Georeferencing accuracy	107
6.2	Quality indicators	112
6.2.1	Ensemble coherence estimator	113
6.2.2	Variance factor	114
6.2.3	Covariance matrix	115
6.2.4	Standard deviation displacements	115
6.2.5	Dilution of Precision for PSI	118
6.2.6	Spatio-temporal consistency	118
6.2.7	Summary quality indicators	118

6.3	Internal and external reliability assessment	120
6.4	Summary	122
7	PSI processing strategies: experimental results	125
7.1	The Las Vegas test case	125
7.2	Application of standard processing	128
7.3	Application of extended deformation models	133
7.4	Deformation Phase Screen (DPS) estimation	135
7.4.1	Algorithm of DPS estimation	135
7.4.2	Application of DPS estimation	138
7.5	Sequential deformation model testing	140
7.5.1	Algorithm of sequential deformation model testing	140
7.5.2	Application of sequential deformation model testing	142
7.6	Prognosis-based densification	144
7.6.1	Algorithm of prognosis-based densification	144
7.6.2	Application of prognosis-based densification	145
7.7	Area of Interest processing	147
7.7.1	Algorithm of Area of Interest processing	147
7.7.2	Application of Area of Interest processing	148
7.8	Time frame processing	151
7.8.1	Algorithm of time frame processing	151
7.8.2	Application of time frame processing	151
7.9	Summary and conclusions	154
8	Conclusions and recommendations	159
8.1	Conclusions	159
8.2	Contributions	162
8.3	Recommendations	163
	Bibliography	165
A	Geodetic data analysis	177
A.1	Estimation	177
A.2	Testing and quality control	178
A.2.1	Detection	180
A.2.2	Identification	180
A.2.3	Adaption	181
A.3	Prediction	181
A.4	Least-squares Variance Component Estimation (VCE)	183
A.5	Integer least-squares	183
A.5.1	Admissible integer estimators	186
A.5.2	On the quality of the solutions: Success rate	189
B	Adopted PSI terminology	191
C	Algorithm implementation	193
	Curriculum Vitae	195

Summary

Persistent Scatterer Interferometry based on geodetic estimation theory

Satellite radar interferometry (InSAR) is a powerful technique to measure motion of the Earth's surface. However, the applicability of the conventional approach is limited due to error sources: temporal decorrelation, geometric decorrelation, and atmospheric signal delay. Radar interferometric time series approaches have been developed to overcome these degrading factors. By using the information content of a full radar image stack, the impact of the error sources can be reduced and time series of the deformation history can be estimated.

The Persistent Scatterer Interferometry (PSI) technique, one of the time series approaches, is based on the coherent phase history of point scatterers. Since the location of these point scatterers is not known beforehand, PSI comprises both an estimation and a detection problem. The complicating factor in the estimation and detection process is the wrapped condition of the phase observations, i.e., phase observations in the $[-\pi, +\pi)$ interval. As a consequence, the coherence of an image pixel in the time domain cannot be assessed directly. Furthermore, assumptions regarding the spatial and/or temporal smoothness of the deformation signal, expressed by a model, are required to estimate the unknown phase ambiguities. Therefore, both the correctness of the model used, and the actual phase persistence of the pre-selected pixels should be assessed. The multiple, model dependent, possible solutions, in combination with the uncertainty in the actual noise level of a certain image pixel, require a balanced procedure in the estimation and detection process. Hereby, the number of false detections and false rejections of these Persistent Scatterers (PS) should be minimized.

This thesis describes the design, implementation, and evaluation of a new Persistent Scatterer Interferometry algorithm, the Delft implementation of PSI (DePSI). The algorithm is based on a framework of geodetic estimation, testing, and quality control techniques, known as the 'Delft school'. Using this framework, the algorithm is able to detect point scatterers with consistent reflection properties over time, for which the deformation time series can be estimated with sufficient reliability.

For the design and implementation of the algorithm, three main problems can be identified: algorithm design, ambiguity resolution, and Persistent Scatterer detection. The design of the algorithm is inspired by previously developed PSI approaches and methodologies applied to conventional geodetic measurement techniques. The performance of three ambiguity resolution techniques, integer least-squares (ILS), integer bootstrapping (IB), and the ambiguity function (AF), is evaluated based on simulations. To assess the best strategy to optimize the number of detected PS, seven different processing strategies are applied to real data of Las Vegas, USA.

The design of the algorithm is characterized by a hierarchic structure of PS networks and an iterative approach to improve the stochastic model used for the estimations. The hierarchic structure is based on first- and higher-order networks of PS, comparable to the concept used for conventional geodetic techniques. The first-order network forms the backbone of the analysis and aims to ensure the overall integrity of the full area analyzed, whereas the higher-order networks provide a further densification of the measurement points. In each iteration, a phase screen of an error source, such as atmospheric signal delay or orbit error, is estimated and removed, followed by an update of the stochastic model by least-squares variance component estimation.

The phase ambiguities are resolved in a two-step procedure. First, an estimation in the temporal domain is performed for the differential phase observations of each arc between two Persistent Scatterer Candidates (PSC), which are initially selected based on the amplitude dispersion in the data stack. The simulations show that the integer least-squares and ambiguity function estimator provide equivalent success rates for moderate deformation rates per arc. However, the advantage of the ILS estimator is that more than two model parameters can be estimated and that a proper error propagation can be obtained. Because of the limited computational load of the IB estimator with respect to the ILS estimator, the IB estimator is a good alternative.

The second step in the ambiguity resolution is a spatial integration of the estimated arcs based on a novel testing scheme to remove wrongly estimated arcs and inconsistent PSC. The testing is based on the integer ambiguities, instead of the real-valued parameters. This approach enables the use of varying deformation models in the temporal phase unwrapping, thereby ensuring a consistent network. Hence, models adapted to the local deformation behavior can be evaluated instead of a general model applied to the full area.

The assessment of the detected PS and estimated deformation time series of the Las Vegas data set shows that the use of spatially local deformation models instead of a general model improves the PSI results. Furthermore, it is shown that although the amplitude dispersion is a good indicator of the most phase persistent scatterers, many PS with a low amplitude dispersion exist. Therefore, when computational resources allow, all pixels with a local amplitude maximum should be evaluated. Nevertheless, the amplitude provides useful information which should be better exploited.

Despite the thorough testing of the ambiguities, the seven evaluated processing strategies still show a certain degree of falsely detected PS. Therefore, additional quality indicators are required to obtain a final selection of PS. Local quality indicators, such as the Spatio-Temporal Consistency (STC) or local ensemble coherence estimator, give a better performance because they are less sensitive to model imperfections and therefore give a better estimate of the noise level in the deformation time series.

Samenvatting

Persistent Scatterer Interferometrie gebaseerd op geodetische schattingstheorie

Satellietradarinterferometrie (InSAR) is een effectieve techniek om beweging van het aardoppervlak te meten. De toepasbaarheid van de conventionele aanpak is echter beperkt vanwege foutenbronnen: temporele decorrelatie, geometrische decorrelatie, en atmosferische signaalvertraging. Om deze versturende factoren te ondervangen zijn radarinterferometrische tijdreeksmethoden ontwikkeld. Door de informatie-inhoud van de volledige set radarbeelden te gebruiken kan de invloed van de foutenbronnen worden vermindert en kunnen tijdreeksen met de deformatiehistorie worden geschat.

De Persistent Scatterer Interferometrie (PSI) techniek, één van de tijdreeksmethoden, is gebaseerd op de coherente fasegeschiedenis van puntreflecties. Omdat de locatie van deze puntreflecties op voorhand onbekend is, omvat PSI zowel een schattings- als een detectieprobleem. De complicerende factor in het schattings- en detectieproces is de teruggevouwen staat van de fasewaarnemingen, dat wil zeggen, fasewaarnemingen in het $[-\pi, +\pi)$ interval. Als gevolg daarvan kan de coherentie van een beeldpixel in het tijdsdomein niet rechtstreeks worden bepaald. Bovendien zijn veronderstellingen met betrekking tot de ruimtelijke en/of temporele gladheid van het deformatiesignaal nodig, beschreven door een model, om de onbekende fasemeerduidigheden te schatten. Daarom moeten zowel de juistheid van het model, als de daadwerkelijke fasestabiliteit van de voorgeselecteerde pixels worden bepaald. De meerdere, modelafhankelijke, mogelijke oplossingen vereisen, samen met de onzekerheid in het werkelijke ruisniveau van een bepaald beeldpixel, een evenwichtige procedure in het schattings- en detectieproces. Hierbij moet het aantal valse detecties en valse verwerpingen van deze Persistent Scatterers (PS) worden geminimaliseerd.

Dit proefschrift beschrijft het ontwerp, de implementatie en de evaluatie van een nieuw Persistent Scatterer Interferometrie algoritme, de Delftse implementatie van PSI (DePSI). Het algoritme is gebaseerd op een raamwerk van geodetische schattings-, toets-, en kwaliteitscontroletechnieken, bekend als de 'Delftse School'. Met behulp van dit raamwerk is het algoritme in staat punten met stabiele reflecties in de tijd te detecteren, waarvoor de deformatietijdreeks met voldoende betrouwbaarheid kan worden geschat.

Voor het ontwerp en de implementatie van het algoritme kunnen drie belangrijke problemen worden geïdentificeerd: algoritme ontwerp, meerduidigheidsbepaling, en Persistent Scatterer detectie. Het ontwerp van het algoritme is geïnspireerd door eerder ontwikkelde PSI aanpakken en methoden die zijn toegepast voor conventionele geodetische meettechnieken. De prestatie van drie meerduidigheidsbepalingstechnieken, geheeltallige kleinstekwadraten (ILS), geheeltallige conditionele afronding (IB), en de meerduidigheidsfunctie (AF), is geëvalueerd op basis van simulaties. Om de beste strategie voor

het optimaliseren van het aantal gedetecteerde PS te bepalen zijn zeven verschillende verwerkingsstrategieën toegepast op echte data van Las Vegas, VS.

Het ontwerp van het algoritme wordt gekenmerkt door een hiërarchische structuur van PS netwerken en een iteratieve benadering voor het verbeteren van het stochastisch model dat wordt gebruikt voor de schattingen. De hiërarchische structuur is gebaseerd op eerste- en hogere-orde PS netwerken, vergelijkbaar met het concept dat gebruikt wordt voor conventionele geodetische technieken. Het eerste-orde netwerk vormt de ruggraat van de analyse en zorgt voor de algehele integriteit van het volledige geanalyseerde gebied, terwijl de hogere-orde netwerken een verdere verdichting van de meetpunten verzorgen. In iedere iteratie wordt een fasebeeld van een foutenbron, bijvoorbeeld de atmosferische signaalvertraging of een baanfout, geschat en verwijderd, gevolgd door een aanpassing van het stochastisch model door kleinstekwadraten variantiecomponentenschatting.

De fasemeerduidigheden worden in twee stappen opgelost. Allereerst wordt een schatting in het temporele domein uitgevoerd voor de differentiële fasewaarnemingen van elke verbinding tussen twee Persistent Scatterer Kandidaten (PSC), die aanvankelijk zijn geselecteerd op basis van de amplitudespreiding in de dataset. De simulaties tonen dat de geheeltallige kleinstekwadraten- en de meerduidigheidsfunctieschatter een gelijkwaardige slagingskans hebben voor bescheiden deformatiesnelheden per verbinding. Echter, het voordeel van de ILS-schatter is dat meer dan twee modelparameters kunnen worden geschat en dat een gedegen foutvoortplanting kan worden verkregen. Vanwege de beperkte berekeningsbelasting van de IB-schatter ten opzichte van de ILS-schatter, vormt de IB-schatter een goed alternatief.

De tweede stap in de meerduidigheidsbepaling is een ruimtelijke integratie van de geschatte netwerkverbindingen gebaseerd op een nieuwe toetsprocedure om foutief geschatte verbindingen en inconsistente PSC te verwijderen. De toetsing is gebaseerd op de geheeltallige fasemeerduidigheden in plaats van de parameters met reële waarden. Deze aanpak maakt het gebruik van verschillende deformatiemodellen in de temporale meerduidigheidsbepaling mogelijk, waarbij een consistent netwerk wordt gewaarborgd. Hierdoor kunnen modellen die zijn aangepast aan het lokale deformatiegedrag worden geëvalueerd in plaats van een algemeen toegepast model voor het volledige gebied.

Uit de beoordeling van de gedetecteerde PS en de geschatte deformatietijdreeksen van de Las Vegas dataset blijkt dat het gebruik van ruimtelijk lokale deformatiemodellen in plaats van een algemeen model leidt tot een verbetering van de PSI resultaten. Verder wordt aangetoond dat hoewel de amplitudespreiding een goede indicator is van de meest stabiele reflectiepunten, er ook veel PS met een lage amplitudespreiding voorkomen. Daarom zouden, als de verwerkingsmiddelen het toelaten, alle pixels met een lokaal amplitude maximum moeten worden geëvalueerd. Niettemin geeft de amplitude nuttige informatie die beter moet worden benut.

Ondanks de strenge toetsing van de fasemeerduidigheden tonen de resultaten van de zeven geëvalueerde verwerkingsstrategieën nog steeds een zekere mate van foutief gedetecteerde PS. Aanvullende kwaliteitsindicatoren zijn daarom nodig om tot een definitieve selectie van PS te komen. Lokale kwaliteitsindicatoren, zoals de Spatio-Temporal Consistentie (STC) en de lokale ensemble coherentieschatter, presteren beter omdat ze minder gevoelig zijn voor onvolkomenheden in het model en geven daardoor een betere schatting van het ruisniveau in de deformatietijdreeksen.

Nomenclature

List of acronyms

1D	one-dimensional
2D	two-dimensional
3D	three-dimensional
ADOP	Ambiguity Dilution Of Precision
AF	Ambiguity function
ALOS	Advanced Land Observing Satellite
AOI	Area Of Interest
APS	Atmospheric Phase Screen
ASAR	Advanced Synthetic Aperture Radar
BLUE	Best Linear Unbiased Estimator/Estimation
BLUP	Best Linear Unbiased Predictor/Prediction
COSMO-SkyMed	COntellation of small Satellites for the Mediterranean basin Observation
DEM	Digital Elevation Model
DEOS	Delft institute of Earth Observation and Space systems
DePSI	Delft implementation of Persistent Scatterer Interferometry
DIA	Detection, Identification and Adaption
DInSAR	Differential Interferometric Synthetic Aperture Radar
DLR	Deutschen Zentrums für Luft- und Raumfahrt (German Space Agency)
DORIS	Delft Object-oriented Radar Interferometric Software
DPS	Deformation Phase Screen
DSM	Digital Surface Model
DTM	Digital Terrain Model
EGM96	Earth Gravitational Model 1996
Envisat	Environmental satellite
ERS	European Remote Sensing satellite
ESA	European Space Agency
GB	Gigabyte
GIS	Geographic Information System
GNSS	Global Navigation Satellite System(s)
GPS	Global Positioning System
IB	Integer bootstrapping
ILS	Integer least-squares

InSAR	Interferometric Synthetic Aperture Radar
LAMBDA	Least-squares AMBIGUITY Decorrelation Adjustment
LOS	Line of Sight
MCF	Minimum Cost Flow
ML	Maximum Likelihood
MUSIC	MULTiple Signal Classification
NASA	National Aeronautics and Space Administration
OMT	Overall Model Test
OPS	Orbital Phase Screen
PDF	Probability Density Function
PMF	Probability Mass Function
PRF	Pulse Repetition Frequency
PS	Persistent Scatterer
PS1	First-order Persistent Scatterer
PS2	Second-order Persistent Scatterer
PSC1	First-order Persistent Scatterer Candidate
PSC2	Second-order Persistent Scatterer Candidate
PSC	Persistent Scatterer Candidate
PSI	Persistent Scatterer Interferometry
RCS	Radar Cross Section
RSR	Range Sampling Rate
SAR	Synthetic Aperture Radar
SBAS	Small BAseline Subset
SCR	Signal-to-Clutter Ratio
SLC	Single-Look Complex
SRTM	Shuttle Radar Topography Mission
StaMPS	Stanford Method for PS
STC	Spatio-Temporal Consistency
TEC	Total Electron Content
TECU	Total Electron Content Unit
VCE	Variance Component Estimation
WGS84	World Geodetic System 1984

List of symbols

a	Phase ambiguity
A	Amplitude; Design matrix
A_0	Design matrix for predictions
b	Real-valued unknowns
B	Baseline [m]; Design matrix
B_{\parallel}	Parallel baseline [m]
B_{\perp}	Perpendicular baseline [m]
$B_{\perp_{crit}}$	Critical baseline [m]
B_{az}	Azimuth bandwidth [Hz]
B_D	Doppler baseline [Hz]
B_{max}	Maximum baseline
B_r	Range bandwidth [Hz]

B_t	Temporal baseline [year]
c	Speed of light [ms^{-1}]
C_q	Matrix specifying alternative hypothesis of dimension q
D	Deformation in radar Line of Sight
D_A	Normalized amplitude dispersion
e	Residuals (stochastic)
\hat{e}	Adjusted residuals
\hat{e}_0	Residuals under the null hypothesis
\hat{e}_a	Residuals under the alternative hypothesis
f	Carrier frequency
H	Height [m]
H_0	Null hypothesis
H_a	Alternative hypothesis
H_{sat}	Height of satellite
i	Imaginary unit
I	Intensity; Identity matrix
k_α	Critical value
m	Number of observations; master image
M	Master image antenna position
n	Number of unknowns
\underline{n}	Noise (stochastic)
\underline{n}_0	Noise at unobserved location
$\hat{\underline{n}}$	Adjusted noise
$\hat{\underline{n}}_0$	Predicted noise
P	Phasor
P_A^\perp	Orthogonal projector
P_0	Point on reference surface
P_H	Point at height H
q	Number of model imperfections
Q_0	Known part of the covariance matrix
$Q_{\hat{e}}$	Covariance matrix of residuals
$Q_{\hat{e}_0}$	Covariance matrix of prediction error
Q_n	Covariance matrix of noise
Q_{n_0}	Covariance matrix of noise to be predicted
Q_s	Covariance matrix of signal variables
Q_{s_0}	Covariance matrix of signal variables to be predicted
Q_{ss_0}	Cross-covariance matrix of signal variables
$Q_{\hat{\sigma}}$	Covariance matrix of (co-)variance component estimates
$Q_{\hat{x}}$	Covariance matrix of estimated unknowns
Q_y	Covariance matrix of observations
Q_{y_0}	Covariance matrix of observations to be predicted
$Q_{\hat{y}}$	Covariance matrix of adjusted observations
R	Range to master antenna position [m]
s	Slave image
\underline{s}	Signal variables (stochastic)
\underline{s}_0	Signal variables at unobserved location
$\hat{\underline{s}}$	Estimated signal variables

$\hat{\underline{s}}_0$	Predicted signal variables
S	Slave image antenna position; Master atmospheric delay; Number of slave images; Number of interferograms
T_q	Test statistic of dimension q
t_r	Range time
x	Unknown variables
\hat{x}	Estimated unknowns
x_0	Expectation value under null hypothesis
x_a	Expectation value under alternative hypothesis
y	Observations (stochastic)
\underline{y}_0	Variables at unobserved location
\hat{y}	Adjusted observations
$\underline{\hat{y}}_0$	Predicted observations
α	Baseline orientation; Level of significance
β	Level of false rejection of null hypothesis
ΔT	Repeat cycle [days]
Δ_{az}	Azimuth resolution
Δ_{sr}	Slant range resolution
Δ_{gr}	Ground range resolution
$\hat{\underline{\epsilon}}_0$	Prediction error
γ	Coherence; Power of the test
γ_0	General power of the test
γ_{Dc}	Coherence (reduction) due to Doppler centroid decorrelation
γ_{geom}	Coherence (reduction) due to geometric decorrelation
γ_{proc}	Coherence (reduction) due to processing induced decorrelation
γ_{temp}	Coherence (reduction) due to temporal decorrelation
γ_{ther}	Coherence (reduction) due to thermal or system noise
γ_{tot}	Total coherence
λ	Radar wavelength [m]; Non-centrality parameter
μ_A	Mean of amplitude
∇	Vector of model imperfections
ψ	SLC phase
ψ_{atmo}	Atmospheric SLC phase
ψ_{range}	Range dependent SLC phase
ψ_{scat}	Scattering SLC phase
φ	Interferometric phase
φ_{flat}	Flat Earth phase
φ_{topo}	Topographic phase
φ_{defo}	Deformation phase
φ_{atmo}	Atmospheric phase
φ_{orb}	Orbital phase
φ_{scat}	Scattering phase
σ_A	Standard deviation of amplitude
$\sigma_{\hat{\epsilon}}$	Standard deviation of residuals
σ_{n_I}	Standard deviation of imaginary part of SLC signal
σ_{ψ}	Standard deviation of SLC phase

$\hat{\sigma}$	Estimated (co-)variance components
θ	Look angle
θ_{inc}	Incidence angle
ζ	Topographic slope
\mathbb{R}	Domain of real values
\mathbb{Z}	Domain of integer values

List of operators and annotations

$\{\cdot\}$	Stochasticity
$\ \cdot\ _Q^2$	Weighted norm, $\ \cdot\ _Q^2 = (\cdot)^T Q^{-1}(\cdot)$
$\{\cdot\}^{-1}$	Inverse
$\{\cdot\}^T$	Transpose
$\{\cdot\}^*$	Complex conjugate
$[\cdot]$	Rounding to the nearest integer
$\lfloor \cdot \rfloor$	Rounding to the next smaller integer
$d(\cdot, \cdot)$	Distance operator
$\det(\cdot)$	Determinant
$D\{\cdot\}$	Dispersion operator
$\exp(\cdot)$	Exponential function
$E\{\cdot\}$	Expectation operator
$\text{Im}\{\cdot\}$	Imaginary part
$\ln(\cdot)$	Natural logarithm
$\max(\cdot, \cdot)$	Maximum operator
$P(\cdot)$	Probability density function
$\text{Re}\{\cdot\}$	Real part
$\text{tr}(\cdot)$	Trace of matrix, i.e., the sum of the diagonal elements
$\chi^2(q, \lambda)$	χ^2 -distribution with q degrees of freedom and non-centrality parameter λ

1.1 Background

From the late 1980's, space-based Interferometric Synthetic Aperture Radar (InSAR) has been used to measure deformations of the Earth's surface (Gabriel et al., 1989). For the first time it was possible to visualize the consequences of earthquakes (Massonnet et al., 1993), volcanism (Massonnet et al., 1995), oil and gas extraction (van der Kooij, 1997), groundwater flow (Amelung et al., 1999), ice motion (Goldstein et al., 1993), and geotechnical processes such as landslides (Fruneau et al., 1996), as a full 2D picture. Radar interferometry is the only technique capable of measuring these phenomena with the unique combination of high spatial resolution, medium temporal sampling, and wide-scale coverage. Moreover, the available data archive, starting in 1992 with radar images acquired by the ERS-1 satellite, enables the analysis of a large part of the Earth in retrospective.

However, although excellent results have been shown using conventional InSAR, these are often obtained under favorable conditions. In general, the repeat-pass principle applied induces three main degrading factors. First, the variable state of the atmosphere in time and space superimposes an error signal that interferes with the deformation signal. Second, the scattering characteristics of the Earth's surface within a resolution cell may change over time, resulting in temporal decorrelation. Third, the satellite repeat orbits may be too far apart, resulting in incomparable scattering characteristics due to the different imaging geometry, known as geometric decorrelation. As a consequence of these three factors, the information content of an available pair of radar images cannot be fully exploited based on conventional radar interferometry.

To overcome the degrading factors of the conventional approach, InSAR research progressed to *time series analyses*, i.e., the use of a stack of radar acquisitions of the same area. Three main approaches can be distinguished, the *Persistent Scatterer Interferometry* (PSI) approach, the *Small BAseline Subset* (SBAS) approach, and hybrid methods. The PSI technique (Ferretti et al., 2000, 2001) focuses on the subset of points which show relatively constant scattering properties in time. It was recognized that certain features, often man-made, show a stable phase behavior over long time intervals, hence with minimal temporal decorrelation (Usai, 1997; Usai and Hanssen, 1997). Because of the reflection dominance of these point scatterers within an image resolution cell, the effect of geometric decorrelation is also strongly reduced. The PSI technique uses these isolated point scatterers to derive displacement time series. Due to the use of the stack

of radar acquisitions, the temporally uncorrelated atmospheric phase component in the observations can be estimated and removed. Hereby, the contribution of this noise factor in the Persistent Scatterer (PS) deformation time series is reduced.

An alternative approach in radar interferometric time series analysis is based on the use of subsets of interferograms with small baselines, denoted as the *Small Baseline Subset* (SBAS) technique (Berardino et al., 2002; Mora et al., 2003). Baseline here indicates the distance between the two radar images involved, either in satellite position or acquisition time. Hence, by using small baselines, both the geometric and temporal decorrelation effect are reduced, albeit with a degree that is location (land cover) dependent. Due to the small baselines and multi-looking of the image pixels that is often applied, the SBAS approach is particularly suitable for distributed scattering mechanisms, which occur in rural regions with (semi-)bare surfaces.

Based on the PSI and SBAS techniques, a third group of hybrid methods evolved with the objective to retrieve measurements from both point scattering and distributed scattering mechanisms. These methods have in common an increased use of spatial correlation between neighboring pixels. Lanari et al. (2004) extended the SBAS approach by an integrated analysis of the interferograms at both multi-looked and single-look scale. The standard SBAS approach based on the multi-looked interferograms is applied to retrieve the wide-scale deformation patterns. This is followed by an analysis in the time domain at single-look resolution after adaption of the interferometric phases by the wide-scale components. Alternatively, Hooper (2008) used multiple image pixels within a certain radius to estimate spatially correlated parameters, such as deformation and atmospheric signal delay, followed by an estimation of residual phase contributions for individual pixels, e.g., due to the topographic height. Ferretti et al. (2011) applied a clustering of pixels with equivalent scattering characteristics to reduce the noise level compared to the individual pixels. Moreover, a coherence matrix describing the correlation between the radar images is used to optimize the estimation in the time domain.

All methods are based on assumptions regarding the spatial and/or temporal smoothness of the deformation signal, expressed by a model. These assumptions are required due to the *wrapped* phase observations, i.e., phase observations in the $[-\pi, +\pi]$ interval. The model used is either explicit, e.g., a linear deformation rate in time, or implicit, e.g., maximum deformation between neighboring pixels with a phase-equivalent less than π . A variety of techniques is used to unwrap the phase and to estimate the deformation signal. However, the quality control of the results is often only sparsely addressed. Both the correctness of the model used, and the actual phase persistence of the pre-selected pixels should be assessed. Besides, the quality description of the estimates may not be optimal. For example, in many cases the ensemble coherence in the time domain is used to describe the quality. However, due to the cyclic nature of the phases, the coherence estimator is insensitive to phase unwrapping errors. Hence, a PSI implementation should not only provide deformation estimates, but should also enable a profound quality control.

In the last century, Delft University of Technology developed a framework of geodetic estimation (Tienstra, 1956), testing (Baarda, 1968), and quality control (Teunissen, 1990) techniques, known as the 'Delft school'. The framework is characterized by the explicit formulation of a mathematical model, consisting of a functional model describing the relation between stochastic observations and unknown deterministic parameters, and a stochastic model, based on second-order statistics. Hence, instead of the full

probability density function, only the variances and covariances of the observations are considered. Application is possible for every geodetic measurement technique, for example in leveling, tachymetry, and satellite navigation. Regarding radar interferometry, the Delft school techniques are applied to conventional InSAR (Hanssen, 2001), and Persistent Scatterer Interferometry (Kampes, 2006). However, at the start of the underlying study no practical PSI implementation existed at Delft University of Technology. This formed the starting point of this work: establishing a software implementation of Persistent Scatterer Interferometry using the conceptual methodology of the Delft school.

1.2 Research objective

The objective of this research is

to design, implement, evaluate, and document a Persistent Scatterer Interferometry algorithm based on geodetic estimation and testing techniques.

The estimation and testing methodologies developed within the Delft school framework will be used, including advanced methods such as least-squares prediction (Teunissen, 2007), least-squares variance component estimation (Teunissen, 1988; Teunissen and Amiri-Simkooei, 2008), and integer least-squares estimation (Teunissen, 1993).

From a geodetic perspective, PSI is fundamentally different compared to conventional surveying techniques. Whereas conventional techniques are based on pre-defined benchmarks or receivers, Persistent Scatterer Interferometry is characterized by an a-priori unknown location of the measurement points. These locations are dependent on the specific orientation and other characteristics of objects on the surface in relation to the direction of the transmitted radar signal. Hence, an opportunistic set of reflection points is obtained, which do not necessarily sample the signal of interest in an optimal way, as can be achieved with conventional benchmarks. Moreover, it is non-trivial to actually detect these reflection points amidst all pixels in a radar image. As a consequence, PSI comprises not only an estimation problem, but also a *detection* problem. This results in a causality dilemma: to detect the coherent pixels, the phase components should be estimated, however, to estimate the phase components, the coherent points should be known.

Complicating factor in the estimation and detection process are the wrapped phase observations. Estimation of the deformation time series therefore requires the estimation of the integer-valued phase ambiguities. Since the radar images only provide a single observation for each location at a certain epoch, and each observation induces an unknown phase ambiguity, radar interferometric observations lack redundancy. As a consequence, the estimation process is ill-posed and multiple solutions are possible. The solution space is only constrained based on assumptions regarding the spatial and/or temporal smoothness of the deformation signal and additional parameters, such as topographic height, expressed by the mathematical model. The multiple, model dependent, solutions, in combination with the uncertainty in the actual noise level of a certain image pixel, require a balanced procedure in the estimation and detection process. Since the noise level of the different points follows a gradual scale, this leads to a trade-off between quality and point density. That is, a high point density could be obtained at the expense of a reduced quality, or a high quality level is preserved, thereby reducing

the number of detected PS. Hence, sub-optimal conditions in this trade-off might either result in too many *false detections* or *false rejections* of Persistent Scatterers. A false detection is here defined as a selected point which is either not coherent, or has, despite its coherence, an incorrectly estimated deformation time series. A false rejection is a PS which remains undetected. To minimize the number of false detections and false rejections, the Delft school methodology will be applied to test the estimates to obtain an optimal set of detected PS.

The estimation and detection problem imposed by PSI leads to three main components to be addressed in this study: algorithm design, ambiguity resolution, and Persistent Scatterer detection.

1. Algorithm design

The overall question for the algorithm design is how to transform a stack of radar images to reliable deformation time series of a set of detected PS. A typical image stack of 80 ERS-1/2 or Envisat acquisitions, with 25000×5000 pixels ($\sim 100 \times 100$ km) contains 10 billion pixels, with even so many unknown phase ambiguities. This number further increases for very high-resolution satellite missions (TerraSAR-X, Cosmo-SkyMed) or wide-swath acquisitions (Sentinel-1). Hence, even when only a part of the full image frame is analyzed, the algorithm should be efficient. Furthermore, the consistency of the results over the complete analyzed area should be preserved, i.e., the likelihood of ambiguity error propagation needs to be minimized. Finally, the algorithm should be able to estimate error sources, such as atmospheric signal delay and noise, either in functional or stochastic form, to optimize the results.

2. Ambiguity resolution

Due to the wrapped nature of the phase observations, the estimation problem not only contains real-valued, but also integer-valued parameters, i.e., phase ambiguities. These ambiguities occur both in the temporal (1D) and spatial (2D) domain, together forming a 3D ambiguity resolution problem. The method applied in the algorithm to estimate the ambiguities should be flexible regarding the mathematical model used, both in time and in space. Furthermore, it should allow testing of the estimates to detect and resolve errors.

3. Persistent Scatterer detection

The objective of the algorithm is to optimize the number of detected PS, preserving the reliability of the deformation time series. Hence, not only the location of the PS should be retrieved, but the estimated time series should reflect the actual deformation history of the scatterer. Hence, both the number of false rejections and the number of false detections should be minimized. The question is which processing strategy and detection criterion is most suitable to meet this objective.

1.3 Outline and methodology

This thesis contains eight chapters and two appendices. Chapter 2 gives both a brief introduction to radar interferometry and an overview of existing radar interferometric time series analysis methods, including their characteristics. These methods, especially

the original PSI methodology (Ferretti et al., 2001) and the PSI algorithm based on geodetic data processing techniques by Kampes (2006), inspired the design of the algorithm presented in this thesis. In the new design there is a particular focus on an iterative update of the stochastic model, a direct testing of the estimated phase ambiguities, and the ability to apply local deformation models to increase the number of detected PS.

The algorithm, which is denoted as *Delft Persistent Scatterer Interferometry* (DePSI), is described in four parts in Chapters 3–6. Chapter 3 presents the structure of the algorithm, together with the pre-processing steps required to obtain the interferometric data stack. To reduce the amount of data, Persistent Scatterer Candidates (PSC) are selected and side lobes are detected and removed. These selection and detection steps are described in this chapter as well.

The phase ambiguities of the PSC are estimated in a two-step procedure. Chapter 4 discusses the first step, the estimation of the ambiguities in the temporal domain between two nearby PSC. Three estimators are implemented and evaluated based on simulated data: integer least-squares, integer bootstrapping, and the ambiguity function. The second step, the ambiguity resolution in the spatial domain, is presented in Chapter 5. A testing scheme is applied to detect and correct ambiguity errors and to remove non-persistent candidates. Once the ambiguities are resolved, error sources such as orbit errors and atmospheric signal delay can be estimated and removed from the phase observations. The estimation of these *Phase Screens* is also discussed in this chapter.

Chapter 6 describes the procedure to georeference the detected Persistent Scatterers, together with an assessment of the georeference precision. Furthermore, an overview of quality indicators and strategies for quality assessment of the results are given.

The design of DePSI enables the application of different processing strategies. The objective of these strategies is to increase the number of detected PS and the reliability of the results, i.e., the reduction of the number of false rejections and false detections. Chapter 7 contains the description and evaluation of seven processing strategies: 1) the standard approach using a linear deformation model, 2) the use of extended deformation models for the full area, 3) estimation of the Deformation Phase Screen (DPS), 4) the sequential testing of deformation models, 5) densification based on a PS density prognosis, 6) area of interest processing, and 7) time frame processing. These strategies are demonstrated and evaluated based on a data stack of ERS-1/2 images over Las Vegas, USA. This area is chosen because it experiences strong ground motion due to groundwater withdrawal, also associated with seasonal fluctuations, thereby forming a suitable test site. During the evaluation also the criteria used for the actual detection of the PS, i.e., testing of ambiguities and thresholds on quality indicators, are assessed.

The conclusions, contributions and recommendations that follow from this research are formulated in Chapter 8. Appendix A gives a description of the various geodetic data processing techniques applied, such as parameter estimation, testing, prediction, variance component estimation, and integer least-squares. An overview of specific terminology used within DePSI is given in Appendix B. Finally, Appendix C discusses the implementation of the algorithm, which is realized in Matlab®.

The fundamental technique used in this research is known as Interferometric Synthetic Aperture Radar (InSAR). Section 2.1 contains a brief overview of the most relevant characteristics of the technique. As with any technique, InSAR has a number of limitations. To circumvent part of these limitations, recent research (Ferretti et al., 2001; Berardino et al., 2002; Hooper et al., 2004; Kampes, 2006; Hooper, 2008; Ferretti et al., 2011) regarding deformation studies has focused on the use of time series of radar data. In Section 2.2 various radar interferometric time series analysis approaches are discussed and compared.

2.1 Conventional interferometry

Interferometric Synthetic Aperture Radar (InSAR), also known as *radar interferometry*, is based on the interferometric processing of radar images. Two radar images are interfered to extract information about the Earth's surface or atmosphere (Bamler and Hartl, 1998; Hanssen, 2001). The main applications are deformation analysis and topographic mapping. A brief theoretical background of InSAR is described here, starting from the imaging radar observations. For a more detailed discussion the reader is referred to Hanssen (2001).

2.1.1 Imaging radar observations

Radar images are acquired by active radars on-board airborne or spaceborne platforms and contain information about both the intensity of the reflection from, and the travel time to, the Earth's surface. The intensity I of the reflection is commonly represented by the magnitude or *amplitude* $A = \sqrt{I}$, whereas the range travel time determines the measured fractional phase of the received radar signal ψ . The total radar measurement per pixel is denoted by the complex *phasor* P (Hanssen, 2001)

$$P = A \exp(i\psi). \quad (2.1)$$

The real and imaginary part of the phasor, $\text{Re}\{P\} = A \cos(\psi)$ and $\text{Im}\{P\} = A \sin(\psi)$, are stored in a regular grid, forming the two-dimensional radar image, see Figure 2.1. The relation between the complex values $\text{Re}\{P\}$ and $\text{Im}\{P\}$ and the amplitude A and

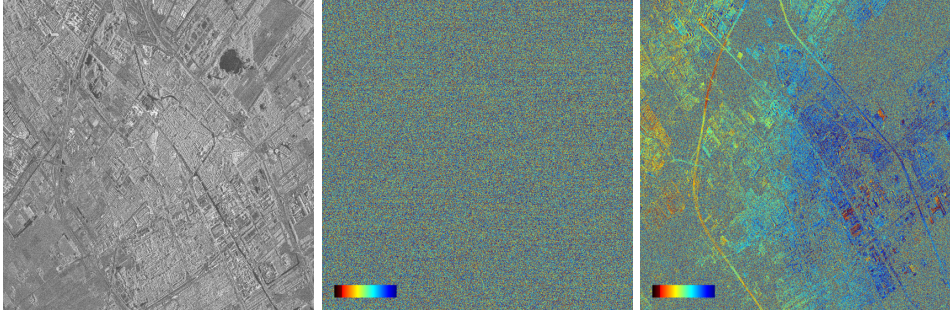


Figure 2.1: Left) Amplitude of an SLC image (Delft, the Netherlands, acquired by the TerraSAR-X satellite). Strong reflections are visualized in white, whereas areas with limited reflection towards the satellite (such as water bodies) are represented in black. Middle) Phase of an SLC image. Only the fractional phase of the received signal is recorded, resulting in phase values between $-\pi$ and $+\pi$. The phase in an SLC image cannot be interpreted directly. Right) Phase of an interferogram. After combination of two SLC images, interpretable phase information is obtained.

range dependent phase ψ is (see also Figure 2.2)

$$A = \sqrt{(\text{Re}\{P\})^2 + (\text{Im}\{P\})^2}, \quad (2.2)$$

$$\psi = \arctan\left(\frac{\text{Im}\{P\}}{\text{Re}\{P\}}\right).$$

The complex value of a resolution cell within the radar image is formed by the summation of all reflections from the corresponding area on the Earth's surface. This is illustrated in Figure 2.2. The strength of reflection is dependent on the physical (e.g., slope, morphology, roughness, inhomogeneities) and electrical (i.e., dielectric constant) properties of the surface (Elachi, 1988). Moreover, the interaction of the signal with the surface depends on the sensor characteristics, such as signal wavelength and incidence angle.

Two extreme cases of reflection can be distinguished: point scattering and distributed scattering. In case of point scattering a strong reflecting object is dominating the radar measurement, whereas the surrounding is only adding noise or *clutter*. Such a reflecting object is known as a *point scatterer*. In case of distributed scattering a large number of small scattering objects form the total measurement together. Both scattering mechanisms can, over time, either be coherent or incoherent. The *coherence* is a measure for the amount of correspondence between two complex observations. When the scattering objects on the surface do not change significantly between two radar acquisitions, the signal is considered coherent in time. The other extreme is complete incoherence. Figure 2.2 visualizes these extreme cases. However, there may be many levels between coherence and incoherence, and point scattering and distributed scattering.

The objective of each radar interferometric analysis is the retrieval of information from the pixels showing sufficiently coherent scattering behavior. In this research, the starting point of the analysis is data in Single-Look Complex (SLC) format. The pre-processing steps of raw radar data, e.g., focusing and range migration (see for example Cumming and Wong (2005) for details), are not considered here.

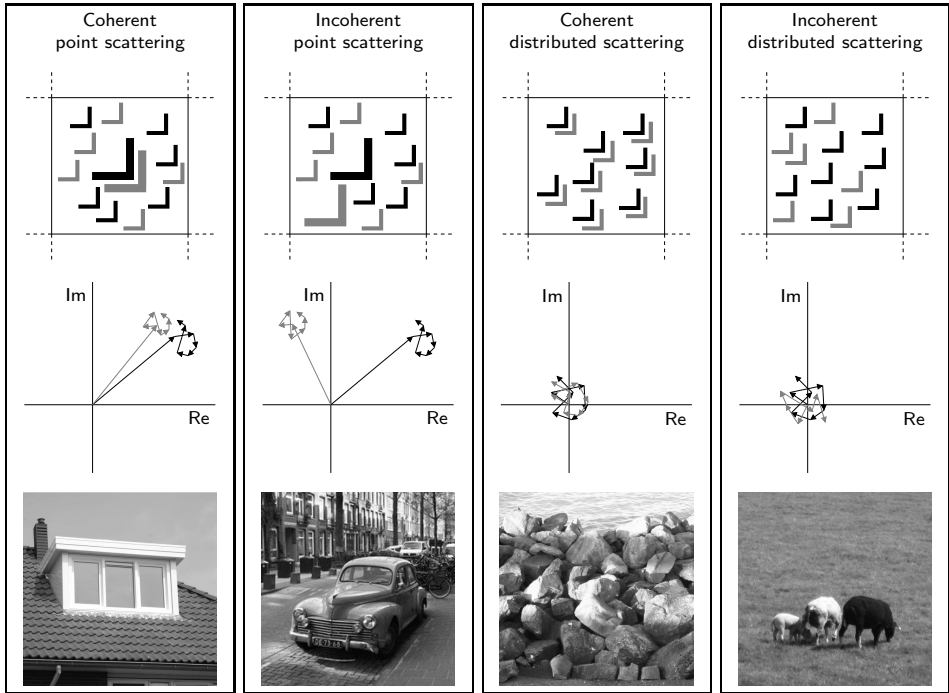


Figure 2.2: Point scattering versus distributed scattering in case of coherence or incoherence. Top) Scattering objects within a resolution cell at two acquisitions (indicated by black and gray reflecting objects). A large object corresponds to a strong reflection, whereas the small objects represent weak reflections. Middle) Phasors for the two acquisitions (again in black and gray). Bottom) Examples of scattering objects.

2.1.2 The Single-Look Complex phase

The observed SLC phase for a single pixel is denoted by

$$\psi = -2\pi a + \psi_{\text{range}} + \psi_{\text{atmo}} + \psi_{\text{scat}} + \psi_{\text{noise}}, \quad (2.3)$$

where a is the phase ambiguity, i.e., the number of full phase cycles, ψ_{range} the range dependent phase, ψ_{atmo} the atmospheric signal delay, ψ_{scat} is the scattering phase and ψ_{noise} is the noise. All terms are defined with respect to the *effective scattering center* of the resolution cell. This is the virtual location of the phasor resulting from the coherent reflecting elements in the resolution cell. The scattering phase represents the clutter, whereas the noise phase describes the measurement noise, e.g., thermal noise. The range phase is related to the two-way geometric distance between the radar antenna and the scattering center.

The atmospheric signal delay is composed of an ionospheric and tropospheric term. The ionosphere, ranging between 70 and 1000 km above the Earth's surface, is a dispersive medium, resulting in a wavelength depending delay. For example, based on a minimum and maximum Total Electron Content (TEC) of 5 and 100 TECU, respectively, the one-way zenith delay ranges from 0.02 to 0.4 m for X-band and 1.2 to 25 m for L-band (Hanssen, 2001; Eineder et al., 2011) (see Table 2.1 for an overview of the different bands). The troposphere, which is non-dispersive and therefore independent

of the radar wavelength, extends from the Earth's surface to a height of less than 11 km over the poles and 16 km at the equator (Lutgens and Tarbuck, 1986). It induces a *hydrostatic* and a *wet* delay. The hydrostatic zenith delay, which is dependent on the pressure and temperature in the troposphere, is in the order of 2.3 m and rather constant (Bevis et al., 1992). The wet zenith delay, caused by the water vapor distribution, is limited to values below 0.35 m (Bevis et al., 1992). However, the wet delay is much more variable compared to the hydrostatic delay. Using a mapping function (Herring, 1992; Niell, 1996), the zenith delays can be transformed to the radar Line of Sight (LOS).

The small radar wavelength (3 to 20 cm) in comparison with the pixel spacing, atmospheric delays and scattering objects distribution, cause that the SLC phase observations cannot be interpreted directly, see Figure 2.1, middle. However, information can be extracted from the difference between two SLC's, i.e., from an interferogram (see Figure 2.1, right).

2.1.3 The interferometric phase

A complex interferogram is created by the complex conjugated multiplication of two aligned or *coregistered* SLC images, obtaining

$$P^{ms} = P^m P^{s*} = A^m A^s \exp(i(\psi^m - \psi^s)), \quad (2.4)$$

where $(.)^*$ denotes the complex conjugate and m, s are the *master* and *slave* image, respectively. Here, a repeat-pass acquisition scheme is assumed. The interferometric phase φ^{ms} for a single pixel is

$$\begin{aligned} \varphi^{ms} &= \psi^m - \psi^s \\ &= -2\pi a + \varphi_{\text{flat}} + \varphi_{\text{topo}} + \varphi_{\text{defo}} + \varphi_{\text{atmo}} + \varphi_{\text{orb}} + \varphi_{\text{scat}} + \varphi_{\text{noise}}. \end{aligned} \quad (2.5)$$

Here, the interferometric range difference is split in a flat Earth φ_{flat} , topographic φ_{topo} and a deformation φ_{defo} part. Errors in the orbit parameters of the master and slave acquisitions introduce an additional error term φ_{orb} . The orbit errors typically cause a (small) trend in the interferogram (Hanssen, 2001). The other phase contributors are discussed in more detail in the next sections.

Flat Earth phase

The flat Earth and topographic phase are both related to the difference in position of the master and slave antenna, known as the *baseline* B . The flat Earth phase describes the contribution due to a reference surface, e.g., an ellipsoid. The flat Earth phase at a point P_0 on the reference surface is (see Figure 2.3)

$$\varphi_{\text{flat}} = \frac{-4\pi}{\lambda} (d(\vec{M}, \vec{P}_0) - d(\vec{S}, \vec{P}_0)), \quad (2.6)$$

where λ is the radar wavelength, \vec{M}, \vec{S} denote the master and slave antenna position and $d(., .)$ is the distance operator. The factor 4π instead of 2π accounts for the two-way travel path of the radar signal. The minus sign is based on a convention ensuring consistency between the Doppler history and the phase delay (Rosen et al., 2000).

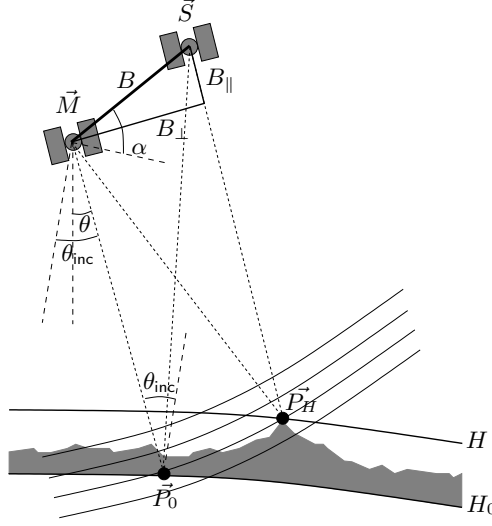


Figure 2.3: Baseline configuration in case of repeat-pass radar interferometry. The orbit trajectories are into the paper. The baseline B is defined as the distance between the master and slave antenna position (\vec{M} and \vec{S}). The parallel baseline B_{\parallel} determines the so-called flat Earth phase, which is the phase contribution due to a reference surface (H_0) through point \vec{P}_0 . The topographic height H of a point (\vec{P}_H) above the reference surface determines the topographic phase, which is a function of the perpendicular baseline B_{\perp} . The parallel and perpendicular baseline are both dependent on the baseline orientation α and the incidence angle θ_{inc} . The latter is a little larger compared to the look angle θ due to the curvature of the Earth.

Using the *far-field* or *parallel-ray* approximation (Zebker and Goldstein, 1986), where the travel paths to the master and slave antenna's are assumed to be parallel, the flat Earth phase can be approximated by (Hanssen, 2001)

$$\begin{aligned}\varphi_{\text{flat}} &= \frac{4\pi}{\lambda} B \sin(\theta_{\text{inc}} - \alpha), \\ &= \frac{4\pi}{\lambda} B_{\parallel},\end{aligned}\quad (2.7)$$

where θ_{inc} is the incidence angle, α the baseline orientation, and B_{\parallel} the *parallel* baseline. The flat Earth phase appears as a strong trend in the interferogram, but can be removed based on orbit and reference surface parameters.

Topographic phase

The topographic phase φ_{topo} describes the influence of topography above the reference surface. It is defined as (see Figure 2.3)

$$\begin{aligned}\varphi_{\text{topo}} &= \frac{-4\pi}{\lambda} ((d(\vec{M}, \vec{P}_H) - d(\vec{S}, \vec{P}_H)) - (d(\vec{M}, \vec{P}_0) - d(\vec{S}, \vec{P}_0))), \\ &= \frac{-4\pi}{\lambda} (d(\vec{S}, \vec{P}_0) - d(\vec{S}, \vec{P}_H)),\end{aligned}\quad (2.8)$$

where \vec{P}_H is a point at height H . The distances to the master antenna position \vec{M} cancel each other because they are by definition equal for a certain pixel, see also Figure 2.3.

Again using the far-field approximation, the topographic phase can also be expressed as function of the baseline (Zebker and Goldstein, 1986)

$$\begin{aligned}\varphi_{\text{topo}} &= \frac{-4\pi}{\lambda} \frac{B \cos(\theta_{\text{inc}} - \alpha)}{R \sin(\theta_{\text{inc}})} H, \\ &= \frac{-4\pi}{\lambda} \frac{B_{\perp}}{R \sin(\theta_{\text{inc}})} H,\end{aligned}\quad (2.9)$$

where B_{\perp} is the perpendicular baseline and R is the range to the master antenna.

From Eq. (2.9) it can be derived that the sensitivity for height increases with increasing baseline. To estimate topography from an interferogram the remaining phase contributors in Eq. (2.5) should be minimal, e.g., by taking an interferometric pair with a short time span to reduce the effect of possible deformation in the area. A good example is the Digital Elevation Model (DEM) obtained by the Shuttle Radar Topography Mission (SRTM) (Farr et al., 2007), where the two required radar images are acquired simultaneously from different locations on the same platform. Because the signal paths are nearly equal, the atmospheric signal delay cancels.

For deformation studies the effect of topography in the interferometric phase should be eliminated. As Eq. (2.9) shows, the phase is insensitive to topography in case of a perpendicular baseline of zero. Since B_{\perp} is never (completely) zero and varies for pixels across the interferogram, the topographic phase is removed based on additional information. This operation is known as *zero-baseline steering* (Ferretti et al., 2001). The additional information can either be another interferogram with favorable conditions for topography, i.e., large B_{\perp} and limited deformation and atmospheric signal, or an existing DEM, e.g., acquired by the SRTM. The interferogram obtained is denoted as a *Differential* interferogram (DInSAR).

Deformation phase

The deformation phase is the result of a displacement of the surface. Due to the displacement the signal travel path length changes, resulting in the differential phase term

$$\varphi_{\text{defo}} = \frac{-4\pi}{\lambda} D_{\text{LOS}}, \quad (2.10)$$

where D_{LOS} is the deformation in the radar Line of Sight (LOS).

Due to the skewed incidence angle of the signal, the LOS measurement is sensitive to both horizontal and vertical deformation. The measurement is the projection of the actual three-dimensional deformation vector, denoted by the components D_e , D_n and D_u in East, North and Up direction, respectively, in the LOS direction. For a satellite with an orbit heading α_h , defined with respect to the North (see Figure 2.4), the relation is (Hanssen, 2001)

$$\begin{aligned}D_{\text{LOS,R}} &= D_u \cos(\theta_{\text{inc}}) - \sin(\theta_{\text{inc}})[D_n \cos(\alpha_h - 3\pi/2) + D_e \sin(\alpha_h - 3\pi/2)], \\ &= D_u \cos(\theta_{\text{inc}}) - \sin(\theta_{\text{inc}})[-D_n \sin(\alpha_h) + D_e \cos(\alpha_h)],\end{aligned}\quad (2.11)$$

where θ_{inc} is the local incidence angle and $(\alpha_h - 3\pi/2)$ corresponds with the angle to the azimuth look direction, which is perpendicular to the satellite orbit. This angle applies

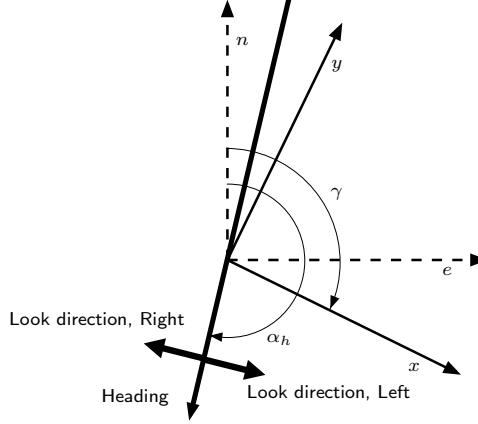


Figure 2.4: The acquisition geometry in the horizontal plane assuming zero-Doppler processing of the radar images, i.e., the effective look direction is perpendicular to the orbit heading. The orbit heading angle α_h is specified with respect to the North n . For the decomposition of the horizontal deformation the original East-North system is transformed into a local x, y -system by a rotation over the adopted orientation γ of the horizontal component of the deformation vector, see Eq. (2.13). This direction corresponds to the x -axis.

to a right-looking satellite, which is most common. In case of a left-looking satellite ($D_{\text{LOS,L}}$), the angle changes to $(\alpha_h - \pi/2)$, resulting in

$$\begin{aligned} D_{\text{LOS,L}} &= D_u \cos(\theta_{\text{inc}}) - \sin(\theta_{\text{inc}})[D_n \cos(\alpha_h - \pi/2) + D_e \sin(\alpha_h - \pi/2)], \\ &= D_u \cos(\theta_{\text{inc}}) - \sin(\theta_{\text{inc}})[D_n \sin(\alpha_h) - D_e \cos(\alpha_h)]. \end{aligned} \quad (2.12)$$

Hence, the difference between a right-looking and left-looking geometry is a change of sign for the horizontal components. Moreover, the equations show that the measurement of the deformation in the Up (vertical) direction is only dependent on the incidence angle, and therefore not on the orbit heading.

Although the forward problem described by Eqs. (2.11) and (2.12) is straightforward, the inverse problem, i.e., the estimation of the three-dimensional deformation components based on the measurement D_{LOS} , is ill-posed. That is, it is not possible to determine the three deformation components from a single measurement. Therefore, often an assumption is made based on a-priori knowledge regarding the deformation phenomenon under investigation.

Sometimes the specific horizontal direction of the deformation can be assessed a-priori. For example in case of water defense structures, a deformation in the longitudinal direction of a structure can normally be disregarded, thereby constraining the horizontal deformation to the direction perpendicular to the object. To isolate the horizontal deformation in this direction, it is useful to transform the decomposition from the North-East domain to a local x, y -system using a rotation matrix, obtaining

$$\begin{bmatrix} D_e \\ D_n \end{bmatrix} = \begin{bmatrix} \sin \gamma & -\cos \gamma \\ \cos \gamma & \sin \gamma \end{bmatrix} \begin{bmatrix} D_x \\ D_y \end{bmatrix}, \quad (2.13)$$

where γ is the orientation of the horizontal component of the deformation vector defined with respect to the North direction, see Figure 2.4. The deformation in the expected

direction is denoted by D_x , whereas D_y is the deformation perpendicular to this direction. Since we assumed that $D_y = 0$, Eq. (2.13) becomes

$$\begin{bmatrix} D_e \\ D_n \end{bmatrix} = \begin{bmatrix} \sin \gamma \\ \cos \gamma \end{bmatrix} D_x. \quad (2.14)$$

Substitution of Eq. (2.14) into Eq. (2.11) gives

$$D_{\text{LOS,R}} = D_u \cos(\theta_{\text{inc}}) + D_x \sin(\theta_{\text{inc}}) \sin(\alpha_h - \gamma). \quad (2.15)$$

For the left-looking geometry, $D_{\text{LOS,L}}$, a sign change applies for the horizontal component. The equation shows that the LOS measurement is most sensitive to horizontal deformation in case the horizontal deformation occurs perpendicular to the orbit heading (hence, $\alpha_h - \gamma = \pm 90^\circ$). This situation, in the so-called *zero-Doppler* plane, is visualized in Figure 2.5. The figure illustrates the sensitivity of the measurement to deformation in various directions, using the Envisat satellite with a look angle of 23° as an example. Here, the assumption is made that a deformation in the LOS of 5 or -5 mm is measured. A standard deviation of the measurement of 3 mm is adopted, which is a reasonable value for a point scatterer (Marinkovic et al., 2008). The figure shows that the same measurement of -5 mm can be caused by a strictly vertical deformation of -5.4 mm, a horizontal deformation of -12.8 mm, or any other deformation vector on the line perpendicular to -5 mm deformation in the LOS. The sensitivity of the measurements is expressed by the standard deviation, also indicated by error bars. Hence, a measurement precision of 3 mm corresponds to a precision of 7.7 mm in horizontal direction. In case a positive deformation value is measured, the direction of the deformation changes with 180° , with equal precision. When the actual deformation vector is perpendicular to the LOS, the measurement is insensitive for the deformation, indicated with an infinitive large standard deviation.

A similar sensitivity analysis is performed in case the horizontal deformation is not restricted to the zero-Doppler plane, see Figure 2.6. Again the Envisat satellite is used as illustration, applying an orbit heading of 193° . Also here, a LOS measurement with a precision of 3 mm is assumed, showing the 7.7 mm accuracy in the zero-Doppler direction. Figure 2.6 also shows the sensitivity in other directions. In North-South direction, the precision becomes extremely low (34.1 mm), indicating that deformations in that direction cannot be measured. That is, a small deformation in the order of millimeters in North-South direction would require a measurement accuracy level that is not feasible. Hence, the signal-to-noise (SNR) is in this case too low. In the along-track direction, the measurements are completely insensitive for deformation, indicated by an infinitively large standard deviation. Since all radar satellites have a near-polar orbit, resulting in orbit headings close to the North-South direction for the largest part of the orbit, radar interferometric measurements are in principle only able to measure horizontal deformation in approximately East-West direction. Exceptions are the polar regions, where the rotation of the orbit heading creates a sensitivity to North-South deformation.

Sometimes the ground motion is extremely large (dm-m level) in relation to the radar wavelength, for instance due to a strong earthquake or glacial flow. In those cases it may be possible to use the offset vectors obtained during the alignment process or *coregistration* of the two radar images to obtain information regarding horizontal deformation, also in North-South direction (Gray et al., 1998; Elliott et al., 2007). However,

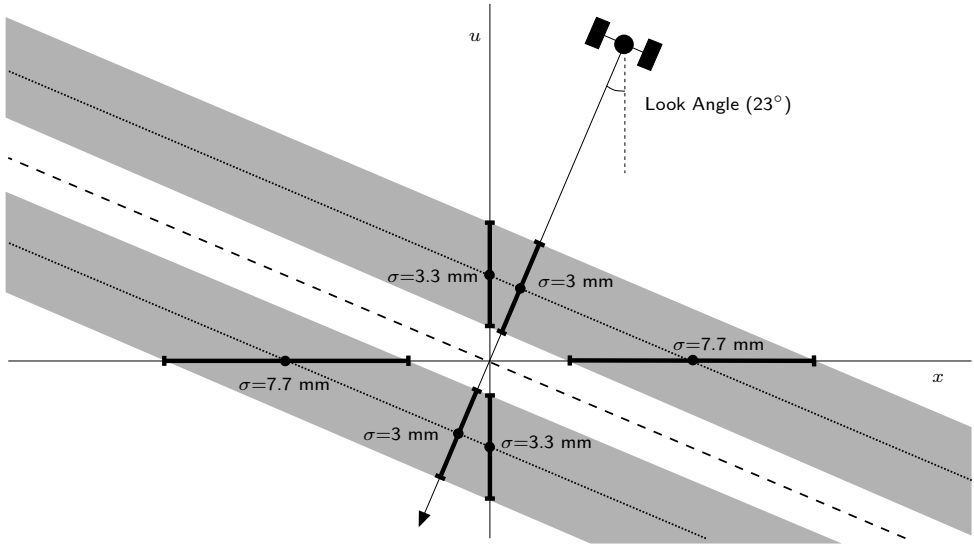


Figure 2.5: Illustration of the sensitivity of a deformation measurement in the radar Line of Sight (LOS) for vertical and horizontal deformation in the zero-Doppler plane (i.e., the plane perpendicular to the orbit heading). The Envisat satellite with an average look angle of 23° is used as an example. Since the measurement is the projection of the actual deformation vector to the LOS direction, the measurement can reflect a vertical, horizontal or any other deformation on the line perpendicular to the LOS direction. The sensitivity is expressed by the standard deviations σ . Hence, a measurement precision of 3 mm corresponds to a sensitivity of 7.7 mm for horizontal deformation. The measurement is insensitive for deformations perpendicular to the LOS, indicated with the dashed line.

the precision of the result obtained will be much lower compared to radar interferometric measurements.

The near-polar orbit of the radar satellites causes that a certain location on Earth is imaged twice, while the satellite is heading from South to North (ascending orbit) and while heading from North to South (descending orbit). In case of a right looking satellite, the ascending orbit results in a radar image acquired from the West, while the descending orbit observes the Earth from the East. While from a single radar dataset no distinction can be made between horizontal or vertical deformation, as discussed above, the availability of an ascending and descending orbit gives an additional observation for the decomposition of the deformation vector.

Since with two observations it is still not possible to retrieve a three-dimensional deformation vector, an assumption regarding the direction of the horizontal deformation is still required. Using Eq. (2.15), the LOS deformation measurements D_a and D_d obtained from the ascending and descending orbit, respectively, can be decomposed in a vertical D_u and horizontal D_x deformation using the system of equations

$$\begin{bmatrix} D_a \\ D_d \end{bmatrix} = \begin{bmatrix} \cos(\theta_{inc,a}) & \sin(\theta_{inc,a}) \sin(\alpha_{h,a} - \gamma) \\ \cos(\theta_{inc,d}) & \sin(\theta_{inc,d}) \sin(\alpha_{h,d} - \gamma) \end{bmatrix} \begin{bmatrix} D_u \\ D_x \end{bmatrix}. \quad (2.16)$$

Here, the assumed direction of the horizontal deformation is specified by γ . The specific incidence angles θ_{inc} and orbit headings α_h of both the ascending and descending dataset are indicated by a , d , respectively. This system also enables the combination

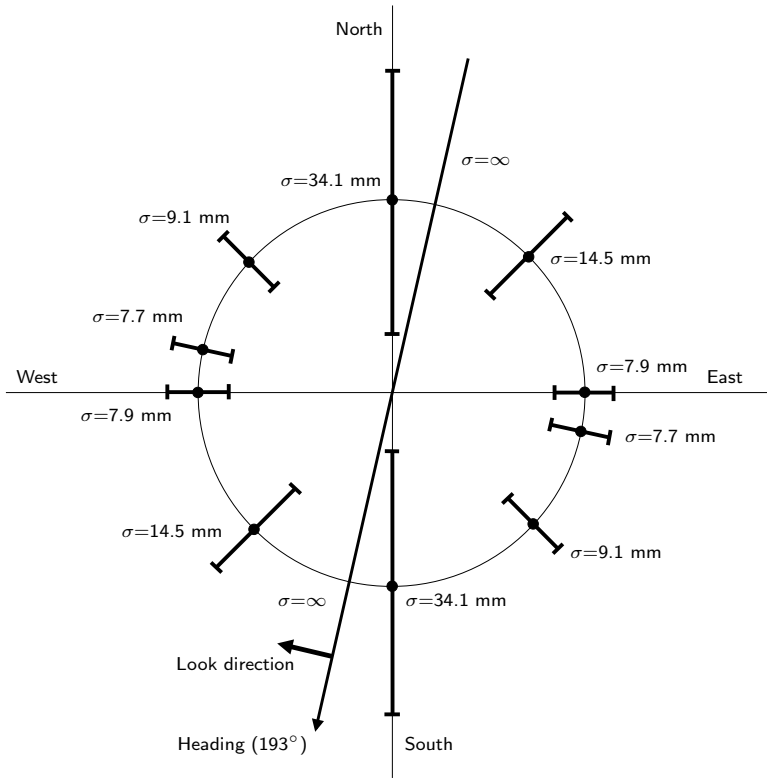


Figure 2.6: Illustration of the sensitivity of a deformation measurement in the radar Line of Sight (LOS) to horizontal deformations. The Envisat satellite, adopting an orbit heading of 193° is used as an example. A measurement precision of 3 mm in the LOS is assumed. The standard deviations of the horizontal deformations, as shown in the figure, indicate the sensitivity of the measurement for horizontal motions. Due to the North-South orientation of the orbit heading of radar satellites, radar interferometric measurements are predominantly sensitive for horizontal deformation in East-West direction. Deformations in North-South direction cannot be measured because the signal-to-noise ratio (SNR) becomes too low, indicated by a large or even infinite standard deviation σ .

of datasets acquired by different radar satellites, possibly having different observation characteristics, e.g., radar wavelength. Since two observations are available to determine two unknown deformation values, the system has a unique solution. The accuracy of the measurements propagates therefore directly to the final result. In principle it is possible to add additional ascending and descending datasets to the system. This will improve the precision. However, because of the insensitivity of the deformation vector in North-South direction, the full three-dimensional vector can still not be resolved and an assumption regarding the direction of the horizontal deformation remains required.

Atmospheric phase

The atmospheric phase φ_{atmo} is caused by the difference between the atmospheric states during the two acquisitions. Because a large part of the total atmospheric delay is rather constant, i.e., the ionospheric and hydrostatic troposphere delay (see Section 2.1.2),

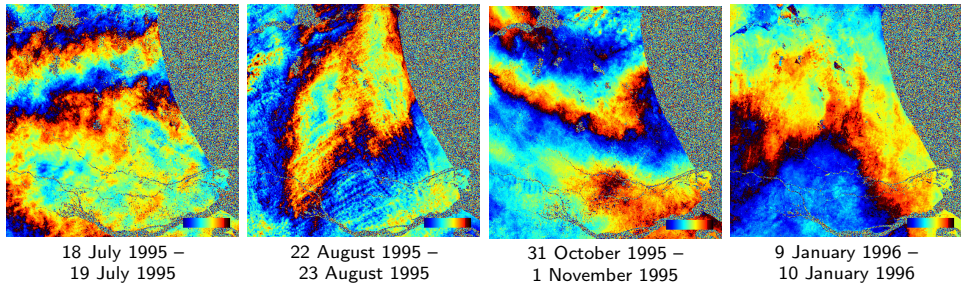


Figure 2.7: Atmospheric signal delay over the western part of the Netherlands in four ERS-1/2 tandem mission interferograms. Due to the 1 day temporal baseline between the radar acquisitions, the interferograms do not contain any deformation signal. Due to the flatness of the terrain, topographic phase contributions are negligible. However, orbital inaccuracies still cause a phase contribution.

the differential delay is relatively small, yet strongly variable. Two contributors to this differential delay can be distinguished (Hanssen, 2001):

1. Turbulent mixing. Turbulent processes in the atmosphere cause spatial (3D) heterogeneity of the delay, effectively due to the water vapor distribution (wet delay).
2. Vertical stratification. Different vertical delay profiles during the two acquisitions cause, in case of mountainous terrain, a differential signal delay which is correlated with topography.

The differential atmospheric delay is in the order of mm-cm's. Its spatial correlation makes it difficult to distinguish the atmospheric signal from deformation, topography or orbital errors in case of a single interferogram. A number of examples of (primarily) atmospheric signal delay over the western part of the Netherlands is shown in Figure 2.7. By using data obtained by the so-called ERS-1/2 tandem mission, with a temporal baseline between the ERS-1 and 2 acquisitions of 1 day, any deformation signal can be excluded. Topographic phase contributions are limited in this flat area. However, orbital inaccuracies may still be visible.

Scattering phase and noise

The interferometric scattering phase φ_{scat} is effectively an additional noise term. It describes the difference between the scatter characteristics of the observed area within a resolution cell during the two acquisitions. Change in these scatter characteristics results, together with thermal and processing noise, in *decorrelation*. The amount of decorrelation is expressed by the magnitude of the coherence $|\gamma| \in [0, 1]$.

Several sources of decorrelation can be distinguished (Zebker and Villasenor, 1992; Hanssen, 2001)

- Temporal decorrelation (γ_{temp}), caused by physical changes of the Earth's surface within the resolution cell. A typical source of temporal decorrelation is vegetation. Since signals with longer wavelengths are less sensitive to vegetation, the decorrelating effect is smaller for L or P band compared to X or C band (see Table 2.1 for an overview of radar bands). Another example of temporal decorrelation is the

Table 2.1: Overview of radar bands used for remote sensing (Lillesand and Kiefer, 1994).

Band	Frequency range [GHz]	Wavelength range [cm]
K _a	26.5 – 40	0.75 – 1.1
K	18 – 26.5	1.1 – 1.67
K _u	12.5 – 18	1.67 – 2.4
X	8 – 12.5	2.4 – 3.75
C	4 – 8	3.75 – 7.5
S	2 – 4	7.5 – 15
L	1 – 2	15 – 30
P	0.3 – 1	30 – 100

signal obtained from water bodies, where the change of the water surface instantly causes complete decorrelation, see also Figure 2.8.

- Geometric decorrelation (γ_{geom}), caused by different incidence angles of the radar signal during the two acquisitions (Gatelli et al., 1994). The different incidence angles cause a shift between the data frequency spectra of the images involved, resulting in noise due to the non-overlapping parts of the range spectrum. The geometric decorrelation, in case of a rectangular spectral window, is defined as

$$\gamma_{\text{geom}} = \max\left(\frac{B_{\perp\text{crit}} - |B_{\perp}|}{B_{\perp\text{crit}}}, 0\right). \quad (2.17)$$

where $B_{\perp\text{crit}}$ is the *critical baseline*. This critical baseline is the baseline causing a spectral shift equal to the range bandwidth B_r . It is a function of the wavelength, incidence angle, range bandwidth and topographic slope ζ , i.e.,

$$B_{\perp\text{crit}} = |\lambda(B_r/c)R \tan(\theta_{\text{inc}} - \zeta)|, \quad (2.18)$$

where c is the speed of light and R is the range to the master antenna. For example, the ERS-1/2 and Envisat critical baseline is approximately 1.1 km for flat terrain. See Table 3.1b (p.35) for an overview of critical baselines for other satellites. The geometric decorrelation effect is illustrated in Figure 2.8 by four ERS-1/2 interferograms with increasing perpendicular baseline.

- Doppler centroid decorrelation (γ_{Dc}), caused by different Doppler centroid frequencies during the two acquisitions. The Doppler centroid frequency f_{Dc} is the center frequency of the azimuth spectrum of an acquisition. The Doppler centroid frequency is dependent on the so-called squint angle of the antenna. The squint angle is the difference between the *zero Doppler* direction, i.e., perpendicular to the flight direction, and the pointing direction of the antenna, see also Figure 4.2A (p.60).

Doppler decorrelation is the azimuthal equivalent of geometric decorrelation. The Doppler coherence factor γ_{Dc} decreases linearly with increasing Doppler centroid baseline B_{Dc} —which is defined as the difference between the Doppler centroid frequencies f_{Dc} of the two SLC images involved— as

$$\gamma_{\text{Dc}} = \max(1 - |\Delta B_{\text{Dc}}|/B_{\text{az}}, 0), \quad (2.19)$$

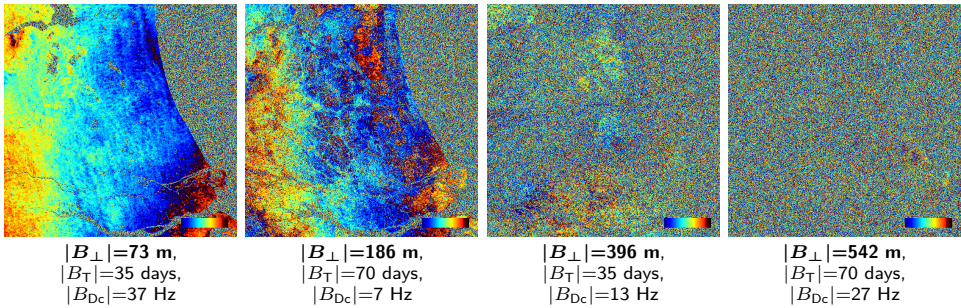


Figure 2.8: Illustration of geometric decorrelation over the western part of the Netherlands using four ERS-1/2 interferograms with increasing perpendicular baseline. Note that the absolute temporal B_{τ} and Doppler B_{Dc} baselines are equivalent, and the same instrument and processing settings are used. Hence, the majority of decorrelation is due to the increasing perpendicular baseline. The water area on the right sides of the images is completely decorrelated due to fast temporal change of the water surface.

where B_{az} is the azimuth bandwidth. Normally the Doppler centroid variation is maintained within a limited range by proper orientation of the radar antenna, thereby minimizing the effect of Doppler decorrelation. Exceptions are the Doppler values for ERS-2 images acquired after 15 January 2001. Due to failure of the on-board gyroscopes, the antenna could no longer be steered. As a result, only a limited number of images acquired after this date are suitable for interferometric applications.

- Thermal or system decorrelation (γ_{ther}), caused by instrumental thermal noise during the acquisitions. This decorrelation factor is dependent on the system characteristics of the instrument involved.
- Processing decorrelation (γ_{proc}), caused by the processing of the radar images to obtain interferograms, e.g., due to coregistration and interpolation errors. Hanssen (2001) derived that, assuming a coregistration precision better than 1/8th of a pixel (in both directions), the processing results in a correlation factor of 0.96.

Zebker and Villasenor (1992) showed that the listed coherence terms are multiplicative, resulting in the total coherence

$$\gamma_{tot} = \gamma_{temp} \cdot \gamma_{geom} \cdot \gamma_{Dc} \cdot \gamma_{ther} \cdot \gamma_{proc} \quad (2.20)$$

High coherence indicates a small contribution of scattering phase φ_{scat} to the observed phase φ^{ms} , see Eq. (2.5). High coherent pixels therefore have a higher chance of accurate, i.e., precise and reliable, estimation of the remaining phase contributions, e.g., topography, deformation and atmosphere. The coherence can be optimized by proper selection of the interferometric combinations (e.g, small baselines) and/or by applying additional data processing operations. One of these operations is oversampling of the data.

Oversampling

The interferometric phase is obtained by complex conjugated multiplication of the master and slave images, see Eq. (2.4). Because multiplication in the time domain is equal to a

convolution in the frequency domain, the spectrum of the interferogram is twice as wide as that of the radar images. Since the sampling frequency of the interferogram remains equal to that of the SLC images, spectral contributions above the Nyquist frequency are obtained, which induces an aliasing effect (Hanssen, 2001).

To avoid aliasing, the master and slave SLC images should be oversampled by a factor 2 in both range and azimuth direction. This is achieved efficiently, after a Fourier transform, by *zero padding* of the master and slave spectrum by the same number of samples as already contained in the original spectrum. By applying an inverse Fourier transformation, harmonically interpolated master and slave images are obtained which now contain twice as many samples. Due to the oversampling, the noise level of the interferogram is reduced, because the aliasing effect is prevented.

Additional processing steps

Once the interferogram is created, in original image resolution or oversampled form, the interferogram can be interpreted. To improve the interpretation, a number of additional processing steps can be applied (beforehand). Examples of these processing steps are

- Spectral filtering. The noise level in the interferogram can be reduced by filtering the non-overlapping parts of the spectra of the master and slave images before interferogram formation. The spectral filtering is applied separately in azimuth and range direction. Hereby, the geometric and Doppler centroid decorrelation is reduced.
- Spatial filtering. Remaining noise, for example caused by temporal decorrelation, can be reduced by a spatial (smoothing) filter on the complex interferometric observations.
- Phase unwrapping. The interferogram obtained still contains phase values wrapped to the $[-\pi, +\pi)$ interval. Hence, the interferogram shows color cycles known as *fringes*, see for example Figure 2.7. To obtain absolute phase values, which can be translated to topographic height information or deformation values, the phase needs to be *unwrapped*. An overview of methods for phase unwrapping can be found in Ghiglia and Pritt (1998).

The objective of a radar interferometric analysis may be to study the deformation, topography, or atmospheric conditions in a certain area. In case of deformation studies, the deformation phase φ_{defo} should be isolated from the other phase contributors in Eq. (2.5). In practice, especially the atmospheric signal, together with temporal and geometric decorrelation, are the limiting factors regarding interpretation in case of a single interferogram. To circumvent these disturbing factors, often multiple interferograms of the same area are used for deformation studies: radar interferometric time series analysis.

2.2 Time series interferometry

To overcome the major limitations of radar interferometry, that is, temporal and geometric decorrelation, and atmospheric signal delay, at the turn of the century radar interferometric time series analysis methods were introduced (Ferretti et al., 2000; Usai,

2001; Berardino et al., 2002). Within these methods, instead of single interferograms, multiple interferograms are analyzed in a consistent framework. Hereby the lack of redundancy in a single interferogram is circumvented, enabling a separation of the various phase contributions, e.g., deformation, topography and atmospheric signal delay. The introduction of radar time series analysis has dramatically increased the applicability of radar interferometry to various deformation phenomena under varying reflection conditions of the surface.

The main objective of a radar interferometric time series analysis method is the detection of those pixels for which the deformation time series can be estimated with sufficient reliability. The reliability of the time series is directly related to the correct estimation of the phase ambiguities or *phase unwrapping*. The ability to estimate these ambiguities correctly depends both on the characteristics of the measurements and of the signal of interest. In particular

1. the noise level of the observations. This level is determined by the amount of decorrelation, see Section 2.1.3. Hence, for pixels which show strong geometric and/or temporal decorrelation, the ability to estimate the actual deformation time series is reduced.
2. the spatio-temporal variability of the atmospheric signal delay. In all methods the ambiguities are resolved based on spatial (and temporal) phase differences. When strong spatial gradients in the atmospheric signal occur, correct ambiguity resolution becomes more difficult.
3. the spatio-temporal smoothness of the actual deformation signal. To resolve the ambiguities certain assumptions regarding the spatial and/or temporal smoothness of the deformation signal have to be made. Sudden changes, either in space or in time, make the ambiguity resolution more difficult or, in case a wavelength dependent threshold is exceeded, even impossible. Here, also the spatial distance between coherent pixels and the acquisition repeat cycle determine the ability to estimate the correct solution.

Radar interferometric time series analysis methods are designed to account for these limitations. In the last decade various methods have been proposed. The methods can be distinguished based on:

- the baseline configuration of the images used,
- the image resolution used,
- the ambiguity resolution method applied,
- the a-priori pixel selection method applied,
- the a-posteriori pixel selection method applied, and
- the atmospheric signal estimation/prediction method applied.

An overview of various methods and their characteristics is given in Table 2.2. In Sections 2.2.1-2.2.6 these characteristics are further discussed. The specific characteristics of Tomographic SAR time series analysis (Reigber and Moreira, 2000; Lombardini, 2005; Fornaro et al., 2009; Zhu and Bamler, 2010), which enables the detection of multiple scatterers within the same image range bin, are not considered here.

Table 2.2: Radar interferometric time series analysis methods and their characteristics.

Method	Baseline configuration	Resolution ($a \times r$)	Phase unwrapping	A-priori selection	A-posteriori selection	Atmospheric signal	Assumption
Stacking (Zebker et al., 1993; Wright et al., 2004)	Independent pairs	Multilooked (40×8)	2D + 1D (averaging)	Coherence	-	Averaging	Spatial smoothness of deformation, linear deformation in time
Phase gradient approach (Sandwell and Freese, 1998)	Small baseline interferograms	Multilooked (4×2)	1D (assumed unwrapped) + 2D (least-squares)	Coherence and phase gradient	-	Weighted averaging	Spatial smoothness of deformation, linear deformation in time
Permanent Scatterers (Ferretti et al., 2000, 2001)	Single master	Original	1D + 2D (ambiguity function + integration)	Amplitude dispersion	Temporal coherence	High-pass/low-pass filtering	Deformation model in time
Database approach (Ursi, 2001, 2003)	Small perpendicular baseline subsets	Multilooked (10×2)	2D + 1D (interpolated interferogram)	Spatial coherence	Closed loop test	Averaging	Spatial smoothness of deformation, interpolation based on linear deformation
SBAS (Berardino et al., 2002)	Small perpendicular baseline subsets	Multilooked (20×4)	2D (sparse MCF) + 1D (SVD)	Mean spatial coherence	-	High-pass/low-pass filtering	Spatial smoothness of deformation
(Mora et al., 2003)	Small perpendicular baseline subsets	Multilooked (20×5)	1D (ambiguity function + SVD) + 2D (integration)	Mean spatial coherence	Temporal coherence	High-pass/low-pass filtering	Linear deformation model in time
(Schmidt and Burgmann, 2003)	Small perpendicular baseline	Multilooked (40×8)	2D + 1D (SVD)	Coherence	-	Temporal smoothing	Spatial and temporal smoothness of deformation
STUN (Kampos and Hansen, 2004; Kampos, 2006)	Single master	Oversampled (2×2)	1D + 2D (ILS/ bootstrap ping + MCF)	Amplitude dispersion/SCR	Parameter testing	Stochastic model	Deformation model in time
SBAS+ (Lanari et al., 2004)	Small perpendicular baseline subsets	Multilooked (20×5) and original	2D (sparse MCF) + 1D (SVD), followed by 1D (ambiguity function + SVD)	Mean spatial coherence	-	High-pass/low-pass filtering	Spatial smoothness of deformation, linear deformation model in time
Stamps (Hooper et al., 2004, 2007)	Single master	Original	1D (ambiguity function) + 2D (global probability optimization)	Amplitude dispersion	PS probability (temporal coherence + amplitude dispersion)	High-pass/low-pass filtering (adapted)	Spatial smoothness of deformation
Stamps+ (Hooper, 2008)	Single master + Small baseline (perpendicular, temporal, Doppler)	Original	1D (ambiguity function) + 2D (global probability optimization)	Amplitude dispersion	PS probability (temporal coherence + amplitude dispersion)	High-pass/low-pass filtering (adapted)	Spatial smoothness of deformation
SqueaSAR (Ferretti et al., 2011)	Single master after phase triangulation	Oversampled (1×2)	1D + 2D (ambiguity function + integration)	Statistical test	Temporal coherence	High-pass/low-pass filtering	Deformation model in time
DePSI (this work)	Single master	Oversampled (2×2)	1D + 2D (ILS/ bootstrap ping + ambiguity adaptation)	Amplitude dispersion	Ambiguity testing + quality threshold (various)	High-pass/low-pass filtering, stochastic model	Deformation model in time

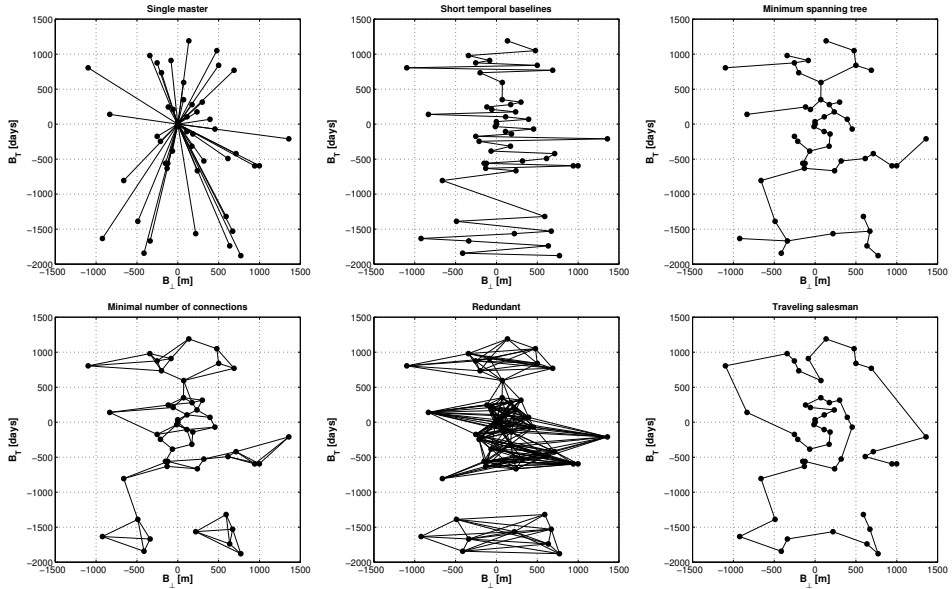


Figure 2.9: Examples of baseline configurations. Different strategies can be applied to minimize the noise level in the interferometric data stack. The final choice can for example be dependent on the dominant type of scattering (point scattering or distributed scattering) and the expected deformation behavior.

2.2.1 Baseline configuration

The baseline configuration determines the set of interferometric image pairs that is used in the time series analysis. The baseline is defined as the distance between the two SLC images involved, either in terms of antenna position (perpendicular baseline), acquisition time (temporal baseline), or Doppler centroid (Doppler baseline). The objective is to find a configuration that minimizes the noise level in the data set, hence to minimize the amount of decorrelation (see Section 2.1.3). Examples of frequently applied baseline configurations are the single master stack (Ferretti et al., 2001), the short temporal and/or perpendicular baseline configuration (Berardino et al., 2002; Schmidt and Bürgmann, 2003), a redundant network (Perissin et al., 2008), a minimal number of connections graph, a traveling salesman solution (van Leijen and Hanssen, 2004), and the minimal spanning tree (Perissin et al., 2008). Figure 2.9 gives an example of a number of these baseline configurations in the form of a baseline plot in case only the perpendicular and temporal baseline are considered.

The single master configuration, where all SLC's are interferometrically connected to a unique master SLC, is often used for a Persistent Scatterer Interferometry (PSI) analysis (Ferretti et al., 2001; Kamps, 2006). Since the main focus of PSI is on point scatterers, which are assumed to be only minimally affected by geometric and temporal decorrelation, relatively large baselines can be applied. For these point scatterers even baselines extending the critical baseline (see Section 2.1.3 and Table 3.1b (p.35)) can be used. As a result, normally all available SLC images are used in a PSI analysis, with the advantage that the number of interferograms is minimized.

Radar interferometric time series analysis methods focusing on distributed scattering

pixels are often based on baseline configurations with small baselines. The reasoning is that distributed scattering is much more sensitive to geometric and temporal decorrelation compared to point scatterers. For instance, the SBAS method (Berardino et al., 2002; Mora et al., 2003) uses such a configuration of small baseline interferograms. By setting a maximum baseline length, the decorrelation effect is constrained. Hereby, a configuration of redundant interferograms is obtained, that is, more interferograms are created than strictly required to connect the SLC images. Disadvantage of a baseline threshold is that disconnected sets of interferogram clusters may be obtained, see also Figure 2.9. This would result in separate deformation time series for each cluster with unknown offsets with respect to each other. Within the original SBAS approach (Berardino et al., 2002; Mora et al., 2003) the clusters are connected by applying a Singular Value Decomposition (SVD), resulting in a least-squares solution with a minimum norm constraint. That is, the Moore-Penrose pseudo-inverse (Moore, 1920; Penrose, 1955) incorporated within the SVD solution minimizes the norm of the solution vector, obtaining deformations which are in general as close to zero as possible. Note that in case all interferograms form a single cluster, the SVD solution is equal to a standard least-squares approach. Two alternative approaches have been presented. Usai (2003) simulates a connecting interferogram based on the assumption of linear deformation behavior between successive acquisitions. The approach by Costantini (2003) is based on the minimization of the curvature of the resulting deformation time series. Here, additional constraints are added to the system of equations to minimize the variation in deformation velocity between consecutive intervals between acquisitions. To reduce the amount of interferograms, a constraint on the minimal number of connections for each SLC image can be applied, resulting in the minimal connection configuration, see Figure 2.9, bottom-left.

Hybrid baseline configurations are possible as well. The short temporal baseline approach results in a cascade of interferograms between successive images. This configuration is suitable in case the expected deformation is large and/or irregular in time. Connecting each individual spatial unwrapped interferogram results in the desired deformation time series. Disadvantage of this approach is that unwrapping errors cannot be detected, resulting in the risk of propagation errors. Minimizing the baselines, but still using all available SLC's can be accomplished by the Traveling salesman approach (van Leijen and Hanssen, 2004) or the minimum spanning tree (Perissin et al., 2008).

2.2.2 Image resolution

The image resolution used in the radar interferometric time series analysis is mainly dependent on the type of scattering that is expected or aimed to detect, i.e., primarily point scattering or distributed scattering. In both cases the aim of using a certain resolution is to reduce the amount of noise in the observations. In case of point scattering, often oversampled images are used (with a minimum oversampling factor of two), to prevent additional noise due to aliasing in the interferometric phase, see Section 2.1.3. Sometimes the oversampling step is omitted, hence, resulting in the use of the original image resolution.

In case of distributed scattering often a multilook of a certain number of pixels is applied to reduce the noise level, see Hanssen (2001). Multiple pixels are averaged to obtain a new resolution cell. Often the multilook factors in range and azimuth direction

are chosen such that approximately square pixels are obtained. The reduced noise level in the image pixels typically improves the result of phase unwrapping in the spatial domain. The unwrapped multilooked interferograms can also be used to steer the unwrapping of the original, full resolution, interferograms, see Lanari et al. (2004), in case full resolution results are desired.

2.2.3 Phase unwrapping

The critical step in any radar interferometric time series analysis approach is the unwrapping of the phase, also known as *ambiguity resolution*. Unwrapping errors, i.e., phase jumps of 2π , severely affect the quality of the results. The challenge is to unwrap the 3D data stack (two dimensions in space and one in time) with the highest possible reliability. Various methods for phase unwrapping have been proposed in the past. In case of Persistent Scatterer Interferometry, often a 1D+2D approach is applied (Ferretti et al., 2001; Hooper et al., 2004; Kampes, 2006; Hooper, 2010). Hence, the phase observations for a certain pixel in the data stack are first unwrapped in time, followed by a spatial unwrapping. In case of SBAS, a 2D+1D approach is used. Here, the interferograms are first unwrapped spatially, followed by an integration in time. In both cases the first step is the most crucial one, which depends strongly on the smoothness of the signal (see also Section 2.2). For PSI a certain smoothness of the deformation signal in time is required. However, since the phase of every scatterer is unwrapped independently, also autonomously moving points can be detected. For SBAS approaches, a smoothness of the deformation signal in space is assumed. Here the advantage is that fluctuations in the deformation behavior in time may better be assessed.

An integrated 3D phase unwrapping approach, thereby taking advantage of both the temporal and spatial correlations in the data, is desirable. Hooper and Zebker (2007) introduce such a method. The challenge in the approach is the weighting between the spatial and temporal domain. These weights are required to determine whether ambiguity inconsistencies should be resolved via a path in the temporal or spatial domain. The same applies for the 2D+2D method introduced by Pepe and Lanari (2006). Here, not only the temporal baselines are used, but also the perpendicular baselines. A Minimum Cost Flow (MCF) approach in the perpendicular-temporal baseline domain is used to unwrap the phase for each pixel, followed by a MCF spatial unwrapping.

2.2.4 A-priori pixel selection

Each radar interferometric time series analysis approach starts with an a-priori selection of suitable pixels. The main objectives are: 1) the improvement of the results, by disqualifying low quality pixels which may influence the results in a negative manner, and 2) the reduction of computational efforts. The selection can either be based on amplitude or phase information. In case of PSI techniques, often the amplitude stability in a data stack is used as a proxy for phase stability, see also Section 3.3.1. Ferretti et al. (2000, 2001) introduced the normalized amplitude dispersion, which can be derived for each pixel in the data stack individually. An alternative is the consistency of the Signal-to-Clutter (SCR) Freeman (1992); Adam et al. (2004), where the SCR is estimated for each point scatterer and its stability in time is used as proxy. The disadvantage of this method is that also surrounding pixels (representing the clutter) are needed for the assessment.

For radar interferometric time series analysis methods which focus on distributed scattering mechanisms and do not require the use of full or oversampled resolution radar data, the consistency of the spatial coherence is often used. The spatial coherence determines the spatial consistency of the complex observations in a number of neighboring pixels. Since the original data are multilooked to reduce the noise, the same pixels can be used to estimate the coherence. Alternatively, a moving window can be used. The consistency of the coherence in the data stack determines the final selection of pixels to be used in the analysis.

2.2.5 A-posteriori pixel selection

For some radar interferometric time series analysis methods a second, a-posteriori pixel selection is applied, see Table 2.2. Here, the objective is to detect the reliably estimated pixels in the total set of pixels analyzed. This selection step is mainly applied in the methods which start with a 1D phase unwrapping in the time domain, hence, where an independent solution for each pixel is obtained. Ideally, the a-posteriori selection is performed before the spatial integration step, to circumvent the influence of erroneous pixels in the final result. Various quality indicators can be used for the selection, such as the local ensemble coherence or variance factor, see Section 6.2. These quality indicators can also be applied in combination with a testing scheme based on the parameters of interest (Kampes, 2006) or the phase ambiguities (van Leijen et al., 2006a).

For methods that start with a 2D spatial unwrapping, this second, a-posteriori, pixel selection is usually omitted, since each initially selected pixel will influence the final result. Hence, the a-priori pixel selection should be conservative in order not to incorporate (too many) incoherent pixels. However, when applying an iterative approach in the spatial phase unwrapping, an a-posteriori pixel selection could be used to remove unreliable pixels, thereby converging to a final solution.

2.2.6 Atmospheric signal decomposition

The radar interferometric time series analysis methods can also be distinguished based on the approach applied to isolate the atmospheric delay signal from the deformation signal. Main assumption for each decomposition approach is that the atmospheric delay due to turbulent mixing is uncorrelated in time. As a result, the expectation value of the differential atmospheric delay is zero.

In case of stacking (Zebker et al., 1997; Wright et al., 2001, 2004) the influence of the atmospheric signal delay is reduced by (weighted) averaging of various interferograms, thereby obtaining an estimate of the average linear deformation rate. Ferretti et al. (2000) introduce an alternative approach to isolate the atmospheric signal in an interferometric single master data stack. Here, a sequence of high-pass and low-pass filters in time and space is applied, see also Section 5.3. First, for each pixel the average residual phase after correction for estimated model parameters, such as height and (linear) deformation, is taken to obtain an estimate for the atmospheric signal in the master image. Subsequently, the time series of residuals are high-pass filtered to separate the atmospheric signal of the slave acquisitions (plus noise) from unmodeled deformation. Last step is a low-pass filter in the spatial domain, which separates the noise from the atmospheric signal. The final result is an estimate of the atmospheric signal delay for each acquisition. Various radar interferometric time series analysis methods

have adopted this approach (possibly in an adapted form), e.g., Berardino et al. (2002); Mora et al. (2003).

Kampes (2006) does not estimate the atmospheric signal delay explicitly, but describes it by a stochastic model. In this case the stochastic model should ensure that the parameters of interest are minimally affected by the atmospheric signal delay. The final deformation time series will however also contain the atmospheric signal contribution, thereby showing a higher noise level. Nevertheless, an optional filter of the estimated deformation time series is suggested to remove the atmospheric signal a-posteriori. Also Hooper et al. (2004); Hooper (2008) maintain the atmospheric delays in the time series. They apply a combination of the high-pass/low-pass filtering and stochastic modeling, to benefit from the advantages of both methodologies, see Section 5.3.

The assumption of an uncorrelated atmospheric signal delay in time may not hold in cases of strong topography. Here, apart from signal delay due to turbulent mixing of water vapor, also homogeneous differences in pressure, temperature and humidity between two acquisitions will result in a differential signal. This phenomenon is known as vertical stratification (Hanssen, 2001), see Section 2.1.3. Seasonal effects in the weather condition can result in a temporal correlation between these atmospheric signals. Ferretti et al. (2005) estimate the vertical stratification effect by inserting an additional parameter in the functional model. Another approach is to model the effect based on data from a numerical weather model (NWM). Liu (2012) shows that the vertical stratification effect can very well be modeled by the weather models. The same study shows that this conclusion does not apply for the turbulent mixing part of the atmospheric delay.

2.2.7 Summary

Various radar interferometric time series analysis methods exist, each with its own characteristics, as summarized in Table 2.2. Similar to conventional radar interferometry, the crucial step remains the correct unwrapping of the phase. Once the phase is unwrapped, the challenge is to separate the various phase contributors, such as due to topography, deformation, and atmosphere. Here, assumptions regarding the spatio-temporal smoothness of the different signal components is required.

The most suitable approach for a certain study depends on a number of properties, such as the number of available radar images (in case of a low number of images, a small baseline approach is preferable above PSI), the surface cover (methods based on multilooked images are more suitable for arid regions compared to areas with abundant vegetational growth), and the expected deformation signal (smoothness of the signal in time or space). For regions with a moderate maritime climate, such as north-western Europe, characterized by a vegetated surface cover, an approach based on persistent scattering objects is most suitable. The design and implementation of the Delft PSI (DePSI) approach is described in Chapters 3-6.

The Delft Persistent Scatterer Interferometry (DePSI) algorithm performs an analysis of a single master stack of interferograms to detect Persistent Scatterers (PS) and estimate their deformation time series. The algorithm is described in Chapters 3–6. This chapter discusses the general structure of the algorithm and the first (pre-)processing steps. Section 3.1 presents the algorithm design. The algorithm is composed of separate processing steps. Each step is discussed shortly, including a reference to the particular section with a detailed description.

The creation of the input data for DePSI, the interferometric data stack, is described in Section 3.2. Section 3.3 discusses the selection of Persistent Scatterer Candidates (PSC), which aims to reduce the amount of data to be analyzed and to pre-assess the quality of the reflection points. Section 3.4 covers the so-called side lobes. The effect of these spurious reflection points in the data, which are caused by the reflection signature of strong point scatterers, is discussed. Furthermore, the section describes the procedure applied in DePSI to remove these side lobes from the data. Once the side lobes are removed, a first-order network is constructed based on the selected PSC, see Section 3.5. The first-order network aims to ensure the integrity of the analysis across the analyzed area. Finally, Section 3.6 provides a summary of the steps described in this chapter.

3.1 PSI algorithm design

The Delft Persistent Scatterer Interferometry (DePSI) algorithm transforms a radar interferometric data stack into a set of detected Persistent Scatterers, including their estimated deformation time series, geolocation and quality description. The algorithm uses a framework of geodetic estimation and testing methodologies, known as the 'Delft school' (see Appendix A), to embed PSI into the range of geodetic measurement techniques.

The DePSI approach is based on a hierarchical structure of PS, as conventionally applied in geodetic networks, see also Appendix B. The first-order PS (PS1) are assumed to be of the highest precision and thoroughly tested. These PS form a sparse initial network, which is used to model and estimate error sources, such as the atmospheric signal delay and orbit errors, and acts as the reference network for densification with higher-order PS (e.g., second order, PS2). The detection of PS (first and higher-order) is based on the testing of Persistent Scatterer Candidates (PSC), which are selected

a-priori based on the radar reflection intensity in the same radar data stack.

The estimation and testing procedures within DePSI are based on a mathematical model, containing both a functional and a stochastic model. The functional model describes the relation between the observations and the unknown parameters, whereas the stochastic model contains the statistic properties of the observations. The stochastic model contains both noise terms and (co-)variances due to error signals, such as atmospheric signal delay and orbit errors. Within DePSI an iterative scheme is applied to re-estimate the stochastic model by Variance Component Estimation (VCE) after estimation and correction of each error signal. Hence, the stochastic model is continuously updated to describe the observations as close as possible.

DePSI has a modular setup, which enables a project-based processing flow and the ability to re-run a processing step, if desired. The flowchart of DePSI is shown in Figure 3.1. Nine modules can be distinguished within DePSI, indicated in Figure 3.1 by a number. Some modules are re-occurring, indicated by a subsequent letter. The nine modules of DePSI are:

1. Initialization

DePSI is initialized by reading the metadata specifying the interferometric data set, see Section 3.2, and the process parameters defining the DePSI processing flow, such as the deformation models to apply and point selection thresholds. These processing parameters are tuned for a specific project based on a-priori information, for example the expected deformation signal.

2. Persistent Scatterer Candidates (PSC) selection

The Persistent Scatterer Candidates (PSC) are selected based on amplitude information in the interferometric stack, see Section 3.3. First-order as well as higher-order PS are selected. Due to the selection of the PSC, the amount of data to be analyzed is strongly reduced. During the selection process the pixels corresponding to side lobes of point scatterers are detected and removed from the data, see Section 3.4.

3. Network construction

A reference network based on the first-order PS is constructed. The reference network is used for Atmospheric and Orbital Phase Screen estimation and further densification of the PS. The set of detected PS is obtained after analysis of the first-order PSC. Here, four steps can be distinguished: 1) Estimation of the precision of the data, based on Variance Component Estimation (VCE) (see Section 4.4); 2) Formation of a spatial network between the PSC (see Section 3.5); 3) Temporal ambiguity resolution for each arc in the network (see Chapter 4); and 4) Spatial ambiguity resolution (see Section 5.1). These four steps are repeated after each phase screen estimation.

4. Trend estimation (optional)

Per interferogram a two-dimensional trend is optionally estimated to account for orbit errors. Orbit inaccuracies cause a low-frequency error signal in the interferograms, known as the *Orbital Phase Screen* (OPS), which influences the estimates for the deformation signal. After estimation of this error signal, based on the ref-

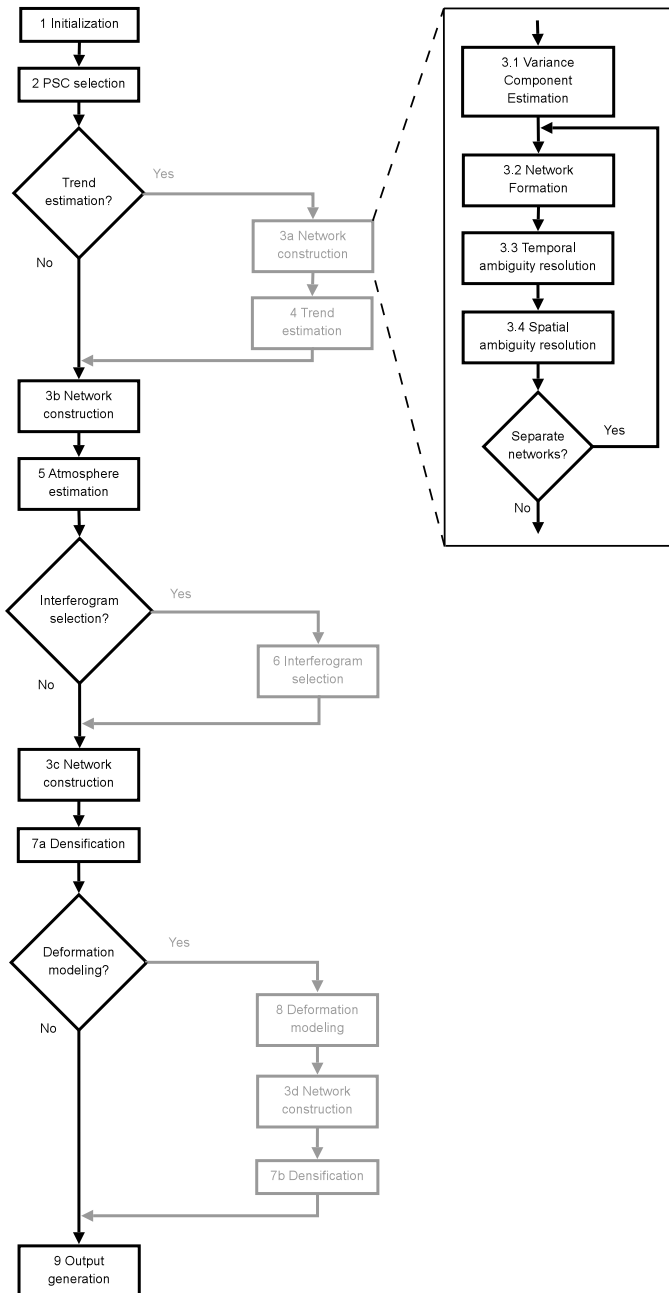


Figure 3.1: DePSI flowchart. Nine modules can be distinguished, indicated by a number. Re-occurring modules have an additional letter. The standard processing flow is shown in black, optional steps are indicated in gray.

erence network of PS, the original PSC interferometric phases are corrected, see Section 5.2.

5. **Atmosphere estimation**

The error signal due to atmospheric delay is estimated for each interferogram, known as the *Atmospheric Phase Screen* (APS). For an individual interferogram this atmospheric signal cannot unambiguously be distinguished from a deformation signal. However, using the full stack of interferograms, the assumption that the atmospheric signal delay is uncorrelated in time is used to separate the atmospheric signal from the deformation, see Section 5.3. After estimation of the APS, the PSC interferometric phases are corrected.

6. **Interferogram selection (optional)**

A selection from the total set of available interferograms is made for a deformation analysis of a limited time span, see Section 7.8. This approach is applicable when a certain deformation phenomenon only covers a limited time span in a relatively small area. An example is an area where during the acquisition time span a civil work is constructed, e.g., a railway track. Hence, whereas after the construction numerous PS may be present, before and during the construction the same image pixels will not provide a consistent reflection. In principle a standard PSI analysis based on a smaller data stack can be performed, however, for the estimation of error signals such as the atmospheric delay it is beneficial to use as many radar acquisitions as possible. Therefore, with this option a selection from the total stack can be made for the deformation analysis of this construction, whereas the total stack is used for the estimation of the spatially correlated error signals based on the surroundings.

7. **Densification**

Once the reference network is established after correction for the Atmospheric (and Orbital) Phase Screen, the network is densified with higher-order PS (see Section 5.4). The higher-order PSC are connected to close-by first-order PS and the ambiguities are resolved in time (see Chapter 4). When more connections per PSC are used, the estimated ambiguities are tested to increase the reliability of the solution. Based on the unwrapped phase observations, the parameters of interest are estimated, such as the residual height and the deformation parameters, and the final deformation time series if obtained.

8. **Deformation modeling (optional)**

The estimated deformation time series of the PS are used to estimate a deformation model per interferogram, the *Deformation Phase Screen* (DPS), see Section 7.4. The model can either be parametric, e.g., a subsidence bowl, or obtained by interpolation, e.g., by least-squares prediction or *Kriging* (Krige, 1951). After correction of the original PSC interferometric phases, the network construction and densification modules are repeated. Due to the removal of the deformation signal, which can also contain so far unmodeled deformation elements due to separate prediction per interferogram, potentially more PS can now be detected.

9. **Output generation**

Once the ambiguities are resolved and the parameters of interest are estimated,

the output is generated in a desired format. Here the PS are georeferenced to obtain coordinates in WGS84 (Section 6.1) and additional precision indicators are calculated (Section 6.2).

The main processing steps are described in detail in Chapters 3–6. The optional steps to improve the detection of PS, i.e., the selection of interferograms and deformation modeling, are presented in Chapter 7.

3.2 Interferometric data stack creation

The PSI analysis is based on a set of radar images of the area under consideration. Whereas the phase is the prime source of information, the intensity of the images is used during the analysis as well. DePSI can be applied to data acquired by any sensor, irrespective of the radar wavelength and polarization. However, a particular analysis is restricted to a homogeneous dataset, i.e., obtained by a single sensor with a specific polarization. An overview of past, current and future radar satellite missions including their characteristics is given in Tables 3.1a and 3.1b.

The interferometric processing of the radar data is performed using the Delft Object-oriented Radar Interferometric Software (DORIS) (Kampes and Usai, 1999; Kampes et al., 2003).

3.2.1 Master image selection

Typically all available images of a dataset are used in an analysis using the DePSI algorithm. This has two major advantages. Primarily, the derived deformation time series is as long and contains as much detail as possible. Second, error sources such as the atmospheric signal delay can be optimally estimated.

The interferograms are constructed in a single master configuration. Hence, all slave images are inferred with a unique master. The master image is selected based on three criteria:

1. Maximization of the expected stack coherence. Although the effect of decorrelation is minimal for point scatterers—even in case the perpendicular, temporal and Doppler baselines become larger than the critical baseline (see Section 2.1)—, the quality and number of detected PS can be optimized by minimizing the noise due to decorrelation. The optimal master can be selected visually by selecting an acquisition in the center of a *baseline plot*, see Figure 3.2 for an example, or can be based on the modeled stack coherence. The modeled stack coherence γ^m for master m is obtained by (Kampes and Adam, 2003)

$$\gamma^m = \frac{1}{S} \sum_{s=1}^S g(B_{\perp}^{ms}, B_{\perp\max}) \cdot g(B_{\top}^{ms}, B_{\top\max}) \cdot g(B_{\text{Dc}}^{ms}, B_{\text{Dc}\max}), \quad (3.1)$$

where

$$g(B, B_{\max}) = \max(1 - |B|/B_{\max}, 0). \quad (3.2)$$

Here s is the slave image, S the total number of slave images, B_{\perp} is the perpendicular baseline, B_{\top} is the temporal baseline, B_{Dc} is the Doppler centroid baseline,

Table 3.1a: Past, current and future radar satellite missions, and their characteristics, part I (stripmap mode, single polarization).

Mission (Number of satellites)	Period	λ [cm]	f_0 [GHz]	Band	θ [deg]	Pol.	Swath [km]	ΔT [days]
ERS-1 (1)	1991-2000	5.6	5.300	C	23	VV	100	35*
ERS-2 (1)	1995-2011	5.6	5.300	C	23	VV	100	35
ENVISAT (1)	2002-2010	5.6	5.331	C	23	HH,VV	105	35
ENVISAT Ext** (1)	2010-2012	5.6	5.331	C	36	HH,VV	60	30
ALOS (1)	2006-2011	23.6	1.270	L	8-60	HH,VV	40-70	46
Radarsat-2*** (1)	2007-	5.5	5.405	C	20-49	HH,VV	100	24
TerraSAR-X (2)	2007-	3.1	9.650	X	20-45	HH,VV	30	11
Cosmo-Skymed (4)	2007-	3.1	9.600	X	20-60	HH,VV	40	4
Sentinel-1 (2)	2014-	5.5	5.405	C	29-46	HH,VV	250	6

λ , wavelength; f_0 , carrier frequency; θ , look angle; ΔT , repeat interval.

* For the periods 1993-1994, 1995-2000. Within the other periods alternative orbit configurations were applied.

** Envisat Extended mission, swath IS6.

*** Standard mode.

and B_{\max} are the maximum baselines that scale the effect of the different decorrelation factors. Suitable values for the different maximum baselines differ per sensor, i.e., dependent on the range and azimuth bandwidth, and the wavelength. The perpendicular B_{\max} can for example be chosen equal to the critical baseline $B_{\perp \text{crit}}$. See Table 3.1b for the specific values per sensor. The $B_{T_{\max}}$ is normally set to at least half the time span of radar acquisitions, resulting in an optimal master somewhere halfway the acquisition time span. The modeled stack coherences are evaluated for all images and ordered to obtain a ranking of most suitable master images.

2. Minimum atmospheric signal delay. Each interferogram in the single master stack contains the atmospheric signal delay of the master image. Since the Atmospheric Phase Screen (APS) (see Section 5.3) is predicted based on a sparse distribution of PS, the prediction error will be larger for a highly turbulent atmosphere. Since the master atmosphere is contained in each APS, a master acquisition with moderate weather conditions enhances the performance of APS prediction per interferogram. External meteorological data can be used to assess the weather conditions per acquisition, to select the optimal master. Hereby, acquisitions during heavy rain or thunderstorms can be excluded.
3. Minimum expected clutter. For optimal estimation of the deformation parameters the scattering phase φ_{scat} (see Eq. (2.5)) should be as low as possible. This scattering phase is dependent on the amount of temporal decorrelation in the resolution cell. The scattering characteristics of a resolution cell can for example change due to vegetational grow or snow cover, particularly affecting the *clutter*. To minimize the interferometric scattering phase, the clutter of the master image should be as low as possible, hence have a high Signal-to-clutter ratio (SCR). Therefore an image where minimal vegetational grow is expected, e.g., in the winter, although without snow cover, is desirable.

Once the master image is selected, the interferometric stack can be processed.

Table 3.1b: Past, current and future radar satellite missions, and their characteristics, part II (stripmap mode, single polarization).

Mission (Number of satellites)	H_{sat} [km]	Δ_{az} [m]	Δ_{sr} [m]	Δ_{gr} [m]	B_r [MHz]	RSR [MHz]	B_{az} [Hz]	PRF [Hz]	$B_{\perp\text{crit}}$ [km]
ERS-1	785	4.0	7.9	20.0	15.55	18.96	1378	1680	1.1
ERS-2	785	4.0	7.9	20.0	15.55	18.96	1378	1680	1.1
ENVISAT	785	4.0	7.8	20.1	16.0	19.2	1316	1652	1.1
ENVISAT Ext**	785	3.8	7.8	12.0	16.0	19.2	1347	1742	2.2
ALOS	691	3.1	4.7	7.5	28	32	1707	2155	12.7
Radarsat-2***	798	4.9	11.8	21.1	11.6	12.7	900	1353	1.2
TerraSAR-X	514	1.9	1.3	2.1	150	165	2765	4113	5.4
Cosmo-Skymed	620	2.3	0.8	2.2	156	195	2559	3046	6.8
Sentinel-1	693	17.4	2.3	3.7	48	61.5	313	1252	6.3

H_{sat} , satellite altitude; Δ_{az} , azimuth spacing; Δ_{sr} , slant range spacing; Δ_{gr} , average ground range spacing; B_r , range bandwidth; RSR, range sampling rate; B_{az} , range azimuth; PRF, pulse repetition frequency; $B_{\perp\text{crit}}$, critical perpendicular baseline (flat terrain, see Hanssen (2001)).

** Envisat Extended mission, swath IS6.

*** Standard mode.

3.2.2 Image crop selection

Often the area of interest for a deformation analysis is limited to a certain crop of the full radar image. This crop can be selected at two stages in the processing chain: 1) during the processing of the interferometric stack, or 2) during the PSI analysis. In the first case the images are cropped based on the geographic center coordinates of the crop. Because the crop per image is based on the orbit and timing parameters which may contain errors, the crop should be taken larger than the finally desired extent. In case of the second option the complete images are taken to calculate the interferograms and a certain crop is selected within DePSI. Advantage of this option is that multiple crops of the same dataset can be analyzed ensuring equal interferometric processing characteristics, e.g., coregistration and resampling, see Section 3.2.4. This is especially important when DePSI results of different crops are merged afterwards.

3.2.3 Image oversampling and filtering

Once the original SLC data is read and, if desired, a crop is selected, the complex radar data is oversampled with a factor two in both range and azimuth direction. Oversampling is needed to avoid aliasing in the interferometric phase, see Section 2.1.3. Point scatterers cause a sinc-shaped signal in the radar image, which requires the full spectrum in the frequency domain to be described. When part of the oversampled spectrum would be low-pass filtered, the sinc is broadened and the phase of the point scatterer would change, introducing noise. As a result of oversampling and not downsampling, the radar images become four times bigger than the original crops (and the pixel spacing twice as small).

For the same reason of preservation of the phase for point scatterers no spectral filtering is applied. This holds for both the range and azimuth direction. Moreover, the remaining common band for the full data stack would be very limited, strongly reducing the resolution. As a result of not filtering, the effect of geometric and Doppler decorrelation (see Section 2.1.3) remains in the interferogram, affecting pixels with distributed

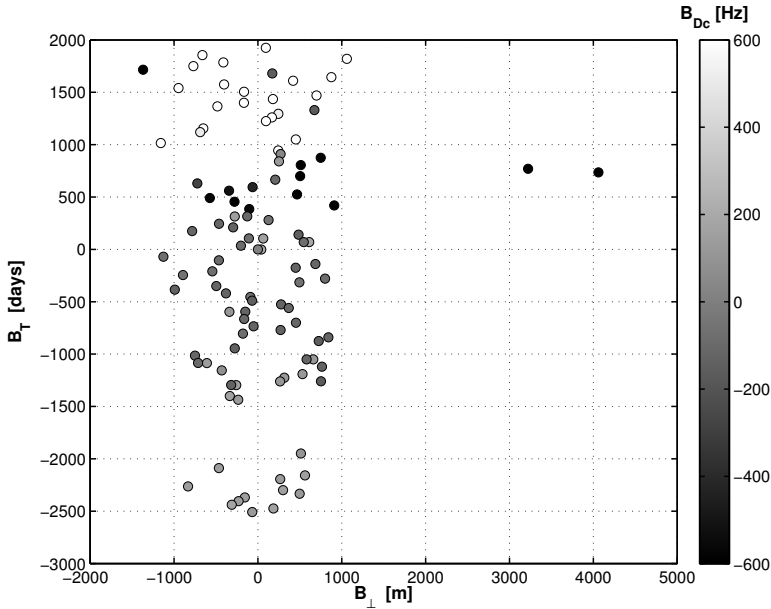


Figure 3.2: Baseline plot for the ERS-1/2 data stack of the Gardanne region, France. The plot shows the configuration of the acquisitions regarding the perpendicular baseline (B_{\perp}), the temporal baseline (B_T), and the Doppler centroid baseline (B_{Dc}), with respect to the master acquisition. The Doppler centroid baselines are indicated with a grayscale.

scattering. Hence, the chance of detection of PS with distributed scattering is reduced. An alternative would be to keep the spectrum of the master image fixed and only filter the slave spectra. A large part of the decorrelation effect is hereby removed. However, the phase of point scatterers will still be affected.

3.2.4 Image coregistration

To be able to calculate the interferograms, the oversampled slave images should be aligned to the master image. That is, the pixels of both the master and slave images should cover the same area of the Earth's surface. This procedure is known as *coregistration*. The original images are all shifted, rotated, stretched, and distorted with respect to each other due to changes in the orbit, antenna orientation and acquisition timing in combination with the topography.

Inaccuracies in the coregistration introduce an additional decorrelation effect, hence, noise in the phase observations, see Section 2.1.3. Especially point scatterers are sensitive to coregistration inaccuracies. Therefore, high accuracy in the coregistration is required. A precision of 1/8th of an oversampled resolution cell in range and azimuth direction is desirable to maintain a coherence due to the coregistration of 0.99 (Just and Bamler, 1994; Hanssen, 2001). Two algorithms can be used, correlation based coregistration and the newly implemented Digital Elevation Model (DEM) based coregistration (Adam et al., 2003; Sansosti et al., 2006; Arikan et al., 2008).

Correlation-based coregistration

Traditionally, coregistration is performed by a large number of matching windows (e.g., > 5000) between the master and slave image. The matching is based on correlation of the amplitude. The windows should be homogeneously distributed over the scene. Once an estimate of the offset between master and slave is obtained for each window, a warp function is estimated that describes the offset for each pixel. Normally a 2D polynomial of a certain degree, e.g., between two and five, for both the range and azimuth direction is used. During the estimation process of the polynomial, a testing scheme is applied to remove outliers. The testing procedure is continued until the desired accuracy of the warp function is obtained.

The initial distribution of correlation windows can either be systematic or directed. The systematic approach automatically ensures a homogeneous distribution of windows. However, a large part of these windows will cover areas with a homogeneous radar reflection signature, e.g., agricultural fields or water bodies, which makes it difficult to determine the corresponding window position in the slave image. The effect is increased by the large baselines in the single master stack. As a result, the final set of matched windows after testing may be limited and badly distributed. Therefore often a directed distribution approach is used (Ketelaar, 2009). Here, the windows are positioned around strong (point) scatterers in the master image, ensuring good correlation conditions. A selection grid ensures a homogeneous distribution over the scene.

Although good results can be obtained with the correlation-based method for relatively flat terrain with a certain degree of urbanization, success is not guaranteed under less favorable conditions. Two reasons can be distinguished. First, a sufficient amount, and distribution of, reliable correlation windows cannot be ensured. Second, the estimated warp function may not be able to describe the offsets with enough accuracy in case of strong topography. Therefore, a more generic method is desirable, which is obtained with the DEM-based coregistration approach.

DEM-based coregistration

In case of the DEM-based coregistration approach the coregistration offsets are determined per pixel based on external topographic data and orbit information of the satellite (Adam et al., 2003). The advantage compared to the window correlation approach is that topographic details can be accounted for and that a limited number of reliable correlation windows between the master and slave images is sufficient to account for remaining timing errors. The approach is especially useful for sensors with a wide bandwidth, i.e., high spatial resolution, such as TerraSAR-X and Cosmo-Skymed (see Table 3.1b). Due to the high resolution, topography can easily cause shifts in radar coordinates, resulting in failure of achieving the required sub-pixel coregistration accuracy with the traditional correlation approach.

A DEM obtained by the Shuttle Radar Topography Mission (SRTM) (Farr et al., 2007) can for example be used, having near-global coverage and a spatial resolution of 3 arcseconds (≈ 90 meter). However, a higher resolution will improve the performance. Precise orbits, for example provided by the Delft University of Technology for the ERS-1/2 and Envisat satellites (Scharroo and Visser, 1998), are used for optimal orbit parameters. The method is implemented in DORIS (Arikan et al., 2008).

The algorithm consists of four steps:

1. Estimation of the master timing error in range and azimuth direction. The master amplitude is correlated with a simulated amplitude image based on the DEM (Eineder, 2003), see Figure 3.3. The DEM is assumed to be georeferenced correctly. The offsets between the correlation windows are translated to timing errors.
2. Estimation of the relative timing error between master and slave image. The slave timing error with respect to the corrected master image is estimated based on orbit information and correlation window offsets. Because timing errors cause a constant shift in both azimuth and range direction, only a limited number of suitable correlation windows are required, of which the distribution is of no importance. Alternatively, the slave image can also be corrected directly based on the simulated amplitude image, however the master-slave correlation is more precise due to the higher resolution of the radar images involved compared to the DEM. As a result, an error in the master timing will propagate to the slave timing. However, the relative DEM positioning is consistent.
3. Radarcoding of the DEM in both the master and the slave image geometry, obtaining the offsets per DEM point. For each element of the DEM the (real valued) radar coordinates in both the master and slave image are calculated using the precise orbits. The Doppler, range and ellipsoid equations are used (see Section 6.1), hence, no approximations are applied. The difference between the master and slave coordinates represent the coregistration offsets.
4. Interpolation of the estimated offsets, known in real valued master coordinates, to the grid of integer-valued master coordinates. A linear interpolation based on a Delaunay triangulation is used to obtain an offset value per pixel.

The estimated offsets can now directly be used to resample the slave image to the master image geometry, instead of obtaining these offsets from the warp function as in case of the correlation based method.

The implemented algorithm is evaluated by Nitti et al. (2008). The evaluation shows that the improvement is indeed significant for sensors with high spatial resolution. For ERS and Envisat images, there is no significant improvement. This is also observed by Arikan et al. (2008). The lack of improvement can be partly explained by the limited bandwidth of ERS and Envisat. Additionally, Nitti et al. (2008) state the relatively coarse resolution of the SRTM data used induces an extra noise term in the DEM based coregistration. Nevertheless, due to the robustness the DEM based coregistration approach is recommended for images of all sensors.

3.2.5 Interferogram formation

Once all images are resampled to the geometry of the master image, the interferograms are calculated by complex multiplication between master and slave. Subsequently the flat Earth reference phase is computed and subtracted based on precise orbit information. The Doppler, range and ellipsoid equations are used to avoid approximations (see Section 6.1). The equations are also applied for the calculation of the topographic phase,

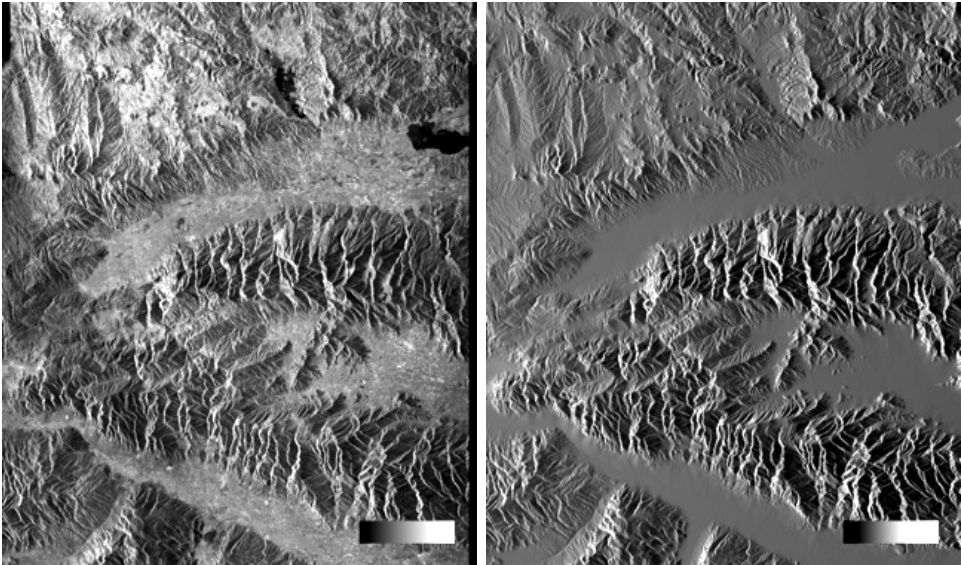


Figure 3.3: Left) Amplitude image of a mountainous area in Turkey. Right) Simulated amplitude image based on SRTM DEM of the same area. The timing errors of the image are corrected by correlation with the simulated image. Images taken from the DORIS user manual (Kampes, 1999).

which is modeled based on a DEM. Correction for the topography is not a strict requirement, because during the DePSI analysis the (residual) topographic height is estimated as well. However, when the topographic phase is subtracted, the solution space for the height estimate is reduced, decreasing the computation time and increasing the success-rate of correct ambiguity resolution and parameter estimation in DePSI, see Chapter 4. Therefore, use of a DEM is recommended, especially in mountainous terrain.

Both during the computation of the flat Earth phase and the topographic phase the so-called height-to-phase conversion factor is computed, see Eq. (2.9). This factor is slowly changing, yet unique for every pixel in an interferogram. Therefore an array of the same size as the interferogram is formed and saved. During the flat Earth computation, the conversion factor is based on the WGS84 ellipsoid, whereas during the topographic phase computation the DEM is considered. Since the latter is more accurate (see also Section 4.2.1), these values are preferably used in DePSI, however, are only available when the topographic phase is calculated with DORIS.

The processing of the interferometric stack by DORIS (Kampes and Usai, 1999; Kampes et al., 2003) results in three sets of files which are used by DePSI: interferograms, height-to-phase conversion factors and resampled radar images (including the master image). The latter are used for their amplitude information.

With the interferometric data stack the DePSI analysis can be started. The first step is the selection of the Persistent Scatterer Candidates.

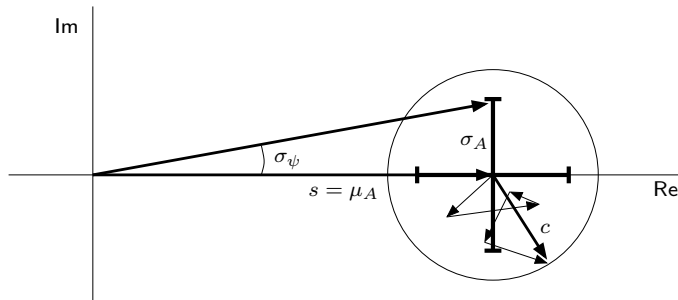


Figure 3.4: Phasor of a point scatterer. Amplitude information is used to detect points with stable phase behavior, i.e. small σ_ψ . Detection is for example based on the normalized amplitude dispersion D_A , which is defined as the ratio between the standard deviation of the amplitude σ_A and the mean amplitude μ_A of a single pixel in a radar image stack. Alternatively, the Signal-to-clutter ratio (SCR) can be used, which describes the relative strength of the signal s with respect to the surrounding clutter c . For the relation between the clutter (in the complex domain) and the standard deviation of the amplitude applies $c = \sqrt{2} \sigma_A$.

3.3 Persistent Scatterer Candidate selection

The radar interferometric data stack typically contains billions of image pixels. The objective of the PSI analysis is to detect the pixels with coherent phase behavior and to estimate their deformation behavior. To enable an efficient analysis, a pre-selection of the most promising scatter locations is made, the Persistent Scatterer Candidates (PSC). Besides data reduction, the pre-selection is also used to establish a hierarchy in the pixels, obtaining first-order and higher-order PSC (see Appendix B). The first-order pixels are used to form a network across the analyzed area (see Section 3.5), whereas the higher-order PSC are used for the densification of the PS distribution.

This section describes the PSC selection criteria that can be used, the calibration of the radar amplitude in the data stack, and the PSC selection algorithm applied.

3.3.1 PSC selection criteria

The finally detected PS are obtained after testing of Persistent Scatterer Candidates on phase stability or *coherence*. Because the original interferometric phase is wrapped and is composed of a large number of phase contributors (Eq. (2.5)), the PSC cannot be selected based on phase. Therefore, amplitude information is used as a proxy for phase stability.

There is a statistical relation between calibrated amplitude stability (see Section 3.3.2) and phase stability (Ferretti et al., 2001). This relation is visualized in Figure 3.4, where the phasor of a point scatterer surrounded by clutter is shown. It indicates that when a strong point scatterer, which by definition has a large amplitude, dominates the resolution cell, the influence of clutter on the phase is only limited. This phenomenon is used to select pixels with a high likelihood of having a stable phase based on amplitude.

Possible selection methods are the normalized amplitude dispersion, amplitude thresholding, Signal-to-Clutter ratio (SCR), and supervised selection.

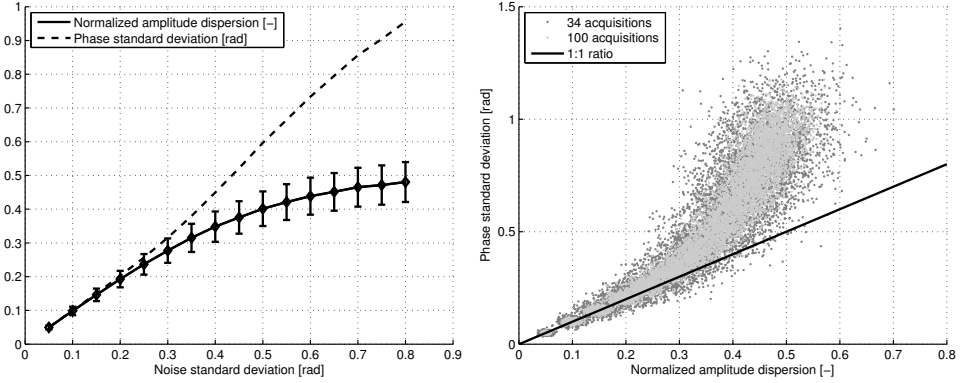


Figure 3.5: Numerical simulation of the relation between amplitude dispersion D_A and phase standard deviation σ_ψ (Ferretti et al., 2001), modified after Hooper (2006). A complex variable $z_i = s + n_i$ is simulated 5000 times. The signal is fixed to $s = 1$, while the standard deviation, σ_n , of both the real and imaginary components of the noise, n_i , is incremented from 0.05 to 0.8. Left) Mean values of D_A and σ_ψ are plotted, together with error bars for D_A , assuming 34 radar acquisitions ($i = 1, \dots, 34$). Small values of the normalized amplitude dispersion are a good proxy for phase stability. Right) Scatter plot of D_A versus σ_ψ assuming 34 respectively 100 radar acquisitions. With a higher number of available radar acquisitions, D_A becomes more reliable as a proxy for phase stability.

Normalized amplitude dispersion

The normalized amplitude dispersion D_A is based on the analysis of the amplitude time series per pixel. The relation between the phase standard deviation σ_ψ and D_A is (Ferretti et al., 2001)

$$\sigma_\psi \approx \tan(\sigma_\psi) = \frac{\sigma_A}{\mu_A} \doteq D_A \text{ [rad]}, \quad (3.3)$$

where μ_A and σ_A are the mean and standard deviation of amplitude in the time series, see Figure 3.4. Hence, a pixel with a relatively constant amplitude in time is expected to have a low phase dispersion. The validity of this relation is evaluated by Ferretti et al. (2001) by means of a numerical simulation, see Figure 3.5. The left figure shows the correspondence between σ_ψ and D_A for different noise levels. It shows that D_A is only a good proxy for phase stability in case of low σ_ψ values. However, the figure does not show the phase variability for a given amplitude dispersion. A better indication of this relation is shown by the scatter plot in Figure 3.5 (right). A D_A of 0.3 indicates a range for σ_ψ of about 0.25 to 0.54 rad when 34 radar acquisitions are used (Hooper, 2006). The range decreases when more acquisitions are available. Hence, the D_A becomes a more reliable proxy for phase stability with an increasing number of available acquisitions. The figure further shows that assuming a maximum σ_ψ for coherent point scatterers of e.g. 0.6 (Colesanti et al., 2003b), the corresponding D_A is maximally 0.4.

Amplitude thresholding

An alternative PSC selection criteria is based on amplitude thresholding (Kampes and Adam, 2004). A pixel is selected as PSC if its normalized radar cross section σ^0 (RCS),

i.e., the calibrated intensity, is above a threshold N_2 in at least N_1 SLC images

$$\sum_{k=0}^K n_k \geq N_1, \quad \text{with } n_k = \begin{cases} 1, & \text{if } \sigma_k^0 > N_2, \\ 0, & \text{otherwise,} \end{cases} \quad (3.4)$$

where K is the number of radar acquisitions. Kampes and Adam (2004) propose a N_1 of $0.65K$ and, based on ERS characteristics, a N_2 of -2 dB. This method has two drawbacks, both related to the value of N_2 . First, an absolute radiometric calibration of the images is required to relate the measured intensity to the radar cross section, see Section 3.3.2. This in contrast to other methods, where a relative calibration is sufficient. Second, the radar cross section is dependent on the sensor characteristics, requiring a different threshold N_2 for each sensor.

Signal-to-Clutter ratio

The phase stability can also be assessed using the Signal-to-Clutter ratio (SCR) (Adam et al., 2004). A pixel is selected when the average SCR in time is above a certain threshold. The SCR is defined as

$$\text{SCR} = \frac{s^2}{c^2}, \quad (3.5)$$

where s is the amplitude, in this context referred to as the signal, and c represents the clutter. A spatial estimation window is used to estimate the SCR per pixel. The assumption is that surrounding pixels contain clutter that is equal to the clutter within the resolution cell. The amplitude of the central pixel represents the signal. Similar as for the amplitude dispersion, a relation can be derived between the phase standard deviation σ_ψ and the SCR, see Figure 3.4,

$$\sigma_\psi \approx \tan(\sigma_\psi) = \frac{\sigma_A}{\mu_A} = \frac{c/\sqrt{2}}{s} = \frac{1}{\sqrt{2} \cdot \text{SCR}} \quad [\text{rad}]. \quad (3.6)$$

Adopting a threshold on the noise level in the phase observations of 30° or 0.5 rad, a threshold for the average SCR over all images of 2 dB is obtained (Adam et al., 2004).

Disadvantage of the method is that the clutter is likely to be overestimated in urban areas, because neighboring pixels may also contain point scatterers (Adam et al., 2004). As a result, the method could lead to rejection of suitable PSC.

Supervised selection

Instead of data reduction by the selection of PSC based on amplitude information, the PSC can also be determined based on external information or assumptions. By *supervised selection* an area of interest within the total crop is selected, in which all pixels are labeled as PSC. For example, an area of special interest such as a civil work is selected (Arikan and Hanssen, 2008). Alternatively, a buffer around all roads is used to exclude agricultural fields, which have a small likelihood to contain PS, from the data (Humme, 2007). This procedure is also followed for the monitoring of water defense structures (Hanssen and van Leijen, 2008a,b; van Leijen et al., 2008).

Default selection method

The default method for the selection of Persistent Scatterer Candidates within DePSI is the normalized amplitude dispersion. This choice is based on minimizing the false rejection rate and the computational speed.

The normalized amplitude dispersion is based on a single pixel within a data stack, hence, without incorporation of surrounding pixels which can influence the result, as is the case for the Signal-to-Clutter ratio. Hence, the method also enables the detection of point scatters with a low intensity or pixels with distributed scattering characteristics. Hereby, the method has the potential to detect more coherent pixels.

The pixel based retrieval of the normalized amplitude dispersion is based on simple average and standard deviation operators, and does not require the absolute calibration of the radar images, as is the case for the amplitude thresholding approach. Therefore, the amplitude dispersion approach is computationally very efficient.

Apart from the normalized amplitude dispersion for the selection of first and higher-order PS, a supervised selection can be used for a detailed analysis of a certain area of interest.

3.3.2 Amplitude calibration

The PSC selection methods based on amplitude require a radiometric calibration of the SLC images. Differences in sensor (e.g., ERS-1 and ERS-2), radiometric sensor stability and processing algorithm of the raw data induce the need for a radiometric correction of the data (Laur et al., 2002). An absolute calibration is obtained by a constant correction per acquisition (calibration constant, replica pulse power), a range dependent correction (incidence angle, range spreading loss, antenna pattern gain) and a correction factor that varies over the entire image (power loss). The advantage of such an absolute calibration is that the result relates to the physical properties of the reflections. However, implementation of absolute calibration algorithms for the various sensors is complex and for the objective of most PSC selection methods not necessary, as discussed in Section 3.3.1.

Therefore, a relative radiometric calibration procedure is implemented in DePSI (Ketelaar, 2009). One SLC is randomly selected as reference and a relative calibration factor is calculated for the remaining SLC's. This can be compared with a histogram equalization procedure. However, in this case not the complete images are used but only a set of pre-selected stable scatterers (based on amplitude dispersion). The effect of disturbing reflection differences, for example due to moisture differences of agricultural fields and variations in water surface roughness, is thereby eliminated. Hence, the calibration is based on the actual stable scatterers that are of interest. The relative calibration factors are obtained after a least-squares adjustment and testing scheme (see Section 5.1) and Variance Component Estimation (see Section 4.4). To avoid the accidental selection of calibration pixels in water surfaces, a water mask can be applied to exclude these surfaces from the calibration procedure.

3.3.3 PSC selection algorithm

Once the radar images are calibrated, the PS candidates are selected. A distinction is made between the first order and higher-order PSC (see Section 3.1).

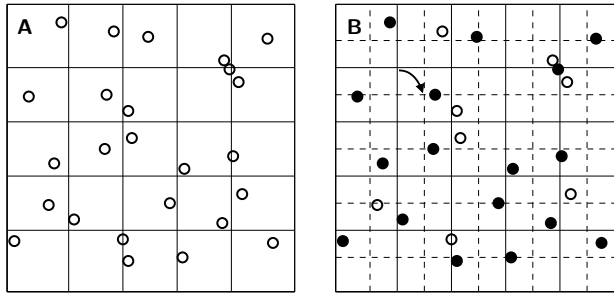


Figure 3.6: A) Initial selection of PSC using a grid to ensure a homogeneous distribution. B) Final selection by shifted grid (dashed lines) in both range and azimuth direction, indicated by arrow, to avoid nearby PSC. The PSC with the lowest amplitude dispersion in the shifted grid cell is selected (black dots).

First-order PSC selection

The first-order Persistent Scatterers form the reference network and are used to estimate the Atmospheric and Orbital Phase Screens. The first-order PS candidates should therefore be homogeneously distributed over the image. This is accomplished by defining a grid which directs the distribution of PSC (Kampes and Adam, 2003), see Figure 3.6A. The resolution of the grid is typically 200-500 m. Per grid cell the best candidate is selected based on amplitude dispersion (see Section 3.3.1). Then, a threshold can be applied to discard pixels with too low amplitude stability, e.g., to remove points in agricultural fields or *water pixels*, in case no water mask is applied¹. The normalized amplitude dispersion threshold is dependent on the number of available images, but normally lies in the range 0.2-0.3 rad. However, the choice can be made not to use a threshold and to select a PSC for each grid cell (Samiei-Esfahany, 2008). The network will become denser, but the number of points with instable phase will (relatively) increase. This may cause a division of the network into several separate network patches during the spatial ambiguity resolution (see Section 5.1.2). Although an iterative scheme is applied to construct a single first-order network, separate networks could remain when the maximum number of iterations is reached.

To avoid nearby PSC to be too close by, the grid is shifted with half the grid size in both range and azimuth direction (Kampes and Adam, 2003), see Figure 3.6B. Per new grid cell the PSC with the lowest amplitude dispersion is selected. Hereby, the final set of PSC is obtained.

Higher-order PSC selection

In one of the last steps of DePSI, the first-order network is densified by evaluation of higher-order Persistent Scatterer Candidates (PSC) (see Section 5.4). The higher-order PSC can either be selected during the PSC selection step, or during the densification step itself. Advantage of the first option is that the interferometric data stack only has to be read in DePSI once. This is beneficial, because typically only a small percentage of the total amount of pixels experience stable amplitude (and potentially stable phase)

¹There is always a 'best' pixel, therefore also when the the grid cell is fully covered by water.

behavior. Hence, a significant data reduction can be obtained. Advantage of the second option is that the selection of PSC can be tuned during the actual densification process according to the results, see Section 7.6.

In case the higher-order PSC are selected in the PSC selection step, again the normalized amplitude dispersion is used as criterion. However, the threshold is increased to select more PSC compared to the set of first-order points. A typical value for the threshold is around 0.4-0.45. Since the normalized amplitude dispersion is biased (Ferretti et al., 2001), these thresholds correspond to a phase noise level of 0.5-0.7 rad (30° - 40°), see Figure 3.5. Here, no grid or other additional criterion is applied, hence, simply all points below the threshold are selected. As a result, the second-order PSC (PSC2) selected here also contain the first-order PSC (PSC1), see Appendix B. This situation is maintained because PSC1 could be rejected during the spatial network unwrapping, whereas the same points could be accepted as PS2 after Atmospheric (and Orbital) Phase Screen correction, see Sections 5.2 and 5.3.

The PSC selection criteria, such as the normalized amplitude dispersion, are in principle applied to all image pixels in the data stack. However, point scatterers cause spurious reflection points in the data, so-called side lobes. Since these side lobe pixels do not contain a representative signal for their associated image location, they are detected and removed during the PSC selection process. The side lobe detection is described in the next section.

3.4 Side lobe detection

The spatial signature of a point scatterer in a radar image is a sinc function (Cumming and Wong, 2005). This sinc pattern causes *side lobes* in the radar image, both in azimuth and range direction, see Figure 3.7 (top image). The significance of the side lobes is dependent on the strength of the point scatterer. The effect of the spatial signature on the phase is that every second side lobe has the same phase as the main lobe, whereas the phase of the intermediate side lobes is shifted with π . Hence, the phase observations of the side lobes are not independent and therefore do not add new information. However, due to their direct relation to the main lobe, the side lobes have a reasonable likelihood to be selected as PSC and accepted as PS. The same applies to the pixels directly surrounding the single pixel containing the actual point scatterer. Especially after oversampling of the data, the main lobe will cover multiple pixels. The surrounding pixels are denoted here as *sub-main lobe* pixels.

Both the side lobe and sub-main lobe pixels are unwanted in the final set of detected PS. Ideally they are excluded in an early stage, i.e. during the PSC selection. Before describing the algorithm applied to detect the side lobes (including the sub-main lobes), first the effect of undetected side lobes on the deformation analysis is discussed.

3.4.1 Effect of side lobes

Because the side lobes contain the same phase information as the main lobe, the estimates of parameters of interest (e.g. deformation and height) should be the same for all lobes. However, the different location of the side lobes in the radar image introduce an error signal in range direction due to the applied reference phases (flat Earth and DEM).

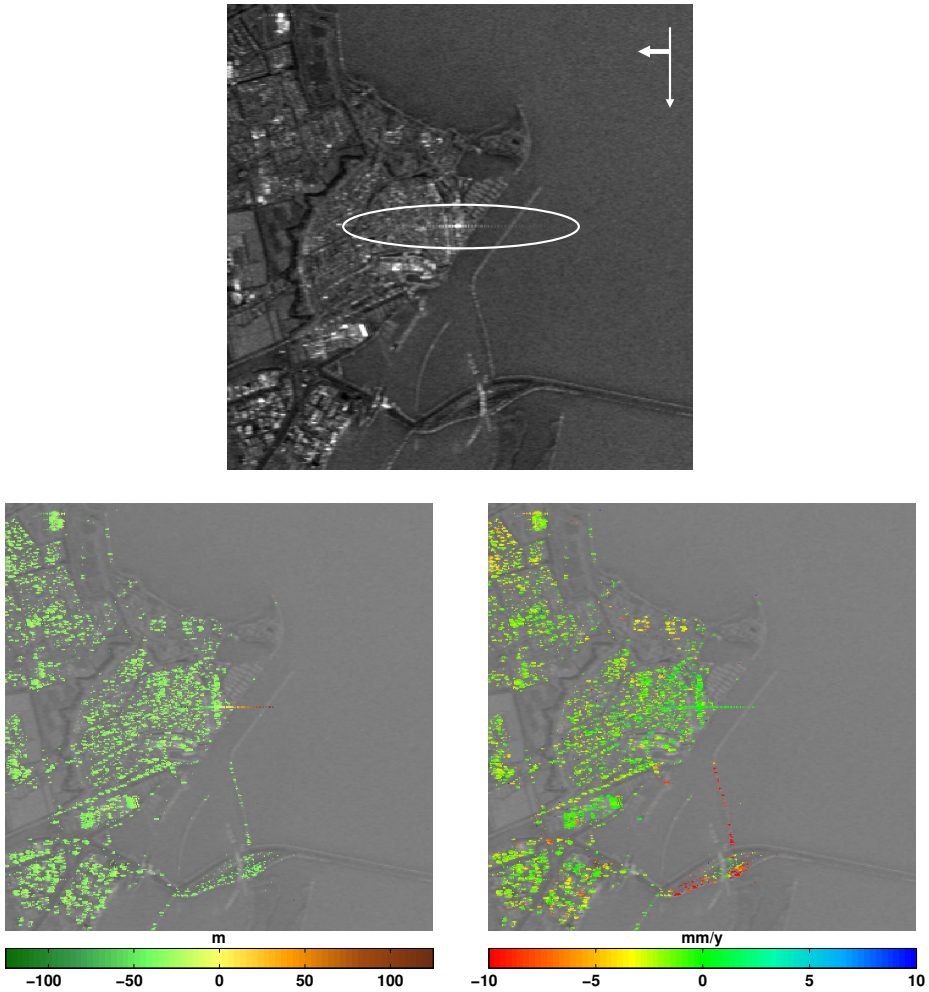


Figure 3.7: Top) Example of a strong point scatterer with side lobes in Enkhuizen, the Netherlands (white ellipse). The data is acquired from a descending orbit and a right-looking antenna, indicated by the long and the short arrow, respectively. Left) Estimated residual height [m]. The side lobes cause a height ramp due to the erroneous flat Earth reference phase applied. Right) Estimated linear deformation rate [mm/y]. The deformation is not affected by the erroneous reference phase of the side lobes.

That is, the reference phases are calculated based on the radar coordinates of the side lobes, whereas the actual measured phases are related to the main lobe (location). The DEM reference phase, which is a function of the perpendicular baseline, does not cause a problem, because the residual height is estimated during the DePSI analysis, correcting the introduced error. The effect of the erroneous flat Earth reference phase, which is a function of the parallel baseline, is however less trivial.

The flat Earth reference phase φ_{fE} under the far-field approximation is defined as (Hanssen, 2001)

$$\varphi_{\text{fE}} = \frac{4\pi}{\lambda} B \sin(\theta_i^m - \alpha). \quad (3.7)$$

The variation of the reference phase as function of the look angle is

$$\partial\varphi_{\text{fE}} = \frac{4\pi}{\lambda} B \cos(\theta_i^m - \alpha) \partial\theta. \quad (3.8)$$

The effect of a deviation in the reference phase $\partial\varphi_{\text{fE}}$ on the estimated height ∂H_i (see Eq. (2.9)) can be derived using the equality

$$\frac{4\pi}{\lambda} B \cos(\theta_i^m - \alpha) \partial\theta = \frac{-4\pi}{\lambda} \frac{B \cos(\theta_i^m - \alpha)}{R_i^m \sin(\theta_i^m)} \partial H_i. \quad (3.9)$$

Elimination gives

$$\partial H_i = -R_i^m \sin(\theta_i^m) \partial\theta. \quad (3.10)$$

Equations (3.9) and (3.10) show that an error in the flat Earth reference phase causes an error in the estimated height which is independent of the baseline parameters and radar wavelength. Moreover, due to the direct relation between the reference phase and the height, the error in φ_{fE} is totally absorbed by the estimated height. Therefore, the erroneous reference phase for side lobes does not influence the deformation parameters. This can also be observed in the example in Figure 3.7 (bottom right image). All side lobe pixels show the same deformation rate, whereas a clear trend in the estimated height is visible, see Figure 3.7 (bottom left image).

The effect of side lobes on the height estimate can easier be shown by writing Eq. (3.10) as function of slant range R . Neglecting the curvature of the Earth, the look angle is related to the slant range by

$$\theta_i^m = \arccos\left(\frac{H_{\text{sat}}}{R_i^m}\right). \quad (3.11)$$

The variation of the look angle in relation to the slant range is

$$\frac{\partial\theta}{\partial R} = \frac{H_{\text{sat}}}{(R_i^m)^2 \sqrt{1 - (H_{\text{sat}}/R_i^m)^2}}. \quad (3.12)$$

Using

$$\cos(\theta_i^m) = \frac{H_{\text{sat}}}{R_i^m}, \quad (3.13)$$

this results in

$$\partial\theta = \frac{\cos(\theta_i^m)}{R_i^m \sin(\theta_i^m)} \partial R. \quad (3.14)$$

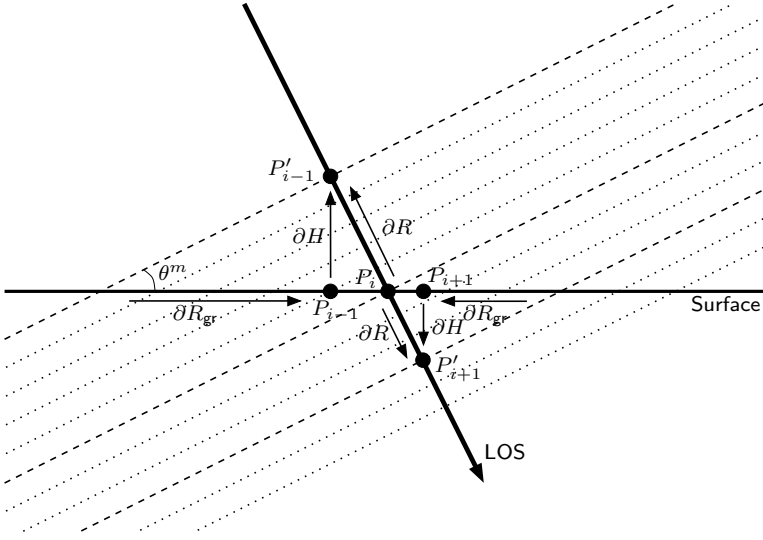


Figure 3.8: The geolocation of side lobes. The flat Earth reference phase applied at the side lobe locations causes the side lobes to be mapped close to the location of the main lobe. The large arrow indicates the Line of Sight (LOS). In this example the main lobe of scatterer P_i is located at the reference surface. Because the phase of the side lobe is similar to the observed phase at the main lobe, a similar height would be estimated for the side lobe. However, due to the reference phase applied for a side lobe at slant range distance ∂R of the main lobe an additional height ∂H is estimated, see Eq. (3.15). This results in the 3D positions P'_{i-1} and P'_{i+1} for side lobes at both sides of the main lobe, respectively. These positions can be mapped to the P_{i-1} and P_{i+1} positions at the reference surface, at ground range distance ∂R_{gr} of the position that would be obtained without the erroneous flat Earth reference phase applied, see Eq. (3.19). Hence, side lobes that are not removed from the set of selected pixels beforehand, are mapped close to, but not completely at, the main lobe location. The deviation is only dependent on the incidence angle θ^m .

Combining Eqs. (3.10) and (3.14), the height error due to the flat Earth reference phase as function of the slant range becomes

$$\partial H_i = -\cos(\theta_i^m) \partial R. \quad (3.15)$$

Hence, the height error in side lobes due to a wrong flat Earth reference phase is directly related to the look angle and independent of other specific sensor characteristics. The factor $-\cos(\theta_i^m)$ relating the height error to the slant range distance between the main lobe and the side lobe for a range of look angles is visualized in Figure 3.9A. To give an example, the slant range spacing ∂R of Envisat of 7.8 m results in a height error of -7.2 m per pixel. Note that this phenomenon is equal to the effect occurring for the range sub-pixel position, see Section 4.2.4. In both cases an erroneous reference phase causes an additional contribution in the estimated height. Only the scale, i.e. sub-pixel versus multiple pixels in case in side lobes, is different.

The error in estimated height also influences the geolocation of the side lobe pixels. The relation between height error and ground range distance is (see also Figure 3.8)

$$\partial R_{gr} = \frac{\partial H_i}{\tan \theta_i^m}. \quad (3.16)$$

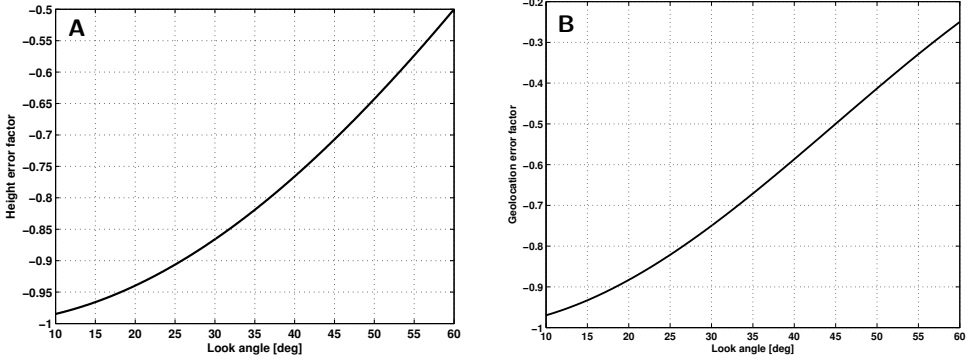


Figure 3.9: A) Factor between the height error and slant range distance between the main lobe and a side lobe, due to a wrong flat Earth reference phase for the side lobe pixel, see Eq. (3.15). This factor is only dependent on the look angle of the sensor. B) Corresponding compensation factor in geolocation of a sidelobe, see Eq. (3.19). A factor of -1 would result in an exact mapping of the side lobe at the main lobe location. A factor of -0.5 results in a geolocation of the side lobe at half the ground range distance in the image geometry.

Combination of Eqs. (3.15) and (3.16) results in

$$\begin{aligned}\partial R_{\text{gr}} &= \frac{-\cos \theta_i^m}{\tan \theta_i^m} \partial R, \\ &= \frac{-\cos^2 \theta_i^m}{\sin \theta_i^m} \partial R.\end{aligned}\quad (3.17)$$

Using the relation between the slant range and ground range distance

$$\partial R = \sin \theta_i^m \partial R_{\text{gr}}, \quad (3.18)$$

the effect on the georeferencing can be written as

$$\partial R_{\text{gr,out}} = -\cos^2 \theta_i^m \partial R_{\text{gr,in}}. \quad (3.19)$$

Hence, the error in flat Earth reference phase causes, via a conversion to the corresponding height, a geolocation error with a factor $-\cos^2 \theta_i^m$. This relation is visualized in Figure 3.9B. Hence, especially for small look angles, the side lobes are mapped to a geolocation close to the main lobe location (due to the minus sign in the factor). For the Envisat example given above, assuming a look angle of 23° , a side lobe at a slant range distance of 7.8 m is mapped at 1.2 m from the main lobe, see Figure 3.8. As a result, side lobes that are not removed are georeferenced in a line with equidistant positions near the main lobe. However, it is recommended to detect and remove the side lobes in the early stages of the analysis.

3.4.2 Side lobe detection procedure

Within DePSI side lobes are detected following a procedure which is derived from the approach described by Perissin (2006). It makes use of both the amplitude and the phase information of the full stack of interferograms. Three steps can be distinguished to detect side lobes:

1. (*Optional.*) Exclusion of pixels with high amplitude dispersion (or similar selection criterion, see Section 3.3.1). Pixels which are not selected as PS candidates do not have to be considered further. When all pixels are considered as PSC, this step is omitted.
2. Determination of local amplitude maxima from the remaining pixels. These local maxima are possibly representing main lobes. The excluded pixels are labeled as side lobes (or actually sub-main lobes).
3. Phase correlation check between nearby local maxima. The correlation is defined as (Perissin, 2006)

$$\rho_{ij} = \frac{1}{S} \left| \sum_{s=1}^S \exp(j(\varphi_j^{0s} - \varphi_i^{0s})) \right|. \quad (3.20)$$

Here, use is made of the characteristic that the phase difference between a side lobe and the main lobe is either 0 or π , leading in a noise-free situation to a correlation of 1. When applying to real data, a certain threshold is applied. In case the correlation between the nearby maxima is higher than the threshold, the pixel with the lowest amplitude is considered to be a side lobe. This procedure is repeated iteratively, in range and azimuth direction, until no more side lobes are detected. The correlation threshold is dependent on the number of images (Perissin, 2006), however, a threshold of 0.8 appears to be an appropriate default value.

The detection procedure works particularly well for side lobes nearby the main lobe. Side lobes further away may remain undetected. However, due to the increasing reference phase error, the estimated heights for these side lobes will show extreme values, which can be used to remove them from the final results (Perissin, 2006). However, this additional threshold is not implemented in DePSI.

3.5 Network formation

After selection of the PSC, with the detected side lobes removed, the first-order reference network is constructed. The network is meant to ensure the integrity of the analysis across the full area analyzed. It forms the basis for the Atmospheric and Orbital Phase Screen estimation and acts as reference for the further densification with higher-order PS.

Two network formation algorithms are implemented, a Delaunay triangulation and a more redundant network (Kampes, 2006), see Figures 3.10C and D. As shown in Figure 3.10C, the number of connecting arcs between the first-order PS Candidates (PSC1) after a Delaunay triangulation is limited, especially for the PSC1 on the outer sides of the crop. Furthermore, arcs which are too long, for example longer than the maximum correlation length of the atmosphere, are removed. As a result, the redundancy in the network, which is used for testing and resolving the ambiguities in the spatial unwrapping step (Section 5.1), is limited.

To improve the redundancy, Kampes (2006) developed the second algorithm. Here, a minimal number of connecting arcs per PSC1 is specified. The network is obtained by equally dividing the area around each PSC1 in a certain number of partitions, and

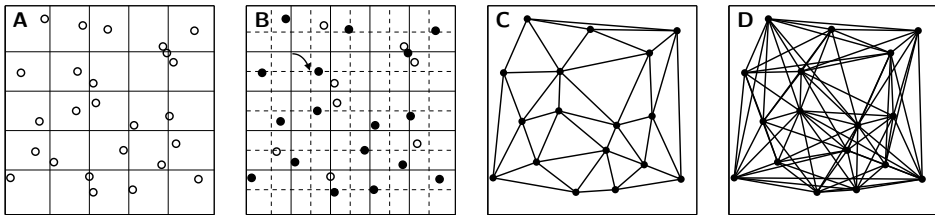


Figure 3.10: A) Initial selection of PSC using a grid to ensure a homogeneous distribution, see Section 3.3. B) Final selection by shifted grid in both range and azimuth direction (thick lines) to avoid nearby PSC. The PSC with the lowest amplitude dispersion is selected (black dots). C) First-order network obtained by Delaunay triangulation. D) First-order network ensuring a minimal number of connections per PSC.

selecting the closest PSC1 in each direction in a circular order, see Figure 3.11. If no PSC1 is found in the particular direction or when the arc length between the PSC1 is too long, the partition is skipped. This procedure is repeated, possibly resulting in multiple rounds, until the minimal number of connections is reached. As a result, also PSC1 at the outer sides of the crop are well connected.

The effect of the choice of the network is evaluated by van Leijen et al. (2006b). Here, a number of corner reflectors which are deployed by Delft University of Technology are used for a quality assessment (Marinkovic et al., 2008). The displacements of the corner reflectors are measured by leveling to validate the results. The results show that the use of a more redundant network indeed increases the reliability of the results compared to those obtained by a Delaunay triangulation. Errors in the ambiguity resolution can better be detected. Furthermore, the experiment shows that weak spots in the network construction, e.g., due to large agricultural fields or water bodies, increase the chance on undetected unwrapping errors. Therefore, the use of a network with high redundancy is beneficial to increase the robustness.

Once the network is constructed, the differential phase observations per arc φ_{ij} are calculated. These are input for the temporal ambiguity resolution step, see Chapter 4.

3.6 Summary

The Delft Persistent Scatterer Interferometry (DePSI) algorithm analyzes a radar interferometric data stack to detect Persistent Scatterers (PS) and estimate their deformation time series. In principle all available radar images acquired from the same repeat orbit of a certain satellite are used within the analysis. A single master baseline configuration is applied to form the interferograms, where the master image is selected based on minimum overall decorrelation in the data stack.

DePSI has a modular structure, enabling a tailored processing flow according to the characteristics of the analyzed area and the expected deformation phenomena. After initialization of the algorithm, the first step is the selection of Persistent Scatterer Candidates (PSC). This selection reduces the computational load of the analysis, since only a subset of the total number of pixels is considered further. The selection is based on the consistency in time of the reflection amplitude of a certain pixel, which is a proxy for

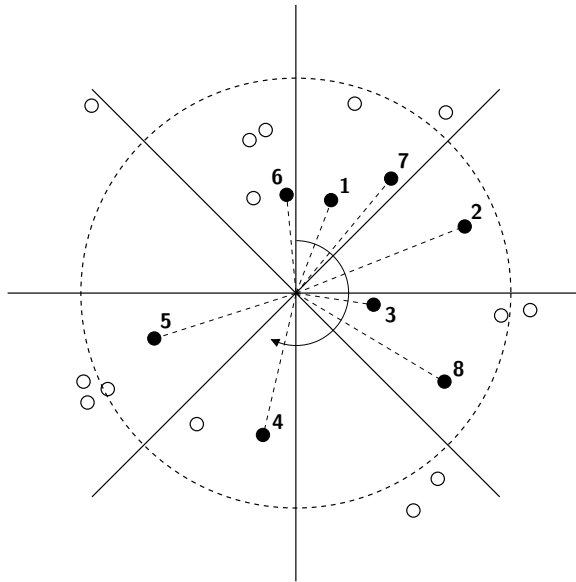


Figure 3.11: Construction of a redundant first-order PSC network. The area around each PSC is divided in a certain number of partitions. Subsequently, a connection is created to the closest neighboring PSC in each partition within the range of the maximum arc length (dashed circle). This procedure is repeated clockwise until the specified number of connections are established. In this example eight connections are created based on eight partitions.

the persistence of the phase. To select the PSC, both the normalized amplitude dispersion and the amplitude thresholding method are implemented in DePSI. It is concluded that the normalized amplitude dispersion is preferable, since no absolute radiometric calibration of the radar images is required.

The assessment of the amplitude consistency, either based on amplitude dispersion or an alternative method, also enables a classification of the PSC. In DePSI, a classification in first-order and higher-order PSC is made. The first-order PSC, which possess the most consistent amplitude signals, are used to form the first-order network. This network aims to preserve the integrity of the total area analyzed. This approach is similar to the procedure applied for conventional geodetic techniques, where also a hierarchy of benchmarks is used. The first-order network can be based on a Delaunay triangulation or a dedicated algorithm to form a more redundant network. The higher redundancy of the latter approach increases the ability to detect phase ambiguity errors and thereby the robustness of the network.

Due to the reflection signature of a strong point scatterer, the interferometric data stack does not only contain pixels associated with actual reflection points, but also pixels with signals due to side lobes. Since the amplitude of these artificial points is relatively high and stable due to the relation with the point scatterer, these pixels are often selected as PSC. Because the phase of these PSC is dominated by a copy of the phase of the main lobe, the side lobes have a high likelihood of being detected as a PS after phase analysis. Therefore, a side lobe detection algorithm is applied prior to the PSC selection to remove these pixels from the dataset.

In DePSI the phase ambiguities in the interferometric data stack are resolved in a two-step procedure. This chapter describes the first step, the resolution of the differential phase ambiguities per arc in the time domain. The second step, ambiguity resolution in space, is presented in Chapter 5. The temporal ambiguities are estimated using a mathematical model, see Section 4.1. The mathematical model consists of both a functional model and a stochastic model. The contents of these models in case of temporal ambiguity resolution in DePSI are presented in Section 4.2 and Section 4.3, respectively. The case-dependent stochastic properties of the phase observations are estimated from the data by Variance Component Estimation (VCE), which is described in Section 4.4. Within DePSI three techniques to estimate the phase ambiguities are implemented: integer least-squares (ILS), integer bootstrapping (IB) (both discussed in Section 4.5), and the ambiguity function (AF, see Section 4.6). The techniques are described, and compared regarding the success rate of correct ambiguity resolution. Section 4.8 contains the conclusions of this chapter.

4.1 Mathematical model

The temporal ambiguity resolution problem is formulated by a mathematical model. The general form of the mathematical model is denoted in Gauss-Markov form by

$$E\{\underline{y}\} = Ax \quad ; \quad D\{\underline{y}\} = Q_y \quad (4.1)$$

where the underline denotes the stochasticity of the measurements and

$E\{\cdot\}$	expectation operator,
\underline{y}	vector of observations,
\overline{A}	design matrix,
x	vector of unknowns,
$D\{\cdot\}$	dispersion operator,
Q_y	covariance matrix.

The first part of Eq. (4.1) represents the functional model, which describes the relation between the observations and the parameters of interest. The second part denotes the stochastic model, containing the statistical properties of the observations. The content of both the functional and the stochastic model as applied in DePSI are described separately in the next sections.

4.2 Functional model

The functional model for the double-difference¹ phase observations per arc between points i and j , and master 0 and slave s , is

$$\begin{aligned}\varphi_{ij}^{0s} &= \varphi_j^{0s} - \varphi_i^{0s}, \\ &= -2\pi a_{ij}^{0s} + \varphi_{ij,H}^{0s} + \varphi_{ij,D}^{0s} + \varphi_{ij,S}^{0s} + \varphi_{ij,P}^{0s} + \varphi_{ij,n}^{0s},\end{aligned}\quad (4.2)$$

where a is the integer valued phase ambiguity, φ_H the phase due to the (residual) height, φ_D the deformation phase, φ_S the phase due to the atmospheric delay, φ_P the sub-pixel position phase and φ_n noise. The functional form of each of the phase contributors is described separately.

4.2.1 Residual height

The residual height is defined as the height difference between the reference surface and the effective scattering center of the pixel. The reference surface is either the flat Earth, i.e. a reference ellipsoid, or a DEM, e.g. obtained by the Shuttle Radar Topography Mission (SRTM) (Farr et al., 2007). The functional relation between the residual height H and the corresponding phase φ_H for a single point i is (see also Section 2.1.3)

$$\begin{aligned}\varphi_{i,H}^{0s} &= \frac{-4\pi}{\lambda} \frac{B_i^{0s} \cos(\theta_i^0 - \alpha_i^{0s})}{R_i^0 \sin(\theta_i^0)} H_i, \\ &= \frac{-4\pi}{\lambda} \frac{B_{\perp,i}^{0s}}{R_i^0 \sin(\theta_i^0)} H_i, \\ &= \beta_i^{0s} H_i.\end{aligned}\quad (4.3)$$

Here B is the baseline between the master and slave antenna position, α the baseline orientation, B_{\perp} the perpendicular baseline, θ the local incidence angle and R the slant range. The *height-to-phase conversion factor* is denoted by β . The indices indicate the dependency on the master, slave and point position. They show that the height-to-phase conversion factor is different for each point, although the variations are very gradual, especially when the flat Earth is taken as reference instead of a DEM.

To illustrate the dependency on the baseline orientation and the look angle (and thereby the related incidence angle), values for β are calculated based on the Envisat ASAR characteristics (see Table 3.1a) and a spherical Earth ($R=6378137$ m), see Figure 4.1. The height-to-phase factors for a baseline of 1000 m, three different look angles and a complete cycle of baseline orientations is shown. A height of the satellite of 800 km above the surface is assumed. The figure shows that the instrument is more sensitive to height in case of a small look angle, hence, a large β . Furthermore, the sensitivity is strongly dependent on the baseline orientation. Maximum sensitivity is reached when α is equal to θ , as can also be derived from Eq. (4.3). The figure scales linearly for different values of B .

As β is defined per point, the double-difference phase relation per arc is

$$\varphi_{ij,H}^{0s} = \beta_j^{0s} H_j - \beta_i^{0s} H_i, \quad (4.4)$$

¹Double-differences are differences in time and space.

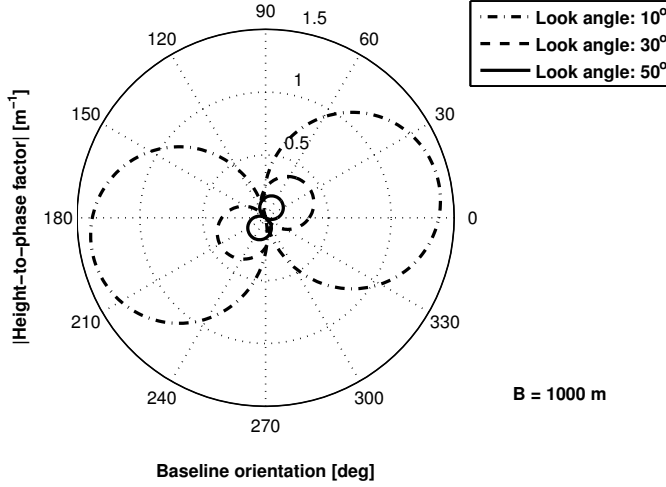


Figure 4.1: Absolute height-to-phase factor β as function of baseline orientation α and look angle. Envisat ASAR mission characteristics are used and a baseline B of 1000 m is assumed. The figure scales linearly with baseline.

In principle both heights H_i and H_j can be estimated from the phase observations. However, the strong correlation between the height-to-phase factors β_i and β_j cause an ill-conditioned estimation problem. Therefore, one of the heights is set to zero ($H_i=0$) and the height difference H_{ij} is estimated, resulting in

$$\varphi_{ij,H}^{0s} = \beta_j^{0s} H_{ij}. \quad (4.5)$$

For each arc in the network the functional model used in the temporal ambiguity step should be adapted. To reduce the computational effort, in DePSI the average height-to-phase factor $\bar{\beta}$ over the area analyzed is used instead. Hence, the model only needs to be constructed once. This results in

$$\begin{aligned} \varphi_{ij,H}^{0s} &= (\bar{\beta}^{0s} + \Delta\beta_j^{0s}) H_{ij}, \\ &= \bar{\beta}^{0s} H_{ij} + \Delta\beta_j^{0s} H_{ij}, \end{aligned} \quad (4.6)$$

where $\Delta\beta$ denotes the error in the height-to-phase factor for a specific arc. Neglecting of the second term on the right hand side obviously results in an erroneous estimation. However, due to the strong correlation between $\bar{\beta}$ and $\Delta\beta$, the error is largely absorbed by the estimate of the residual height H_{ij} . Hence, the effect on the other parameters of interest, such as deformation parameters, is minimal. Most importantly, the effect on the ambiguity resolution is therefore limited as well. Hence, despite an error in the estimated residual height, the ambiguities are assumed to be resolved correctly using the average $\bar{\beta}$.

After the spatial ambiguity step (see Section 5.1), when all the estimated ambiguities are tested for consistency in the spatial domain, the parameters of interest are estimated again based on the unwrapped phase obtained. At that stage, the point-wise functional models for residual height (Eq. (4.5)) are used instead of the average value. Hence, here the unbiased residual height estimate is obtained.

4.2.2 Deformation

The deformation phase is modeled as

$$\varphi_{ij,D}^{0s} = \sum_{p=1}^P \alpha_p (B_T) D_p, \quad (4.7)$$

where D_p are the deformation parameters, P is the number of models, and α_p describes a deformation model as function of the vector B_T with temporal baselines. The temporal baseline is defined as the time difference between the master and a slave acquisition, where a negative baseline is applied when the slave image is older than the master image, and vice versa, hence $B_T = T^s - T^0$.

The simplest model uses one parameter to describe a linear deformation rate

$$\alpha_1 = \frac{-4\pi}{\lambda} B_T. \quad (4.8)$$

The acquisition repeat cycle and the wavelength of the signal determine the theoretical maximum deformation rate that can be measured. When the deformation phase between two subsequent acquisitions is larger than π , the true deformation cannot be retrieved unambiguously. This corresponds to a maximum deformation of $\lambda/4$ per repeat interval ΔT . Hence, the maximum range of deformation rates that can be retrieved unambiguously is (Kampes, 2006)

$$\Delta D_{\max} = \frac{\lambda/4}{\Delta T/365.25}, \quad (4.9)$$

where ΔT is expressed in days. Using the sensor characteristics shown in Table 3.1a, the theoretical maximum measurable line-of-sight deformation rate for Envisat is 147 mm/y. For TerraSAR-X and ALOS, a maximum rate of 257 mm/y and 468 mm/y applies, respectively. Whether these deformation rates can actually be estimated from the data is dependent on the phase ambiguity resolution technique used and the noise level of the data, see Section 4.5. Moreover, the deformation history during the considered time span is never completely linear. In general, small deviations from the linear model still allow the correct unwrapping of the time series. However, when the deviations are larger, a more advanced deformation model should be applied. For instance when the deformation profile can be characterized by two subsequent deformation regimes, separated by an event. Examples of such an event are the start of oil or gas subtraction, or an earthquake. Assuming linear displacement before and after the event, a model is constructed using breakpoint B_T^{0b} . In case the breakpoint occurs after the master acquisition, hence $B_T^{0b} \geq 0$, the model is

$$\begin{aligned} \alpha_1 &= \frac{-4\pi}{\lambda} [B_T^{01} \dots B_T^{0b} \quad B_T^{0b} \dots B_T^{0S}]^T, \\ \alpha_2 &= \frac{-4\pi}{\lambda} [0 \dots 0 \quad (B_T^{0b+1} - B_T^{0b}) \dots (B_T^{0S} - B_T^{0b})]^T. \end{aligned} \quad (4.10)$$

If $B_T^{0b} < 0$, the model changes to

$$\begin{aligned} \alpha_1 &= \frac{-4\pi}{\lambda} [(B_T^{01} - B_T^{0b}) \dots (B_T^{0b-1} - B_T^{0b}) \quad 0 \dots 0]^T, \\ \alpha_2 &= \frac{-4\pi}{\lambda} [B_T^{0b} \dots B_T^{0b} \quad B_T^{0b} \dots B_T^{0S}]^T. \end{aligned} \quad (4.11)$$

These models are continuous at the breakpoint. When based on a-priori knowledge a discontinuity is expected, an alternative model can be used based on two completely separate linear models. The consequence is that an extra parameter needs to be included to account for the offset of the second part of the model. The time of the breakpoint can either be based on a-priori knowledge of the deformation history in the area or can be estimated from the data. The latter demands a large computational effort, because the phase needs to be unwrapped sequentially applying $B_T^{0b} = B_T^{02} \dots B_T^{0S-1}$ to find the best fit, see also Section 7.5.

The breakpoint model can be extended to a multiple breakpoints model. This is for instance valuable in case the start and end of a mining activity, or oil or gas extraction, falls within the acquisition time span. Here, three subsequent linear displacement regimes with two breakpoints $B_T^{0b_1}$ and $B_T^{0b_2}$ are assumed. In case both $B_T^{0b_1} \geq 0$ and $B_T^{0b_2} \geq 0$, the resulting model is (Samiei-Esfahany, 2008)

$$\begin{aligned}\alpha_1 &= \frac{-4\pi}{\lambda} [B_T^{01} \dots B_T^{0b_1} \quad B_T^{0b_1} \dots B_T^{0b_1} \quad B_T^{0b_1} \dots B_T^{0b_1}]^T, \\ \alpha_2 &= \frac{-4\pi}{\lambda} [0 \dots 0 \quad (B_T^{0b_1+1} - B_T^{0b_1}) \dots (B_T^{0b_2} - B_T^{0b_1}) \\ &\quad (B_T^{0b_2} - B_T^{0b_1}) \dots (B_T^{0b_2} - B_T^{0b_1})]^T, \\ \alpha_3 &= \frac{-4\pi}{\lambda} [0 \dots 0 \quad 0 \dots 0 \quad (B_T^{0b_2+1} - B_T^{0b_2}) \dots (B_T^{0S} - B_T^{0b_2})]^T.\end{aligned}\quad (4.12)$$

If $B_T^{0b_1} < 0$ and $B_T^{0b_2} \geq 0$, the model changes to

$$\begin{aligned}\alpha_1 &= \frac{-4\pi}{\lambda} [(B_T^{01} - B_T^{0b_1}) \dots (B_T^{0b_1} - B_T^{0b_1}) \quad 0 \dots 0 \quad 0 \dots 0]^T, \\ \alpha_2 &= \frac{-4\pi}{\lambda} [B_T^{0b_1} \dots B_T^{0b_1} \quad B_T^{0b_1+1} \dots B_T^{0b_2} \quad B_T^{0b_2} \dots B_T^{0b_2}]^T, \\ \alpha_3 &= \frac{-4\pi}{\lambda} [0 \dots 0 \quad 0 \dots 0 \quad (B_T^{0b_2+1} - B_T^{0b_2}) \dots (B_T^{0S} - B_T^{0b_2})]^T,\end{aligned}\quad (4.13)$$

and in case both $B_T^{0b_1} < 0$ and $B_T^{0b_2} < 0$, the model is

$$\begin{aligned}\alpha_1 &= \frac{-4\pi}{\lambda} [(B_T^{01} - B_T^{0b_1}) \dots (B_T^{0b_1} - B_T^{0b_1}) \quad 0 \dots 0 \quad 0 \dots 0]^T, \\ \alpha_2 &= \frac{-4\pi}{\lambda} [(B_T^{0b_1} - B_T^{0b_2}) \dots (B_T^{0b_1} - B_T^{0b_2}) \\ &\quad (B_T^{0b_1+1} - B_T^{0b_2}) \dots (B_T^{0b_2} - B_T^{0b_2}) \quad 0 \dots 0]^T, \\ \alpha_3 &= \frac{-4\pi}{\lambda} [B_T^{0b_2} \dots B_T^{0b_2} \quad B_T^{0b_2} \dots B_T^{0b_2} \quad B_T^{0b_2+1} \dots B_T^{0S}]^T.\end{aligned}\quad (4.14)$$

An alternative is the use of a higher-order polynomial

$$\alpha_p = \frac{-4\pi}{\lambda} B_T^p, \quad \text{for } p = 1, 2, \dots \quad (4.15)$$

This model provides the ability to retrieve non-linear deformation profiles with increasing complexity depending on the degree. A profile with an accelerating or decelerating deformation rate can for instance be modeled by a second degree polynomial. Furthermore, a higher-order polynomial can be an alternative for the breakpoint model, with the advantage that the time of the event does not need to be specified or estimated.

Because many deformation phenomena contain a seasonal effect, e.g. ground water fluctuations and thermal dilatation of buildings, addition of a periodic model may be useful or even a requirement for correct estimation of the phase ambiguities. This periodic model can be used in combination with any of the deformation models presented previously. The functional relation between the phase observations and the periodic model is (Kampes, 2006)

$$\varphi = -\frac{4\pi}{\lambda}(A \sin(2\pi(B_T - t_0)) + A \sin(2\pi t_0)), \quad (4.16)$$

where A is the amplitude and t_0 is the offset of the model. A periodic repeat interval of one year is adopted and the temporal baselines B_T should be specified in years. The second term assures that the total deformation is zero at $B_T=0$. Unfortunately, the model in Eq. (4.16) is not linear. However, it can be re-written to the linear model

$$\varphi = -\frac{4\pi}{\lambda}(\sin(2\pi B_T) \cdot A \cos(2\pi t_0) + (\cos(2\pi B_T) - 1) \cdot -A \sin(2\pi t_0)). \quad (4.17)$$

Hence, the model is parameterized by

$$\begin{aligned} \alpha_1 &= \frac{-4\pi}{\lambda} \sin(2\pi B_T), \\ \alpha_2 &= \frac{-4\pi}{\lambda} (\cos(2\pi B_T) - 1), \end{aligned} \quad (4.18)$$

resulting in the estimates

$$\begin{aligned} D_1 &= A \cos(2\pi t_0), \\ D_2 &= -A \sin(2\pi t_0). \end{aligned} \quad (4.19)$$

From these terms, the amplitude and offset can be reconstructed by

$$A = \sqrt{D_1^2 + D_2^2} \quad (4.20)$$

and

$$t_0 = -\text{sgn}(D_2) \cdot \arccos(D_1/A)/2\pi. \quad (4.21)$$

This formulation ensures that the amplitude is always positive and that the offset differentiates between signals of opposite periodicity.

Note that all deformation models described meet the constraint that the deformation is zero when $B_T=0$. Obviously alternative deformation models can be designed, possibly based on a-priori knowledge about the deformation history in the area.

4.2.3 Atmosphere and noise

The double-difference phase due to the atmospheric signal delay is

$$\varphi_{ij,S}^{0s} = (\varphi_{j,S}^0 - \varphi_{i,S}^0) - (\varphi_{j,S}^s - \varphi_{i,S}^s). \quad (4.22)$$

Hence, the atmospheric delay is the superposition of four states of the atmosphere. The contributions due to the atmosphere during the master acquisition re-occur however in

each interferometric combination. This enables the estimation of the master atmospheric delay S (in meters) per arc

$$\varphi_{ij,S}^0 = \frac{-4\pi}{\lambda} S_{ij}^0. \quad (4.23)$$

The atmospheric delays during the slave acquisitions cannot be estimated functionally because there is no redundancy in the phase observations. The slave atmospheric delay is therefore initially treated stochastically, see Section 4.3. After the spatial ambiguity resolution step (see Section 5.1), the phase residuals together with the estimated master atmospheric delay are used to obtain an estimate for the differential Atmospheric Phase Screen (APS) per interferogram (Section 5.3).

Note that the functional relation of the noise term in Eq. (4.2) is equivalent to that of the atmosphere

$$\varphi_{ij,n}^{0s} = (\varphi_{j,n}^0 - \varphi_{i,n}^0) - (\varphi_{j,n}^s - \varphi_{i,n}^s). \quad (4.24)$$

Therefore, the master atmosphere and master noise cannot be separated in this single arc estimation. The estimate for S_{ij}^0 will therefore also contain the master noise n_{ij}^0 . Spatial information is used during the Atmospheric Phase Screen estimation (Section 5.3) to reduce the effect of noise in the final APS estimates.

4.2.4 Sub-pixel position

Additional phase terms in the interferometric phase observation are caused by the so-called *sub-pixel position* of the effective scattering center. As discussed in Section 3.2.5, the interferograms are corrected for the flat Earth reference phase. However, this reference phase is calculated based on the leading edge of a pixel, i.e., the near-range, early-azimuth corner, and not at the exact location of the scattering center. As a result, part of the reference phase is not compensated and causes a phase term in both azimuth and range direction (Colesanti et al., 2003c; Kampes, 2006).

Azimuth sub-pixel position

The component of the reference phase in azimuth direction is caused by the difference in squint angle ϑ of the master and slave acquisition. The squint angle is the difference between the *zero Doppler* direction, i.e., perpendicular to the flight direction, and the look direction of the antenna, see Figure 4.2A.

The azimuth sub-pixel phase is (Kampes, 2006)

$$\varphi_{i,\xi}^{0s} = \frac{-4\pi}{\lambda} (\sin \vartheta^m - \sin \vartheta^s) \cdot \xi_i, \quad (4.25)$$

where ξ [m] is the azimuth sub-pixel position. Using the simplified relation (Bamler and Schättler, 1993)

$$f_{Dc} = \frac{-2v}{\lambda} \sin \vartheta, \quad (4.26)$$

where f_{Dc} is the Doppler centroid frequency and v is the velocity of the satellite, the azimuth sub-pixel position can also be expressed as

$$\varphi_{i,\xi}^{0s} = \frac{2\pi}{v} (f_{Dc}^m - f_{Dc}^s) \cdot \xi_i. \quad (4.27)$$

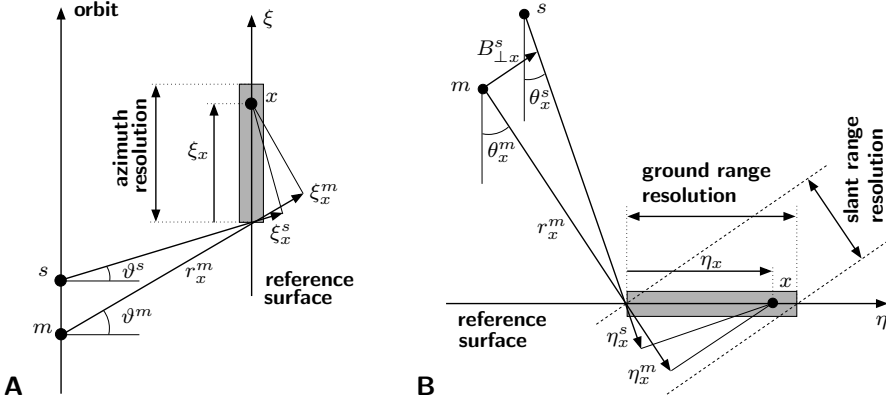


Figure 4.2: A) Azimuth sub-pixel position. A difference in the squint angle ϑ , or equivalent a difference in Doppler centroid, causes a change in signal path length and thereby a phase term due to the sub-pixel position of the point scatterer. B) Range sub-pixel position. Additional phase term due to difference in look angle θ between the master and slave acquisitions. Illustrations adapted from Marinkovic et al. (2008).

Here the velocity of the platform is assumed equal during both acquisitions. This equation shows that there is an interferometric phase term due to the sub-pixel position in azimuth direction in case of different Doppler centroid frequencies. In other words, although the position of the scattering center will never coincide with the leading edge of the pixel, it is only observable in case f_{Dc} differs between master and slave. In practice, the f_{Dc} is kept rather stable during a satellite mission, which makes the estimation of the azimuth sub-pixel position badly conditioned. Moreover, there may be a temporal drift in the Doppler centroid, introducing a correlation with the deformation. Part of the signal may therefore leak to the deformation parameters. This effect occurs for example in case of a combined ERS-1/2 dataset, because there is an offset between the average ERS-1/2 Doppler centroids and the majority of ERS-1 images are acquired before the ERS-2 time span.

An exception in the f_{Dc} stability is visible in the ERS-2 dataset after January 2001. Failure of the gyroscopes on-board the platform which controlled the direction of the antenna results in a strong variation in the f_{Dc} values. This increases the estimability of the azimuth sub-pixel position. However, the increased decorrelation effect due to the high Doppler values in the single master stack (see Section 2.1.3) reduced the coherence of especially not ideal point scatterers. Therefore, often the choice is made not to include these images in the image stack, see Section 3.2.

The variability of f_{Dc} , or equivalently ϑ , within an image is assumed to be small, enabling the use of a single value for all arcs. Therefore, the double-difference phase contribution due to the sub-pixel position in azimuth direction becomes

$$\varphi_{ij,\xi}^{0s} = \frac{2\pi}{v} (f_{Dc}^m - f_{Dc}^s) \cdot \xi_{ij}. \quad (4.28)$$

Equivalent to the sub-pixel position in azimuth direction, a similar effect occurs in range direction.

Range sub-pixel position

The range sub-pixel position phase is (Kampes, 2006)

$$\varphi_{i,\eta}^{0s} = \frac{-4\pi}{\lambda} (\sin \theta^m - \sin \theta^s) \cdot \eta_i, \quad (4.29)$$

where η [m] is the range sub-pixel position, see also Figure 4.2B.

It can be shown (Kampes, 2006) that the sub-pixel phase can also be written as

$$\varphi_{i,\eta}^{0s} = \frac{4\pi}{\lambda} \frac{B_{\perp}}{R} \cos \theta^m \cdot \eta_i. \quad (4.30)$$

This relation indicates that the sub-pixel position in range direction is dependent on the perpendicular baseline B_{\perp} , just as the residual height (Eq. (4.3)). As a result, these two terms cannot be separated based on the phase observations. In other words, the estimated height will have an error ΔH due to the contribution of the range sub-pixel phase $\varphi_{i,\eta}^{0s}$. The size of this error can be derived based on the following equality

$$\varphi_{i,\eta}^{0s} = \frac{4\pi}{\lambda} \frac{B_{\perp}}{R} \cos \theta^m \cdot \eta_i = \frac{-4\pi}{\lambda} \frac{B_{\perp}}{R \sin \theta^m} \Delta H_i. \quad (4.31)$$

Simplification gives

$$\Delta H_i = -\cos \theta^m \sin \theta^m \eta_i. \quad (4.32)$$

Hence, the range sub-pixel position of the effective scattering center causes, due to the error in the flat Earth reference phase, an error of the estimated height which is a direct function of the local incidence angle. In case of Envisat, assuming oversampling with a factor 2, the ground range spacing is about 10 m. The mean range sub-pixel spacing is therefore 5 m. With a mean local incidence angle of 23° , this results in a mean height error ΔH_i of -1.8 m. This height error also affects the geolocation (see Section 6.1). Based on the same Envisat characteristics, a mean geolocation error of -4.2 m is obtained.

The derivations above show that in range direction it is not possible to estimate the sub-pixel position from the phase observations, and in azimuth direction only in case of (strongly) variable Doppler centroid values. Therefore, estimation of the sub-pixel position based on radar intensity information is more suitable. By matching a sinc-shaped kernel to detected point scatterers in the radar data stack, the sub-pixel position of the scatterer can be estimated. This sub-pixel position can then be used to correct the phase observations, and thereby the estimated height and geolocation of the scatterer. Obviously this approach works best for strong point scatterers and not for pixels with a more distributed scattering behavior.

4.3 Stochastic model

The stochastic model describes the statistical properties of the phase observations. The model for the double-difference phase observations per arc φ_{ij}^{0s} , described by the covariance matrix Q_{φ} , is derived from the stochastic model of the original SLC observations $\underline{\psi}$ by error propagation (Hanssen, 2004). The SLC observations for two points i and j ,

and the corresponding covariance matrix Q_{ψ} , are denoted as

$$\begin{aligned} \underline{\psi} &= \begin{bmatrix} \underline{\psi}_i \\ \underline{\psi}_j \end{bmatrix} = \begin{bmatrix} \underline{\psi}_i^0 & \cdots & \underline{\psi}_i^S & \underline{\psi}_j^0 & \cdots & \underline{\psi}_j^S \end{bmatrix}^T, \\ D\{\underline{\psi}\} &= Q_{\psi} = Q_{\text{noise}} + Q_{\text{atmo}} + Q_{\text{defo}}, \end{aligned} \quad (4.33)$$

where S is the number of slave acquisitions and 0 indicates the master. The covariance matrix is a superposition of contributions due to noise and model imperfections, e.g., atmospheric signal delay and unmodeled deformation. The noise is mainly due to scattering noise, resulting in a loss of coherence, and thermal noise in the measurements, described by the block-diagonal matrix Q_{noise} . The atmospheric signal delay is spatially correlated but uncorrelated in time, i.e., provided that the acquisitions are taken at least a few hours apart (Hanssen, 2001). Therefore, Q_{atmo} is a block matrix with only elements on the diagonals. Because orbit errors also result in a temporal uncorrelated but spatial correlated signal, the influence of orbit inaccuracies can be added to the atmospheric term. The unmodeled deformation is assumed to be correlated in both time and space, and results therefore in a full matrix Q_{defo} . Apart from the atmospheric (and orbit) and deformation contribution, other model imperfections, e.g. due to azimuth sub-pixel position (Samiei-Esfahany et al., 2008), can easily be added.

The full and symmetric covariance matrix Q_{ψ} has the form

$$D\left\{ \begin{bmatrix} \underline{\psi}_i^0 \\ \vdots \\ \underline{\psi}_i^S \\ \underline{\psi}_j^0 \\ \vdots \\ \underline{\psi}_j^S \end{bmatrix} \right\} = \begin{bmatrix} \sigma_{\psi_i^0}^2 & & & & & & \\ & \ddots & & & & & \\ & & \sigma_{\psi_i^S}^2 & & & & \\ \sigma_{\psi_i^0, \psi_i^S} & \cdots & \sigma_{\psi_i^S}^2 & & & & \\ \sigma_{\psi_i^0, \psi_j^0} & \cdots & \sigma_{\psi_i^S, \psi_j^0} & \sigma_{\psi_j^0}^2 & & & \\ & \ddots & \vdots & \vdots & \ddots & & \\ \sigma_{\psi_i^0, \psi_j^S} & \cdots & \sigma_{\psi_i^S, \psi_j^S} & \sigma_{\psi_j^0, \psi_j^S} & \cdots & \sigma_{\psi_j^S}^2 & \end{bmatrix}, \quad (4.34)$$

where sym indicates a symmetric matrix and (Hanssen, 2004)

- $\sigma_{\psi_i^s}^2$ is the total variance of a SLC phase observation, consisting of thermal noise, scattering noise, atmospheric and orbital signal, and unmodeled deformation.
- $\sigma_{\psi_i^s, \psi_j^s}$ is the covariance between two points at the same acquisition. This covariance is mainly dependent on the atmospheric and orbital signal, plus unmodeled deformation, and is therefore a function of the distance between the two points.
- $\sigma_{\psi_i^{s1}, \psi_i^{s2}}$ is the covariance at one point between two acquisitions. Here the effect of the coherence plays a dominant role; a large coherence implies a large similarity, hence a large covariance. Furthermore, unmodeled deformation increases the covariance.
- $\sigma_{\psi_i^{s1}, \psi_j^{s2}}$ is the covariance between two points and two acquisitions. This term is solely due to spatio-temporal correlation in the unmodeled deformation.

The covariance matrix of the interferometric phases for two points (*single-differences*²) is obtained by error propagation (Kampes, 2006; van Leijen et al., 2006a)

$$Q_{\varphi_i} = \Lambda Q_{\psi} \Lambda^T, \quad \text{where} \quad \Lambda = I_2 \otimes [e_S \quad -I_S]. \quad (4.35)$$

Here, I is the identity matrix, e a vector of ones, S is the number of slave acquisitions, and \otimes is the Kronecker product. The *interferogram matrix* Λ is constructed for a single master stack as used in DePSI, hence the indices 0, s for the master and slave image, respectively. Finally, the covariance matrix of the double-difference phase observations per arc is

$$Q_{\varphi_{ij}} = \Omega Q_{\varphi_i} \Omega^T, \quad \Omega = [-1 \quad 1] \otimes I_S, \quad (4.36)$$

where Ω is the *connection matrix*. Here, the connection matrix for a single arc is used.

The variances and covariances of $Q_{\varphi_{ij}}$ are

$$\sigma_{\varphi_{ij}^{0s}}^2 = \sum_{p=i,j} \sum_{q=0,s} \sigma_{\psi_p^q}^2 - 2(\sigma_{\psi_i^0, \psi_j^0} + \sigma_{\psi_i^s, \psi_j^s} + \sigma_{\psi_i^0, \psi_i^s} + \sigma_{\psi_j^0, \psi_j^s}) + 4\sigma_{\psi_i^0, \psi_j^s}, \quad (4.37)$$

and

$$\begin{aligned} \sigma_{\varphi_{ij}^{0s_1}, \varphi_{ij}^{0s_2}} = & \sum_{p=i,j} \sigma_{\psi_p^0}^2 - 2\sigma_{\psi_i^0, \psi_j^0} + \sum_{p=i,j} (\sigma_{\psi_p^{s_1}, \psi_p^{s_2}} - \sigma_{\psi_p^0, \psi_p^{s_1}} - \sigma_{\psi_p^0, \psi_p^{s_2}}) \\ & + 2(\sigma_{\psi_i^0, \psi_j^{s_1}} + \sigma_{\psi_i^0, \psi_j^{s_2}} - \sigma_{\psi_i^{s_1}, \psi_j^{s_2}}). \end{aligned} \quad (4.38)$$

The elements of the covariance matrix can be obtained from a model, be estimated from the data, or a combination thereof. In case of a model, the (co-)variance of the different contributors, e.g., noise, atmosphere and deformation, is described by a parametric covariance function. Ketelaar (2009) proposed the following covariance model to obtain both the variances and the covariances of the double-difference phase observations

$$\begin{aligned} \sigma_{\varphi_{ij}^{0s_1}, \varphi_{ij}^{0s_2}} = & \delta^{s_1 s_2} (\sigma_{n_i}^{2s_1} + \sigma_{n_j}^{2s_1}) + \sigma_{\text{defo}}^2 \exp\left(-\left(\frac{l_{ij}}{L_{\text{defo}}}\right)^2\right) \exp\left(-\left(\frac{t^{s_1 s_2}}{T_{\text{defo}}}\right)^2\right) + \\ & \delta^{s_1 s_2} \sigma_{\text{atmo}^{s_1}}^2 \exp\left(-\ln(2)\left(\frac{l_{ij}}{L_{\text{atmo}}}\right)^2\right), \\ \text{with } \delta^{s_1 s_2} = & \begin{cases} 1, & \text{if } s_1 = s_2, \\ 0, & \text{otherwise.} \end{cases} \end{aligned} \quad (4.39)$$

Here,

$\sigma_n, \sigma_{\text{defo}}, \sigma_{\text{atmo}}$	standard deviation of noise, unmodeled deformation and atmosphere,
l, t	spatial and temporal difference,
$L_{\text{defo}}, T_{\text{defo}}$	spatial and temporal correlation length of unmodeled deformation,
L_{atmo}	correlation length of atmosphere.

The structure of the different components of the covariance model and the total covariance matrix obtained is visualized in Figure 4.3. For point scatterers, the variance of

²Single-differences are differences either in time or in space.

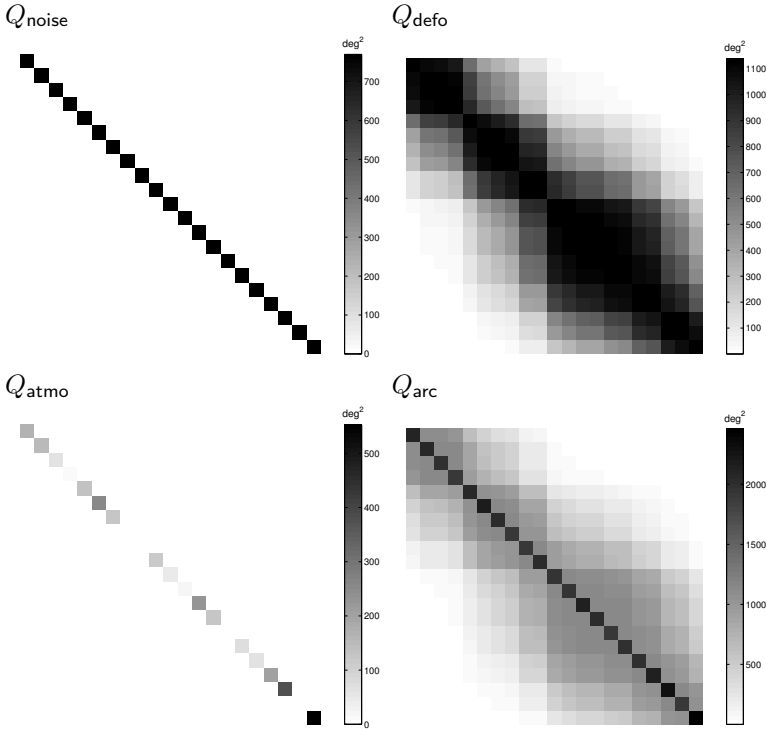


Figure 4.3: Example of Q_{noise} , Q_{defo} , and Q_{atmo} , together forming the covariance matrix Q_{arc} for an arc between two PS, based on the model in Eq. (4.39). In the example, the interferometric noise per PS is based on Eq. (4.40), assuming a coherence of 0.9, which results in a standard deviation of about 20° . The deformation model is based on a standard deviation of 3 mm, which is transformed into a corresponding phase, and a spatial and temporal correlation length of 1600 m and 3 years, respectively. The standard deviation of the atmospheric signal delay is simulated based on a Gaussian distribution with a standard deviation of 1 mm. Further, an atmospheric correlation length of 2000 m is applied. The two PS forming the arcs are assumed to be separated by 800 m.

the noise in the interferometric phase σ_n^2 can be derived as a function of the coherence γ close to 1 by (Bendat and Piersol, 1986; Just and Bamler, 1994)

$$\sigma_n^2 = \frac{1 - \gamma^2}{2\gamma^2} \quad [\text{rad}^2], \quad (4.40)$$

The covariance model for the atmosphere is derived by Kampes (2006), by approximating the results obtained by numerical simulations based on fractal surfaces which represent atmospheric turbulence. Alternatively, a Matern class covariance function can be used, which has a direct relation with the spectral behavior of the turbulent atmosphere (Grebentcharsky and Hanssen, 2005).

The variances σ_n^2 , σ_{defo}^2 , σ_{atmo}^2 are dependent on external factors which are different for each point, acquisition, e.g., atmosphere, and area, i.e., deformation behavior. Therefore, they should be based on a-priori knowledge or estimated from the data. In DePSI the (co-)variances are estimated, using a simplified model, by least-squares Variance Component Estimation (VCE).

4.4 Least-squares Variance Component Estimation (VCE)

In DePSI least-squares Variance Component Estimation (VCE) is applied to adjust the stochastic model to the precision of the data set used, the atmospheric conditions during the acquisitions and the deformation behavior of the area under consideration. Because only a limited number of (co-)variance components can be estimated, the stochastic model per arc as described by Eqs. (4.36)-(4.38) is simplified. Hence, one covariance matrix is assumed applicable for all arcs and the full covariance matrix is transformed into a matrix with a simplified structure. The simplification is accomplished by neglecting the correlation between the different slave acquisitions, e.g., due to coherence, and the cross-correlation between the two different points in different acquisitions, e.g., due to unmodeled deformation.

Two variants of the simplified covariance matrix can be applied, dependent whether or not the master atmospheric signal delay plus master noise (see Section 4.2.3) is incorporated in the functional model, see Eq. (4.2), or in the stochastic model, see Eq. (4.33). When inserted in the stochastic model (Kampes, 2006), the model of Eq. (4.36) simplifies to

$$\begin{aligned}
 Q_{\varphi_{ij}} &= \sum_{k=1}^K \sigma_k Q_k, \\
 &= (\sigma_{\psi_i^0}^2 + \sigma_{\psi_j^0}^2 - 2\sigma_{\psi_i^0, \psi_j^0}) \cdot E_S + \\
 &\quad \sum_{s=1}^S (\sigma_{\psi_i^s}^2 + \sigma_{\psi_j^s}^2 - 2\sigma_{\psi_i^s, \psi_j^s} - 2\sigma_{\psi_i^0, \psi_i^s} - 2\sigma_{\psi_j^0, \psi_j^s}) \cdot C_s, \quad (4.41) \\
 &\approx \underbrace{(\sigma_{\psi_i^0}^2 - \sigma_{\psi_i^0, \psi_j^0})}_{\sigma_1} \underbrace{2E_S}_{Q_1} + \sum_{s=1}^S \underbrace{(\sigma_{\psi_i^s}^2 - \sigma_{\psi_i^s, \psi_j^s} - 2\sigma_{\psi_i^0, \psi_i^s})}_{\sigma_{2\dots K}} \underbrace{2C_s}_{Q_{2\dots K}}.
 \end{aligned}$$

Here, E_S is a $S \times S$ matrix of ones and C_s is a $S \times S$ with only a one on the main diagonal at position s , where S is the number of slave acquisitions. The first component describes the influence of the master acquisition, whereas the remaining components represent the slaves. Therefore, in total K (co-)variance components σ_k are estimated, where K ($=S+1$) is the number of acquisitions.

In case the master atmospheric signal delay plus noise is incorporated in the functional model, the master contribution can largely be removed from the stochastic model. This results in

$$\begin{aligned}
 Q_{\varphi_{ij}} &= \sum_{s=1}^S \sigma_s Q_s, \\
 &\approx \sum_{s=1}^S \underbrace{(\sigma_{\psi_i^s}^2 - \sigma_{\psi_i^s, \psi_j^s} - 2\sigma_{\psi_i^0, \psi_i^s})}_{\sigma_s} \underbrace{2C_s}_{Q_s}. \quad (4.42)
 \end{aligned}$$

Hence, a diagonal matrix is obtained, with a variance term for each slave acquisition. This variance describes the noise level of the slave image, the atmospheric signal delay during the slave acquisition, and the level of coherence with respect to the master

acquisition. By default, the latter model is used in DePSI, since in general the master atmosphere is estimated explicitly, either using the integer least-squares or integer bootstrapping estimator, or the ambiguity function, see Sections 4.5 and 4.6.

The (co-)variance components in Eq. (4.41) or (4.42) are estimated based on the double-difference phase observations of arcs between the first-order PS (PS1) by least-squares variance component estimation (VCE), see Appendix A.4. Exception is the first estimation, hence, before the estimation of the first phase screen (see Figure 3.1), where the observations of the PS Candidates are used, because the PS1 are not identified yet at this stage. To obtain an unbiased estimate of the variance components, independent phase observations for the arcs are retrieved by performing a Delaunay triangulation between the points and removing arcs until all remaining arcs are separated (Kampes, 2006). When a maximum arc length is specified, arcs with an exceeding arc length are omitted. Because the estimations should be based on unwrapped phase observations, the ambiguities are resolved first using one of the techniques described in Sections 4.5-4.6. Here, a certain deformation model is assumed. Unwrapped arcs with a low quality indicator, e.g. ensemble coherence or variance factor (see Section 6.2), which are assumed to have a higher likelihood of unwrapping errors, are removed depending on the threshold set. Per remaining arc the (co-)variance components are estimated using Variance Component Estimation, see Eq. (A.32) in Appendix A. For the model in Eq. (4.41), the estimation is initiated with covariance matrix Q_y based on $\sigma_1 = 15^\circ$ and $\sigma_k = 20^\circ$ for $k = 2 \dots K$. These initial values are based on the assumption that the total interferometric phase standard deviation is below 30° and that the slave images have a higher noise level due to a slight mis-registration (Kampes, 2006). The initial values are lower compared to the values applied in (Kampes, 2006), because the assumption is made that the PSC in the first-order network have a low phase noise. When applying the model in Eq. (4.42), an initial value of $\sigma_1 = 30^\circ$ is used to represent the noise level of the total interferometric phase. Application shows that multiple iterations do not result in considerable changes of the estimated values and are therefore omitted. The final estimate for a certain variance component is obtained by the mean value of the individual estimates per arc. In case the estimation process is badly conditioned and a negative component is obtained, the component is set to a minimum value of 10° (Kampes, 2006).

The VCE procedure is repeated after correction with a certain phase screen, e.g., describing the influence of orbit errors (OPS), atmosphere (APS) or deformation (DPS). Hence, the stochastic model is updated regularly, to represent the statistical properties of the data as close as possible.

Once the stochastic model is estimated, the ambiguities of the double-difference phase observations can be resolved. Three techniques to resolve the ambiguities are implemented in DePSI: integer least-squares (ILS), integer bootstrapping (IB), and the ambiguity function (AF). These techniques are described in the next sections. An alternative approach based on Bayesian estimation (Caro Cuenca et al., 2011) is not considered here.

4.5 Integer least-squares and integer bootstrapping

Two techniques to resolve the ambiguities in the double-difference phase observations are integer least-squares (ILS) and integer bootstrapping (IB). Because the two techniques

are closely related, they are discussed simultaneously. The general theory of integer least-squares is described in Appendix A.5, also addressing integer bootstrapping. Here, the specific application of ILS and bootstrapping for PSI is discussed.

4.5.1 Integer least-squares in DePSI

Apart from application to GNSS observations (Teunissen and Kleusberg, 1998), the integer least-squares technique can also be used for ambiguity resolution within Persistent Scatterer Interferometry (PSI). The concept of integer least-squares for PSI was introduced by Hanssen et al. (2001) and fully implemented and applied to real data by Kampes and Hanssen (2004); Kampes (2006).

Application of ILS for PSI is not straightforward because of a lack of redundancy in the functional model. In case of GNSS, the satellite-receiver signals are tracked in time and the unknown ambiguities remain unchanged as long as no *cycle slips* occur. Hence, multiple observations as function of time are available to estimate an ambiguity. This is unlike the situation for PSI, where only one observation per measurement point per acquisition is available. Furthermore, the GNSS functional model for precise applications can considerably be aided by the availability of code observations and multi-frequency phase observations (Teunissen and Kleusberg, 1998). These additional observations are missing in case of PSI.

Hence, in case of PSI for every phase observation an ambiguity needs to be estimated. As a consequence, the number of unknown parameters to be estimated is always higher than the number of phase observations, resulting in a lack of redundancy. To circumvent this problem, additional constraints are added to the model in the form of *pseudo-observations*. The original mathematical model Eq. (A.35) is therefore changed in the regularized model

$$E\left\{\begin{bmatrix} \varphi \\ \underline{b}_0 \end{bmatrix}\right\} = \begin{bmatrix} A_1 & B_1 \\ A_2 & B_2 \end{bmatrix} \begin{bmatrix} a \\ b \end{bmatrix}; \quad D\left\{\begin{bmatrix} \varphi \\ \underline{b}_0 \end{bmatrix}\right\} = \begin{bmatrix} Q_\varphi & 0 \\ 0 & Q_{b_0} \end{bmatrix}, \quad (4.43)$$

where

φ	double-difference phase observations,
\underline{b}_0	pseudo-observations,
A_1, A_2, B_1, B_2	design matrices,
a	unknown ambiguities (integer-valued),
b	unknown parameters of interest (real-valued),
Q_φ, Q_{b_0}	covariance matrices of observations and pseudo-observations.

For each parameter of interest in b a pseudo-observation is added in \underline{b}_0 . Without a-priori knowledge, the pseudo-observations are set to zero. Alternatively, an approximate value can be derived by an alternative computation technique, e.g. the ambiguity function, see Section 4.6. Or, several sets of pseudo-observations can be evaluated to find the smallest ambiguity search space χ^2 , see Appendix A.5. The covariance matrix Q_{b_0} contains a-priori chosen variances for the unknown parameters. These variances provide *soft bounds* to the range of possible values for the parameters of interest.

Evaluation of the regularized model in Eq. (4.43) for the case of PSI results in

$$E\left\{\begin{bmatrix} \varphi^{01} \\ \vdots \\ \varphi^{0S} \\ b_{0,1} \\ \vdots \\ b_{0,P} \end{bmatrix}\right\} = \begin{bmatrix} -2\pi & & & \rho_1^{01} & \dots & \rho_P^{01} \\ & \ddots & & \vdots & \ddots & \vdots \\ & & -2\pi & \rho_1^{0S} & \dots & \rho_P^{0S} \\ & & & 1 & & \\ & & & & \ddots & \\ & & & & & 1 \end{bmatrix} \begin{bmatrix} a^{01} \\ \vdots \\ a^{0S} \\ b_1 \\ \vdots \\ b_P \end{bmatrix}; \quad (4.44)$$

$$D\left\{\begin{bmatrix} \varphi \\ \underline{b}_0 \end{bmatrix}\right\} = \begin{bmatrix} Q_\varphi & 0 \\ 0 & Q_{b_0} \end{bmatrix}, \quad (4.45)$$

where P is the number of parameters of interest involved. A standard approach comprises the estimation of the residual height, atmosphere plus noise of the master acquisition, and a linear deformation rate, hence three parameters. However, additional deformation parameters can easily be added. The functional relations between the parameters of interest and the phase observations, as described in Section 4.2, are represented by ρ .

The system of equations in Eq. (4.44) is resolved using integer least-squares in a three-step procedure, as described in Appendix A.5: float solution estimation, ambiguity resolution and fixed solution estimation.

4.5.2 Float solution

The float solution is obtained by conventional least-squares estimation, thereby neglecting the integer characteristic of the ambiguities a (Teunissen, 1993). The solution $\hat{\underline{c}}$ and the accompanying covariance matrix $Q_{\hat{\underline{c}}}$ are denoted as

$$\hat{\underline{c}} = \begin{bmatrix} \hat{\underline{a}} \\ \hat{\underline{b}} \end{bmatrix}; \quad Q_{\hat{\underline{c}}} = \begin{bmatrix} Q_{\hat{\underline{a}}} & Q_{\hat{\underline{a}}\hat{\underline{b}}} \\ Q_{\hat{\underline{b}}\hat{\underline{a}}} & Q_{\hat{\underline{b}}} \end{bmatrix}. \quad (4.46)$$

Since in the case of PSI the number of unknown parameters is equal to the number of observations, the functional model has no redundancy. As a result, the system is exactly determined, irrespective of the stochastic model used. Hence, both the covariance matrix of the phase observations Q_φ and the variances set for the pseudo-observations Q_{b_0} do not influence the float solution.

The exact determined system causes that the float solution of the real-valued parameters b_k is equal to the pseudo-observations. The float solution of the ambiguities $\hat{\underline{a}}$ is efficiently calculated by

$$\hat{\underline{a}} = \frac{\underline{\varphi}}{-2\pi} + \sum_{p=1}^P \frac{\rho_p b_{0,p}}{2\pi}. \quad (4.47)$$

In case the pseudo-observations b_0 are set to zero, the second term on the right-hand side vanishes.

4.5.3 Ambiguity resolution

The integer ambiguities \tilde{a} are obtained based on the minimization criterion (Teunissen, 1993)

$$\tilde{a} = \min_{a \in \mathbb{Z}} (\hat{a} - a)^T Q_{\hat{a}}^{-1} (\hat{a} - a). \quad (4.48)$$

To avoid a search through the complete solution space of integers \mathbb{Z} to find the optimal solution, a constraint χ^2 on the solution space can be set. A convenient approach to determine this constraint is to use the integer bootstrap solution, see Appendix A.5. As a result, a hyper-ellipsoidal solution space is obtained, centered around the float solution \hat{a} and shaped by the covariance matrix $Q_{\hat{a}}$.

Influence of pseudo-observations

The minimization criterion (Eq. (4.48)) shows in combination with Eq. (4.47) that the pseudo-observations, determining the float solution \hat{a} , directly influence the ambiguity resolution. The larger the difference between the pseudo-observations and the true solution, the larger the bias in the minimization criterion. This is illustrated in Figure 4.4 for the case with two ambiguities (a^{01} and a^{02}). The float solution vector \hat{a}_1 , in combination with the solution search space (dashed ellipse), is too far from the true solution a . That is, the true solution lies outside the solution search space. This can for example be the case when the pseudo-observations are by default set to zero, whereas in reality a strong deformation rate or a large height difference occurs. Since the solution space was chosen large enough to contain integer values, an erroneous solution will be selected. With adapted pseudo-observations an alternative float solution \hat{a}_2 is obtained. Here, the true solution is contained within the solution space. These adapted pseudo-observations could be based on an earlier iteration with the integer least-squares (ILS), integer bootstrap (IB), or ambiguity function (AF) estimator. However, a convergence to the true solution is not guaranteed and the computational load will increase, depending on the technique used (see Figure 4.10).

To investigate the influence of the size of the bias on the success rate of correct ambiguity resolution, a simulation is performed. The results are shown in Figure 4.5. Phase observations per arc are simulated with an increasing linear deformation rate and constant pseudo-observations of zero, resulting in an increasing bias. The simulation is based on the Envisat ASAR characteristics and the availability of 30 and 50 single master interferograms, respectively. Both integer least-squares and integer bootstrapping are applied to resolve the ambiguities. For comparison, also the results for the ambiguity function (see Section 4.6) are shown. For the ambiguity function fixed bounds of the solution space of 160 mm/y are applied. This is a large range of deformation values, especially since the estimations are applied to arcs between PSC of maximally a few kilometers long. However, the full capabilities of the estimators are assessed here. The simulations are repeated for noise levels per point ranging from 20 to 50 degrees. To assess the impact of the stochastic model of the phase observations, the success rates are calculated both by applying the variance factors estimated by variance component estimation (solid lines, see Section 4.4) and by applying a constant variance of 40² degrees (dashed lines).

The results show that the bias due to the pseudo-observations cause a drop of the success rate, depending on the noise level of the data. Moreover, the estimation of the

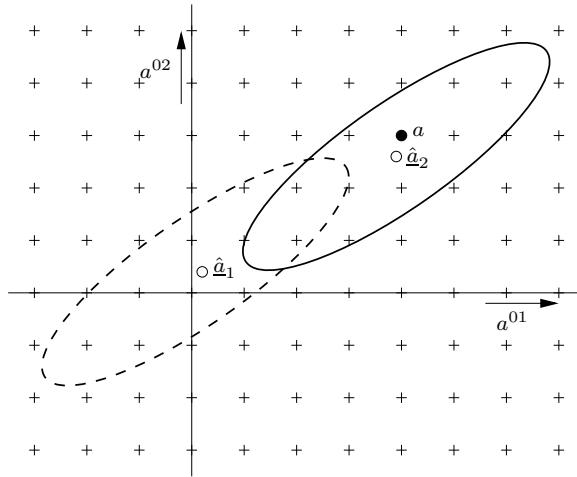


Figure 4.4: Example of the influence of a bias in the float solution \hat{a} on the ability to retrieve the correct solution of the ambiguity vector a , applied to a case with two ambiguities (a^{01} and a^{02}). The bias is caused by a deviation between the pseudo-observations used and the true solution. In case of float solution \hat{a}_1 and the accompanying search space (dashed ellipse), the correct solution cannot be retrieved. When pseudo-observations are used which are closer to the true solution, resulting in \hat{a}_2 (together with solid ellipse), the correct solution can be found. Note that the optimal solution is selected based on the metric of the variance matrix, i.e., not the shortest distance in the Euclidean space.

variance components shows an improvement of the success rate in general, and a strong decrease in the sensitivity to the bias. Also the number of interferograms affects the level of success. Using integer least-squares, linear deformation rates up to 100 mm/y can be resolved in case of a noise level of 20 degrees and the availability of 30 interferograms. When the noise level increases to 40 degrees, the success rate already starts to drop at 20 mm/y. When 50 interferograms are available, the success rate remains above 0.9 in case of a noise level of 20 degrees, until the theoretical maximum retrievable rate due to aliasing of 147 mm/y is reached (vertical dashed line in Figure 4.5, see Section 4.2.2). With higher noise levels, the success rate drops fast. Hence, in practical applications with varying noise levels, the phase ambiguities resulting from large deformation rates cannot be resolved correctly without adaption of the pseudo-observations to more realistic values, that is, a value closer to the true value compared to the default zero value. In contrast, the ambiguity function shows a constant performance over the full range of deformation rates. Hence, for larger deformation rates the ambiguity function is more robust.

The success rates of integer bootstrapping show a decrease with respect to integer least-squares over the full range of deformation values. Hence, the integer least-squares technique is superior to integer bootstrapping, as is also theoretically shown in Appendix A.5.1.

The success rates of the ambiguity function clearly show the effect of aliasing beyond 147 mm/y. Since the estimator is symmetric around zero, values above ± 147 mm/y (up to 160 mm/y in this example) can also be mapped to the other side of the deformation rate spectrum. As a result, in this case the success rate is halved in the region

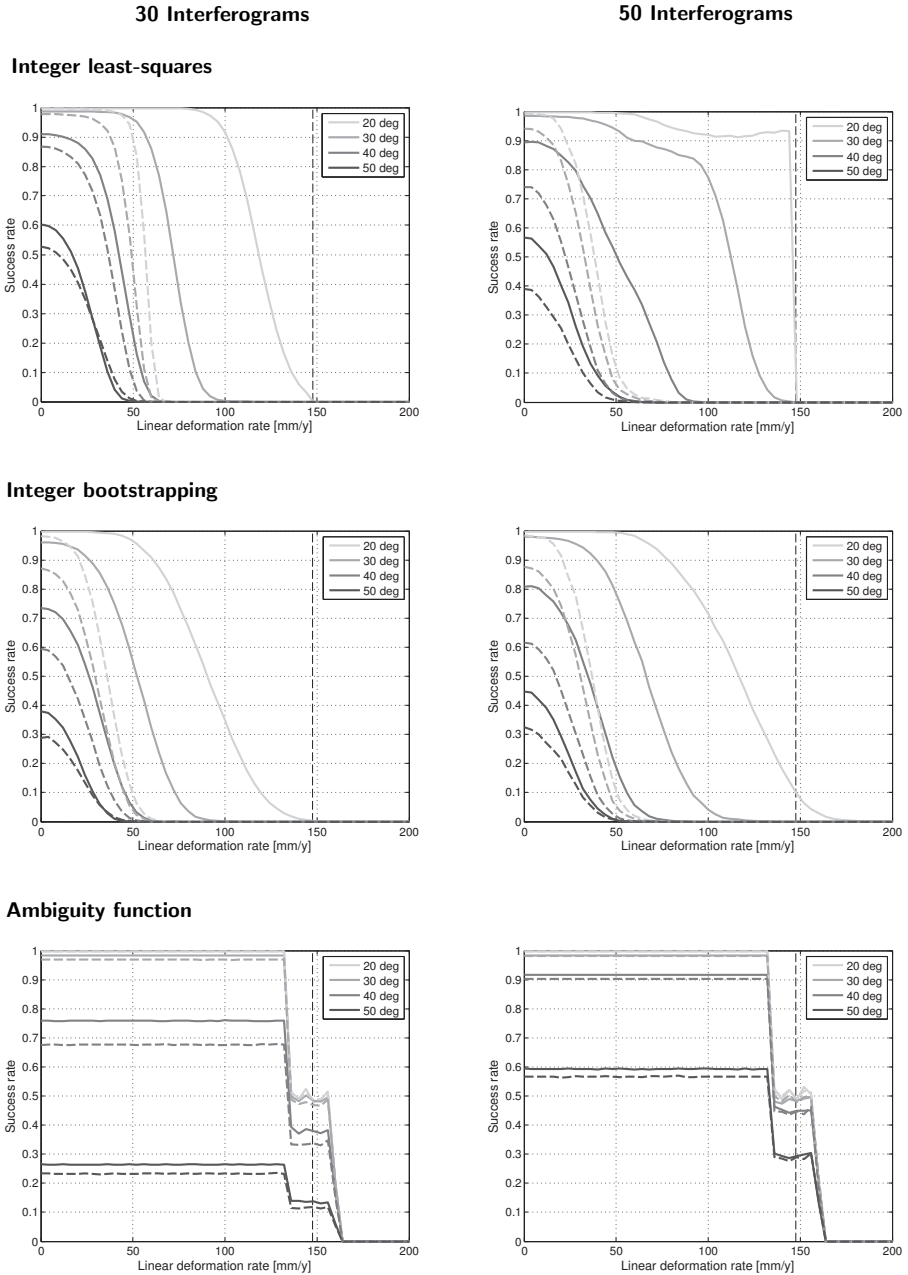


Figure 4.5: Success rate of correct ambiguity resolution as function of the true linear deformation rate between two points spanning an arc based on simulated phase observations. Left) stack of 30 interferograms, Right) stack of 50 interferograms. The success rates by integer least-squares (Top), integer bootstrapping (Middle), and the ambiguity function (Bottom, see Section 4.6) are shown. For integer least-squares and the bootstrap estimator, the default pseudo-observation value of zero for the deformation rate causes a bias in the minimization problem and thereby influences the success rate. (Continued on next page ...)

Figure 4.5: (Continuation of previous page . . .) The analysis is based on simulated phase observations with typical Envisat acquisition characteristics. Besides the increasing deformation rate, also a residual height ($\sigma=20$ m) and master atmospheric delay and noise ($\sigma=5$ mm) is simulated at each point, and differenced to obtain a value for the arc. Gaussian distributed noise with levels at each point of 20° , 30° , 40° and 50° are applied. To avoid misinterpretation of the results due to simulation of phase observations which by definition cannot be unwrapped correctly based on the model adopted, maximum simulated values per arc of 60 m for residual height, 14 mm (quarter of wavelength) for master atmospheric delay, and 180° for the noise vector are enforced. The covariance matrix Q_y is constructed based on estimated variance components (solid lines, see Section 4.4) or a fixed standard deviation of $\sqrt{2}\cdot 40^\circ$ for all observations in the arc (dashed lines), and a covariance matrix for the pseudo-observations Q_{b_0} using $\sigma_D=10$ mm/y, $\sigma_S=10$ mm and $\sigma_H=30$ m. In case of the ambiguity function, fixed bounds of the solution search space of ± 160 mm/y (deformation rate) and ± 120 m (residual height) are adopted. The weights used in the weighted ambiguity function (solid lines) are defined as $1/\sigma$, where σ is the standard deviation of the phase observations as determined by the variance component estimation. The maximum resolvable deformation rate of 147 mm/y due to aliasing is indicated by the dashed vertical line. The simulation is repeated 1000 times. For all estimators hold that these simulation results are based on a linear deformation behavior. Strong unmodeled deformation effects will further reduce the success rates.

147 ± 13 mm/y. Hence, the maximum allowable deformation rate for the ambiguity function should be set to the Nyquist rate, see Section 4.6. Furthermore, the success rates of the ambiguity function show that there is a significant performance increase between the use of 30 and 50 interferograms, and that the effect of the estimated variance components reduces.

A comparison of the success rate of the different estimators for the most frequently occurring deformation rates per arc between 0 and 20 mm/year is visualized in Figure 4.6. For small data stacks, here assessed by 30 interferograms, the ILS estimator outperforms the weighted AF estimator. However, for larger datasets the weighted AF estimator appears to be slightly more robust. The effect of the number of available interferograms on the success rate of correct ambiguity resolution is further assessed in Section 4.7.

Influence of covariance matrix

The minimization criterion for ambiguity resolution (Eq. (4.48)) shows that, apart from the float solution \hat{a} and thereby the pseudo-observations, the second factor influencing the solution of the ambiguities is the metric spanned by the covariance matrix of the ambiguities $Q_{\hat{a}}$. This matrix can be obtained by the solution of a partitioned model (Teunissen, 2000a; Kampes, 2006)

$$Q_{\hat{a}} = (\bar{A}^T Q_y^{-1} \bar{A})^{-1}, \quad (4.49)$$

where $\bar{A} = P_B^\perp A$; $P_B^\perp = I - B(B^T Q_y^{-1} B)^{-1} B^T Q_y^{-1}$. However, due to the uniquely determined system of equations as applies here, the covariance matrix is also obtained efficiently, without matrix inversions, by

$$Q_{\hat{a}} = \frac{1}{4\pi^2} (Q_\varphi + B_1 Q_{b_0} B_1^T). \quad (4.50)$$

This relation clearly illustrates the influence of both the precision of the phase observations and the variance of the pseudo-observations. Regardless the form of Q_φ , i.e.,

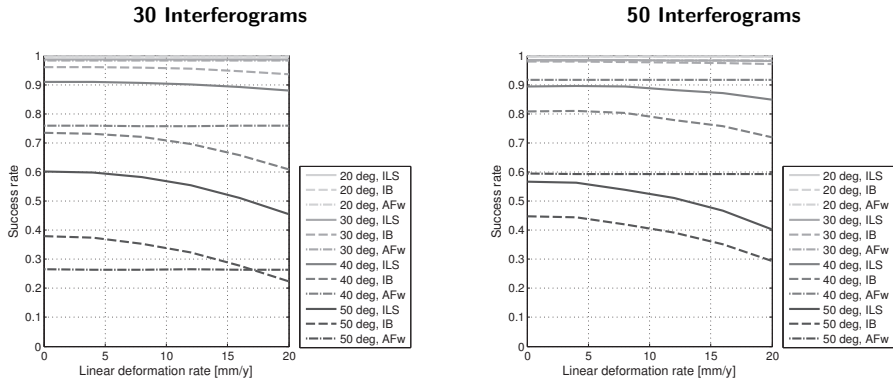


Figure 4.6: Success rate of correct ambiguity resolution as function of the true linear deformation rate between two points spanning an arc based on simulated phase observations, obtained by the integer least-squares (ILS), integer bootstrap (IB), and weighted ambiguity function (AFw) estimator. The figure shows the same results as visualized in Figure 4.5, focusing on the most frequently occurring deformation rates per arc between 0 and 20 mm/year. Left) stack of 30 interferograms, Right) stack of 50 interferograms. For a relatively low number of interferograms of 30, the ILS technique clearly outperforms the other estimators. When the number of interferograms increases, the ambiguity function performs slightly better, see also Figure 4.10.

a diagonal matrix or a full matrix, (additional) correlation between the ambiguities is introduced by the variances of the pseudo-observations. To assess the effect of these variances on the success rate of correct ambiguity resolution, a simulation is performed. The results are shown in Figure 4.7. Both the ILS and the IB estimator are applied to a series of simulated phase observations per arc. A range of standard deviations for the (pseudo-) observations is applied. The results show that the highest success rates are obtained when the standard deviations of the pseudo-observations have equivalent values as the actual parameters of interest, hence around 10 mm/y for the deformation rate and 30 m for the residual height. Hence, a balanced tuning of the standard deviations is required for optimal results.

LAMBDA method

Based on $\hat{\underline{a}}$ and $Q_{\hat{\underline{a}}}$ the ambiguities are resolved using either the integer least-squares or integer bootstrap estimator, see Appendix A.5. In both cases the Least-squares AMBiguity Decorrelation Adjustment (LAMBDA) method is applied (Teunissen, 1993). The LAMBDA method performs a decorrelation of the ambiguities, which results in a more efficient shape of the ambiguity search space. Application of the LAMBDA method leads to the paradoxical situation that the correlation between the ambiguities that was introduced by the variances of the pseudo-observations (see Eq. (4.50)) is reduced again by the decorrelation operation of the LAMBDA method. However, it is shown that the decorrelation does not influence the ILS solution (Teunissen (1994), see also Eq. (A.55)), only the speed of computation. In case of integer bootstrapping, the decorrelation matrix Z does have an influence on the solution. Whereas the original float solution $\hat{\underline{a}}$ only contains values between -0.5 and 0.5 (assuming zero values for the pseudo-observations, see Eq. (4.47)), the decorrelated solution $\hat{\underline{z}} = Z^T \hat{\underline{a}}$ better

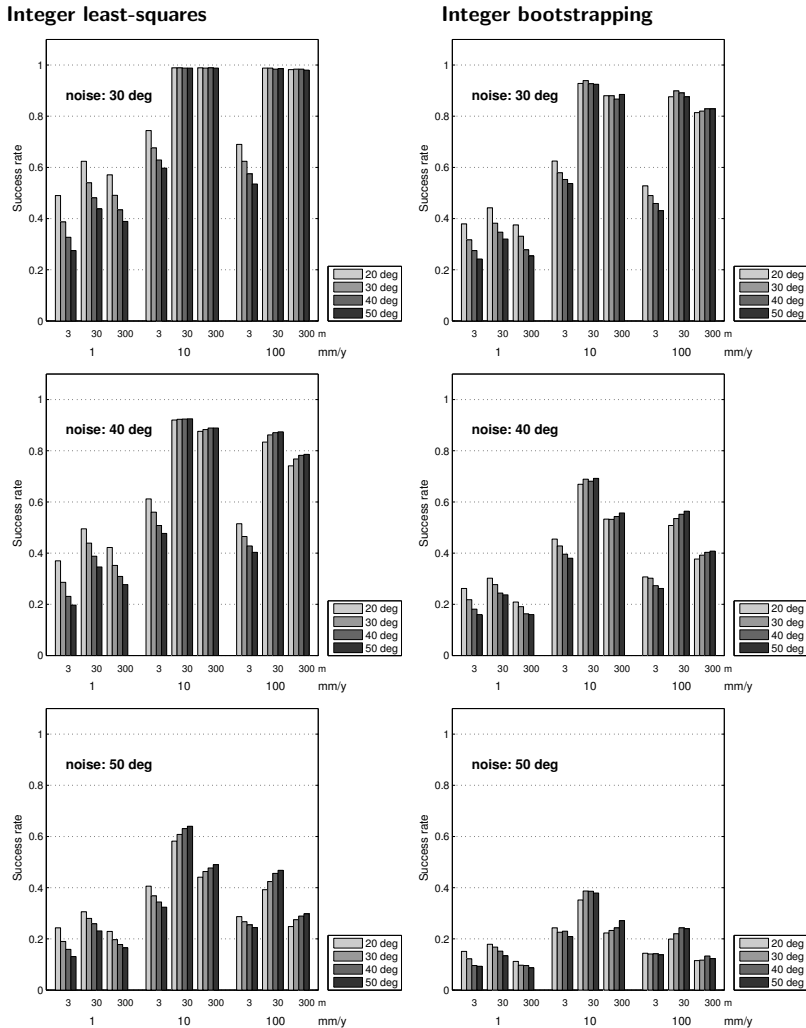


Figure 4.7: Success rate of correct ambiguity resolution for a range of variances for the (pseudo-) observations based on simulated phase observations. Both the integer least-squares (left column) and the integer bootstrap estimator (right column) are evaluated. The simulation is based on simulated phase observations per arc between two points assuming 30 interferograms and typical Envisat acquisition characteristics. Gaussian distributed noise with levels at each point of 30° (top row), 40° (middle row), and 50° (bottom row) are applied. The phase observations are based on simulated deformation rates ($\sigma=5$ mm/y), residual height ($\sigma=20$ m), and master atmospheric delay and noise ($\sigma=5$ mm) at each point, and differenced to obtain a value for the arc. To avoid misinterpretation of the results due to simulation of phase observations which by definition cannot be unwrapped correctly based on the model adopted, maximum simulated values per arc of 20 mm/y for deformation rate, 60 m for residual height, 14 mm (quarter of wavelength) for master atmospheric delay, and 180° for the noise vector are enforced. The covariance matrix Q_y is constructed applying a diagonal matrix Q_φ with σ_n ranging from $\sqrt{2}\cdot 20^\circ$ to $\sqrt{2}\cdot 50^\circ$, and a covariance matrix for the pseudo-observations Q_{b_0} using $\sigma_D=1, 10, \text{ or } 100$ mm/y, $\sigma_S = 10$ mm and $\sigma_H=3, 30, \text{ or } 300$ m, respectively. The simulation is repeated 1000 times. The simulations show that the highest success rates are obtained when the standard deviations of the pseudo-observations have equivalent values as the actual parameters of interest, hence around 10 mm/y for the deformation rate and 30 m for the residual height. The noise level σ_n has only a marginal effect.

reflects the functional relation between the ambiguities. This improves the performance of the conditional rounding as applied in the integer bootstrap estimator significantly. Actually, the success rate of integer bootstrapping for PSI without decorrelation is so poor, that application of LAMBDA is a strict requirement. Once the best estimate for the decorrelated ambiguities $\check{\underline{z}}$ is obtained, either by ILS or IB, the solution of the original ambiguities is retrieved by $\check{\underline{a}} = Z^{-T}\check{\underline{z}}$.

To improve the success rate of correct integer estimation in case of integer bootstrapping, within DePSI an adapted estimation scheme is applied. Besides the default solution, N alternative solutions are determined by sequentially selecting the second-closest integer solution for the particular ambiguity $n = 1 \dots N$ (Kampes, 2006). Hence, $N + 1$ solutions are obtained. The solution with the smallest criterion χ^2 is finally selected as the best estimate.

The success rate of correct integer estimation can be improved by adding hard constraints on the range of values for the real-valued parameters involved, see Bianchi (2003). Hence, maximum allowed deformation parameters and height values can be specified. However, these thresholds prevent the potential detection of points with extreme values. Therefore, within DePSI the choice is made to work without constraints. Possible errors in the estimated ambiguities are detected and resolved in the spatial ambiguity resolution step, see Section 5.1.

4.5.4 Fixed solution

After resolving the phase ambiguities $\check{\underline{a}}$, the fixed solution is obtained by

$$\check{\underline{b}} = (B_1^T Q_\varphi^{-1} B_1)^{-1} B_1^T Q_\varphi^{-1} \check{\underline{\varphi}}, \quad (4.51)$$

where the unwrapped phase is

$$\check{\underline{\varphi}} = \underline{\varphi} - A_1 \check{\underline{a}}. \quad (4.52)$$

Note that this relation is different compared to the standard approach indicated in Eq. (A.44). The reason is that by using Eq. (4.51) the pseudo-observations and variances no longer affect the solution, as is desirable. Hence, the pseudo-values are only used to enable the resolution of the ambiguities.

4.5.5 Precision indicator: a-posteriori variance factor

An indicator of the precision of the ILS or bootstrap solution is the *a-posteriori variance factor*

$$\sigma_b^2 = \frac{\check{\underline{\varphi}}^T Q_\varphi^{-1} \check{\underline{\varphi}}}{q}, \quad (4.53)$$

where q is the redundancy and $\check{\underline{\varphi}}$ is the vector of residuals

$$\check{\underline{\varphi}} = \underline{\varphi} - B_1 \check{\underline{b}}. \quad (4.54)$$

An estimated variance factor of 1.0 indicates that the vc-matrix Q_φ gives a good description of the dispersion of the phase observations, whereas a factor of 2.0 shows that the stochastic model applied was a factor two too optimistic. Hence, this scaling factor indicates the noise level (plus potential unmodeled deformation) of each arc, which can be used as a selection criterion or weighting factor, see Section 6.2.

4.6 Ambiguity function

As an alternative to the stochastic ambiguity resolution techniques, i.e., integer least-squares and bootstrapping, also deterministic approaches can be used. Within radar interferometric time series analysis techniques often the ambiguity function (AF) is used, also known as the periodogram (Ferretti et al., 2000, 2001). Due to the irregular sampling of the data along the baseline domains (e.g., perpendicular baseline for height, see Section 4.2), the solution of the function cannot be obtained directly. A discrete search in the solution space is required to find the optimal solution.

This ambiguity function technique is, apart from the integer least-squares and integer bootstrap estimator, this ambiguity function technique is implemented in DePSI to resolve the phase ambiguities. The AF estimator searches the solution space to find the parameters b that maximize the *temporal coherence* $|\gamma|$

$$\begin{aligned} \arg \max_b |\gamma| &= \left| \frac{1}{S} \sum_{s=1}^S \exp(j(\varphi_{\text{obs}}^{0s} - \varphi_{\text{model}}^{0s}(b))) \right|, \\ &= \left| \frac{1}{S} \sum_{s=1}^S \exp(j(\underline{e}^{0s}(b))) \right|, \end{aligned} \quad (4.55)$$

where $\varphi_{\text{obs}}^{0s}$ is the observed phase and $\varphi_{\text{model}}^{0s}(b)$ is the modeled phase based on the parameters b . The difference is equal to the residual $\underline{e}^{0s}(b)$. Apart from the unweighted ambiguity function, also a weighted ambiguity function can be applied. Here, each residual is weighted with a certain factor to account for the (relative) precision of the phase observations. The weights can for example be based on the results from Variance Component Estimation, see Section 4.4. The weighted ambiguity function (AFw) estimator is denoted by

$$\arg \max_b |\gamma| = \left| \frac{1}{\sum W^{0s}} \sum_{s=1}^S W^{0s} \exp(j(\underline{e}^{0s}(b))) \right|, \quad (4.56)$$

where W^{0s} are the weights per interferogram. In Figure 4.8 a graphical representation of both the unweighted and the weighted ambiguity function is given. It shows how the final solution is obtained by maximizing the coherence.

The phasor with maximal coherence is retrieved by a discrete search to find the optimal modeled phase $\varphi_{\text{model}}^{0s}(b)$. The functional models that relate the parameters b , e.g., height and linear deformation, to the modeled phase are described in Section 4.2. In principle any number of parameters can be used. However, with each extra parameter an additional dimension of the solution space is created, increasing the computational load considerably. Therefore, in practice the number of parameters is limited to two (height and linear deformation), although also the estimation of an additional periodic signal is proposed (Colesanti et al., 2003d).

The practical implementation of the ambiguity function technique is based on the *solution bounds* b_{max} and the *solution step size* Δb . The solution bounds limit the possible solutions (see Figure 4.5C and D), whereas the step size specifies the resolution of the discrete search. This is illustrated for the case of one parameter in Figure 4.9. The values of the solution bounds are a trade-off between the chance to miss the solution due to too tight bounds, and the chance of selection of a wrong solution with coincidental

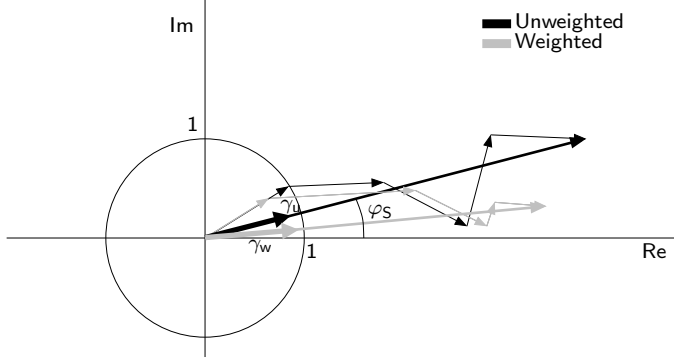


Figure 4.8: Graphical representation of the ambiguity function estimator for a time series in the complex domain. In case of the unweighted ambiguity function (in black) each residual of the time series is represented by a phasor of length 1. The angle of each phasor with respect to the real axis is equal to the residual phase plus the master acquisition contribution (atmosphere and noise). The parameters that maximize the coherence of the unweighted ambiguity function $\gamma_u \in [0, 1]$, indicated by the thick black arrow, are selected as the final solution. When the weighted ambiguity function is applied (in gray), the individual residuals are weighted based on a precision estimate per acquisition, resulting in an alternative solution with coherence γ_w . The phase of the solution phasor φ_S is the estimate of the phase due to the noise and atmospheric signal delay during the master acquisition.

small residues in case the solution space is large. Moreover, the bounds directly influence the computation time. This also applies for the step size. Here, a trade-off is made between the chance to miss the correct coherence maximum, and the computation time. Part of this is circumvented by an iterative approach, where the initial coarse settings for the bounds and step size are refined after a first indication of the solution is obtained.

In DePSI the initial settings for the solution bounds are specified manually per analysis taking the characteristics (i.e., expected residual height differences and deformation phenomena) of the area into account. The initial step size Δb_0 is based on the characteristics of the radar data stack, that is, the range of temporal and perpendicular baselines. That is, the step size should be set such that the sampling of the modeled phase φ_{model} is high enough to detect the solution with maximum coherence. This is achieved by sampling the full phase cycle of 2π with at least two times the maximum absolute value of the functional model ρ_p (which is a function of a particular baseline, i.e., perpendicular or temporal baseline), see the functional model in Eq. (4.44). Hereby, the opportunity is ensured that for at least one evaluated model by the ambiguity function all phasors of the residuals within the time series are enclosed within the same half of the complex domain, see the example in Figure 4.8. Within DePSI a sampling factor of five is applied to ensure the identification of the global coherence maximum in case of increasing noise level, hence

$$\Delta b_{p,0} = \max_{s=1 \dots S} \frac{2\pi}{5|\rho_p^{0s}|} \quad \text{for } p = 1 \dots P, \quad (4.57)$$

where P is the number of parameters and S is the number of slave images. Hence, this relation applies to all parameters b_p independently, for example, the residual height and deformation parameters. Therefore, for each parameter an individual step size is obtained. Using these initial step sizes, at least once all residual phasors are contained

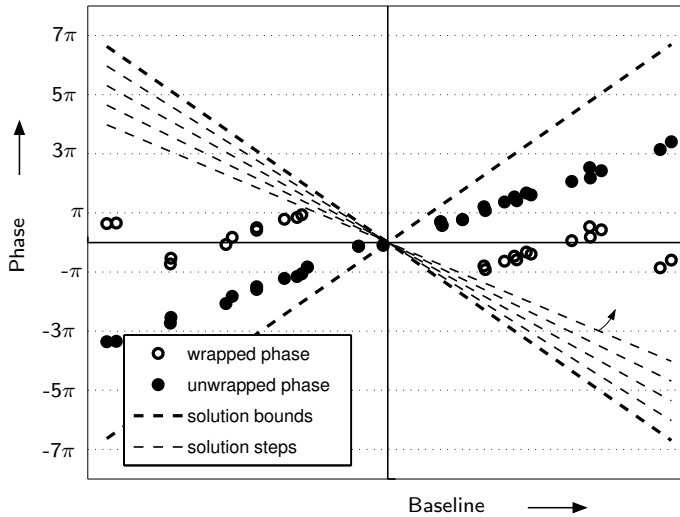


Figure 4.9: Illustration of the discrete search in the solution space by the ambiguity function technique for a one-dimensional case. The solution bounds and solution steps are set a-priori.

within the same half space of the complex solution domain, as shown in Figure 4.9. Hereby, a rough indication of the maximum coherence vector is obtained. Subsequently, the solution bounds are reduced to values around the initial solution and the initial step sizes $\Delta b_{p,0}$ are iteratively decreased with a factor 10. The iteration is repeated until the desired amount of significant numbers for the parameters of interest b are obtained.

Although the phase ambiguities a are not estimated implicitly by the ambiguity function, they can be derived from the unwrapped phase which is obtained based on the estimated parameters. Hence, regardless the ambiguity resolution method applied (i.e., integer least-squares, integer bootstrap estimator, or the ambiguity function) a solution for the ambiguities \check{a}_{ij} per arc is obtained. These ambiguities are used in the spatial ambiguity resolution step to detect unwrapping errors and to unwrap the data with respect to a single reference PS, see Section 5.1. The performance of the different ambiguity resolution techniques described is assessed in the next section.

4.7 Comparison of ambiguity resolution techniques

Three techniques to estimate the ambiguities in the phase time series per arc are described in the previous sections: integer least-squares (ILS), integer bootstrapping (IB), and the ambiguity function (AF). The performance of these techniques is assessed based on simulations using the Envisat mission characteristics.

The impact of the noise level of the phase observations in relation to the deformation rate is visualized in Figure 4.5. Here, Envisat data sets of 30 and 50 single master interferograms are simulated. The figure shows that the success rate of correct ambiguity resolution using the ambiguity function is only dependent on the noise level of the

data. This in contrast to the performance of the integer least-squares (ILS) and integer bootstrap (IB) estimator, where there is a drop in the success rate due to an increasing bias with respect to the pseudo-observations used. These results are based on a fixed value of zero for the pseudo-observations used in the ILS and IB techniques. When the pseudo-observations would be adapted to the particular range of deformation values based on an earlier iteration with the ILS, IB or AF estimator, the current zero-based success rates would shift towards these values. However, a convergence to the true solution is not guaranteed. Alternatively, a set of pre-defined pseudo-observations could be evaluated. Whether these pre-defined values or an iterative scheme would be applied, the computational load will increase.

When the pseudo-observations are not adapted, there is a high likelihood that the ambiguities of scatterers with large deformation rates will not be estimated correctly by the ILS or IB estimator. However, the estimates are arc based. Hence, when the deformation phenomenon has a smooth spatial character, e.g., a large subsidence bowl, multiple arcs are involved to capture the total range of deformation. Hence, the deformation per arc may be sufficiently small to be estimated correctly. The success rates for the most frequently occurring deformation rates between 0 and 20 mm/year are shown in more detail in Figure 4.6. The figure shows that for small deformation rates the ILS estimator outperforms the AF estimator in case of small data stacks, but that the success rates fall in the same range when the size of the stack increases. Since the results by the ILS estimator are accompanied by a solid quality description based on the stochastics of the phase observations (see Appendix A.5), which enables a propagation of the errors, the ILS estimator is preferred.

The success rates in Figure 4.5 further show that the estimation of the variance components (solid lines) strongly improves the performance of the ILS and IB estimator. Hence, a proper description of the quality of the phase observations by the stochastic model is of importance for the ambiguity resolution. Here, only a single variance per interferogram is used. Refinement of the stochastic model by the incorporation of covariances between the interferograms may further improve the results. However, a significant part of this covariance is already introduced in the covariance matrix $Q_{\hat{a}}$ of the float solution by the variances of the pseudo-observations in combination with the baseline configuration in the functional model, see Eq. (4.50). Hence, only deviations of the true covariances with respect to this model could potentially contribute to an improvement of the success rates. This is especially relevant for pixels characterized by distributed scattering. For example seasonal effects related to vegetation growth and snow cover can affect the covariance between interferograms. For point scatterers, this effect is more limited. Another strategy to improve the result is to use local variance matrices instead of a single matrix for the whole area (Caro Cuenca et al., 2011), thereby accounting for the local noise characteristics.

Also the performance of the ambiguity function can be improved by assigning weights to the phase observations. Here, the weights are defined as $1/\sigma$, where σ is the standard deviation of the phase observations as determined by the variance component estimation. However, whereas a significant improvement in the success rate is obtained in case of a stack of 30 interferograms, with 50 interferograms the improvement is insignificant. It appears that the success rate using 50 interferograms is overall higher compared to the use of 30 interferograms. The weights used here do not contribute to a further

improvement. However, alternative weights may further improve the performance. More research is required to determine the optimal weighting scheme for the ambiguity function.

The relation between the noise level in the phase observations, the number of interferograms in the single master image stack, and the required computation time is visualized in Figure 4.10. In the simulation a fixed deformation rate per arc of 4 mm/y is applied, together with a simulated residual height ($\sigma=20$ m) and master atmospheric delay and noise ($\sigma=5$ mm) at both points of the arc. The simulation of phase values is based on a fixed length of the satellite mission. As a result, the average sampling rate of acquisitions in time is higher in case of a large number acquisition. Alternatively, a fixed sampling rate could have been adopted, resulting in a changing acquisition time span. However, the approach applied here gives a better representation of the true situation of variable dataset sizes available for a certain mission.

The success rates show that for small noise levels (up to 30 degrees) all estimators perform equally well, regardless the number of available interferograms. With a noise level of 40 degrees (equivalent to ~ 3 mm) the success rates start to drop, especially for the lowest analyzed number of 30 interferograms. When applying the ambiguity function, there appears to be a large difference between the use of 30 and 50 interferograms in case of a noise level of 50 degrees. Hence, besides the noise level, for the ambiguity function the number of interferograms has a significant impact on the success rate. When comparing the weighted and unweighted ambiguity function, the effect of the variance based weights applied here appears to be limited.

The success rates of the ILS estimator decrease with an increasing number of interferograms, especially for high noise levels. This is partly caused by a specified maximum number of ambiguity solutions that are evaluated in the solution space during the search for the optimal solution. This maximum number is set to S^3 , where S is the number of interferograms (Kampes, 2006). Hence, the number is dependent on the size of the data stack. Especially when the noise level in the phase observations is high, the bootstrap solution, which is used to set the boundary, may cause a large solution space. Without a maximum number of evaluations, the computational load would become too large for practical application. When the maximum number of evaluations is reached, the ILS search is aborted and the bootstrap solution is adopted. Since the success rate of the IB solution is always equal or smaller than that of the ILS solution (Teunissen, 1999a), the ILS success rate drops due to the aborted search. Figure 4.10 shows that indeed the success rates of the ILS and IB estimator converge to the same level with an increasing number of interferograms.

The bootstrap estimator shows an increasing success rate with an increasing number of interferograms. This is caused by a denser sampling of the interferograms over the time span adopted for the simulations. Hence, when 30 interferometric phases are simulated, the average time span between successive acquisitions may be multiple months, whereas in case of 110 interferograms this time span is shorter (up to the 35 day repeat cycle of the Envisat mission). With a denser sampling, the signal can be better reconstructed by the successive rounding applied by the bootstrap estimator, resulting in a higher success rate.

Overall, the success rates show that a certain ambiguity resolution technique is preferable based on the number of available interferograms. Since in PSI analysis scat-

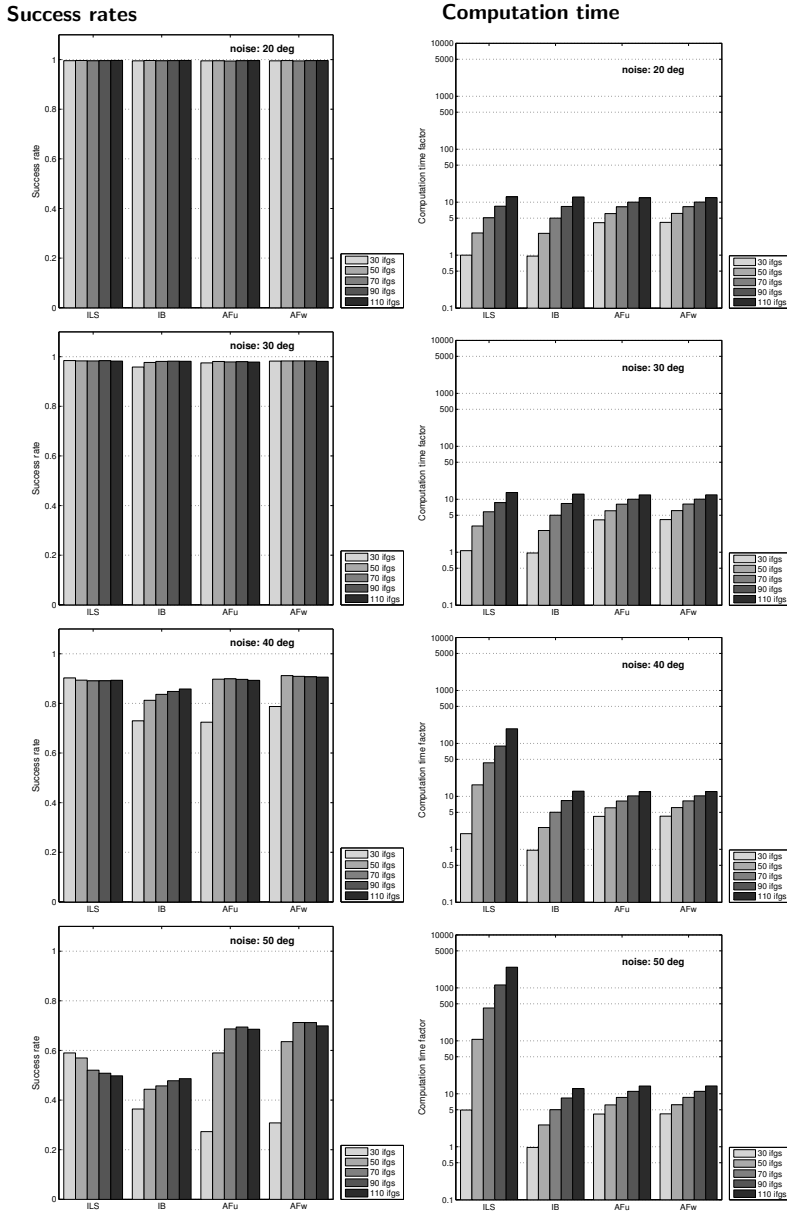


Figure 4.10: Success rate of correct ambiguity resolution based on simulated phase observations (left column) and normalized computation time (right column) related to the number of available interferograms. The integer least-squares (ILS) estimator, the integer bootstrap (IB) estimator, the unweighted ambiguity function (AFu), and the weighted ambiguity function (AFw) are applied. A fixed deformation rate of 4 mm/y per arc is simulated. Moreover, a residual height ($\sigma=20$ m) and master atmospheric delay and noise ($\sigma=5$ mm) is simulated at each point, and differenced to obtain a value for the arc. The remaining simulation settings are the same as applied in Figure 4.5. Gaussian distributed noise with levels at each point of 20° , 30° , 40° and 50° is used. The simulation is repeated 10000 times. The computation times are normalized with respect to the time required by the ILS estimator for a data stack of 30 interferograms with a point noise of 20° , resulting in a computation time factor for each case. The computation times are plotted on a logarithmic scale.

ters with various noise levels will occur, the worst-case scenario of 50 degree noise shown here is the best benchmark. Based on the success rates it follows that for small data stacks the ILS estimator is superior, whereas for stacks larger than 50 single master interferograms the ambiguity function performs better. However, in this assessment the computation time required to estimate the solution is not incorporated.

The computation times required for the various ambiguity estimators are also indicated in Figure 4.10. The computation times are normalized with respect to the time required by the ILS estimator in case of a data stack of 30 interferograms and a noise level of 20 degrees, resulting in a computation time factor for each case. Although these computation time factors are strongly dependent on the efficiency of the implementation and should therefore not be interpreted in a strict sense, the relative differences between the various techniques show the dependency of the results according to the characteristics of the data set, such as noise level and the number of available interferograms.

The figure shows the increase of the computation time with increasing number of interferograms. For low noise levels the estimators require equivalent computation times. When the noise increases, the computation times remain more or less the same for the bootstrap estimator and the ambiguity function. However, with a growing noise level the computation time of the ILS estimator becomes increasingly large. This increase in computation time is caused by enlarged ambiguity search spaces, which are based on the IB solution. The increasing noise level deteriorates the bootstrap solutions obtained and thereby increases the size of the search spaces. For example, a dataset with 110 interferograms and a noise level of 50 degrees takes about 200 times longer to compute the ILS solution compared to the IB or ambiguity function solution. Application of the ILS estimator is therefore infeasible from a practical point of view for large data stacks and/or large image crops. Therefore, often the bootstrap estimator is used instead. However, since the success rate of the ILS estimator is higher, a speed-up of the current ILS implementation is desirable. Various algorithmic improvements are feasible. For example, alternative approaches are based on a more flexible construction of the ambiguity search space χ^2 . Giorgi et al. (2008); Teunissen et al. (2010) presented the *Search and Shrink* approach and Park and Teunissen (2003); Buist (2007) introduced the *Expansion* approach. Furthermore, Jazaeri et al. (2012) demonstrated the transformation of the integer least-squares problem into the equivalent closest lattice point problem. Application of lattice point search techniques appears to result in a reduction of the computation time compared to the LAMBDA approach. It is recommended to evaluate the approaches mentioned for application in PSI.

The computation times to estimate the ambiguities are based on a model with the residual height and a linear deformation rate. In case of the ILS and IB estimator, the model can easily be extended with more advanced deformation models, e.g., a seasonal signal, without a significant increase of the computation time, see Section 7.9. This does however not apply for the ambiguity function. For each additional parameter in the model an extra dimension in the solution space needs to be evaluated. For example, common solution bounds and solution steps applied for the residual height and deformation rate (see Figure 4.9) results in a solution space of 10^2 solutions each, giving 10^4 solutions to evaluate. With two additional parameters for a seasonal signal, the solution space increases to 10^8 unique solutions. Such a solution space is infeasible from a practical point of view. Therefore, when multiple deformation parameters are incorporated

in the model, the bootstrap estimator is adopted instead. Although the IB estimator has a lower success rate compared to the ILS estimator, the significant shorter computation time is decisive. In Chapter 7 the application of the bootstrap estimator for various deformation models is demonstrated.

After the estimation of the phase ambiguities per arc in time by either the integer least-squares estimator, the bootstrap estimator, or the ambiguity function, the ambiguities can be integrated in space to connect all PSC with respect to a common reference point. A process based on a geodetic testing scheme is applied to detect ambiguity errors and incoherent PSC. The process is described in Chapter 5.

4.8 Summary

The key step for PSI is the estimation of the integer-valued phase ambiguities. Within DePSI a two-step approach is applied, where the ambiguities are resolved in time first, followed by a controlled integration in space using a testing scheme (see Chapter 5).

The temporal ambiguity resolution is based on a parameterization within the framework of a mathematical model. The mathematical model consists of a functional model, describing the relation between the observations and the unknown parameters, and a stochastic model, describing the statistical properties of the observations.

The functional model contains the topographic height error, the master atmosphere, and a deformation model, which minimally contains a linear deformation rate. The model can be extended with a periodic term, a higher-order polynomial and/or breakpoints in case of a sudden event during the acquisition time span. The deformation model can be selected based on a-priori knowledge of the expected deformation phenomenon or derived from the data using a testing scheme, see Chapter 7.

The stochastic model is estimated from the data by variance component estimation (VCE). The model is updated after each estimation and removal of a phase screen, describing an error source such as the atmospheric signal delay or orbit errors. This iterative approach ensures that the stochastic model describes the stochastics of the observations as close as possible.

To estimate the phase ambiguities, three estimators are implemented in DePSI: integer least-squares (ILS), integer bootstrapping (IB) and the ambiguity function (AF). For a low number of available single master interferograms the ILS estimator outperforms the alternative techniques, whereas for a high number of interferograms an equivalent success rate is obtained by the ambiguity function. However, the ambiguity function is better able to correctly estimate the phase ambiguities in case of large deformation rates. Another advantage of the ambiguity function, together with the IB estimator, is the computation speed. Yet, the computation time increases significantly when more model parameters would be inserted. The ILS and IB estimators have the advantage that model parameters can easily be added, without additional processing time. Moreover, by using ILS the stochastic properties of the observations can be fully incorporated in the processing flow, enabling a proper error propagation. Further improvement of the efficiency of the ILS algorithms used will further strengthen the benefits of this estimator. Until then, often the IB estimator is used to exploit both the computation speed and the ability to add additional parameters to the model.

Drawback of the current approach within DePSI is the dependency on a single

master stack. As a result, the coherence of the interferometric phases used is not optimal. Interferometric combinations with shorter baselines, both in the temporal and perpendicular baseline domain, will reduce the noise and thereby increase the information content of the data. The hypothesis is that this will also improve the correct estimation of the phase ambiguities. Moreover, flexibility in baseline configuration will improve the possibilities to account for (seasonal) surface scattering effects, such as vegetation growth and snow cover.

This chapter describes the processing steps acting in the spatial domain, in particular the spatial ambiguity resolution and the estimation of error sources at an area-wide scale, known as phase screens. Based on the estimated differential phase ambiguities per arc in the first-order network (see Chapter 4), the ambiguities are integrated in space, thereby applying a testing scheme to detect errors in the ambiguities and incoherent PSC, see Section 5.1. Based on the resolved first-order network, the phase screens due to orbit errors (Section 5.2) and atmospheric signal delay (Section 5.3) are estimated. After each phase screen correction the stochastic model is updated using Variance Component Estimation, as described in Section 4.4, and the network construction is repeated, resulting in an iterative scheme. Section 5.4 presents the final densification of PS by temporal ambiguity resolution between higher-order PSC and first order network PS, and a test of the estimated ambiguities to detect inconsistencies. The chapter is summarized in Section 5.5.

5.1 Spatial ambiguity resolution

Once the phase ambiguities \check{a}_{ij} are resolved in time per arc of the first-order network (see Chapter 4), a two-dimensional spatial ambiguity resolution step is required to obtain unwrapped phases with respect to a single reference PS. If all ambiguities would be resolved correctly in time, this can be accomplished by a simple spatial integration along an arbitrary path. However, possible errors in the temporal ambiguity resolution prevent such a straightforward approach. Therefore, the ambiguity errors or *phase unwrapping errors* should be accounted for first.

To remove possible errors in the estimated ambiguities, often a two-step approach is taken (Ferretti et al., 2000). First, a certain threshold is applied to exclude arcs from the data set with a low quality indication, e.g., temporal coherence, see Eq. (4.55). Regardless whether a low coherence indicates a high noise level or strong model imperfections, e.g., unmodeled deformation (see also Section 6.2.1), in both cases the ambiguity resolution is assumed to be unreliable and the arc is therefore excluded. As a consequence, coherent points with strong unmodeled deformation behavior will be excluded from the first-order network. This may lead to an unnecessary weakening of the network. The second step in the general approach is the actual ambiguity resolution, where often a sparse Minimum Cost Flow (MCF) algorithm is used (Costantini and Rosen, 1999; Ferretti et al., 2000). Here, the solution for a consistent network is selected that minimizes

the number of ambiguities that needs to be adapted, hence an L1-norm. Because a solution can always be found, there is no guarantee that the solution obtained is indeed correct.

To account for the drawbacks of the procedure described above, in DePSI a different approach is used, denoted as the testing of the ambiguities approach.

5.1.1 Testing of the ambiguities

The testing of the ambiguities approach is based on geodetic testing theory, see Section A, and shows strong resemblance with the method used in Kampes (2006). The basic concept is that errors in the network, which can either be wrongly unwrapped arcs or incoherent points, are detected and removed from the network. However, whereas in Kampes (2006) the testing is based on the estimated parameters of interest, in DePSI the testing is applied to the ambiguities directly (van Leijen et al., 2006a). *Testing of the ambiguities* has two major advantages. First, different functional and stochastic models can be applied for the temporal ambiguity resolution of different arcs. Although the parameters of interest estimated by these different models will result in closing errors in the network, the estimated ambiguities (and equivalently, the unwrapped phases) need to be consistent, enabling testing. This approach also enables the concept of sequential testing of deformation models, see Sections 7.5 and 7.6. The second advantage of testing of the ambiguities is the ability of *ambiguity adaptation*. Once the arcs with the largest unwrapping errors and the incoherent points are removed from the network, ambiguity errors in the remaining arcs are adapted to fit the network. The advantage is that when only one or a few ambiguities in a certain arc are wrong, e.g., due to strong atmospheric effects during some acquisitions or significant unmodeled deformation, the arc is not removed from the network, but adapted. This way the strength of the network is largely preserved. The condition for correct adaptation of the ambiguities is that the majority of connecting arcs to a PS are resolved correctly. Because a least-squares approach is used, hence providing an L2-norm, it is more likely that the biggest ambiguity errors are resolved first in the iterative adaptation scheme, compared to the sequence of adjustment using the L1-norm in case of a MCF approach.

Testing of the ambiguities is possible provided that the constructed double-difference phase observations per arc in the network φ_{ij} are not re-wrapped to the $[-\pi, +\pi)$ interval. This can be seen as follows. Assume a small network of three points forming a triangle, see Figure 5.1A. Each point has a true (unwrapped) interferometric phase ϕ_i , composed of an unknown ambiguity a_i and an observed wrapped phase φ_i . Constructing the double-differences results in

$$\begin{aligned}\phi_{12} &= (2\pi a_2 + \varphi_2) - (2\pi a_1 + \varphi_1) = 2\pi(a_2 - a_1) + (\varphi_2 - \varphi_1) = 2\pi a_{12} + \varphi_{12}, \\ \phi_{23} &= (2\pi a_3 + \varphi_3) - (2\pi a_2 + \varphi_2) = 2\pi(a_3 - a_2) + (\varphi_3 - \varphi_2) = 2\pi a_{23} + \varphi_{23}, \\ \phi_{31} &= (2\pi a_1 + \varphi_1) - (2\pi a_3 + \varphi_3) = 2\pi(a_1 - a_3) + (\varphi_1 - \varphi_3) = 2\pi a_{31} + \varphi_{31},\end{aligned}\tag{5.1}$$

where ϕ_{ij} are the true unwrapped double-difference phases. Note that $\varphi_{ij} \in [-2\pi, +2\pi)$. By definition, the unwrapped phases ϕ_{ij} form a closed loop. As the φ_{ij} are not re-wrapped, their sum is also zero. Consequently, the ambiguities a form a closed loop as

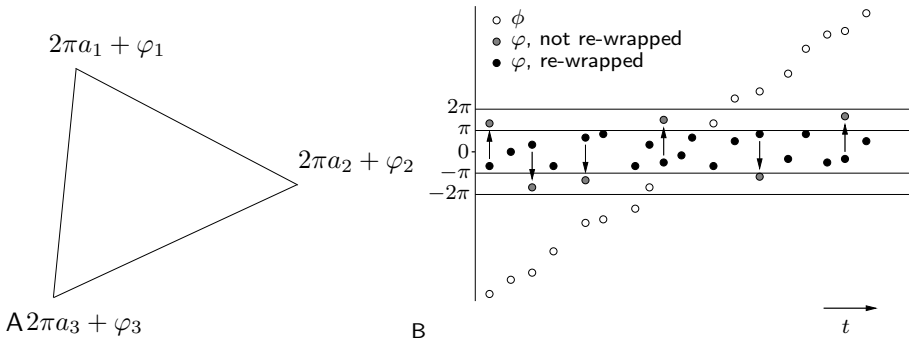


Figure 5.1: A) Triangle of interferometric phases, composed by an unknown ambiguity a and an observed wrapped phase φ . B) The effect of not re-wrapping double-difference phase observations for a single arc. Both the gray and black dots can be used to estimate the final unwrapped time series indicated by the open dots. However, the advantage of using the not re-wrapped phase observations (gray dots) is that the estimated ambiguities can be used for the detection of ambiguity errors, since they should form closed loops within the network.

well, which can be used in the testing. Wrapping of the double-difference phases φ_{ij} will result in phase residues, and the closure of the ambiguities no longer holds. Hence, re-wrapping of phases results in a loss of information for this application. This is in contradiction to branch-cut unwrapping methods, where the phase residues are the prime source of information. The consequence of not re-wrapping the double-difference phases is illustrated in Figure 5.1B for a single time series. Since the temporal ambiguity resolution techniques (see Chapter 4) estimate the number of integer ambiguities required to minimize the residues between the observations and the model, both the re-wrapped and not re-wrapped differential phase observations per arc can be used to estimate the final unwrapped time series. However, the advantage of using the not re-wrapped phase observations is that the estimated ambiguities can be used for the detection of ambiguity errors, since they should form closed loops within the network.

The complete algorithm of spatial ambiguity resolution consists of a number of steps, which are described in detail in the next section.

5.1.2 Spatial ambiguity resolution algorithm

The spatial ambiguity resolution algorithm as implemented in DePSI consists of six steps:

1. **Removal of arcs with a low quality indication (optional).** In case the ambiguity function is used for the temporal ambiguity resolution, the temporal coherence estimator is used as indicator (Eq. (4.55)), whereas in case of integer least-squares or bootstrapping, the variance factor is used, see Eq. (4.53). The specified threshold determines the influence of this step. By applying a very low (temporal coherence) or high (variance factor) threshold, all arcs are accepted and the detection of errors is completely based on the testing scheme. The advantage is that PSC with a non-linear deformation behavior, resulting in a low quality indication, are potentially maintained in the network.
2. **Removal of arcs and PSC that cannot be tested.** In case a quality threshold on the arcs is applied, some PSC may only be connected by one or two arcs. Since

the correctness of single-arc connected PSC and the corresponding arc cannot be tested, these PSC and arcs are removed. Although errors can be detected when a PSC is connected by two arcs, the erroneous arc cannot be identified. A minimum number of three connecting arcs per PSC is therefore required to identify errors. Hence, untestable arcs are removed.

3. **Selection of the reference PSC.** After spatial ambiguity resolution, all PSC are referred to a single reference PSC. The choice of the reference PSC is in principle arbitrary. That is, without loss of information a simple transformation can be applied to change the reference PSC. However, since the noise of the reference PSC propagates to the time series of each PSC, interpretation of the time series becomes easier when a reference PSC is chosen with limited (scattering) noise, i.e., the most *coherent* PSC. In case the ambiguity function is applied to resolve the temporal ambiguities, one of the PSC constructing the arc with highest temporal coherence is chosen as reference. When ILS or bootstrapping is applied, a PSC from the arc with lowest variance factor identifies the reference. The choice of the reference PSC based on coherence does not indicate anything about the physical characteristics of the reference PSC, e.g., height or deformation. To ease interpretation of the final results, it is beneficial to adopt a reference point for which can be assumed that it experiences no deformation. Although such a non-deforming reference PS can be adopted at the end of the full processing chain, it can also be specified at this stage. However, in that case the coordinates of the PS need to be known, e.g., based on earlier results.
4. **Testing of the ambiguities.** An iterative testing scheme is applied to test the ambiguities in a spatial network. The testing scheme is an adapted form of the Detection, Identification and Adaption (DIA) procedure (Teunissen, 2000b), see Section A.2. Within the testing procedure the integer nature of the ambiguities is neglected, hence, the ambiguities are assumed to be real values. The mathematical model used per interferogram is

$$\begin{bmatrix} \tilde{a}_{12}^{0s} \\ \tilde{a}_{13}^{0s} \\ \tilde{a}_{14}^{0s} \\ \tilde{a}_{26}^{0s} \\ \vdots \\ \tilde{a}_{ij}^{0s} \\ \vdots \end{bmatrix} = \begin{bmatrix} -1 & 1 & 0 & 0 & \dots & 0 & \dots \\ -1 & 0 & 1 & 0 & \dots & 0 & \dots \\ -1 & 0 & 0 & 1 & \dots & 0 & \dots \\ 0 & -1 & 0 & 0 & \dots & 1 & \dots \\ \vdots & \vdots & \vdots & \vdots & \vdots & \vdots & \vdots \\ \vdots & \vdots & \vdots & \vdots & \vdots & \vdots & \vdots \\ \vdots & \vdots & \vdots & \vdots & \vdots & \vdots & \vdots \end{bmatrix} \begin{bmatrix} \tilde{a}_1^{0s} \\ \tilde{a}_2^{0s} \\ \tilde{a}_3^{0s} \\ \tilde{a}_4^{0s} \\ \vdots \\ \tilde{a}_6^{0s} \\ \vdots \end{bmatrix}, \quad D\{\tilde{\mathbf{a}}\} = Q_y, \quad (5.2)$$

where the ambiguity estimates per arc \tilde{a}_{ij}^{0s} are the observations, the design matrix describes the network relation between the arcs and the PSC, and the ambiguities per PSC \tilde{a}_i^{0s} are the unknowns. The reference point is set by removing the corresponding ambiguity from the vector of unknowns and corresponding column from the design matrix. The dispersion of the ambiguities is set by Q_y , which should in this case be interpreted as the inverse of a weight matrix. Since the ambiguities per arc were resolved individually, they are assumed uncorrelated, causing Q_y to be diagonal. Both a weighted as well as an unweighted estimator can be applied.

In case of an unweighted approach, Q_y is set equal to the identity matrix. When weighting is applied, the diagonal elements are dependent on the temporal ambiguity resolution approach used. In case the of ILS or bootstrapping, the matrix is set based on the a-posteriori variance factors σ_b^2

$$Q_y = \text{diag}(\sigma_{b,ij}^2). \quad (5.3)$$

When the ambiguity function is used, the weight matrix is defined by the ensemble coherence estimator $|\gamma_{ij}|$ as

$$Q_y = \text{diag}(1 - |\gamma_{ij}|). \quad (5.4)$$

To give even more weight to high precision arcs compared to those with lower precision, also the element-wise squared version of Q_y can be applied as weight matrix.

Three alternative hypothesis H_a are tested in the iterative DIA procedure, the Overall Model Test (OMT), the test per observation (w-test) and the point test, respectively. The OMT is used to *detect* a model error. The test statistic $\underline{T}_{q=m-n}^{0s}$ per interferogram is, see Appendix A

$$\underline{T}_{q=m-n}^{0s} = \hat{\underline{\epsilon}}_0^T Q_y^{-1} \hat{\underline{\epsilon}}_0, \quad (A.18)$$

where q is the degree of freedom, m is the number of observations, n is the number of unknowns, and $\hat{\underline{\epsilon}}_0$ are the residues of the model under the null hypothesis H_0 . Instead of testing the ambiguities per interferogram, the whole data stack is tested simultaneously. This is done by summation of the test statistics \underline{T}^{0s} of the different interferograms, leading to

$$\text{reject } H_0 \text{ if } \sum_{s=1}^S \underline{T}_{q=m-n}^{0s} > k_{\alpha_{q=m-n}} \quad (5.5)$$

Because the ambiguities of the arcs form a closing network when all errors are identified and adapted, hence, the residuals become zero, the OMT should only be accepted when the test statistic is zero. Hence, the *critical value* $k_{\alpha_{q=m-n}}$ is set to zero (or actually a very small number to allow numerical errors), in order to continue testing until all the errors are identified.

For the identification of errors in the ambiguities both a one-dimensional test per observation ($\underline{T}_{q=1}$) and a point test per PSC ($\underline{T}_{q=p}$) is performed. The alternative hypothesis of the observation test for a certain arc is specified by

$$C_{q=1} = [0 \ \cdots \ 0 \ 1 \ 0 \ \cdots \ 0]^T. \quad (A.19)$$

Because the ambiguities are assumed to be uncorrelated, the test statistic can be calculated by

$$\underline{T}_{q=1} = \frac{\hat{\underline{\epsilon}}_0^2}{\sigma_{\hat{\underline{\epsilon}}}^2}. \quad (A.20)$$

In case of the point test, the alternative hypothesis is specified by

$$C_{q=p} = \begin{bmatrix} 0 & \cdots & 0 & 1 & 0 & \cdots & 0 \\ 0 & \cdots & 1 & 0 & 0 & \cdots & 0 \\ 0 & \cdots & 0 & 0 & 1 & \cdots & 0 \\ \cdots & \cdots & \cdots & \cdots & \cdots & \cdots & \cdots \end{bmatrix}^T, \quad (5.6)$$

where the ones correspond to ambiguities of arcs that are connected to the point that is tested. Therefore, the dimension of the test may differ per point. Since one of the connecting arcs is required as reference, see e.g., Verhoef (1997), the dimension p is equal to the number of connecting arcs minus one. Using $C_{q=p}$, the test statistic is calculated by

$$\underline{T}_q = \hat{\underline{\epsilon}}_0^T Q_y^{-1} C_q (C_q^T Q_y^{-1} Q_{\hat{\epsilon}_0} Q_y^{-1} C_q)^{-1} C_q Q_y^{-1} \hat{\underline{\epsilon}}_0. \quad (A.12)$$

Using the B-method of testing (see Section A.2), the critical values for the observation and point tests are determined. By comparing the *test quotients*, the most significant model error is identified. Again the sum of the test statistics of all interferograms is taken, providing a test for the full data stack. The alternative hypothesis H_a is selected which has the largest test quotient, hence

$$\text{accept } H_a \text{ for which } \max_{g,h} \left(\frac{\sum_{s=1}^S T_{q_g=1}^{0s}}{k_{\alpha_{q=1}}}, \frac{\sum_{s=1}^S T_{q_h=p}^{0s}}{k_{\alpha_{q=p}}} \right). \quad (5.7)$$

where $g = 1 \dots G, h = 1 \dots H$ indicate the G observation tests and H point tests, respectively. Since the test statistics are only used to identify the most significant error, the absolute values of the k_{α} are of no importance, only the relative ratio, which is accounted for by the B-method of testing. Once the most significant error is identified, the model is adapted by removing an arc or all connecting arcs of a point from the observation vector, and removing the corresponding rows and columns from the design matrix.

In principle this procedure can be repeated until the OMT is accepted and all errors are removed from the network. However, since the testing procedure is applied to the full data stack, also arcs with only one or a few ambiguity errors would be removed. This results in a weakening of the network. To prevent this, the testing procedure is stopped at a certain stage, where the assumption is made that the largest unwrapping errors and all incoherent points are removed from the network. This stop-criterion is

$$\text{stop if } \max_g \left(\frac{\sum_{s=1}^S T_{q_g=1}^{0s}}{k_{\alpha_{q=1}}} \right) < 1. \quad (5.8)$$

This is the only moment where the actual values of Q_y and k_{α} , or better, the ratio thereof, are of importance. Tests on real data show that in case of a Q_y with variances of one in combination with $k_{\alpha_1} = 0.1$ give satisfying results.

In case the testing scheme results in separate networks, a new reference PSC is automatically selected for the sub-network. However, multiple reference points are

undesirable. Therefore, the whole procedure of creating a first-order network is in this case repeated, see module 3 in Figure 3.1. When incoherent points have been removed in the first iteration, the new network will have a different geometry, potentially leading to a single network in the second iteration. This procedure is repeated maximum 5 times. When still not a single network is obtained, the remainder of the analysis will be based on the separate networks and the corresponding reference points.

After the testing procedure is aborted, the remaining ambiguity errors are adapted instead by a procedure denoted as *adaptation of the ambiguities*.

5. **Adaptation of the ambiguities.** Once the largest unwrapping errors and all incoherent points are assumed to be removed from the network by the testing scheme, the remaining ambiguity errors are adapted. Instead of applying corrections to the full data stack, here the adaptation is performed per interferogram. Again an iterative scheme is applied, where the Overall Model Test (OMT) is used to check whether a closing network is obtained. The mathematical model used in the last iteration of the testing scheme Eq. (5.2) is used for this adaptation scheme. Hence, also the same weight matrix is applied. When a misclosure is detected by the OMT, the ambiguity with the largest residue is corrected by subtracting the rounded value of the residue. When the residues become small and the rounded value of the largest residue is zero, the ambiguity is corrected by adding or subtracting one. This procedure is repeated until all misclosures are adapted. To prevent a continuous loop, the maximum number of fixes is set to the number of arcs involved. Therefore, complete adaptation of all misclosures is likely, but not guaranteed.

This step is similar to the approach taken in Kampes (2006). There, a sparse Minimum Cost Flow (MCF) algorithm (Costantini and Rosen, 1999; Eineder and Holzner, 1999) is used to correct remaining misclosures after the testing scheme. Although the minimization criterion is different compared to the approach taken here, the results are expected to be similar. The advantage of the adaptation approach is that the same mathematical framework can be used as applied in the testing scheme. Moreover, the L2-norm resulting from the least-squares method applied indicates that the sequence of adaptation is better ordered. This should increase the chance of convergence to the correct solution.

After correction of all the misclosures the remaining solution after solving the mathematical model (Eq. (5.2)) represents the ambiguities with respect to the reference PS. Based on these ambiguities the phase can be unwrapped and the parameters of interest can be estimated.

6. **Calculation of the unwrapped phase and the parameters of interest.** Based on the ambiguities with respect to the reference PS \tilde{a}_{0i}^{0s} , the unwrapped phase $\underline{\phi}_{0i}^{0s}$ is calculated by

$$\underline{\phi}_{0i}^{0s} = 2\pi \cdot \underline{a}_{0i}^{0s} + \varphi_{0i}^{0s}, \quad (5.9)$$

for slave $s = 1 \dots S$. When calculating the double-difference phase φ_{0i}^{0s} from the original interferometric phases of the two PS, the phase should not be re-wrapped, to be consistent with the resolved ambiguities.

Once the phases of the first-order network are unwrapped, the parameters of interest with respect to the reference PS (see Step 3) are estimated. The same functional relations as described in Section 4.2 about the functional models for temporal ambiguity resolution can be used. The choice of the parameters to estimate is completely independent of the parameters used in the temporal ambiguity resolution step. Since the atmospheric signal is estimated from the residuals obtained here, the parameters, e.g., describing the deformation, should model the remaining phase contributions as good as possible. Therefore, a more sophisticated deformation model can be used here, for example to estimate a periodic signal. The functional model should minimally contain the atmospheric signal delay of the master acquisition S_{0i}^0 , the relative height H_{0i} , and the linear deformation rate D_{0i} , hence

$$E\{\underline{\phi}_{0i}^{ms}\} = \beta_{0i}^{0s} H_{0i} + \alpha_1^{0s} D_{0i} + \frac{-4\pi}{\lambda} S_{0i}^0, \quad (5.10)$$

where α_1^{0s} specifies the linear deformation model (Eq. (4.8)) and β_{0i}^{0s} is the height-to-phase conversion factor (Eq. (4.3)). Here, β_{0i}^{0s} is taken as the mean of the two height-to-phase factors involved, i.e., $\beta_{0i}^{0s} = (\beta_0^{0s} + \beta_i^{0s})/2$. Additional terms, e.g., to estimate extra deformation parameters and sub-pixel position, can easily be added to the model. Unlike for the temporal ambiguity resolution, where different functional models can be applied, here the same model is used for the whole data set.

The stochastic model used to estimate the parameters of interest is the one obtained previously by Variance Component Estimation, see Section 4.4. However, since the noise level per PS will differ, after least-squares estimation the residuals are used to scale the covariance matrix with the *a-posteriori* variance factor $\hat{\sigma}^2$ (see also Eq. (4.53)) to obtain a unique covariance matrix per PS. The variance factor is estimated by

$$\hat{\sigma}^2 = \frac{\hat{\underline{e}}^T Q_y^{-1} \hat{\underline{e}}}{m - n}. \quad (5.11)$$

A value of 1.0 indicates that the covariance matrix describes the dispersion of the observations well, whereas a value larger than 1.0 shows that the stochastic model is chosen too optimistic, and vice versa. By scaling the covariance matrix with $\hat{\sigma}^2$ a matrix consistent with the variance level of the PS is obtained. Although the estimates of the parameters of interest, that is \hat{H} , \hat{D} , \hat{S} and possible additional parameters, do not change, the covariance matrix of the estimated parameters $Q_{\hat{x}}$ does change and becomes unique for each PS. Note that the quality description obtained is based on the assumption that the phase was unwrapped correctly, hence the ambiguity resolution had a success rate of one. The variance factor $\hat{\sigma}^2$ also acts as a quality or coherence indicator, see also Section 6.2.

After completion of the spatial ambiguity resolution step the interferometric phases are unwrapped with respect to the reference PS and the parameters of interest are estimated. The residuals which remain after the parameter estimation are used to estimate the orbital trend (optional) and the atmospheric signal delay per interferogram in the form of phase screens.

5.2 Orbital Phase Screen estimation

Inaccuracies in the orbit parameters cause a trend in the interferometric phases (Small et al., 1993; Hanssen, 2001; Kohlhasse et al., 2003; Bähr and Hanssen, 2012). This phase contribution may result in two effects (or a combination thereof). First, the orbital signal induces an additional noise term in the double-difference phase observations of the arcs in the network since the orbit errors are different for each acquisition. Although this additional noise term may be relatively small at the short distances of the arcs, it may hamper the reliable resolution of the phase ambiguities and thereby possibly the detection of the PS involved, see Section 4.2. Second, a correlation of the orbital inaccuracies with time or baseline causes a bias in the estimated parameters of interest, such as deformation and height. Both effects can be reduced by estimating and removing a two-dimensional phase trend per interferogram, denoted as the *Orbital Phase Screen* (OPS).

Because the orbital phase trend and the atmospheric signal both show a strong correlation in space, the phase contributors could be estimated and predicted simultaneously using a *trend-signal-noise* model, which will be presented in Section 5.3. However, the possible correlation of the orbit inaccuracies with time or baseline, and the resulting bias in the parameters of interest, induce an error in the phase residuals which are used as input for the trend-signal-noise model. Hence, the bias is not corrected using this approach. This problem of correlation in time occurs in case of data sets acquired by the Envisat satellite, where a spatial trend in the estimated linear deformation rates remains in the final result (Ketelaar, 2009). Marinkovic and Larsen (2014) discovered that this trend is caused by a drift of the local oscillator of the ASAR instrument on-board the Envisat. Their empirical derived correction model can now be used to correct the trend in the Envisat data deterministically.

To circumvent this problem of possible correlation of the orbit error with other parameters, the spatial trend due to the orbital inaccuracies, possibly together with a trend in the atmospheric signal, is estimated independently per interferogram based on the unwrapped phase of the first-order network, see module 4 in Figure 3.1. The mathematical model used has the form

$$\begin{bmatrix} \underline{\phi}_{01}^{0s} \\ \vdots \\ \underline{\phi}_{0i}^{0s} \\ \vdots \\ \underline{\phi}_{0I}^{0s} \end{bmatrix} = \begin{bmatrix} l_1 & p_1 & 1 \\ \vdots & \vdots & \vdots \\ l_i & p_i & 1 \\ \vdots & \vdots & \vdots \\ l_I & p_I & 1 \end{bmatrix} \begin{bmatrix} T_{az} \\ T_r \\ T_{off} \end{bmatrix}, \quad D\{\underline{\phi}\} = \sigma_\phi^2 I, \quad (5.12)$$

where $\underline{\phi}_{0i}^{0s}$ is the unwrapped phase in the interferogram with slave s at PS1 i , with line and pixel coordinates l_i and p_i , respectively. The two-dimensional OPS is described by the slopes in azimuth and range direction T_{az} and T_r , and an offset T_{off} . Here, all unwrapped phases are given equal variance σ_ϕ^2 and are assumed uncorrelated, indicated by the identity matrix I . An estimation and testing scheme is applied to remove outliers (see Appendix A), until a good fit is reached. Once the OPS is estimated for all interferograms, the original interferometric phases are corrected and the first-order network is constructed again. Due to the reduction of the noise induced by the orbital inaccuracies,

more PS1 may now be detected, resulting in a stronger network.

Trends in the data with a physical origin other than orbit errors or atmospheric signal delay, e.g., deformation, may also be (partly) remove by the OPS. Hence, this optional processing step should be applied with care. For example, when a certain subsidence bowl is present in the area, the total area analyzed should be large enough to estimate the OPS properly. When this is the case, the testing scheme ensures that the subsidence bowl does not influence the trend estimated.

An alternative approach is to estimate the relative orbit errors before the PSI analysis based on a network of interferograms (Bähr and Hanssen, 2012; Bähr, 2013). Here, interferograms forming a redundant network within the temporal-perpendicular baseline domain are used to estimate the relative orbit errors of the individual acquisitions. Both wrapped and spatially unwrapped interferograms can be used. The advantage of this approach is that a redundancy in the estimation problem is obtained. However, the approach requires a large computational effort.

5.3 Atmospheric Phase Screen estimation

For deformation analysis, as performed with DePSI, the atmospheric signal delay during each acquisition induces an additional noise term. Therefore, the atmospheric signal per interferogram, known as the *Atmospheric Phase Screen* (APS), is estimated and removed from the phase observations. Two steps can be identified to estimate the APS (Ferretti et al., 2000). First, the atmospheric signal delay is separated from the other phase contributions for each PS in the first order network. Second, the isolated atmospheric delays are used to predict a full image APS. Both steps are described in more detail in Sections 5.3.1 and 5.3.2.

5.3.1 Atmospheric phase separation

After ambiguity resolution the unwrapped phase observations per PS in the first-order network are obtained, see Section 5.1.2. Due to a lack of redundancy¹ in the functional model (Eq. (5.10)), the APS per acquisition cannot be estimated directly from these phase observations. Only the atmospheric delay (plus noise) of the master acquisition is estimated functionally, whereas the influence of the slave acquisitions is modeled stochastically. As a consequence, the phase contribution of the slave APS is contained in the residuals \underline{e} . Besides the slave APS φ_S , the residuals also hold the unmodeled part of the deformation φ_{uD} . The remaining phase is regarded as noise of the slave acquisition φ_n . This is denoted by

$$\underline{e}_{0i}^{0s} = \varphi_{0i,S}^s + \varphi_{0i,uD}^{0s} + \varphi_{0i,n}^s, \quad (5.13)$$

where the lower zero indicates the reference PS. To separate the slave atmospheric delay from the unmodeled deformation and the noise, the spatio-temporal characteristics of the different parameters are used. The atmospheric delay is correlated in space but uncorrelated in time, i.e., provided that the acquisitions are taken at least a few hours apart (Hanssen, 2001). On the contrary, the unmodeled deformation is assumed to be

¹The redundancy is the number of observations compared to the number of unknown parameters.

correlated in time (apart from the possible correlation in space). Finally, the noise is regarded to be uncorrelated both in time and in space. These different correlations are used to separate the different phase contributions in a two-step procedure. First, the temporal correlation of the unmodeled deformation is used to isolate this phase term from the atmospheric delay phase and noise. A deterministic low-pass filter is applied to the residuals of each PS by a convolution in time with a triangular, rectangular or Gaussian window. The window is used to assign weights to the observations in the time series. The weights, which have original values ranging from zero to one, are normalized to obtain a sum of weights of one, resulting in an unbiased estimate.

The length of the window is specified by the user in years. This length is a trade-off between the smoothing strength of the filter and the temporal sampling density of the radar acquisitions. When the length is too short, the number of samples within the window may be too low for a profound separation of the deformation. Especially when the temporal sampling of the acquisitions is irregular, a relatively long window length may be required. However, with increasing window length the smoothing effect of the filter becomes stronger, possibly removing any detail in the unmodeled deformation signal. Due to this trade-off, the optimal window length is dependent on the repeat cycle of the satellite. For example, for a dataset acquired by the Envisat satellite with a repeat orbit of 35 days a window length of 1 year is appropriate, whereas for TerraSAR-X (11-day orbit) 0.3 year would be sufficient. The effective filter length is reduced at the far ends of the radar time series. To avoid this, instead of a fixed length a minimum number of samples could be taken to determine the filter. However, in case of an irregular sampling of the acquisitions this would lead to a inhomogeneous filter along the time span. To circumvent this problem and to adapt the filter to the signal involved, a new approach based on least-squares prediction in the time domain has been designed and evaluated (Liu, 2012). Here, the stochastic properties of the different signals involved are estimated from the data by variograms. However, this approach is not implemented in DePSI yet.

Once the unmodeled deformation is calculated per PS and extracted from the residuals, the remaining residual phase only contains the atmospheric phase of the slave acquisitions and noise. Since the atmosphere is spatially correlated and the noise is assumed uncorrelated, a spatial low-pass filter is applied to separate the atmosphere from the noise. The low-pass filtering is performed by Best Linear Unbiased Prediction (BLUP) (or *Kriging*), taking the spatial correlation of the atmospheric signals into account. Since the same algorithm can be used for the spatial prediction of the full scene APS, both steps are combined and described in the next section.

5.3.2 Atmospheric phase prediction

The full scene APS per interferogram is obtained by Best Linear Unbiased Prediction (BLUP) (see Appendix A.3) based on the residual phase observations at the first-order PS. Since an interferometric APS is the superposition of the common master and a slave acquisition, two strategies are possible. Either the master and slave APS are predicted individually and combined afterwards to obtain the interferometric APS, or the interferometric combinations are formed first, followed by the prediction step. Advantage of the first option is the consistency that is obtained by using the same APS for the master

acquisition in all interferometric APS. However, this consistency has the drawback of systematic effects in the final results in case of prediction errors. Therefore, in DePSI the second option is applied, i.e., prediction of the interferometric APS directly. The bias due to errors in the master atmospheric signal are thereby assumed to be reduced.

The interferometric residuals at the first-order PS, which act as input for the APS prediction, are composed by

$$\begin{aligned}\underline{e}_{0i}^{0s} &= \varphi_{0i,S}^0 - \varphi_{0i,S}^s + \varphi_{0i,n}^0 - \varphi_{0i,n}^s, \\ &= \varphi_{0i,S}^{0s} + \varphi_{0i,n}^{0s},\end{aligned}\quad (5.14)$$

The residuals in Eq. (5.14) for $i = 1 \dots I$ are used as observations in the mathematical model for the prediction. The so-called *trend-signal-noise* model has the form (see Eq. (A.23))

$$\underbrace{\begin{bmatrix} \underline{e}_{01}^{0s} \\ \vdots \\ \underline{e}_{0i}^{0s} \\ \vdots \\ \underline{e}_{0I}^{0s} \end{bmatrix}}_{\underline{y}} = \underbrace{\begin{bmatrix} 1 & az_1 & r_1 \\ \vdots & \vdots & \vdots \\ 1 & az_i & r_i \\ \vdots & \vdots & \vdots \\ 1 & az_I & r_I \end{bmatrix}}_A \underbrace{\begin{bmatrix} S_{\text{off}}^{0s} \\ S_{\text{az}}^{0s} \\ S_r^{0s} \end{bmatrix}}_x + \underbrace{\begin{bmatrix} \varphi_{01,S}^{0s} \\ \vdots \\ \varphi_{0i,S}^{0s} \\ \vdots \\ \varphi_{0I,S}^{0s} \end{bmatrix}}_{\underline{s}} + \underbrace{\begin{bmatrix} \varphi_{01,n}^{0s} \\ \vdots \\ \varphi_{0i,n}^{0s} \\ \vdots \\ \varphi_{0I,n}^{0s} \end{bmatrix}}_{\underline{n}}, \quad Q_y = Q_s + Q_n, \quad (5.15)$$

where az, r are the radar image coordinates in azimuth and range direction, respectively, converted to coordinates in meters by the approximate ground spacing of the pixels. The parameters $S_{\text{off}}, S_{\text{az}}$ and S_r model a trend in the APS. This predictor is therefore equal to *Universal Kriging*. The covariance matrices Q_s and Q_n describe the covariance of the atmospheric signal \underline{s} and noise \underline{n} , respectively. When the orbital trend is estimated separately beforehand, see Section 5.2, the effect of the trend model in Eq. (5.15) cancels.

The mathematical model for the prediction of the atmospheric signal (plus trend) φ_{S+} at the yet unobserved points (i.e., higher-order candidate points) $p = 1 \dots P$ is

$$\underbrace{\begin{bmatrix} \varphi_{01,S+}^{0s} \\ \vdots \\ \varphi_{0p,S+}^{0s} \\ \vdots \\ \varphi_{0P,S+}^{0s} \end{bmatrix}}_{\underline{y}_0} = \underbrace{\begin{bmatrix} 1 & az_1 & r_1 \\ \vdots & \vdots & \vdots \\ 1 & az_p & r_p \\ \vdots & \vdots & \vdots \\ 1 & az_P & r_P \end{bmatrix}}_{A_0} \underbrace{\begin{bmatrix} S_{\text{off}}^{0s} \\ S_{\text{az}}^{0s} \\ S_r^{0s} \end{bmatrix}}_x + \underbrace{\begin{bmatrix} \varphi_{01,S}^{0s} \\ \vdots \\ \varphi_{0p,S}^{0s} \\ \vdots \\ \varphi_{0P,S}^{0s} \end{bmatrix}}_{\underline{s}_0} + \underbrace{\begin{bmatrix} \varphi_{01,n}^{0s} \\ \vdots \\ \varphi_{0p,n}^{0s} \\ \vdots \\ \varphi_{0P,n}^{0s} \end{bmatrix}}_{\underline{n}_0}, \quad Q_{y_0} = Q_{s_0} + Q_{n_0}. \quad (5.16)$$

The least-squares predictor of the atmospheric signal is (see Eq. (A.27))

$$\hat{\underline{y}}_0 = A_0 \hat{\underline{x}} + Q_{s_0} Q_y^{-1} (\underline{y} - A \hat{\underline{x}}), \quad (5.17)$$

with the estimator for the trend

$$\hat{\underline{x}} = (A^T Q_y^{-1} A)^{-1} A^T Q_y^{-1} \underline{y}. \quad (5.18)$$

The covariance matrix Q_{s_0s} describes the stochastic relation of the atmospheric signal between the observed and yet unobserved PS.

To construct the required covariance matrices Q_s , Q_n and Q_{s_0s} , a covariance function is needed for both the atmospheric signal and the noise. Assuming second-order stationary, a covariance function C can be derived from a variogram. In DePSI this covariance function is determined indirectly by estimating a variogram from the data. Assuming second-order stationary, the relation between the estimated variogram $V(d)$ and the required covariance function $C(d)$, which are functions of the distance d [m], is (Journel and Huijbregts, 1978)

$$V(d) = C(0) - C(d). \quad (5.19)$$

Although in a strict sense the trend in the mathematical model Eq. (5.15) suggests that the atmospheric signal (plus possible orbital error) may not be second-order stationary, for short distances this effect can be neglected, allowing the use of the relation above. Moreover, when the orbital trend was removed beforehand (see Section 5.2), the likelihood of second-order stationarity increases.

The variogram is estimated by fitting an a-priori model, e.g., an exponential or Gaussian model, to an empirical variogram. The fit is based on a least-squares curve fitting approach, after initialization with approximate values. Alternative to a exponential or Gaussian model, a more advanced model could be applied, e.g., based on the Matern class of models (Grebentcharksky and Hanssen, 2005). By addition of a *nugget* to the model, that is, an additional term at $d = 0$, both the atmospheric and the noise contribution can be parameterized simultaneously. Due to the nugget the prediction at a PS will not coincide with the observation, thereby separating the noise from the atmospheric signal. The precision of the prediction error is described by the covariance matrix (see also Section A.3)

$$Q_{\hat{\epsilon}_0} = Q_{y_0} - Q_{s_0s}Q_y^{-1}Q_{ss_0} + (A_0 - Q_{s_0s}Q_y^{-1}A)Q_{\hat{x}}(A_0 - Q_{s_0s}Q_y^{-1}A)^T. \quad (A.30)$$

The practical implementation of BLUP to estimate the APS is based on a division of the full crop in grid cells. For each grid cell the closest PS of the first-order network is selected and used as observation. By default the closest 100 PS within a maximum distance of 10 km are used.

Once the Atmospheric Phase Screens per interferogram are estimated, the interferometric phases of the first-order and higher-order PSC are corrected and the first-order network algorithm is repeated, see Figure 3.1. Because the noise level of PSC which were rejected before the atmospheric correction will also be reduced, the number of detected PS in the new first-order network may increase. Thereby a stronger network is obtained. Because the Variance Component Estimation step is also repeated, the stochastic model used for the estimations is updated as well. Based on the new first-order network, higher-order PS are detected within the densification step.

5.4 PS densification

After ambiguity resolution and parameter estimation of the first-order PS (PS1), the second-order PS (PS2) are detected. This detection is based on densification of the

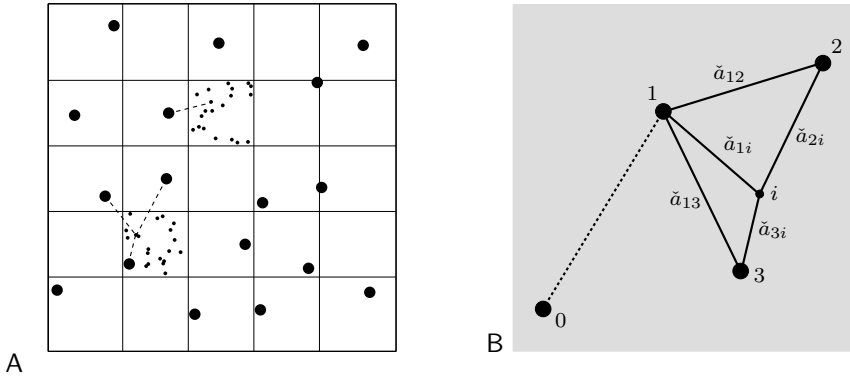


Figure 5.2: A) Detection of second-order PS (small dots) by densification of the first-order network (big dots). A grid is used for computational benefits and to enable distribution of the computations among multiple processors. The second-order PS can either be connected to the closest or a specified number of closest PS1. The latter enables a test on the estimated ambiguities. B) Situation in case the second-order PS is connected to the three closest PS1.

first-order network. Equivalent to the algorithm applied to construct the network, in the densification also a temporal ambiguity resolution and a spatial ambiguity resolution step can be distinguished.

The temporal ambiguity resolution is based on double-difference phase observations between second-order Persistent Scatterer Candidates (PSC2) and close-by PS1, see also Appendix B. To enable testing in the spatial ambiguity step, each PSC2 is connected to a specified number of closest PS1. The default value is three connections. When no testing is desired, only one connection is applied. The full set of PSC2 is subdivided by a grid, see Figure 5.2A. Per grid cell the closest PS1 are determined, which reduces the computational load. Moreover, the grid enables a potential distribution of the computations in the densification step among multiple processors.

The same techniques for temporal ambiguity resolution can be used as previously applied for the first-order network, i.e., integer least-squares, bootstrapping or the ambiguity function, see Chapter 4. Again the ambiguity resolution is based on a functional model, which can be chosen independently of the one used for the first-order network. Because the arcs in the densification step are in general shorter compared to those in the first-order network, the likelihood of a complicated deformation behavior is smaller. Therefore, a more simplistic model, i.e., with less parameters, may be chosen for the densification.

After the ambiguities are resolved in time, in case three connections are applied, a test is performed to decide whether a PSC2 is indeed a coherent point. Provided that the double-difference phase observations are not re-wrapped (see Section 5.1.1), the ambiguities of the three resolved arcs should form a closed network. Using Figure 5.2B, the following equality is derived for PSC2 *i*

$$\check{a}_{1i} = \check{a}_{12} + \check{a}_{2i} = \check{a}_{13} + \check{a}_{3i} \quad (5.20)$$

where $\check{a}_{12}, \check{a}_{13}$ are estimated and tested within the first-order network. Based on the as-

sumption that the ambiguities of coherent points can be unwrapped correctly, the PSC2 is accepted when the equality holds for all ambiguities in the time series. Alternatively, a less strict criterion can be applied by requiring that minimally two out of three solutions are equal. The criteria above apply to the full time series. However, application to real data shows that sometimes only one or a few ambiguities per time series show deviating values (Samiei-Esfahany, 2008). Therefore an alternative approach has been implemented, based on the most occurring solution for a certain ambiguity, hence the *mode* solution.

For the mode solution more than three connections can be used, increasing the reliability of the final solution. When N is the number of occurrences of a certain ambiguity mode value and N_{conn} is the total number of connections, an ambiguity within the time series of a certain PS is accepted when

$$\text{accept } \hat{a}_{ij}^{0s} \text{ if } N > \left\lfloor \frac{N_{\text{conn}}}{2} \right\rfloor, \quad (5.21)$$

where $\lfloor \cdot \rfloor$ indicates the floor of the value. Hence, when three connecting arcs are used, at least two solutions should be the same for each ambiguity in the time series. When for example four arcs are used, this increases to a minimum of three similar estimates.

Once the ambiguities are resolved (and tested), the unwrapped phase of the detected PS2 $\underline{\phi}_{0i}^{0s}$ is calculated with respect to the reference PS by

$$\underline{\phi}_{0i}^{0s} = 2\pi(\check{a}_{01}^{0s} + \check{a}_{1i}^{0s}) + \underline{\varphi}_i^{0s} - \underline{\varphi}_0^{0s}, \quad (5.22)$$

for slave $s = 1 \dots S$, where $\underline{\varphi}_i^{0s}, \underline{\varphi}_0^{0s}$ are the interferometric phases. Again, the difference between these phases should not be re-wrapped to be consistent with the resolved ambiguities.

Based on the unwrapped phases the parameters of interest are estimated using the same functional model as used for the first-order PS, e.g., Eq. (5.10). Note that this model, as in case for the first order PS, can be different compared to the model used for the temporal ambiguity resolution. The stochastic model involved in the estimations is the one previously used for the PS1, which is obtained by Variance Component Estimation, see Section 4.4. The variance factor $\hat{\sigma}^2$ is estimated for each PS2 as well to adapt the stochastic model to the specific coherence level of the PS. The variance factor is estimated by (see Eq.(5.11), which is repeated here for convenience)

$$\hat{\sigma}^2 = \frac{\hat{\underline{e}}^T Q_y^{-1} \hat{\underline{e}}}{m - n}. \quad (5.11)$$

Hereby, the parameters of interest are obtained for each detected PS, together with a covariance matrix describing their precision. This is the main output of DePSI. Next step is the georeferencing of the PS, to enable analysis of the results and integration with other data sources, see Chapter 6.

5.5 Summary

The spatial ambiguity resolution is based on a spatial integration using a testing scheme to remove incoherent Persistent Scatterer Candidates (PSC) and to remove or adapt

ambiguity errors in the arcs between PSC. The testing is based on the ambiguities directly. This innovative approach is possible when the differential phase observations between two PSC are not re-wrapped to the $[-\pi, +\pi)$ interval. In this case, a closing network of ambiguities should be obtained.

A two-step testing procedure is applied. First, the incoherent PSC and arcs with a large number of ambiguity errors are detected and removed based on the full set of ambiguities per arc. The B-method of testing (Baarda, 1968) is used to determine the largest error in each iteration, regardless whether it originates from an ambiguity error or an inconsistent point. Once the remaining errors in the network result in a test statistic below a threshold, thereby assuming that maximally only a few ambiguity errors per arc remain, the second step of the algorithm is applied. In this step, ambiguity inconsistencies in the network are adapted until a closing network is obtained. Here, the testing of the network is applied to each interferogram separately.

This procedure is an alternative approach compared to the method applied in Kampes (2006), where the removal of arcs and inconsistent PSC is based on the testing of the parameters of interest, combined with an additional Minimum Cost Flow (MCF) algorithm to resolve the remaining ambiguity errors. The advantage of the ambiguity removal and adaptation approach applied here is that the same mathematical framework is used for both steps. Moreover, the concept of testing of the ambiguities enables the use of a varying deformation model for each arc. Whereas the estimated parameters of interest using different models will result in closing errors in the network, thereby obscuring the detection of inconsistencies, the ambiguities, and thereby the unwrapped phase, should preserve a consistent network. Hence, the model used can be adapted to local deformation phenomena, see Chapter 7.

The spatial ambiguity resolution is repeated in an iterative scheme. After each iteration, a phase screen of a certain signal is estimated and removed from the phase observations. Hence, based on the most recent tested first-order network, the Orbital Phase Screen (OPS), Atmospheric Phase Screen (APS), and Deformation Phase Screen (DPS, see Section 7.4) is estimated. Regarding the OPS, a linear trend for each interferogram is assumed, which is estimated based on a least-squares estimation procedure including outlier detection. The APS is retrieved in a two-step procedure. First, for each arc the remaining unmodeled deformation signal is separated from the atmospheric phase signal and noise based on a low-pass filter in the time domain. Second, least-squares prediction is applied to predict the APS for each interferogram, thereby applying a low-pass filter in the spatial domain to remove the noise. Once a phase screen is removed from the phase observations and their stochastic model is updated based on variance-covariance estimation, see Section 4.4, the first-order network is resolved again. Previously removed PSC are evaluated again, since the correction by the phase screen may have improved the estimation of the ambiguities of the connecting arcs. Hereby, the assumption is made that a higher density of PS in the first-order network will improve the overall quality of the final PS result.

Once the phase observations are corrected for all phase screens, the first-order network is densified to detect more PS. Again integer least-squares, integer bootstrapping or the ambiguity function can be applied to estimate the phase ambiguities and the parameters of interest. The higher-order PSC are connected to at least three neighboring PS of the network. The independent solutions of the ambiguities per PSC are evaluated for consistency. Three strategies are implemented. The first strategy enforces that all

three solutions are equal. Hence, already with a single deviating ambiguity in one of the three connecting time series, the PS is rejected. A less strict approach requires two out of the three solutions to be equal. An alternative strategy is based on the mode of the estimated ambiguities. Here, for each ambiguity in the time series the mode solution is adopted, provided that a minimum number of occurrences of a certain solution is ensured for each ambiguity in the time series. This approach is less strict, and enables the use of more than three connecting arcs.

After the densification step, a set of selected PS is obtained. Despite the testing strategies, some PSC may erroneously be identified as PS, the so-called *false detections*. Therefore an additional selection step is often applied, based on a quality indicator and an accompanying threshold. These quality indicators are presented in Chapter 6. In Chapter 6 also the procedure for the geolocalization of the PS is discussed, together with a quality assessment.

This chapter covers the quality aspects of DePSI. Both the quality of the estimated PS results and the accuracy of georeferencing of the PS are discussed. Section 6.1 describes the procedure of georeferencing and the factors influencing the accuracy, including an assessment of their contribution in the total error budget. Section 6.2 gives an overview of quality indicators that can be used to describe the quality of the PS results, including the newly developed spatio-temporal consistency (STC). Section 6.3 discusses the reliability assessment of the PSI results based on internal and external reliability checks. A summary is given in Section 6.4.

6.1 Georeferencing

6.1.1 Georeferencing procedure

Once the PS are detected and the parameters of interest are estimated, the PS can be georeferenced. Georeferencing is only possible at this stage, because the estimated height of the PS is required. This height not only influences the vertical component of the 3D position, but, due to the slanted look angle of the radar signal, also the horizontal position. Together with the image coordinates in azimuth and range direction, and the orbit parameters of the master image, the corresponding longitude, latitude and height of the PS in an earth-fixed reference system, represented by an ellipsoid, are calculated.

For georeferencing the absolute heights H_i of the PS P_i with respect to the reference ellipsoid are required, where i indicates a specific PS. As visualized in Figure 6.1, the absolute height can be written as

$$H_i = N_i + h_i + \Delta h_i, \quad (6.1)$$

where N_i is the geoid undulation, h_i is the Digital Elevation Model (DEM) height (assuming that the DEM is defined with respect to the geoid), and Δh_i is the DEM error or *residual height*. A similar expression holds for the height H_0 of the reference PS P_0 ,

$$H_0 = N_0 + h_0 + \Delta h_0. \quad (6.2)$$

These heights are retrieved by a combination of external data and the height difference H_{0i} between the PS and the reference PS, which is estimated in the DePSI analysis. The height difference is defined as

$$H_{0i} = H_i - H_0. \quad (6.3)$$

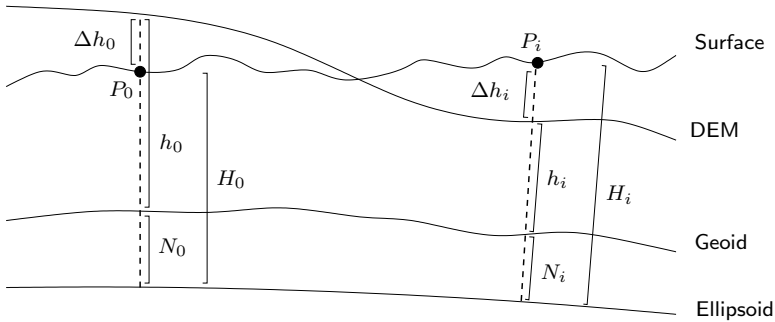


Figure 6.1: Reference surfaces involved in the georeferencing process. Finally the height above the ellipsoid H_i is required for each PS P_i . An error in the DEM height at the reference point P_0 , Δh_0 , causes a bias in all derived heights H_i , affecting the geolocalization with an offset. The DEM height h is either specified with respect to the geoid, in which case the geoid undulation N should be incorporated, or directly to the ellipsoid.

To obtain the absolute height of the PS, three cases can be distinguished, depending whether or not a DEM is used to remove the topographic phase prior to the DePSI analysis: 1) no DEM is used, 2) a DEM with respect to the geoid is used, and 3) a DEM with respect to the WGS84 ellipsoid is applied.

1. **No prior DEM used.** DePSI can be applied without a-priori removal of the topographic phase. Especially in flat terrain, where the height differences over a typical arc length are small, this pre-processing step may not be necessary. However, already in terrain with moderate height differences of 50 m, correction of the topographic phase is beneficial since the success rate of correct phase ambiguity resolution and thereby the detection of PS is improved.

When no a-priori DEM correction is applied, the estimated height difference \hat{H}_{0i} represents the difference between the two absolute heights involved, hence

$$\hat{H}_{0i} = (N_i + h_i + \Delta \hat{h}_i) - (N_0 + h_0 + \Delta \hat{h}_0). \quad (6.4)$$

Based on this estimate, combination of Eqs. (6.1), (6.2), and (6.4) shows that the absolute height of P_i is obtained by

$$\hat{H}_i = \hat{H}_{0i} + N_0 + h_0 + \Delta \hat{h}_0. \quad (6.5)$$

Hence, the geoid undulation and DEM height with respect to the geoid of the reference PS, obtained from external data, should be added to all estimated differential heights to obtain height values with respect to the ellipsoid. The last term in Eq. (6.5), the DEM error at the reference point, remains however unknown, causing a bias in the georeferencing result, see Section 6.1.2.

2. **DEM with respect to geoid used.** For many areas the prior correction of the topographic phase based on a DEM is beneficial. DEM's are often defined with respect to a geoid to provide a physical meaning of the heights. An example is

the DEM acquired by the Shuttle Radar Topography Mission (SRTM) (Farr et al., 2007), which is defined in relation to the EGM96 geoid.

When a DEM with respect to the geoid is subtracted, Eq. (6.4) is modified to

$$\hat{H}'_{0i} = (N_i + \Delta\hat{h}_i) - (N_0 + \Delta\hat{h}_0). \quad (6.6)$$

Hence, only the geoid undulation and DEM error terms remain. Here, the absolute heights H_i is retrieved, combining Eqs. (6.1) and (6.6), by

$$\hat{H}_i = \hat{H}'_{0i} + h_i + N_0 + \Delta\hat{h}_0. \quad (6.7)$$

As the equation shows, in this situation the previously removed DEM height of the individual PS h_i and the geoid undulation of the reference PS are required. Since the undulation can reach values over 100 m (Rapp, 1997), neglect of this term may lead to a bias in the georeferencing of hundreds of meters. Again, the DEM error at the reference point remains unknown.

3. **DEM with respect to ellipsoid used.** In case the topographic phase is removed based on a DEM with respect to the ellipsoid, i.e., $N_0=N_i=0$, the estimated height comprises

$$\hat{H}''_{0i} = \Delta\hat{h}_i - \Delta\hat{h}_0. \quad (6.8)$$

Hence, the estimated height difference reflects the differential DEM error. Based on this estimate, the absolute height H_i is retrieved, combining Eqs. (6.1) and (6.8), by

$$\hat{H}_i = \hat{H}''_{0i} + h_i + \Delta\hat{h}_0. \quad (6.9)$$

Also here, the previously removed DEM height, including the undulation, should be added to retrieve the absolute height.

The retrieval of the absolute heights, as described by Eqs. (6.5), (6.7), and (6.9), have in common that the DEM error at the reference point remains unknown. Since this factor is equal for all PS, it causes a constant offset for the full PS dataset, see Section 6.1.2. Only when the height of the reference PS is known based on an additional measurement, this term can be corrected. Note that this reference point can be different compared to the reference PS applied during the PSI analysis, since the heights can be translated based on the relative height estimates.

Based on the absolute height H_i (Eq. (6.5), (6.7) or (6.9)) above the ellipsoid, together with the line l_i and pixel p_i image coordinates, the equivalent geographic coordinates with respect to the ellipsoid of each PS P_i can be calculated using the so-called *Doppler-Range-Ellipsoid equations* (Schwäbisch, 1995). These equations specify that

1. **Doppler:** P_i lies perpendicular to the orbit, hence

$$E_1 : \quad \dot{\vec{x}}_s \cdot d\vec{x}_i = 0. \quad (6.10)$$

2. **Range:** the geometric distance from P_i to the satellite is equal to the speed of light c times the range time t_r , hence

$$E_2 : \quad d\vec{x}_i \cdot d\vec{x}_i - (ct_{sr})^2 = 0. \quad (6.11)$$

3. **Ellipsoid:** P_i has a height H_i above the reference ellipsoid with semi-major and semi-minor axis a and b , respectively, hence

$$E_3 : \frac{x_i^2}{(a + H_i)^2} + \frac{y_i^2}{(a + H_i)^2} + \frac{z_i^2}{(b + H_i)^2} - 1 = 0, \quad (6.12)$$

with

$$d\vec{x}_i = \vec{x}_i - \vec{x}_s. \quad (6.13)$$

Here, $\vec{x}_i = (x_i, y_i, z_i)$ is the position vector of P_i , and $\vec{x}_s, \dot{\vec{x}}_s$ denote the position vector and velocity vector of the satellite during the master acquisition, respectively. The line l_i , in combination with the first azimuth time $t_{az,0}$ and the pulse repetition frequency (PRF), and the orbit parameters are used to calculate \vec{x}_s and $\dot{\vec{x}}_s$. The first range time $t_{r,0}$ together with the range sampling rate (RSR) are used to calculate the range time t_r for pixel p_i . The solution for \vec{x}_i cannot be obtained directly from Eqs. (6.10)–(6.12), but is estimated by iteration after linearization of these equations.

The linearized mathematical model has the form (Kampes, 1999)

$$E\{\Delta\underline{y}\} = \partial_x A(x^j)\Delta x, \quad (6.14)$$

where

$$\partial_x A(x^j) = \begin{bmatrix} \frac{\partial E_1(x^j)}{\partial x} & \frac{\partial E_1(y^j)}{\partial y} & \frac{\partial E_1(z^j)}{\partial z} \\ \frac{\partial E_2(x^j)}{\partial x} & \frac{\partial E_2(y^j)}{\partial y} & \frac{\partial E_2(z^j)}{\partial z} \\ \frac{\partial E_3(x^j)}{\partial x} & \frac{\partial E_3(y^j)}{\partial y} & \frac{\partial E_3(z^j)}{\partial z} \end{bmatrix} = \begin{bmatrix} \dot{x}_s & \dot{y}_s & \dot{z}_s \\ 2dx^j & 2dy^j & 2dz^j \\ \frac{2x^j}{(a+H_i)^2} & \frac{2y^j}{(a+H_i)^2} & \frac{2z^j}{(b+H_i)^2} \end{bmatrix}, \quad (6.15)$$

and

$$\Delta\underline{y}^j = \underline{y} - A(x^j). \quad (6.16)$$

The estimator of the incremental unknown Δx is

$$\Delta\underline{\hat{x}}^{j+1} = ((\partial_x A(x^j))^T \partial_x A(x^j))^{-1} (\partial_x A(x^j))^T \Delta\underline{y}^j. \quad (6.17)$$

Thereby, the estimator of the coordinates for P_i is obtained by

$$\underline{\hat{x}}^{j+1} = \underline{\hat{x}}^j + \Delta\underline{\hat{x}}^{j+1}, \quad (6.18)$$

where j indicates the iteration step. In DePSI the iteration continues until the increment $\Delta\underline{\hat{x}}^{j+1}$ becomes smaller than 1 mm. The estimations are initiated with approximated values $x^{j=0}$. Here, the center coordinates of the master SLC image are taken. Note that the same algorithm is used in DORIS (Kampes and Usai, 1999; Kampes et al., 2003) to compute the flat Earth reference phase and topographic phase, see Section 3.2.5.

The estimation is repeated for each PS individually. Once the coordinates are obtained, they can be used to visualize the results or integrate them with other data. For the interpretation of the results, especially in case of very localized deformation effects, the accuracy of the georeferencing is of importance (Chang and Hanssen, 2012, 2014).

6.1.2 Georeferencing accuracy

The accuracy of the georeferencing is dependent on the accuracy of the orbit and image parameters, such as the first range time $t_{r,0}$ and first azimuth time $t_{az,0}$, and the estimated heights \hat{H}_i of the PS. Since the number of observations and the number of unknowns in the mathematical model in Eq. (6.14) is equal, a unique solution is obtained. As a consequence, an error in the input parameters or the height of the PS propagates directly to the georeferencing. Here, two effects can be distinguished: errors that apply to individual PS and errors applying to all PS.

Errors applying to individual PS

The effects that influence the geolocation of individual PS are an error in the height estimate and the uncertainty in the sub-pixel position. Both effects are discussed in detail below.

1. **An error in the relative height estimate H_{0i} .** Since these estimates are performed per PS with respect to the reference PS, and assuming that no errors are propagated within the first-order network, no systematic effects are expected. Hence, the precision of the height estimates σ_H [m] propagates directly to the precision of the georeferencing expressed in ground range $\sigma_{R_{gr}}$

$$\sigma_{R_{gr},i} = \frac{\sigma_H}{\tan \theta_{inc,i}}, \quad (6.19)$$

where $\theta_{inc,i}$ is the local incidence angle, see Figure 3.8. Figure 6.2 shows the influence of a height error of 1 m for a range of incidence angles. Assuming a typical precision of the height estimates of 0.5–1 m for a data stack of C-band data (Ferretti et al., 2000; Colesanti et al., 2003b), the geolocation precision for Envisat (incidence angle of $\sim 23^\circ$), in relation to the height inaccuracy, is in the order of 2 m in the ground range direction. An inter-comparison of the heights obtained by four different processing chains (Crosetto et al., 2008) revealed a height standard deviation ranging between 0.9 - 2.0 m. This results in a geolocation precision in range direction of 2.1 - 4.7 m. These relatively high values may partly be explained by neglectation of the range sub-pixel position, which also influences the height estimate, see next item.

2. **Uncertainty in the sub-pixel position.** The effective scattering center of the PS lies somewhere within an image pixel, as discussed in Section 4.2.4. Due to the correlation with the height of the PS, and the typically low range of Doppler centroid variation in the image stack, the sub-pixel position cannot be estimated from the phase. Instead, an estimate of the scattering center can be based on the amplitude response.

When this sub-pixel position is not considered, or the scattering center cannot be determined accurately, the georeferencing is affected. Two effects can be distinguished: the direct and the indirect effect.

- **Direct effect.** Without taking the sub-pixel position into account, the leading edges of the pixel l_i, p_i are used in the georeferencing process, see Figure 6.3. Application of l_i and p_i instead of the actual pixel coordinates l_{ξ_i}

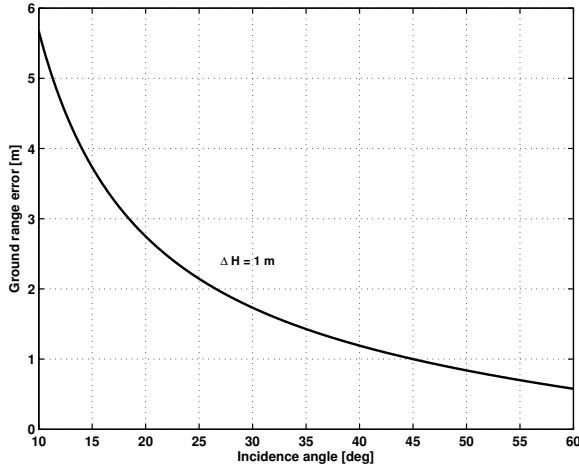


Figure 6.2: Georeferencing error in ground range [m] due to a height error ΔH of one meter. The ground range error is dependent on the incidence angle. The effect scales linearly, hence the ground range error shown here can be multiplied with any height error to obtain the corresponding actual ground range error.

and p_{η_i} directly results in a geolocation error. The effect in range direction is visualized in Figure 6.4. The actual location of P_i , with a projection to P'_i on the ellipsoid, is georeferenced to $P'_{i,dir}$. Since often, based on an aerial photograph, a manual shift in the geocoding is applied to account for the effects influencing all PS (Bateson et al., 2010), it can be assumed that, after the shift, on average the PS are positioned according to the center of the pixels. Based on the assumption that the sub-pixel positions of the PS are uniformly distributed, the remaining mean absolute error is 25% of the pixel spacing, both in azimuth and in range direction. For example, assuming a factor two oversampled dataset of Envisat stripmap data, resulting in a pixel spacing of about 10 m in range and 2 m in azimuth, a corresponding mean direct georeferencing error of 2.5 m and 0.5 m is obtained, respectively.

- **Indirect effect.** In range direction, the sub-pixel position of the effective point scatterer also causes an indirect effect due to an inaccuracy in the flat Earth reference phase correction applied, see Section 4.2.4. The reference phase is calculated based on the leading edge coordinates l_i and p_i , whereas the phase observation is related to the actual position of the point scatterer. The phase error due to a positive sub-pixel position η_i results in a negative height error ΔH (see Eq. (4.32) in Section 4.2.4)

$$\Delta H_i = -\cos \theta_{inc,i} \sin \theta_{inc,i} \eta_i, \quad (6.20)$$

where θ_{inc} is the local incidence angle. A height error results into a georeferencing error, measured in ground range ΔR_{gr} , of

$$\Delta R_{gr,i} = \frac{\Delta H_i}{\tan \theta_{inc,i}}. \quad (6.21)$$

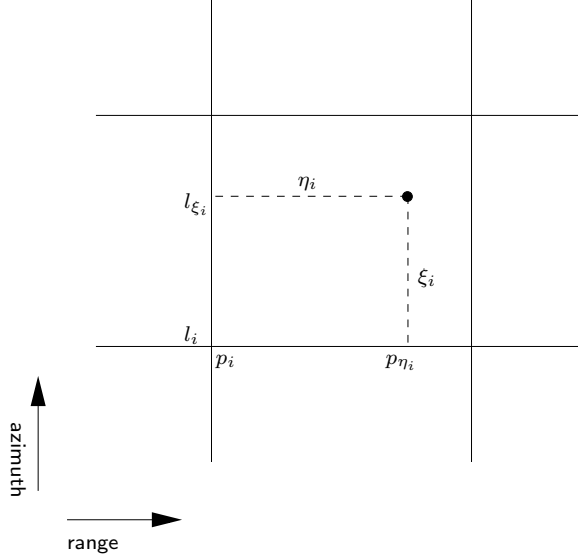


Figure 6.3: Influence of the sub-pixel position on the georeferencing of a PS. Without taking the sub-pixel position (l_{ξ_i}, p_{η_i}) into account, the pixel coordinates of the leading edge l_i and p_i are used. The difference is directly translated into a georeferencing error.

Combination of Eqs. (6.20) and (6.21) gives the georeferencing error as function of the uncompensated sub-pixel position in range direction as

$$\Delta R_{gr,i} = -\cos^2 \theta_{inc,i} \eta_i. \quad (6.22)$$

Hence, when the sub-pixel position of the point scatterer is not accounted for, apart from the direct error η_i , an additional indirect effect with a factor $-\cos^2 \theta_{inc,i}$ applies. The shifted position is indicated in Figure 6.4 with $P_{i,ind}$. The total shift of both the direct and indirect effect due the same sub-pixel position is represented by $P_{i,dir+ind}$.

The situation shown in Figure 6.4 is based on the assumption that the location of the reference PS P_0 corresponds to the leading edge of the pixel in which it resides. However, unlike the direct error, the indirect effect is dependent on specific sub-pixel location of the reference PS. This is due to the estimated height, which is determined relative to the reference point. As a result, the size of the error is dependent on the specific reference point used. Therefore, the relative sub-pixel position $\Delta \eta_i$ should be considered

$$\Delta \eta_i = \eta_i - \eta_0, \quad (6.23)$$

where η_0 is the sub-pixel position of the reference PS, which applies to all PS. For the individual PS, again a mean absolute error of 25% of the range pixel spacing can be adopted. For the same factor two oversampled Envisat stripmap dataset, resulting in a range pixel spacing of 10 m, and an incidence angle of 23° , this leads to a mean indirect georeferencing error in range direction of 2.1 m. Since the direct and indirect effect operate in the same

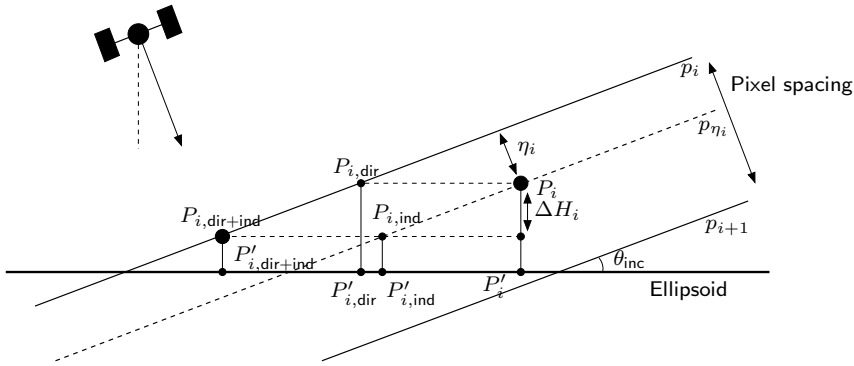


Figure 6.4: Influence of the sub-pixel position in range direction. Both a direct and an indirect effect occur. The true position of the PS P_i (mapped to P'_i) is geolocated to $P_{i,dir}$ due to neglect of the sub-pixel position η_i . Apart from this direct effect, an indirect effect occurs due to a wrong flat Earth reference phase applied. This erroneous phase causes a height error ΔH_i , translating in the position $P_{i,ind}$. The sum of the two effects leads to the final position $P_{i,dir+ind}$.

direction, see Figure 6.4, the total effect of an uncompensated sub-pixel position results in a mean error of 4.6 m for Envisat data.

The examples for Envisat data show that neglect of especially the sub-pixel position in range direction results in a geolocation error of 4.6 m. In addition to the influence of an error in the estimated height of 0.5–1 m, corresponding to a location shift of 1–2 m, this is a considerable effect. Depending on the Signal-to-Clutter ratio (SNR) of the point scatterer it may be possible to estimate the sub-pixel location of the scatterer based on the amplitude information.

Errors applying to all PS

Apart from factors that affect individual PS, there are also factors influencing the geolocation of all PS. These factors are 1) an error in the absolute height of the reference PS, 2) an error in the satellite orbit parameters, 3) an image timing error, 4) an uncertainty in the sub-pixel position of the reference PS, 5) atmospheric signal delay, and 6) geophysical influences. These effects are discussed below.

1. **Height error of reference PS.** The estimated heights \hat{H}_i of all PS are dependent on the DEM error at the reference PS ΔH_0 , see Eqs. (6.5), (6.7), and (6.9). This error depends on the precision of the reference DEM used and whether the DEM describes the layer with the PS reflection point, i.e., a surface model (DSM, including objects) or a terrain model (DTM, excluding objects). The georeferencing error measured in ground range ΔR_{gr} due to the DEM error ΔH_0 is equal to

$$\Delta R_{gr} = \frac{\Delta H_0}{\tan \theta_{inc}}, \tag{6.24}$$

where θ_{inc} is the local incidence angle. The effect of a 1 m reference height error for a range of incidence angles is visualized in Figure 6.2. When for example the radar-based SRTM DEM is used with a standard deviation of the absolute heights

of 6.2 m (Farr et al., 2007), this leads to a geolocalization error for an Envisat dataset, with an incidence angle of 23° , of 14.6 m. This error can be avoided when a co-located GNSS measurement is available for the reference PS.

2. **Orbit errors.** Errors in the satellite orbit parameters can either be in range direction (radial orbit error) or in azimuth direction (along-track orbit error) (Scharroo and Visser, 1998; Bähr, 2013). Using precise orbits the accuracy of the orbits can be assumed to be better than for example 10 cm for ERS-1/2 and Envisat (Scharroo and Visser, 1998; Otten and Dow, 2005) and 4.2 cm for TerraSAR-X (Yoon et al., 2009; Eineder et al., 2011). Bähr (2013) gives a general overview of the orbit accuracies for different radar satellites. The orbit errors directly influence the georeferencing accuracy, however, the effect is relatively small.
3. **Image timing errors.** Both in the along-track direction (slow-time) as in the across-track direction (fast-time) an error can be made in the time annotation. In along-track direction this corresponds to an error in the time of radar pulse transmission, which cannot be distinguished from along-track orbit errors. In across-track direction, the signal travel time to the first range pixel could be biased due to delays in the SAR instrument (Eineder et al., 2011).
4. **Sub-pixel position of reference PS.** It was shown that the relative sub-pixel position $\Delta\eta_i$ (Eq. (6.23)) causes an error for individual PS, see Figure 6.4. However, since these relative positions are all relative to the sub-pixel position of the reference PS η_0 , a general shift applies to all PS. In effect, all estimated heights H_0^i have a bias due to the erroneous reference phase applied to the reference PS, resulting in a location shift. Equation (6.22) can be used to transform the sub-pixel position of the reference point to the associated offset. For an Envisat dataset with an oversampled range spacing of 10 m and incidence angle of 23° , a sub-pixel position of 5 m leads to a shift for all PS of 4.2 m.
5. **Atmospheric signal delay.** The geolocation procedure based on the Doppler-Range-Ellipsoid equations presented in Section 6.1.1 is based on the speed of light c in vacuum. However, the atmosphere reduces the effective speed of the radar signal, causing delays, see Section 2.1.2. These effects should be compensated. The radar frequency dependent ionospheric zenith delay ranges from 0.02 to 0.4 m for X-band and 1.2 to 25 m for L-band data, depending on the Total Electron Content (TEC) of the ionosphere (Hanssen, 2001; Eineder et al., 2011). The specific TEC value varies between day and night, and between periods of solar minimum and maximum (Odijk, 2002). Published TEC maps can be used to obtain an estimate of the electron content at a certain time and location (Eineder et al., 2011). Using a mapping function (Herring, 1992; Niell, 1996), the zenith delays can be transformed to the radar Line of Sight (LOS).

The delay due to the troposphere consists of a hydrostatic part, which is dependent on the pressure and temperature, and a wet part, which is mainly caused by water vapor. The zenith hydrostatic delay in the order of 2.3 m and is relatively constant. The zenith wet delay is limited to values below 0.35 m (Bevis et al., 1992), but strongly variable. Using a mapping function (Herring, 1992; Niell, 1996), the zenith delays can be transformed to the radar Line of Sight (LOS).

6. **Geophysical effects.** Various geophysical effects change the shape of the Earth, thereby affecting the positioning of PS. Examples are Earth tides, polar motion, tidal ocean loading, atmospheric loading, and hydrological loading (Eineder et al., 2011). This paper also provides estimates of the size of the deformation due to the various processes. The Earth tides due to gravitational forces of the Sun and the Moon can cause deformation of up to 40 cm in vertical direction and several centimeters in horizontal direction. The polar motion cause changes up to 25 mm in vertical and 7 mm in horizontal direction. The ocean loading has the strongest effect in coastal regions and in areas with a large tidal range, and can affect the height of the surface with several centimeters. Atmospheric loading can cause height differences of up to 2 cm. The hydrological loading effect is typically several millimeters, with a maximum of 2 cm. Apart from the hydrological contribution, the geophysical effects can largely be compensated based on available models.

The total of the effects described can result in shifts of tens of meters. The contributing error sources affect both the vertical and horizontal position components. A large part of the error can however be circumvented by estimation of the sub-pixel position of the scatterer, and the application of the flat Earth reference phase (Eq. 2.6) according to this position. Moreover, models or nearby GNSS measurements can be used to compensate a large part of the atmospheric and geophysical effects. Eineder et al. (2011) reach a positioning accuracy of several centimeters for a number of corner reflectors based on TerraSAR-X data. Although the application of these modeled corrections is preferable, an alternative approach is to apply a manual shift based on an overlay of the PS on an ortho-rectified aerial photograph or satellite image (Bateson et al., 2010).

6.2 Quality indicators

Based on the testing schemes in DePSI (see Sections 5.1 and 5.4) a selection of the Persistent Scatterer Candidates (PSC) is detected as Persistent Scatterers. However, a number of falsely detected PS will remain, i.e., a point which is either not coherent, or has, despite its coherence, an incorrectly estimated deformation time series. These false detections are caused by the situation that, by coincidence, for a number of these PSC the connecting arcs within the network result in the same erroneous solution. As a consequence, they are not detected by the ambiguity testing algorithms. These falsely detected PS are denoted as type-II errors, see also Section A.2.

To remove the falsely detected PS from the final dataset, additional quality indicators can be used to perform a further selection. Besides a criterion for selection, these quality indicators can also be used to describe the quality of the PS finally obtained. Various quality indicators exist, each with their own characteristics. The ensemble coherence estimator, the variance factor, the covariance matrix of the parameters of interest, the standard deviation of the displacements, the Ambiguity Dispersion of Precision (ADOP), and the spatio-temporal consistency are described here. They are all based on the deformation time series. Here it is assumed that amplitude information was already used to make a pre-selection resulting in the set of PSC, see Section 3.3.1. However, these amplitude-based selection criteria could also be applied at this final selection stage to obtain a further refinement.

The PSI results based on a set of ERS-1/2 data of Las Vegas, USA, are used to

give an example of the various quality indicators, see Figures 6.7a and 6.7b. The results are obtained using the integer bootstrap estimator and a linear deformation model. The same dataset will also be used in Chapter 7 to evaluate different processing strategies to increase the number of detected PS. The case study area is further described in Chapter 7. Here, the results are only used to illustrate the different quality indicators.

6.2.1 Ensemble coherence estimator

The ensemble coherence estimator is a metric to describe the deviation between the deformation time series and the deformation model estimated. The same measure is used by the ambiguity function to select the optimal model solution, see Section 4.6. Both an unweighted and a weighted coherence estimator can be applied. Here, the unweighted ensemble coherence estimator is considered, which is defined as

$$\begin{aligned}\hat{\gamma} &= \left| \frac{1}{S} \sum_{s=1}^S \exp(j(\underline{\varrho}_{0i}^{0s} - \varphi_{0i,\text{model}}^{0s})) \right|, \\ &= \left| \frac{1}{S} \sum_{s=1}^S \exp(j(\underline{\varrho}_{0i}^{0s})) \right|,\end{aligned}\quad (6.25)$$

where S is the number of slave images, $\underline{\varrho}_{0i}^{0s}$ the double-difference phase observations between PS i and the reference PS, φ_{model} the model phase, and $\underline{\varrho}$ are the least-squares phase residuals. The coherence estimator $\hat{\gamma}$ ranges between 0 and 1. A zero coherence indicates complete noise, whereas a value of 1 corresponds to a perfect match between the deformation model used and the deformation time series. The coherence value represents the scattering noise, unmodeled atmospheric signal delay, and the unmodeled part of the deformation. Often a linear deformation model is used, but in principle any model can be applied. By using a more advanced deformation model, the effect of unmodeled deformation on the coherence should be reduced, giving a better representation of the scattering noise. However, a dependency of the parametric deformation model always remains.

The standard ensemble coherence estimator is defined for a PS relative to the reference PS. Since the reference PS is selected based on assumed minimal scattering noise, the coherence value represents primarily the scattering noise level of the PS involved, atmospheric signal delay and the unmodeled deformation. Since the relative error in atmospheric signal delay increases with increasing distance from the reference point, the spatial distribution of coherence values suggest a decrease in quality in relation with the distance to the reference point, see Figure 6.5. This is a correct conclusion when strictly observing the deformation time series with respect to the reference point. However, in a local sense the measurement quality of PS is homogeneous over the full area analyzed.

To assess the local quality of the PSI estimates, an alternative quality indicator is the *local coherence estimator*. Here, the coherence is determined with respect to a local PS, for instance the closest point of the primary network. Disadvantage of the local coherence estimator is that the scattering noise of the network PS is likely higher compared to the reference PS, since the reference PS is chosen based on the lowest noise level of the connecting arcs in the network, see Section 5.1.2. Because the estimated coherence value obtained is based on a mixture of the scattering characteristics of the two PS involved, the noise level of the network PS will bias the coherence value of the

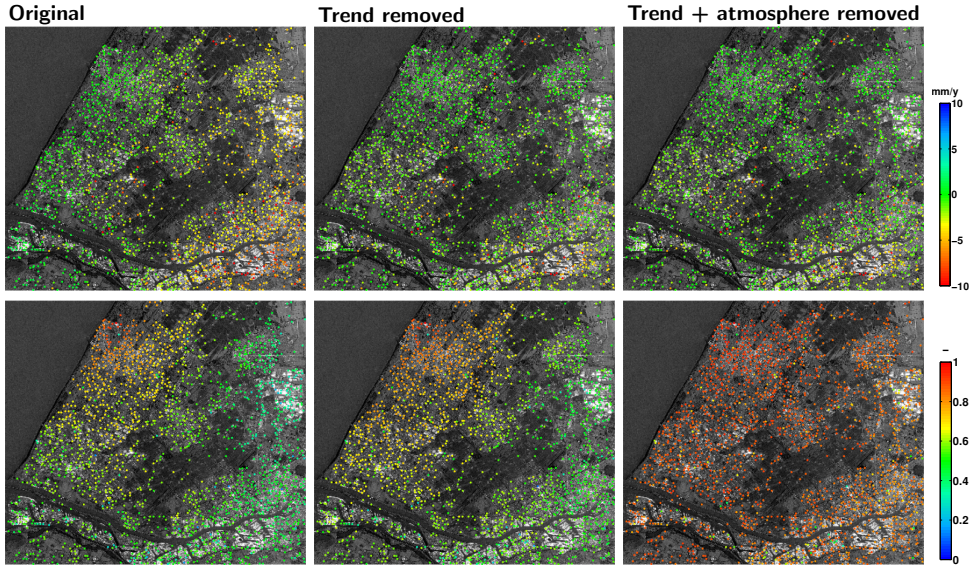


Figure 6.5: The effect of trends and atmospheric signal delay on the ensemble coherence with respect to the reference PS (top-left corner of area). A first-order network covering The Hague and Rotterdam in the Netherlands is shown based on Envisat data acquired between 2003 and 2010. Top row) linear deformation rates. Bottom row) ensemble coherence. The original data (left column) shows a trend in the deformation rates due to a drift in the local oscillator of the instrument (Marinkovic and Larsen, 2014), see Section 5.2. The ensemble coherence decreases with increasing distance to the reference PS due to the influence of the trends and atmospheric signal delay. When the trend per interferogram is removed (middle column, see Section 5.2) the coherence values are only slightly altered due to the correlation between the deformation rates and the time dependent drift of the oscillator. Hence, the phase residuals, and thereby the ensemble coherence, are only slightly changed. However, when the atmospheric signal delay is estimated and removed (right column), the distance dependency of the ensemble coherence is strongly reduced.

PS considered. This drawback can partially be circumvented by selecting the highest coherence value for a certain PS, when multiple connecting arcs are used. Examples of the global and local coherence estimates are given in Figure 6.7a.

A drawback of the coherence estimator (Eq. (6.25)) as a quality measure is that it is insensitive to phase unwrapping errors. Due to the cyclic nature of the phase residuals \underline{e}_{0i}^{0s} involved to compute the coherence, erroneous phase ambiguities are not reflected in the coherence value, see Figure 6.6 for an example.

6.2.2 Variance factor

The variance factor is a scaling factor of the covariance matrix used to describe the stochastic properties of the phase observations. The covariance matrix Q_φ is determined by variance component estimation (VCE), see Section 4.4, and is applied during ambiguity resolution and estimation of the parameters of interest of the PS. For each individual PS the phase residuals \underline{e} determine the variance factor σ^2

$$\sigma^2 = \frac{\underline{e}^T Q_\varphi^{-1} \underline{e}}{q}, \quad (6.26)$$

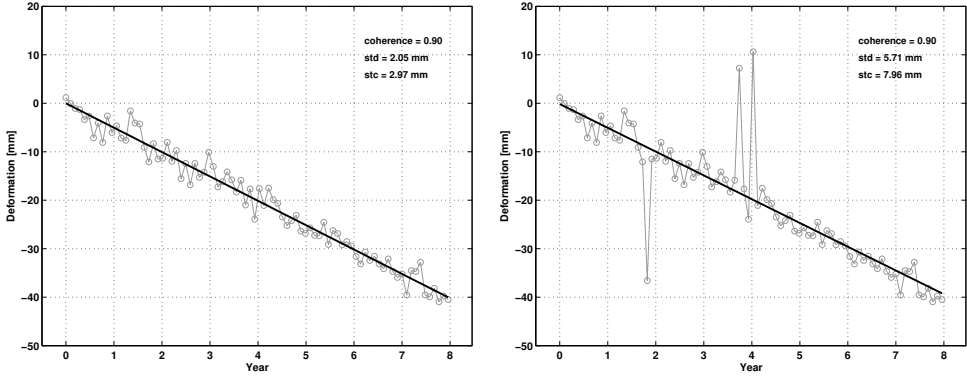


Figure 6.6: Example of quality measures. Left) Deformation time series without phase unwrapping errors. Right) Deformation time series with unwrapping errors. The unwrapping errors do not influence the coherence value. The standard deviation (std) and the spatio-temporal consistency (STC) do reflect the influence of the unwrapping errors.

where q is the redundancy of the model, i.e., difference between the number of phase observations and the number of estimated parameters. A variance factor of 1.0 indicates that the dispersion of the phase observations is well described by the covariance matrix, whereas a factor of 2.0 shows that the covariance matrix was a factor two too optimistic, and vice versa. Hence, this scaling factor indicates the relative noise level (plus unmodeled deformation and atmospheric signal delay) of the PS. The variance factor is determined with respect to the reference PS. An example of estimated variance factors is given in Figure 6.7b. Equivalent to the ensemble coherence estimator, also a *local variance factor* can be derived, reducing the distance dependent effect due to unmodeled atmospheric signal delay.

6.2.3 Covariance matrix

As an alternative to the variance factor, also the elements of the covariance matrix of the parameters of interest $Q_{\tilde{b}}$ can be used. These parameters are the residual height, deformation parameters, and possibly the azimuth sub-pixel position, see Section 4.2. The covariance matrix is obtained by error propagation by

$$Q_{\tilde{b}} = (B^T Q_{\varphi} B)^T, \quad (6.27)$$

where the covariance matrix of the phase observations Q_{φ} is determined by variance component estimation. The covariance matrix $Q_{\tilde{b}}$ contains both the variance of the parameters of interest and the covariances between them.

6.2.4 Standard deviation displacements

The standard deviation of the displacements is defined as the standard deviation of the residuals between the deformation model and the deformation time series

$$\sigma = \sqrt{\frac{1}{S-1} \sum_{s=1}^S (e^{0s} - \bar{e})^2}, \quad (6.28)$$

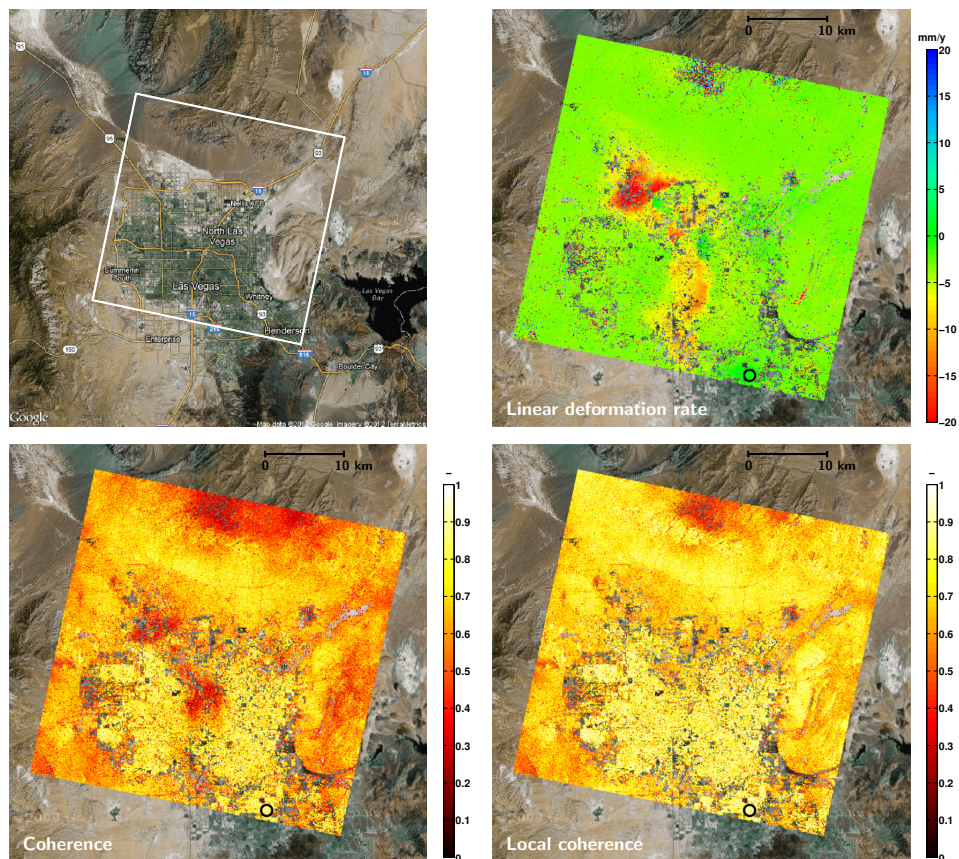


Figure 6.7a: Example of the quality indication of PSI results based on the ensemble coherence estimator and the local ensemble coherence estimator. An ERS-1/2 dataset is used to estimate the deformation time series in Las Vegas, USA. The estimation is based on a linear deformation model and the integer bootstrap estimator to resolve the phase ambiguities. The comparison of the global and local coherence values indicates that the deformation in the center of the subsidence bowls is not well described by a linear deformation model, resulting in relatively low coherence values with respect to the reference PS (black circle). Hence, the global coherence value describes both the noise and the unmodeled deformation. A strict threshold on these coherence values could result in the undesirable rejection of the PS in the middle of the subsidence bowl. Using the local coherence estimator, the coherence values give a better representation of the noise level. Here, the coherence estimates are based on short arcs between the first-order network and the PS considered, which give a better fit to the linear deformation model used.

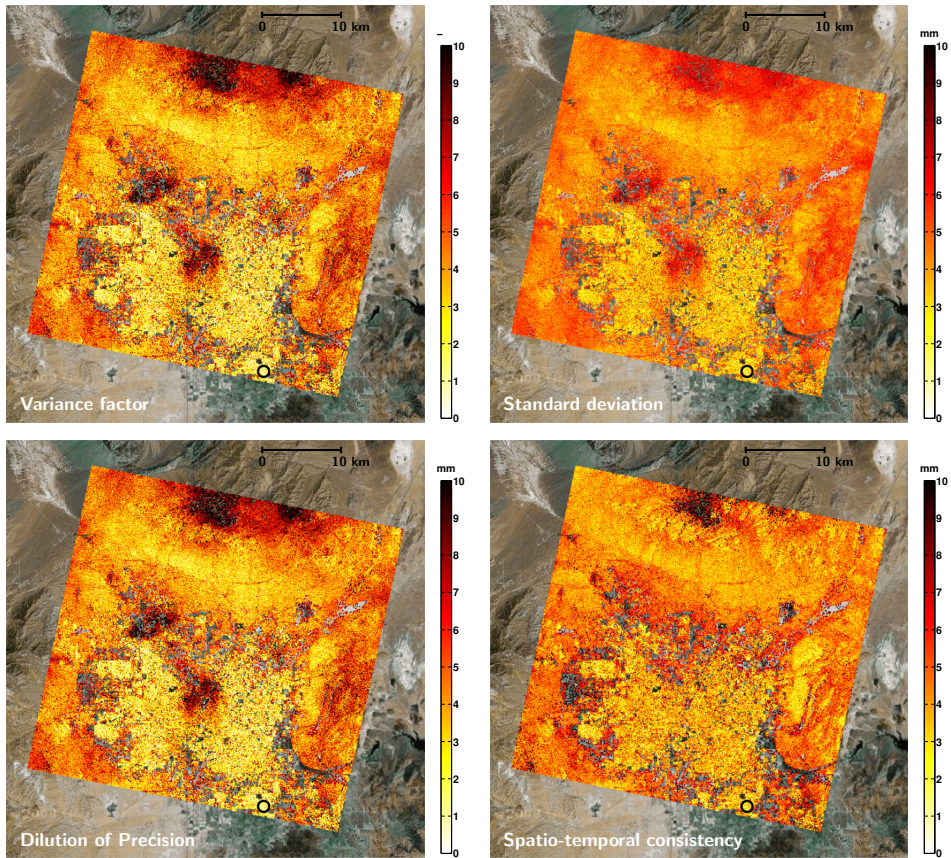


Figure 6.7b: Example of the quality indication of PSI results based on the variance factor, the standard deviation of the displacements, the Dilution of Precision for PSI, and the Spatio-temporal consistency. An ERS-1/2 dataset is used to estimate the deformation time series in Las Vegas, USA. The Spatio-temporal consistency is a local quality indicator and does not show a strong correlation with the deformation signal (see Figure 6.7a). Therefore, it gives a good indication of the noise level of the PS. The other estimators indicate a relation with the deformation signal, similar to the ensemble coherence estimator. However, also these indicators can be evaluated locally.

where \bar{e} is the mean of the residuals. Since \bar{e} will be close to zero due to the least-squares fit of the model parameters, the standard deviation obtained will be equivalent to the RMSE value. The advantage of the use of this the standard deviation (or RMSE) is that a quantity in millimeters is obtained rather than a certain factor, such as the ensemble coherence estimator or variance factor, which makes interpretation easier. An example of estimated standard deviation of the displacements is given in Figure 6.7b. Since the absolute deviations from the model are used, phase unwrapping errors are also reflected in the value obtained, see Figure 6.6.

To assess the lower bound of the precision of the displacements, a corner reflector experiment has been performed (Marinkovic et al., 2008; Ketelaar, 2009). Here, PSI measurements based on ERS-2 and Envisat acquisitions are compared with spirit leveling measurements. The analysis resulted in an estimated standard deviation for the

displacements of 1.5 mm for leveling, 2.6 mm for PSI based on ERS-2 data, and 1.6 mm for PSI based on Envisat data, respectively.

6.2.5 Dilution of Precision for PSI

An alternative scalar representation of the quality is the Dilution of Precision for PSI (DOP_{PSI}). This measure was introduced in Ketelaar (2009) and follows the concept of Dilution of Precision as commonly used for GNSS estimates (e.g., Ambiguity DOP and Position DOP) (Teunissen and Odijk, 1997), see also Eq. (A.61). The Dilution of Precision for PSI [mm] is defined as

$$DOP_{PSI} = \sqrt{\det Q_{\varphi}^{\frac{1}{S}}}, \quad (6.29)$$

where S is the number of slave images and Q_{φ} is the covariance matrix of a specific PS obtained by variance component estimation, see Eq. (5.11). This covariance matrix is obtained by multiplication of the original matrix, used for all PS, and the a-posteriori variance factor σ^2 estimated for the PS involved, see Eq. (6.26). In case the phase observations are assumed uncorrelated, resulting in a diagonal Q_{φ} , the DOP_{PSI} is equal to the mean of the standard deviations. Correlation between the phase observations results in a decreased value. An example of the estimated Dilution of Precision is given in Figure 6.7b.

6.2.6 Spatio-temporal consistency

Whereas all quality indicators previously described were dependent on the temporal deformation model used, this does not apply for the spatio-temporal consistency (STC). The STC is based on the deformation time series of the PS and therefore not related the models applied (except for the models used for the temporal ambiguity estimation). The quality measure was introduced by Hanssen et al. (2008). The STC ρ is defined as the minimum RMSE [mm] of the double-differences between PS i and various surrounding PS j , denoted by

$$\rho_i = \min_{\forall j} \frac{\lambda}{4\pi} \sqrt{\frac{1}{S-1} \sum_{s=1}^{S-1} ((\varphi_j^{0s} - \varphi_i^{0s}) - (\varphi_j^{0s+1} - \varphi_i^{0s+1}))^2}, \quad (6.30)$$

where S is the number of slave acquisitions. By taking the minimum RMSE value, the influence of the spatial deformation pattern is assumed to be minimized, thereby best representing the measurement noise. The surrounding PS j are selected within a specified radius around PS i , which can be case dependent. Apart from the maximum radius, also a minimum radius is applied to reduce the chance of selecting an undetected sub-main lobe (see Section 3.4), see Figure 6.8. Typical values for the minimum and maximum radius are 50 and 250 m, respectively. When no surrounding PS for a particular point are available, the STC value remains undetermined. An example of the estimated spatio-temporal consistency is given in Figure 6.7b.

6.2.7 Summary quality indicators

Various quality indicators are presented and examples the values obtained are given in Figures 6.7a and 6.7b. The quality indicators differ in their quantity, spatial context,

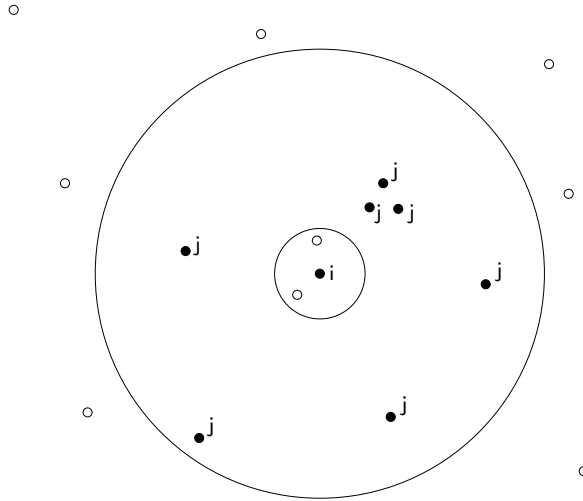


Figure 6.8: Computation of the spatio-temporal consistency (STC). For each PS i the RMSE of the double-difference time series with respect to the surrounding PS j is computed. The minimal STC is assumed to represent the noise level best. A minimum and maximum radius is used to select the surrounding PS (filled dots). Typical values are 50 and 250 m, respectively.

Table 6.1: Characteristics of quality indicators.

Quality indicator	Quantity	Spatial context	Temporal model dependent	Sensitive to unwrapping errors
Ensemble coherence estimator (γ)	factor 0-1	Global or local	Yes	No
Variance factor (σ^2)	scaling factor	Global or local	Yes	Yes
Covariance matrix ($Q_{\hat{x}}$)	parameter dependent	Global or local	Yes	Yes
Standard deviation displacements (σ)	mm	Global or local	Yes	Yes
Dilution of Precision for PSI (DOP_{PSI})	mm	Global or local	Yes	Yes
Spatio-temporal consistency (ρ)	mm	Local	No	Yes

model dependence, and sensitivity for phase unwrapping errors. The characteristics of the quality indicators are summarized in Table 6.1. The ensemble coherence estimator is an often used measure, however, it is insensitive for unwrapping errors, hence, does not allow the detection of phase ambiguity errors, and is dependent on the deformation model used. The Spatio-temporal consistency ρ circumvents these drawbacks. However, ρ cannot be determined for isolated PS. In general, the local quality indicators are less sensitive to the influence of unmodeled deformation and therefore give a better representation of the noise level. A number of the quality indicators presented in this section are applied in Chapter 7, where various advanced processing strategies to increase the number of detected PS are presented and evaluated. Hereby, the performance of the quality indicators is also further assessed.

6.3 Internal and external reliability assessment

Interferometric radar measurements are different compared to other geodetic observations in the sense that the measurements are only acquired once at a certain time or *epoch*. As a result, conventional quality assessment techniques, which use multiple observations to estimate the precision and reliability, cannot be applied. The quality measures described in Section 6.2 give an indication of the precision, however, as discussed, there is a strong dependency on the model assumptions.

The same dependency determines the reliability of the results. The estimated time series, which are based on the estimated integer phase ambiguities, are dependent on the deformation model used. Within DePSI various tests are performed to assess the reliability of the ambiguity resolution and to detect incoherent points. In Chapter 7 different processing strategies are presented and applied to improve the reliability of the estimated time series and to increase the number of detected PS based on local deformation models. Apart from these model dependent tests, additional consistency checks can be considered. These consistency checks are either internal, based on the same dataset, or external, using additional data.

Internal reliability consistency checks

To assess the internal consistency of PSI results, two checks are possible

1. **Consistency based on different first-order networks.** Within DePSI multiple independent sets of first-order Persistent Scatterer Candidates (PSC1) can be selected based on the amplitude dispersion. As a result, independent first-order networks are obtained. Based on these networks, the various processing steps, such as the estimation of the phase screens (e.g., atmospheric), lead to independent results as well. An example of two independent first-order networks is shown in Figure 6.9 for an area covering The Hague and Rotterdam in the Netherlands based on Envisat data acquired between 2003 and 2010. The network show similar deformation rates. Comparison of the final PS results obtained indicate the robustness of the processing and the reliability of the outcomes.
2. **Consistency based on a different master image.** The selected master image fulfills a special role in the data stack. It influences for instance the estimation of the Atmospheric Phase Screens. Hence, the choice of the master image will affect the final estimates. By re-running DePSI with a data stack based on a different master image, the impact of this choice and the reliability of the results can be assessed.

External reliability consistency checks

Whereas the internal consistency checks are based on the same set of radar images, in case of an external check an independent set of data is used. The external consistency checks can be based on

1. **Overlapping swaths.** Depending on the latitude, the radar image swaths (either ascending or descending orbit) have a certain overlap. For instance in case of

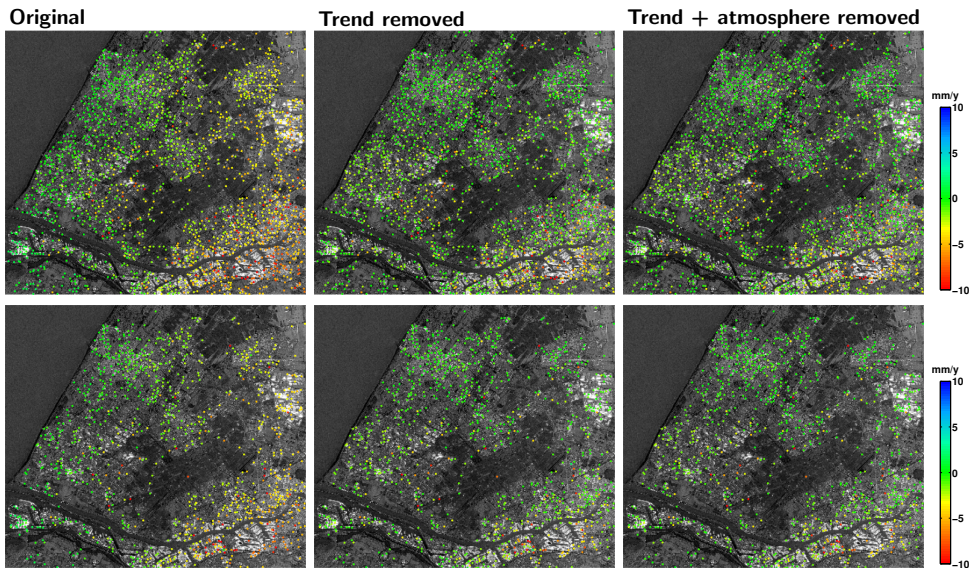


Figure 6.9: The use of two independent first-order networks to assess the consistency of the estimated PSI results. An Envisat dataset acquired between 2003 and 2010 covering The Hague and Rotterdam in the Netherlands is used. Top row) linear deformation rates of the first network, based on the PSC with lowest amplitude dispersion. Bottom row) linear deformation rates of the second network, based on the PSC with second lowest amplitude dispersion. The estimated rates based on the original data (left column), after trend removal (middle column) and after estimation of the atmospheric signal. The networks show similar deformation rates.

ERS-1/2 or Envisat (swath IS2), often an overlap of 50% is obtained. Due to the overlap two independent datasets are obtained. By analyzing both datasets, the consistency of the PS estimates can be tested. However, for two reasons a straightforward comparison is not possible (Ketelaar et al., 2007b,a; Ketelaar, 2009). First, the data is acquired on different dates. Hence, the deformation time series cannot be compared directly. Only interpolated time series or derived deformation parameters can be compared. Second, the look angle is slightly different. In case of Envisat the difference is about 4 degrees. As a result, a number of PS may be detected in the first dataset, but not in the second. Moreover, when horizontal deformation occurs in the overlapping area, the measured deformation values will be affected.

2. **Ascending and descending images.** Instead of overlapping data acquired from the same orbit, also datasets acquired from the ascending and descending orbit can be used. Because the objects on the surface are observed from completely different angles, the sets of detected PS will differ. Besides, horizontal deformation may affect the measurements, depending on the direction, see Figure 2.6.

The external consistency checks can be performed based on data acquired by the same satellite, or data obtained from other sensors. For example data measured with a different signal wavelength can be used. Since the wavelength affects the scattering mechanism on the surface, different distributions of PS should be anticipated, both in location of the PS and in density. However, the general deformation pattern should be similar.

6.4 Summary

The quality of the PSI results concerns both the quality of the estimated deformation time series, together with the estimated parameters of interest, and the accuracy of the georeferencing of the detected PS.

The accuracy of the georeferencing is dependent both on factors applying to all PS and effects that influence PS individually. The geolocation of all PS is affected by an error in the height of the reference PS, the sub-pixel position of the reference PS, and timing errors, both in along-track and across-track direction. The latter may partly be caused by uncompensated atmospheric signal delay. The effect of orbit errors (in position, rather than in time annotation) is regarded to be negligible with the availability of precise orbits. The sum of the effects, which can reach tens of meters, results in a constant shift in both longitude and latitude direction. When the error sources cannot be corrected based on additional information, normally an overlay of the PS on an orthorectified and georeferenced aerial photograph or satellite image is used to estimate the shifts visually. The final accuracy is dependent on the precision and resolution of the reference image used.

Whereas the constant shifts in the geolocalization can to a large extent be corrected, individual inaccuracies per PS remain. These inaccuracies are caused by the error in the estimated topographic height of the PS and uncertainty in the PS sub-pixel position. The height accuracy directly influences the georeferencing with a factor dependent on the local incidence angle. The uncertainty in the sub-pixel position applies to both the range and azimuth direction. In range direction, apart from a direct effect, an indirect effect occurs because of an error in the estimated height of the PS due to a wrong flat Earth reference phase applied. When this sub-pixel position is not accounted for, the combined effect causes a mean error of 4.6 m in range direction for a stack of oversampled Envisat images. In azimuth direction, a mean error of 0.5 m can in this case be assumed. Because of the large impact on the geolocation, the estimation of the sub-pixel position based on the amplitude responds is strongly recommended.

The quality of the estimated deformation time series and parameters of interest can be expressed by various measures. These measures differ in their quantity, spatial context, model dependence, and sensitivity to phase unwrapping errors. An often applied measure is the ensemble coherence. However, this parameter is insensitive to unwrapping errors. Alternative quality indicators are the variance factor and the full covariance matrix of the estimated parameters. From a visualization and interpretation perspective, a single-valued indicator in mm is desirable. Here, the standard deviation of the displacements, the Dilution of Precision, and the Spatio-temporal consistency (STC) are presented. The advantage of the STC is that the indicator is independent of the model used, thereby giving the best representation of the actual measurement noise. A number of quality indicators is applied and further assessed in Chapter 7, where different processing strategies to increase the number of detected PS are evaluated.

Whereas the quality indicators give an impression of the PS precision, a full quality assessment based on conventional geodetic quality control techniques cannot be obtained due to a lack of redundancy in radar interferometric observations. That is, per location only a single observation per epoch is available. To assess the reliability of the PSI results, various consistency checks can be applied. These checks are either based on

the internal consistency within the data stack, or an external consistency analysis. The internal consistency can be assessed by comparison of the PSI results using multiple first order networks based on different sets of Persistent Scatterer Candidates, or by adopting a different master image within the data stack. Alternatively, an additional data stack can be analyzed to enable a comparison of the results. Here, either overlapping swaths from the same orbit direction are used, or the results obtained from ascending and descending data stacks are compared.

A number of quality indicators presented in this chapter are applied in the next chapter, where various advanced processing strategies to increase the number of detected PS are presented and evaluated.

The standard Persistent Scatterer Interferometry (PSI) approach is based on the assumption of linear deformation behavior between nearby PS. Although this assumption often holds, it may not be valid everywhere. As a result, ambiguities may not be resolved correctly and/or PS are not detected. Within DePSI a number of advanced processing strategies is implemented to account for situations with non-linear deformation phenomena. The objective of these strategies is to increase the number of detected PS and the reliability of the estimated deformation time series. The various strategies implemented are described and evaluated in this chapter (see Table 7.1) using a test site around Las Vegas, USA (Section 7.1). As a benchmark, the results obtained by the standard processing approach are shown in Section 7.2. The effect of using extended deformation models is evaluated in Section 7.3. Here, both the combination of a linear with a periodic model, and a linear, quadratic, cubic plus periodic model is applied. An alternative approach is based on the prediction of Deformation Phase Screens (DPS) (Section 7.4), i.e., the iterative prediction of area-wide deformation values based on earlier detected PS. Furthermore, instead of using a single temporal deformation model, multiple deformation models can sequentially be applied and tested (Section 7.5), possibly based on a PS density prognosis based on radar reflection intensity analysis, see Section 7.6. Whereas these processing options can be applied within any analysis, for some studies it is beneficial to apply dedicated settings based on the spatial or temporal characteristics of the deformation signal. In the spatial domain an Area of Interest can be selected, for which all (non-side lobe) pixels are evaluated instead of the conventional selection of points based on amplitude information, see Section 7.7. In other cases the time frame of radar acquisitions used for the final estimations can be limited to account for certain events, such as the completion of large construction works (Section 7.8). The common objective of these processing options is to increase the number of reliable detected PS. The results of the various strategies are compared and discussed in Section 7.9.

7.1 The Las Vegas test case

To evaluate the various advanced processing strategies a test site around Las Vegas is chosen, see Figure 7.1. The area is known to experience strong ground motion due to groundwater withdrawal, also associated with seasonal fluctuations. Due to the non-linear deformation effects occurring, it forms a suitable test site (Kampes, 2006). The site has often been studied using radar interferometry in the past, see for instance

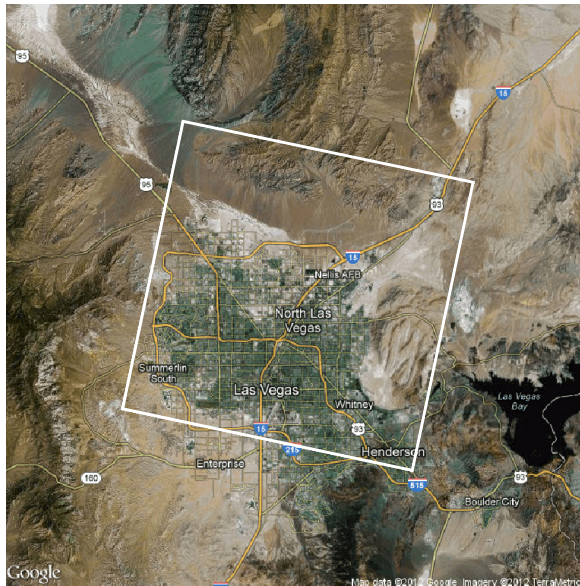


Figure 7.1: The Las Vegas test site (white box). The $\sim 40 \times 40$ km region contains both urban and rural areas.

Amelung et al. (1999); Hoffmann et al. (2001); Bell et al. (2002, 2008b). In this study the focus lies on evaluation of processing strategies.

An ERS-1/2 data set is used to evaluate the processing strategies, because the ground motion in Las Vegas is reducing, but was still relatively strong during the ERS acquisition period. The data set contains 49 radar images acquired between April 1992 and September 2000. The images acquired after that date are omitted due to high Doppler centroid frequencies in the data after failure of the on-board gyroscopes of ERS-2. The image of June 13, 1997 is taken as master. The $\sim 40 \times 40$ km region contains both urban and rural areas, and significant topography. The SRTM DEM (Farr et al., 2007) is used to remove the majority of the topographic phase contribution from the interferograms.

The standard and various advanced processing results are all obtained using the integer bootstrap estimator to resolve the phase ambiguities, see Section 4.5. The advantage of this estimator compared to the ambiguity function is that multiple deformation models can be applied, without a significant increase of the computation time. Compared to the integer least-squares estimator, the computation time is also strongly reduced, see Figure 4.10. The bootstrap estimator is constrained using standard deviations for the pseudo-observations inserted in the model. The standard deviations applied are 30 m for the residual height, 5 mm for the atmospheric signal delay and noise of the master image, 2 cm/y for the linear deformation rate, 1 cm/y² and 1 cm/y³ for the quadratic and cubic model, respectively, and 5 mm for the amplitudes of the periodic terms (see Eq. (4.19)).

Each analysis is based on the construction of a network of first order PS, followed by a densification by estimating the ambiguities and parameters of interest of all remaining PSC. To enable testing of the ambiguity solutions, each PSC is connected to three first-

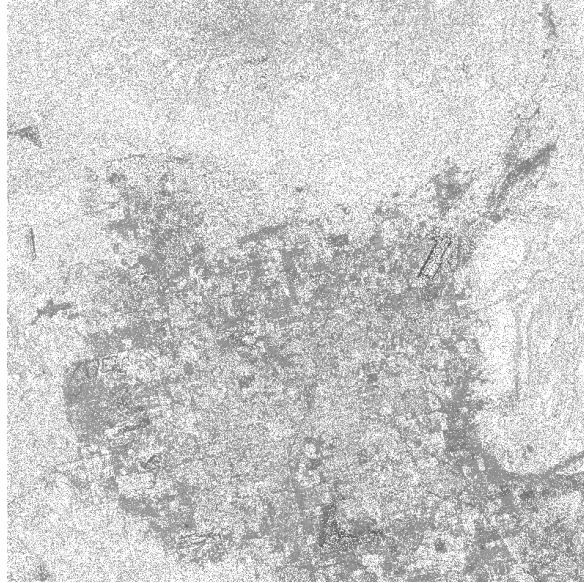


Figure 7.2: Locations of the selected second-order PS candidates (PSC2, white dots) in the original radar image. A normalized amplitude dispersion threshold of 0.45 is applied. The PSC density in the rural areas is relatively high compared to the urban region. This is due to the arid circumstances in these areas, resulting in consistent reflection intensities. The background gives an indication of the area based on the mean intensity of the image stack, with the city of Las Vegas in the middle.

order network PS. The consistency of the solutions determines whether or not the PS is accepted. In the Las Vegas test case the *mode* approach is used, see Section 5.4. Here, for each ambiguity in the PSC time series the most occurring value is determined and only when these most occurring values were estimated at least for two out of the three connections throughout the time series, the PS is accepted.

To enable comparison of the results by the various analyses, the same set of PS Candidates (PSC) is used in each approach. The exception is the set of PSC used in case of the Area of Interest processing (Section 7.7) and time frame processing (Section 7.8), where the Area of Interest approach results in a local increase of the number of PSC. The PSC selection is based on the normalized amplitude dispersion, see Section 3.3.1. A threshold of 0.25 for the first-order network points (PSC1) and of 0.45 for the PSC2 is applied. To reduce the number of PSC1 and ensure a homogeneous distribution, a selection grid is applied to the initial set of PSC1, see Section 3.3.3. Each grid cell only contains one PSC1. In total about 918 PSC1 and $N_{\text{PSCref}}=480625$ PSC2 are selected. The locations of the PSC2 are shown in Figure 7.2.

Apart from the standard approach, six alternative processing strategies are evaluated: the use of extended deformation models, Deformation Phase Screen (DPS) estimation, sequential testing of deformation models, prognosis-based densification, Area of Interest processing and time frame processing, see Sections 7.2-7.8. An overview of the approaches, including the sections where they are described, is given in Table 7.1.

Table 7.1: Overview of the processing approaches presented in this chapter.

#	Approach	Deformation model	Specification	Section
1a	Standard, bootstrapping	Linear	Used as benchmark	7.2
1b	Standard, ILS	Linear		7.2
1c	Standard, ambiguity function	Linear		7.2
2a	Extended	Periodic	Single extended model	7.3
2b	Extended	Periodic+cubic	Single extended model	7.3
3	Deformation Phase Screen	Linear	Phase Screen estimation by Kriging	7.4
4	Sequential	Linear, quadratic, cubic, (+periodic)	Sequential testing of deformation models	7.5
5	Prognosis	Linear, quadratic, cubic, (+periodic)	Sequential testing of deformation models dependent on PS density	7.6
6	Area of Interest	Linear	Evaluation of all local amplitude maxima in certain Area of Interest	7.7
7	Time frame	Linear	Limited time frame for final estimation	7.8

7.2 Application of standard processing

Application of the standard DePSI processing scheme based on linear deformation between nearby points results in the detection of 422496 PS, hence 88% of the number of pre-selected PSC. The linear deformation rates, as well as the quality indicators Spatio-temporal consistency (STC), ensemble coherence and local ensemble coherence estimator (see Section 6.2) are shown in Figure 7.3. The reference point is indicated with a black circle (South-East corner). The rectangular box in Figure 7.3A indicates the area which is visualized with more detail in Figure 7.4.

The linear deformation rates clearly show areas with strong subsidence due to groundwater withdrawal. Rates of more than 20 mm/y are measured. Figure 7.4A also shows the occurrence of isolated PS with anomalous deformation behavior. These PS either show autonomous movement, i.e., actual deformation which is not spatially correlated, or are a falsely detected PS. Despite the ambiguity testing scheme in the processing based on multiple connecting arcs for each PSC, some ambiguity errors remain undetected due to coincidental agreement between the various wrong solutions for the connecting arcs. To distinguish the PS with autonomous movement from the false detections, an additional selection procedure based on one or more quality indicators is required. Here, the ensemble coherence estimator, the local ensemble coherence estimator, and STC are considered, see Figures 7.3 and 7.4, B–D.

In many studies the ensemble coherence estimator (Eq. (6.25)) with respect to the reference point is used for the further selection of PS. However, as is discussed in Section 6.2, the coherence estimator describes both the noise level of the measurements and the unmodeled part of the deformation. This is also visible in Figure 7.3C, where the PS in the subsidence bowls show relatively low coherence values. This may indicate a high noise level in this region, but more likely it shows that the linear deformation model is not the most suitable model for these areas. A strictly applied coherence threshold would result in the undesirable effect of removing these PS from the final data set.

As an alternative, local quality indicators can be used. Both the local ensemble coherence and STC are presented in Figures 7.3 and 7.4, B and D. The figures illus-

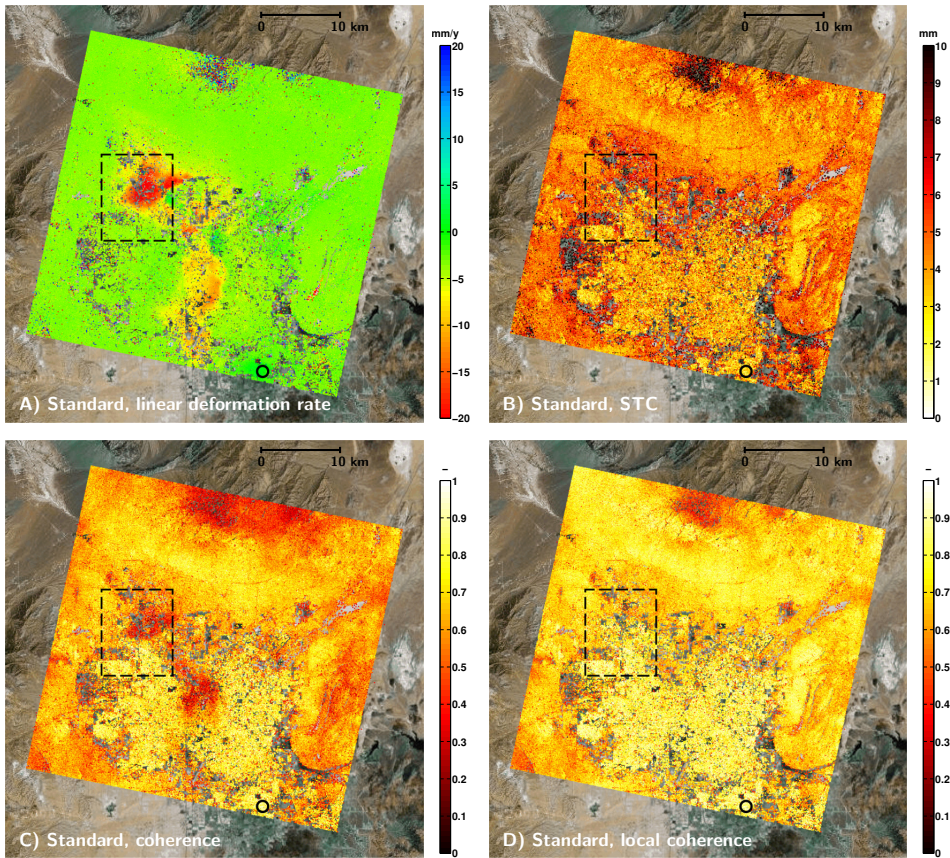


Figure 7.3: Approach 1a. DePSI results of the Las Vegas test site using the standard processing approach based on an ERS-1/2 dataset acquired between April 1992 and September 2000. The linear deformation rates of all detected PS are shown, together with the quality indicators STC, ensemble coherence and local ensemble coherence. The reference point is indicated with a black circle (South-East corner). A detailed view of the PS in the rectangular box is given in Figure 7.4.

trate that these quality indicators are far less sensitive to spatially correlated unmodeled deformation, since the PS in the subsidence bowls show similar values as the surroundings. Hence, by applying a threshold on these indicators a final selection of PS would be obtained which better represents the actual noise characteristics of the PS.

However, regardless whether a local or global quality indicator is used, certain PS may already have been rejected at an earlier stage due to incorrect ambiguity resolution based on the linear deformation assumption. Therefore, advanced processing approaches are applied in the next sections to adjust the deformation model. As a consequence, the ensemble coherence estimator will be less affected by unmodeled deformation. Thereby, the detection of PS based on this global quality indicator is improved. To follow the conventional methodology of PS selection and to enable a comparison between the various advanced processing results, the ensemble coherence estimator is used in the remainder of this study for PS selection. The PS selection based on a coherence threshold of 0.7, 0.6, and 0.5, is visualized in Figure 7.5. The number of PS increases from 154941

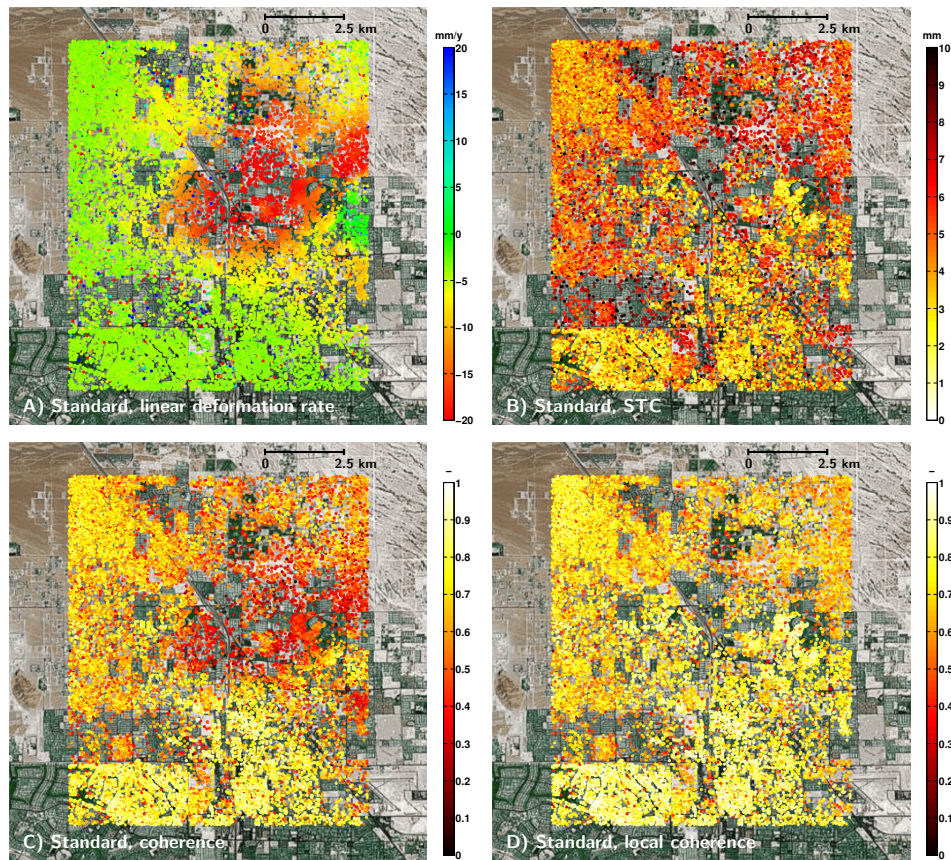


Figure 7.4: Approach 1a. DePSI results of a small region in the Las Vegas test site (see rectangular box in Figure 7.3) using the standard processing approach. The linear deformation rates of all detected PS are shown, together with the quality indicators STC, ensemble coherence and local ensemble coherence.

to 281034 and 363058, respectively. The result based on the 0.5 threshold is used for further comparison in the remainder of this chapter, indicated by N_{ref} .

To assess the impact of the choice of the bootstrap estimator on the results, Figure 7.6 shows the detected PS by bootstrapping, integer least-squares (ILS), and the ambiguity function. The number of detected PS, applying a coherence threshold of 0.5, increases from the $N_{\text{ref}}=363058$ PS by bootstrapping to $1.03N_{\text{ref}}$ PS by ILS and $1.07N_{\text{ref}}$ PS by the ambiguity function. These numbers are in correspondence with the success rates shown in Figure 4.5 based on simulated data, that is, the ambiguity function outperforms the ILS and bootstrap estimators. However, despite the superiority of the ambiguity function especially for strong deformation rates, the PS density of the ambiguity function results in the middle of the subsidence bowl is relatively limited. The hypothesis is that the ILS and bootstrapping estimators are better able to accommodate any non-linear deformation behavior due to leakage of the model imperfections into the covariance matrix used in the estimation. Nevertheless, the ambiguity function gives an overall 7% increase with respect to the bootstrap solution. However, the ambiguity

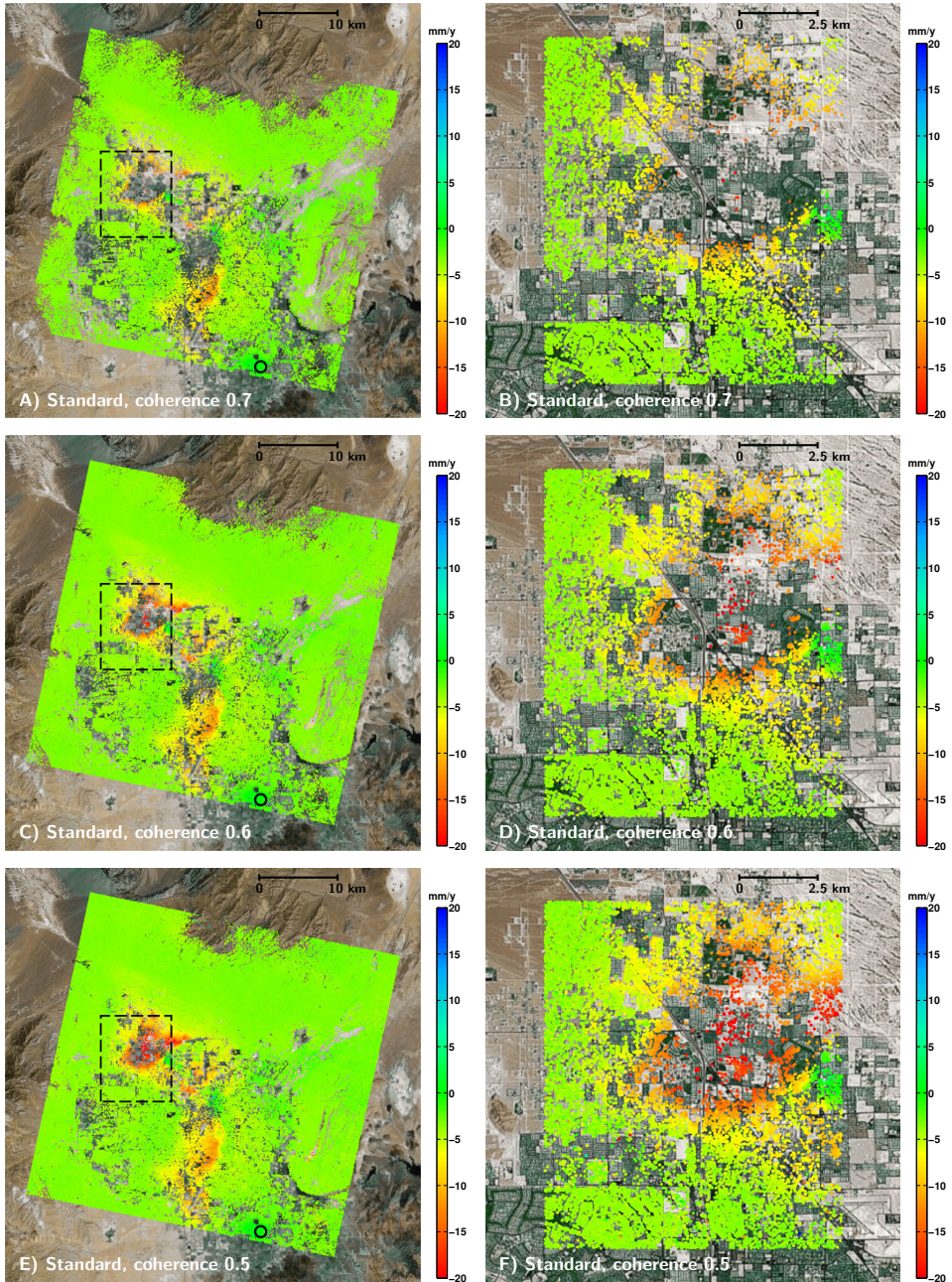


Figure 7.5: Approach 1a. Linear deformation rates after applying the standard processing approach based on a linear deformation model. The PS are selected based on an ensemble coherence threshold of 0.7, 0.6, and 0.5. The right column shows the detailed results within the rectangular box in the figures on the left.

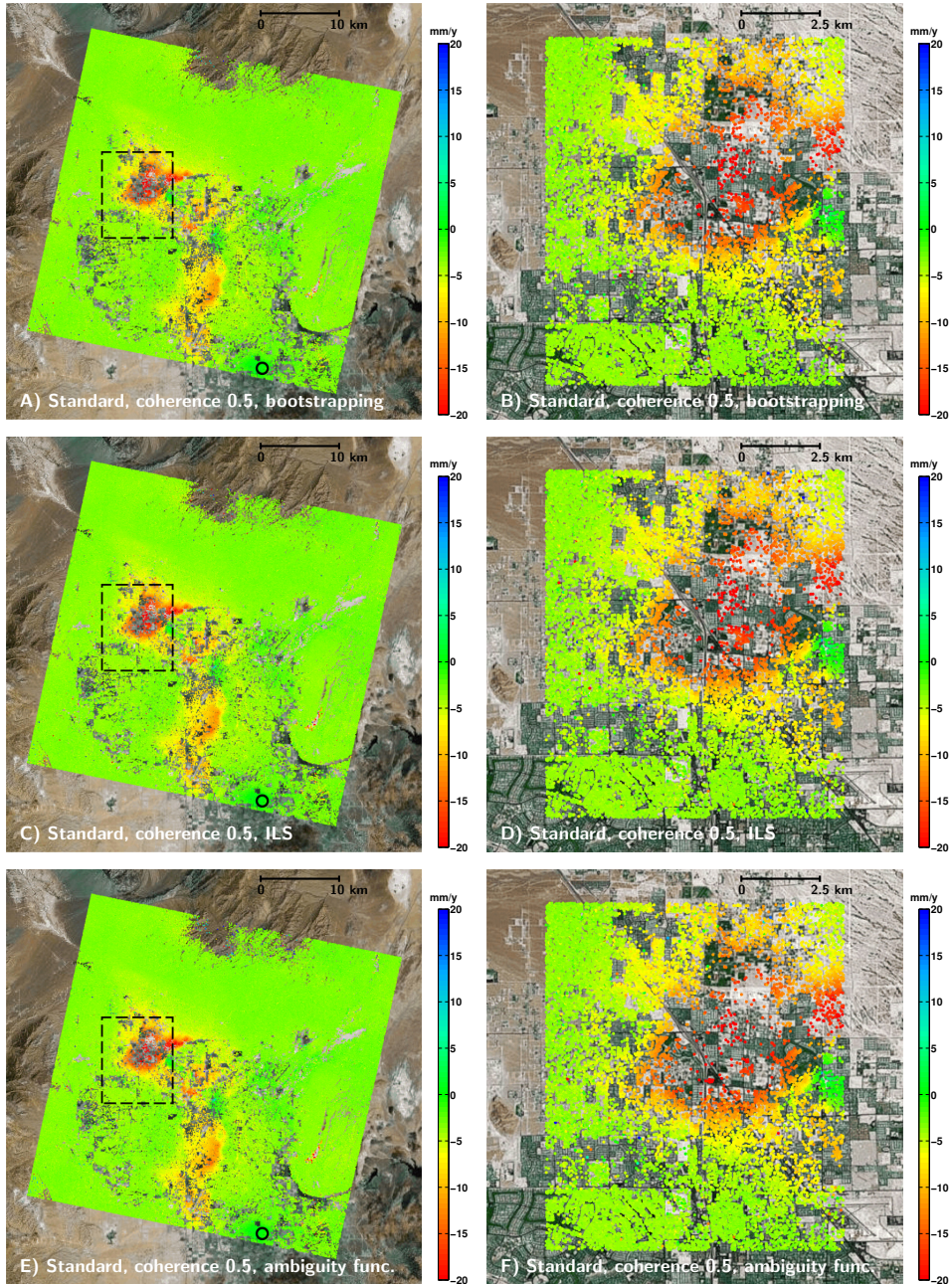


Figure 7.6: Approach 1a–c. Linear deformation rates after applying the standard processing approach based on a linear deformation model using bootstrapping (top), integer least-squares (ILS, middle), and the ambiguity function (bottom). The PS are selected based on an ensemble coherence threshold of 0.5. The right column shows the detailed results within the rectangular box in the figures on the left. The different estimators result in a varying selection of PS. Most PS are detected by the ambiguity function, although the number of PS in the center of the subsidence bowl is smaller compared to the ILS and IB results.

function cannot be applied here to evaluate the various processing strategies, since no additional deformation parameters can be estimated without a unacceptable increase of the computational load. Similar, the ILS estimator requires more than 10 times the computation time needed for the bootstrap solution. Since only a 3% increase in the number of detected PS is achieved by the ILS estimator, the significant shorter computation time required by bootstrapping is determining the choice of the bootstrap estimator for the remainder of this chapter.

7.3 Application of extended deformation models

The most straightforward application of an advanced processing scheme is the use of a general extended deformation models with respect to the linear model. This approach was already proposed by Colesanti et al. (2003a); Kampes (2006). Hence, apart from a linear deformation rate, additional deformation models are added to the estimation scheme. Examples are a periodic model, a higher-order polynomial (e.g., quadratic or cubic), or a breakpoint model, see Section 4.2.

For the Las Vegas test case both a periodic model and a periodic+cubic model are applied. For all models holds that the linear deformation model is included by default. In case of the cubic model, hence a third-order polynomial, also the quadratic term is incorporated. The results are shown in Figures 7.7 and 7.9. In total $0.98N_{\text{ref}}$ PS are detected using the periodic model and applying a threshold on the ensemble coherence of 0.5. Hence, the number of detected PS in case of a periodic model is slightly smaller compared to application of the standard approach. This counter-intuitive reduction is caused by the additional deformation parameters, which increases the degree of freedom in the estimation process. As a result, more inconsistent ambiguity solutions are obtained in the connecting arcs to a certain PSC, resulting in a rejection of the PS in the testing scheme. This effect is even stronger using the periodic+cubic model. Here only $0.76N_{\text{ref}}$ PS are detected. Moreover, the number of isolated PS with apparent anomalous deformation behavior is significantly increased. Most likely, the majority of these points are false detections, which erroneously passed the ambiguity testing scheme. From these results the conclusion can be drawn that application of extended deformation models to the full area does not result in the detection of more PS, as was the objective, but instead decreases the number of detected PS.

More important than the number of detected PS is the reliability of the deformation time series estimate, hence, whether the final solution is actually representing the physical truth. A strict answer can only be provided by validation of the results using ground truth data. Unfortunately, this data is unavailable. Therefore, a qualitative approach is taken by inspecting the deformation time series. In Figures 7.8 and 7.10 the deformation time series of two representative PS are shown, which are detected in all processing results in this chapter. The location of these PS is indicated in Figure 7.7, bottom-left. Both the result of the standard processing and the advanced approach are visualized. The figures show that application of alternative deformation models cause the deformation time series to change, primarily due to a change in phase ambiguity solution. Regarding the time series of PS A using the periodic model (Figure 7.8), the solution by the standard approach appears to be more likely and shows similar values as obtained by Bell et al. (2008a), i.e., -20 – -30 mm/y between 1992-1996 and -10 – -20 mm/y between 1996-2000. In case of the periodic+cubic model (Figure 7.10), an even higher deformation rate

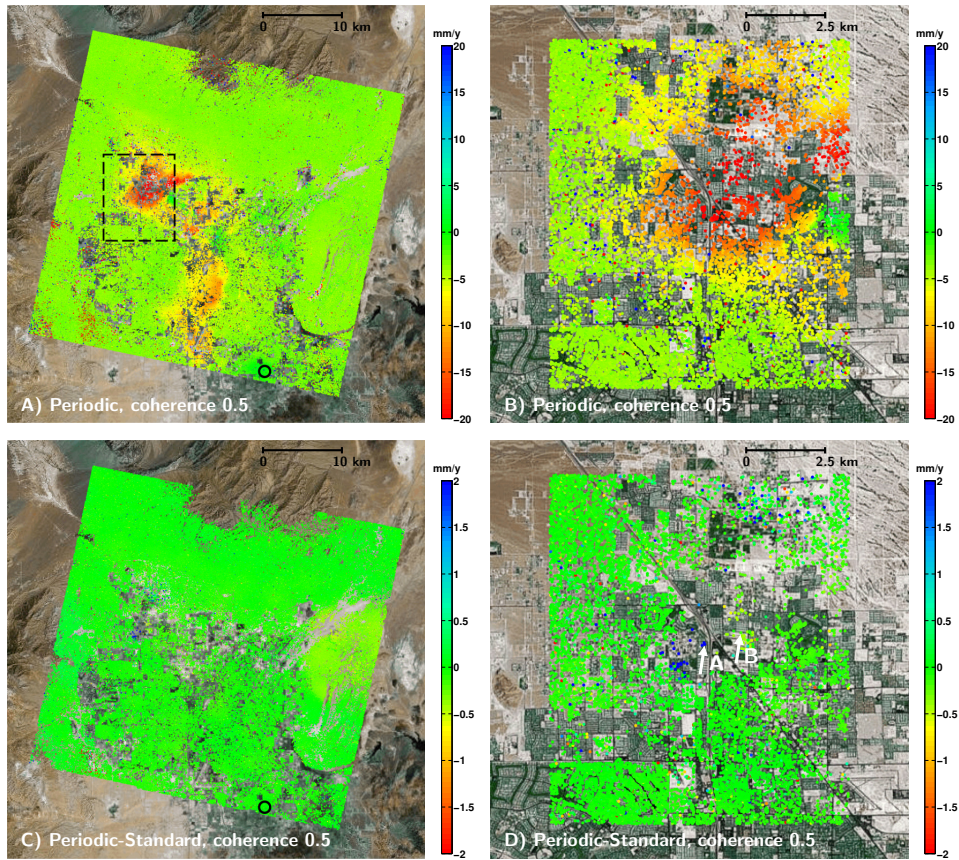


Figure 7.7: Approach 2a. Top row) Linear deformation rates after applying an additional periodic deformation model on top of the linear model. The PS are selected based on an ensemble coherence threshold of 0.5. The right column shows the detailed results within the rectangular box in the figure on the top-left. Bottom row) Difference between the linear deformation rates of the common PS obtained by the standard approach and the periodic model processing. Only the PS which are detected in all advanced processing schemes are shown. The largest differences occur in the region with the strongest subsidence rates (blue dots). However, in most cases the periodic signals (if present) do not affect the linear deformation rates significantly. The time series of PS A and B are shown in Figure 7.8.

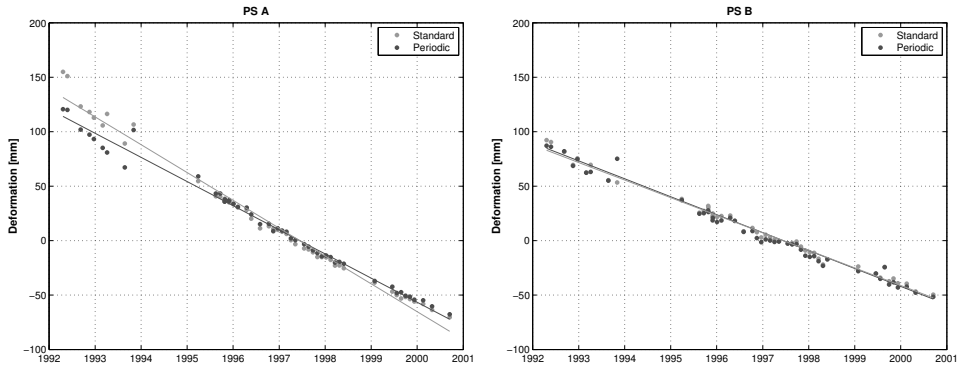


Figure 7.8: Approach 2a. Deformation time series of two representative PS, see Figure 7.7, bottom-right, for the locations A and B. Both the result of the standard processing and using an additional periodic deformation model are shown. The solid lines represent the linear part of the model. For point B the time series are almost identical. Regarding point A, the solution obtained by the periodic model appears visually to be less likely corresponding to the true surface behavior. Since the estimated amplitude of the periodic signal in this area is limited to less than 3 mm, the periodic signal is not distinctive in the time series.

of about -40 mm/y is obtained. Both solutions seem possible. A quality indicator such as the ensemble coherence estimator, STC or variance factor (see Section 6.2) should be compared to indicate the most likely solution. However, it should be noted that the ensemble coherence estimator is insensitive to ambiguity errors, see Section 6.2.1. Regarding PS B, the standard approach and the periodic model result in the same solution, however, the deformation rate in the 1992-1996 period of -17 mm/y is lower compared to the results in Bell et al. (2008a). Using the periodic+cubic model, a rate of -26 mm/y is obtained, which corresponds to the study mentioned.

The results show that using different models different deformation time series are obtained. A quality indicator is required to determine the best fitting model. This concept is used in the sequential testing (see Section 7.5) and prognosis-based densification approach (see Section 7.6). First an alternative approach based on the estimation of a Deformation Phase Screen is introduced.

7.4 Deformation Phase Screen (DPS) estimation

7.4.1 Algorithm of DPS estimation

An alternative approach to attempt to increase the number of detected PS is the estimation of a *Deformation Phase Screen* (DPS) per interferogram (Humme, 2007; van Leijen and Hanssen, 2007a). After a DePSI analysis with a certain temporal deformation model, e.g., linear, the DPS is estimated from the deformation time series of the detected PS, see module 8 in Figure 3.1. Hence, a spatial approach is applied, instead of an adaption of the model in the time domain, as applied in the previous section. The DPS approach is therefore only suitable for deformation phenomena with a certain spatial smoothness.

The DPS can either be parametric or based on least-squares prediction, see Section A.3. An example of a parametric representation is a superposition of K elementary

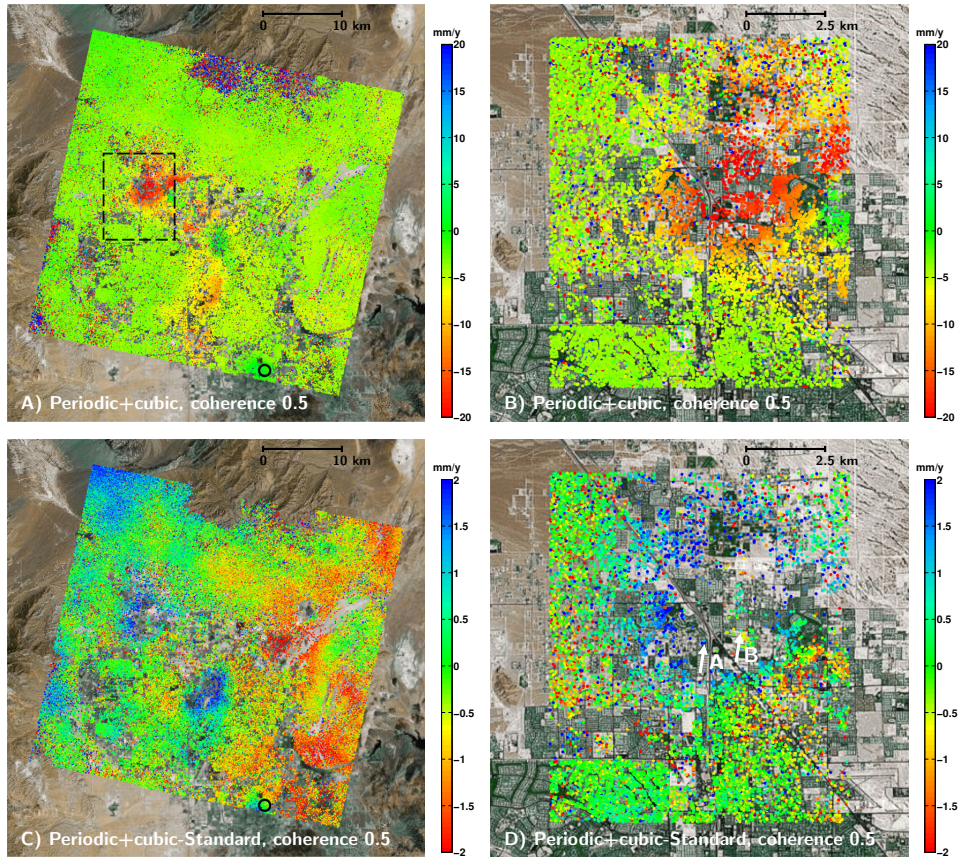


Figure 7.9: Approach 2b. Top row) Linear deformation rates after applying a periodic+cubic deformation model on top of the linear model. The PS are selected based on an ensemble coherence threshold of 0.5. The right column shows the detailed results within the rectangular box in the figure on the top-left. Bottom row) Difference between the linear deformation rates of the common PS obtained by the standard approach and the periodic+cubic model processing. Only the PS which are detected in all advanced processing schemes are shown. Application of the cubic model results in differences in the values of the linear deformation rates compared to the standard approach. Moreover, the number of isolated PS with apparent anomalous deformation behavior increases significantly. This is caused by the additional degrees of freedom due to the extra deformation parameters, which results in erroneous resolution of the phase ambiguities. The time series of PS A and B are shown in Figure 7.10.

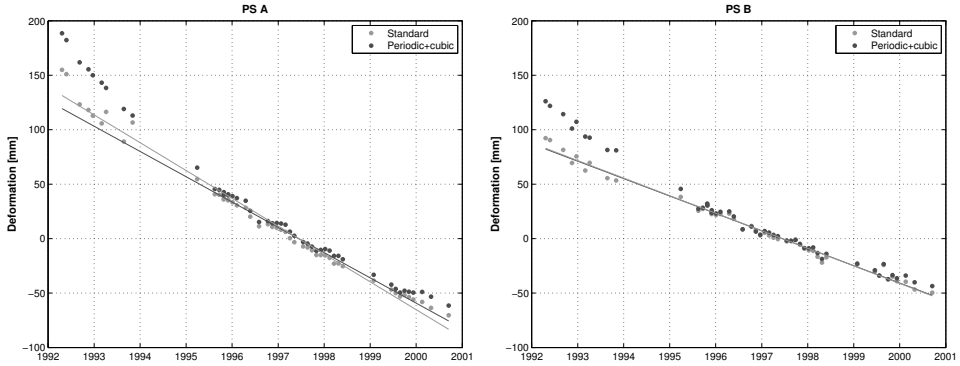


Figure 7.10: Approach 2b. Deformation time series of two representative PS, see Figure 7.9, bottom-right, for the locations A and B. Both the result of the standard processing and using an additional periodic+cubic deformation model are shown. The solid lines represent the linear part of the model. For both points the deformation time series alters by applying the extended deformation model. The most likely true solution cannot be assessed based on the time series plot alone. Since the amplitude of the periodic signal in this area is limited to less than 3 mm, the periodic signal is not distinctive in the time series.

ellipsoidal subsidence bowls (Kenselaar and Quadvlieg, 2001) to describe the deformation phase D_{DPS}^{0s} for each interferogram, resulting in

$$D_{DPS}^{0s} = \sum_{k=1}^K d_k^{0s} \exp\left(-\frac{1}{2}(u_k^{0s} + v_k^{0s})\right), \quad (7.1)$$

with

$$u_k^{0s} = \left(\frac{(x - x_{c,k}^{0s}) \sin(\omega_k^{0s}) + (y - y_{c,k}^{0s}) \cos(\omega_k^{0s})}{a_k^{0s}} \right)^2,$$

$$v_k^{0s} = \left(\frac{(x - x_{c,k}^{0s}) \cos(\omega_k^{0s}) - (y - y_{c,k}^{0s}) \sin(\omega_k^{0s})}{b_k^{0s}} \right)^2,$$

where

- d deformation at center of the subsidence bowl,
- x, y coordinates,
- x_c, y_c coordinates of center bowl,
- ω orientation of the ellipsoid,
- a, b length of ellipsoidal axis.

To estimate the parameters of the subsidence bowls in a least-squares sense, Eq. (7.1) is linearized. An iterative estimation and testing scheme is applied to converge to the solution, initialized by approximate values of the parameters d , x_c , y_c , ω , a and b . In practice these approximate values need to be known accurately to ensure convergence to the solution.

An alternative for parametric modeling is an interpolated deformation field based on least-squares prediction. This approach is similar to the method applied for the predic-

tion of the Atmospheric Phase Screen (APS), see Section 5.3.2. The prediction is based on a spatial covariance function which is estimated from the data per interferogram. Hence, no a-priori information about the deformation field is required in this case. As a consequence, this method is more flexible compared to the parametric modeling and therefore widely applicable. By using a Gaussian covariance function to construct the covariance functions, a predicted phase screen is obtained which is continuous and differentiable. As a consequence, even values outside the observed range of deformation values can be predicted.

Once modeled or predicted, the DPS is subtracted from the original interferometric phase and the DePSI processing is repeated (again using a certain temporal deformation model, e.g., linear). Because the DPS are predicted per epoch using the displacement time series, possible non-linear deformation is modeled as well. As a result, points which were previously rejected as a PS due to too large deviations from the model may now be accepted. Hereby the density of PS could improve. Obviously, this procedure can be repeated iteratively. After the last iteration, the DPS are added to the final estimates to obtain the total deformation time series.

To capture as much detail as possible, the choice is made to base the DPS on the full set of detected PS, see the flowchart in Figure 3.1. Alternatively, the DPS can be predicted at an earlier stage, only using the first-order PS, as is done for the prediction of the Atmospheric Phase Screen (APS). However, the spatial density of the PS1 may be too low for a profound prediction or modeling.

7.4.2 Application of DPS estimation

The DPS approach is applied to the Las Vegas test case using least-squares prediction. The prediction is based on the PS detected by an initial DePSI analysis applying a linear deformation model, hence, the standard approach (see Section 7.2). The predicted Deformation Phase Screens are shown in Figure 7.11. Because the prediction is based on the deformation time series, any non-linearity in the deformation behavior is reflected in the DPS. After removing the DPS from the original interferometric phases, a final first-order network is constructed based on the phase residuals and the PSC are evaluated again, see Figure 3.1.

Application of the DPS approach results in the detection of $1.11N_{\text{ref}}$ PS with a coherence higher than 0.5, see Figure 7.12. Moreover, the number of erroneous detected PS remains limited, especially compared to the results using the cubic deformation model (Figure 7.9). Figure 7.12 (bottom row) shows that the DPS approach primarily affects the center of the subsidence bowl with the strongest deformation rate. Apparently, this region also shows a considerable non-linearity in the deformation, which is captured by the least-squares prediction. This is confirmed by the deformation time series of PS B in Figure 7.13. A solution with a decaying deformation rate is found, equivalent to the results obtained by Bell et al. (2008a). However, because both the standard and the DPS deformation time series show a reasonable result, the most likely true solution cannot be assessed based on the time series plot only. A quality indicator should be used to determine the most likely solution.

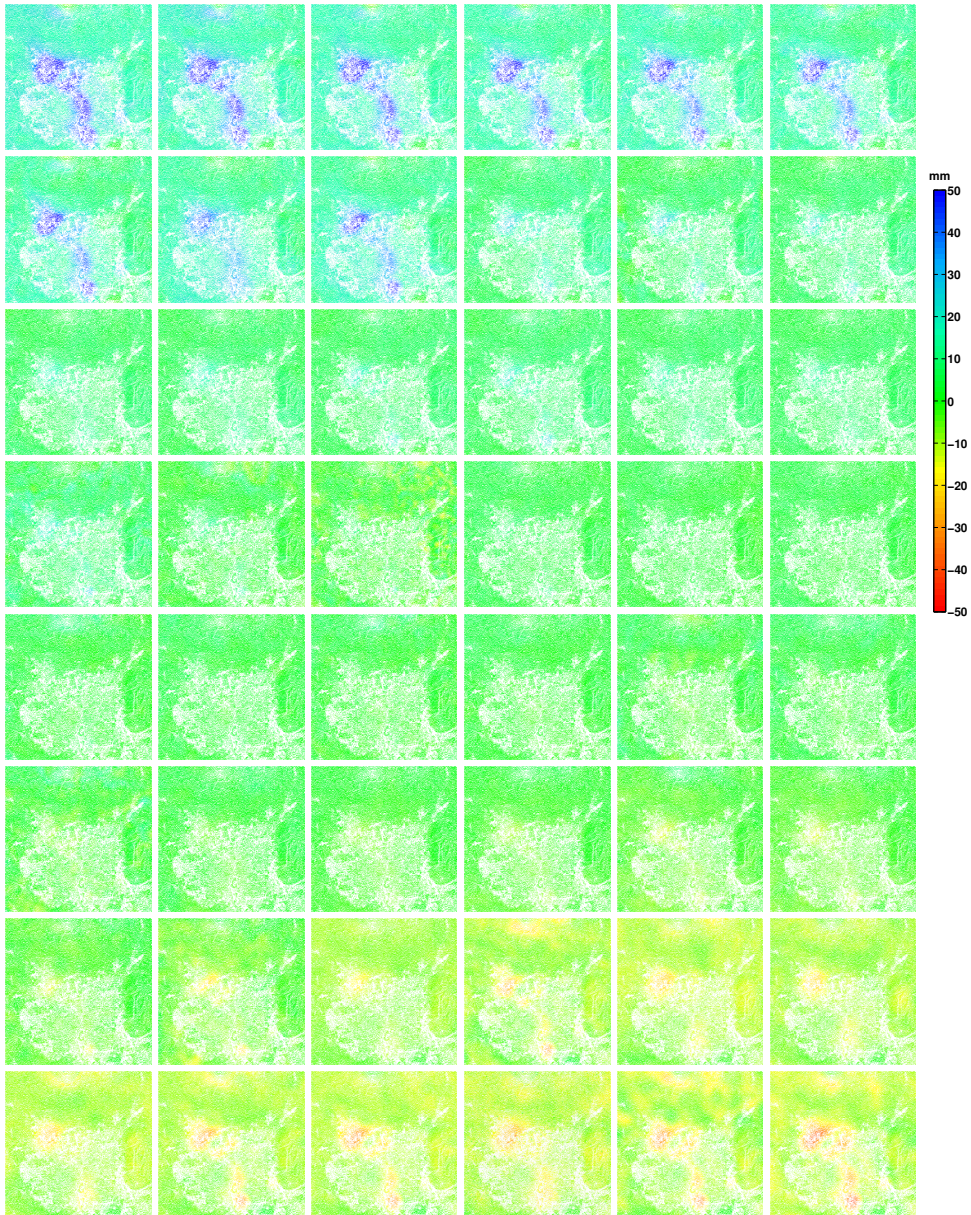


Figure 7.11: Approach 3. Deformation Phase Screens (DPS) for the Las Vegas test case obtained by least-squares prediction. The prediction is based on the PS detected by an initial DePSI analysis applying a linear deformation model (standard approach, equal to results in Section 7.2). Because the prediction is based on the deformation time series, any non-linearity in the deformation behavior is reflected in the DPS.

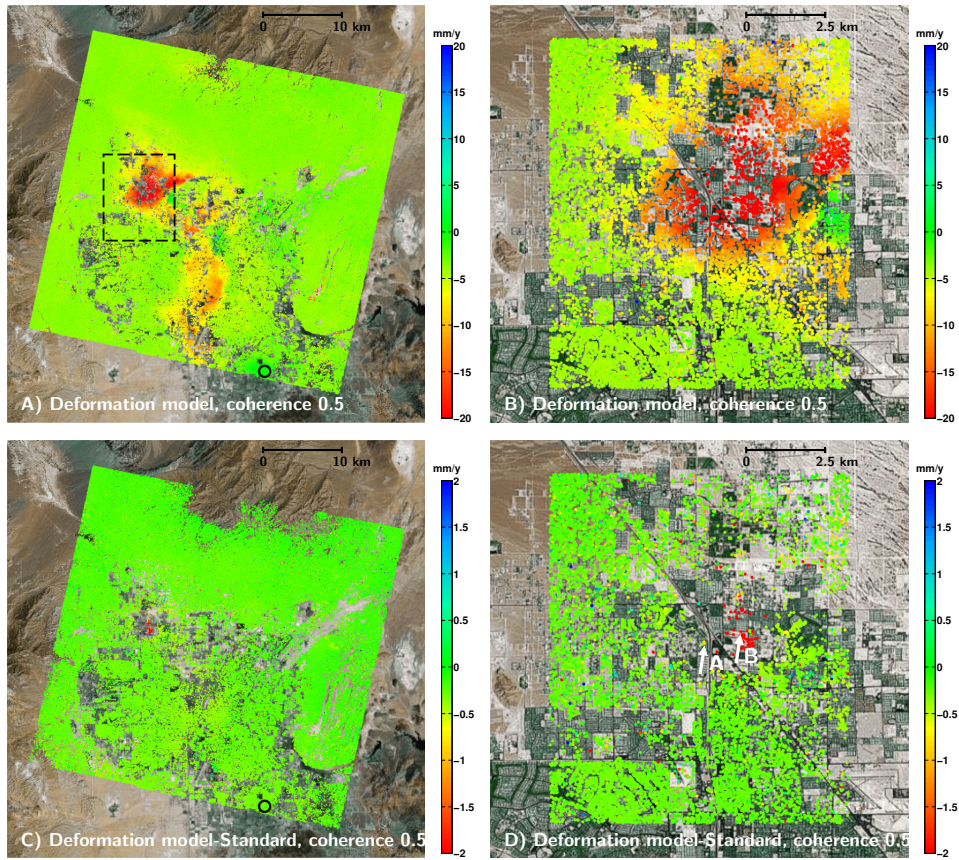


Figure 7.12: Approach 3. Top row) Linear deformation rates after applying the Deformation Phase Screen (DPS) approach. The PS are selected based on an ensemble coherence threshold of 0.5, resulting in $1.11N_{ref}$ detected PS. The right column shows the detailed results within the rectangular box in the figure on the top-left. Bottom row) Difference between the linear deformation rates of the common PS obtained by the standard approach and the DPS processing. Only the PS which are detected in all advanced processing schemes are shown. The largest differences occur in the region with the strongest subsidence rates.

7.5 Sequential deformation model testing

7.5.1 Algorithm of sequential deformation model testing

Another strategy aiming at increasing the number of detected PS is by sequential testing of different temporal deformation models to adapt to the local deformation history (van Leijen and Hanssen, 2007a,b). Conventional PSI algorithms apply global deformation models (Colesanti et al., 2003a; Kampes, 2006) to unwrap the data and estimate the parameters of interest. Hence, a single model is used for the whole area. However, deformation phenomena often have a local character. For example, in case the processed area contains a subsidence bowl with a complex displacement history. Applying global deformation models will either result in an under-parameterization of the subsidence in the bowl or an over-parameterization of the surrounding area. That is, when the global

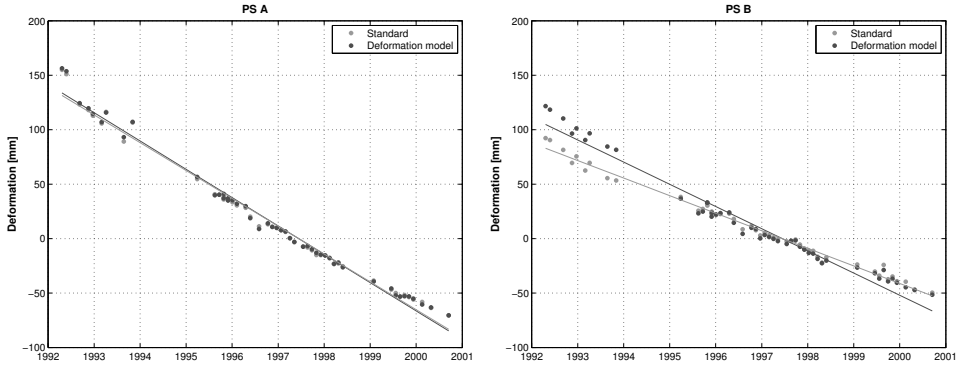


Figure 7.13: Approach 3. Deformation time series of two representative PS, see Figure 7.12, bottom-right, for the locations A and B. Both the result of the standard processing and applying the DPS approach are shown. The solid lines represent the linear deformation rates. For point A the time series are almost identical. Regarding point B, an alternative solution is found. The most likely true solution cannot be assessed based on the time series plot only.

deformation models are based on the surrounding (stable) area, e.g., a linear model, possible non-linear displacement profiles in the subsidence bowl may not allow correct ambiguity resolution. Moreover, even when the phase is unwrapped correctly, the large residues will result in a low quality assessment (e.g., based on coherence, see Section 6.2). The false rejection of PS results in gaps in the PS distribution. On the other hand, when the global deformation models are based on the displacements in the subsidence bowl, the surrounding areas are unwrapped with unnecessary complex models, increasing the chance on unwrapping errors (denoted as type-II errors, see Section A.2 and the results in Section 7.3). Therefore, deformation models adaptive to the local circumstances are desirable.

The sequential testing algorithm can be applied to the temporal ambiguity resolution of both the first-order as higher-order PSC. The algorithm is initialized with the selection of a set of temporal deformation models. Then, each phase double-difference between two PSC is unwrapped in time applying the sequential scheme of alternative hypothesis testing until a deformation model fits to the data sufficiently. A linear model is a suitable *null hypothesis* (see Section A.2) because of the maximum redundancy in the estimation process. The testing criterion for accepting a hypothesis is the a-posteriori variance factor $\hat{\sigma}^2$ denoted by Eq. (4.53), which is repeated here for convenience

$$\hat{\sigma}^2 = \frac{\hat{\underline{e}}^T Q_y^{-1} \hat{\underline{e}}}{m - n}. \quad (4.53)$$

Here, \underline{e} is the vector of residuals between the unwrapped phase and the deformation model, m is the number of observations and n the number of unknown parameters. The covariance matrix Q_y describes the stochastic properties of the interferometric phase observations. A $\hat{\sigma}^2$ of 1.0 indicates that the covariance matrix used in the estimation process correctly describes the dispersion of the observations. Recall that this matrix was obtained by Variance Component estimation (VCE), see Section 4.4. A value of 2.0 means that the stochastic model used is a factor two too optimistic (assuming that the functional model is correct). Hence, the a-posteriori variance factor scales the a-priori

stochastic model for a specific double-difference.

Applying the sequential scheme of hypothesis testing, a certain deformation model is accepted when $\hat{\sigma}^2$ is smaller than 1.0. Otherwise, the next model is tested until the complete set of models is evaluated. For computational efficiency, the sequential testing scheme is performed in batch, that is, a certain model is applied for a set of double-differences, after which the next model is applied to a subset of these arcs which did not pass the test. For each arc the lowest $\hat{\sigma}^2$ and the corresponding model are stored. When all models are evaluated and even the best model for an arc is not fulfilling the threshold, the arc is still considered and the solution with the lowest variance factor is taken. Optionally, an additional variance factor threshold can be applied to remove very low quality solutions. A spatial testing procedure will finally test the correctness of the temporal unwrapping, see Sections 5.1 and 5.4.

7.5.2 Application of sequential deformation model testing

Application of the sequential testing approach results in the PS as shown in Figure 7.14. The deformation models evaluated are the linear, quadratic, and cubic model, with or without an additional periodic signal. In total $0.96N_{\text{ref}}$ PS are detected using the coherence threshold of 0.5, meaning a decrease of more than 10000 PS with respect to the standard approach. When observing the total number of detected PS, i.e., without the additional coherence threshold, only slightly more PS appear to be detected. Hence, only a few PS with a low coherence level are detected, especially compared to the number for the standard approach (422496 PS detected in total, 363058 with a coherence above 0.5). Apparently, a considerable number of low quality PS are discarded by the sequential testing scheme. The cause lies in the selection of different deformation models for the connecting arcs to a certain PSC. The different models result in differences in the estimated ambiguities, causing the rejection of the PSC in the spatial testing scheme. Especially the low quality PS are sensitive to this effect.

Figure 7.14 (bottom row) shows that the linear component of the deformation time series shows differences compared to the standard approach. The pattern is similar to the result obtained by direct application of the periodic+cubic model, see Figure 7.9, since this model is used in the final estimation of parameters based on the unwrapped time series. However, the number of detections is strongly increased ($0.96N_{\text{ref}}$ versus $0.76N_{\text{ref}}$ PS). Hence, the sequential testing scheme is better able to detect PS compared to a general application of an extended deformation model. Moreover, the number of false detections is slightly reduced.

When analyzing the deformation time series of PS A and B, it appears that in both cases an alternative solution is obtained compared to the standard approach, see Figure 7.15. Whereas in the previous approaches no quantitative assessment of the most likely true solution could be given, here the variance factor used during the processing has indicated that this solution best fits to the data. Hence, a gradual decrease of the deformation rate appears to reflect the true physical behavior in the region. This also corresponds to the results obtained by Bell et al. (2008b), where different subsequent periods were analyzed to detect the change in deformation rate. They observed maximum subsidence rates up to -30 mm/y in the 1992-1996 period and maximum rates up to -20 mm/y between 1996 and 2000. However, here an even higher deformation rate between 1992-1996 of -40 mm/y is obtained which appears to fit the data better.

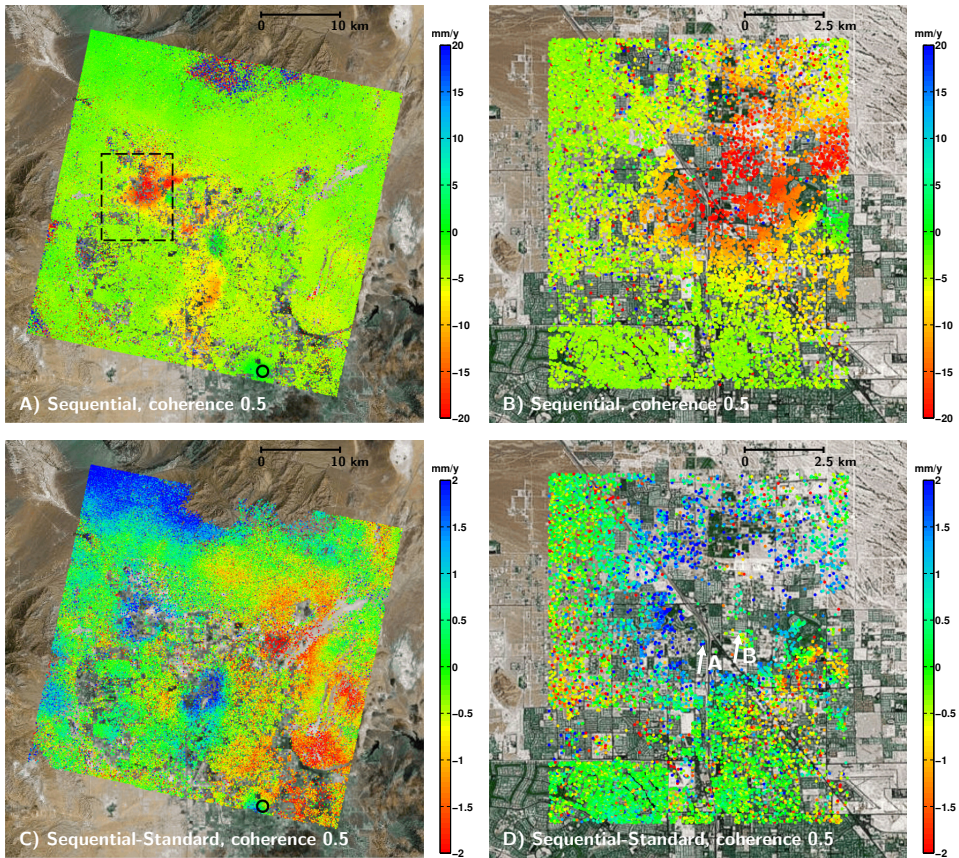


Figure 7.14: Approach 4. Top row) Linear deformation rates after applying the sequential testing approach. The PS are selected based on an ensemble coherence threshold of 0.5, resulting in $0.96 \cdot N_{\text{ref}}$ detected PS. The right column shows the detailed results within the rectangular box in the figure on the top-left. Bottom row) Difference between the linear deformation rates of the common PS obtained by the standard processing scheme and the sequential testing processing. Only the PS which are detected in all advanced processing schemes are shown. Significant changes in the linear component of the deformation time series occur. The pattern is comparable to the result obtained by direct application of the periodic+cubic model, although differences are also visible, see Figure 7.9.

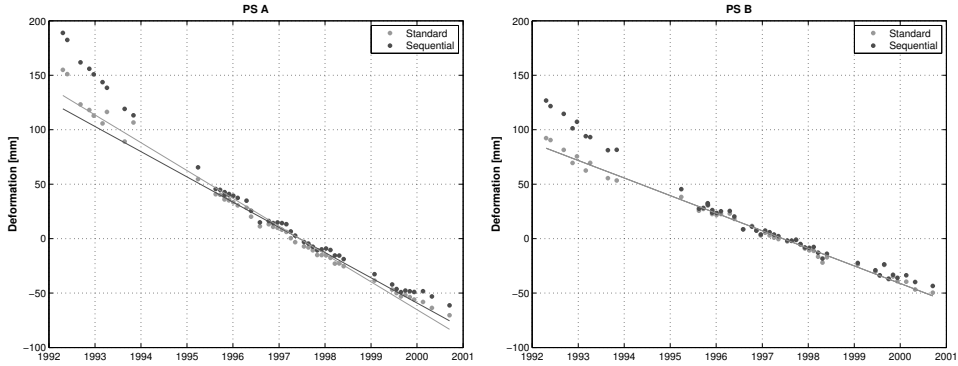


Figure 7.15: Approach 4. Deformation time series of two representative PS, see Figure 7.14, bottom-right, for the locations A and B. Both the result of the standard processing and applying the sequential testing approach are shown. The solid lines represent the linear part of the model. For both PS an alternative solution compared to the standard approach is found. Since the solutions are obtained based on the variance factor indicating the goodness-of-fit to the data, these solutions are assumed to represent the true behavior best.

Hence, extended deformation models are needed to capture the true deformation behavior, which could not be retrieved by the linear model used in the previous study. Note that a similar deformation behavior was also obtained for PS B using the Deformation Phase Screen approach, but not for PS A. In conclusion, although application of the sequential testing scheme results in a lower number of detected PS compared to the standard approach, the reliability of the results increases.

7.6 Prognosis-based densification

7.6.1 Algorithm of prognosis-based densification

Instead of performing the hypothesis testing algorithm for each connecting arc, the prognosis-based densification method only applies an extended deformation model when necessary from a PS density perspective (van Leijen and Hanssen, 2007b). The method is based on a prognosis of the number of PS within a certain area, for example a pre-defined grid cell of a certain size, see also Figure 7.16. The prognosis is based on the normalized amplitude dispersion, which is an indicator of phase stability (Ferretti et al., 2001), see Section 3.3.1. The relation is shown in Figure 3.5. The figure shows that a low normalized amplitude dispersion indicates low scattering noise.

Based on the number of PSC within a certain grid cell, a prognosis is made of the number of PS. When the number of detected PS applying the null hypothesis (e.g., linear model) is significantly lower than the number of predicted PS (for instance less than half), an extended deformation model is applied and tested. This procedure is applied iteratively until the number of detected PS is satisfying. In each iteration, the different connecting arcs to a PSC are used to test the solution. This is different compared to the sequential testing approach, where a sufficiently fitting deformation model is selected first for each arc, followed by a test on the phase ambiguities. Hence, unlike for the sequential testing approach, in the prognosis-based densification the test of the

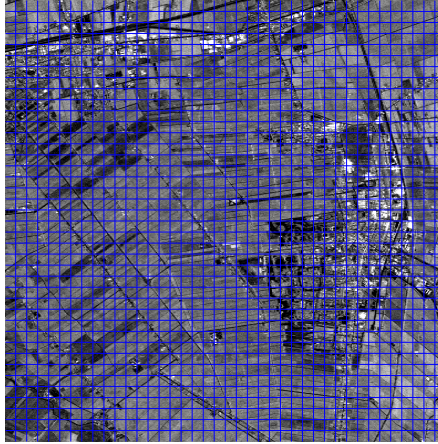


Figure 7.16: Approach 5. Example of a grid used in the prognosis-based densification approach. The number of detected PS within each grid cell in comparison with a prognosis based on the normalized amplitude dispersion is an additional constraint in the testing scheme.

ambiguities is based on equal deformation models. In case a certain model already results in sufficient detected PS, further application of the iteration scheme is not necessary for that particular grid cell. Hence, the computational burden is only increased when required from a PS density point of view. The rationale behind this approach is that for many geophysical phenomena, showing a certain spatial smoothness, a minimal amount of detected PS is sufficient to capture the associated deformation signal. A demanding analysis using all PS Candidates is in this case unnecessary.

7.6.2 Application of prognosis-based densification

The prognosis-based densification approach is applied to the Las Vegas test site using a grid with a spacing of 300 m. The same set of PSC is used as by the other approaches. As in the sequential testing approach, the linear, quadratic, and cubic model, with or without an additional periodic signal, are evaluated. The iterative scheme of model testing is applied until the user defined cut-off percentage of detected PS compared to the total amount of PSC in the grid cell is reached, or until all pre-defined deformation models are evaluated. To reduce the computational load considerably, a percentage of for example 50% could be chosen. Here, a percentage of 80% is applied, to demonstrate the full potential of the iterative use of the various deformation models.

Application of the prognosis approach results in the detection of $1.16N_{\text{ref}}$ PS with a coherence above 0.5, see Figure 7.17. Hence, more than 80% of the number of PSC (480625) is detected. Compared to the standard approach, almost 60000 additional PS are found. Part of this increase is due to an increase in the number of false detections. However, this number is relatively small and smaller compared to the results obtained by the extended deformation models or sequential testing approach. Figure 7.17 also shows the difference with the results obtained by the standard approach, which are equivalent to the results by the sequential approach. This is primarily because the same algorithm is used by both approaches to obtain the first-order network based on the same set of extended deformation models.

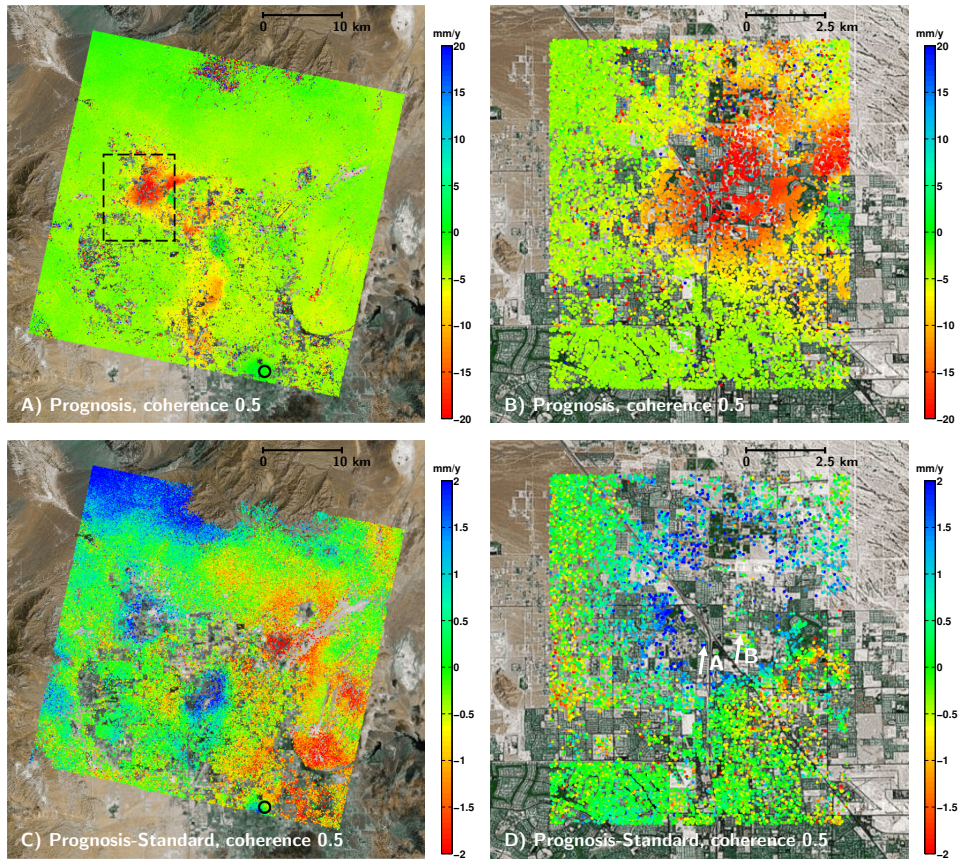


Figure 7.17: Approach 5. Top row) Linear deformation rates after applying the prognosis-based densification approach based on an iteration scheme until at least 80% of the PSC are detected as PS. The PS are selected based on an ensemble coherence threshold of 0.5, resulting in $1.16N_{ref}$ detected PS. The right column shows the detailed results within the rectangular box in the figures on the left. Bottom row) Difference between the linear deformation rates of the common PS obtained by the standard approach and the prognosis based processing. Only the PS which are detected in all advanced processing schemes are shown. Significant changes in the linear component of the deformation time series occur. The pattern is comparable to the result obtained by the sequential testing approach, primarily because the same first-order network is used.

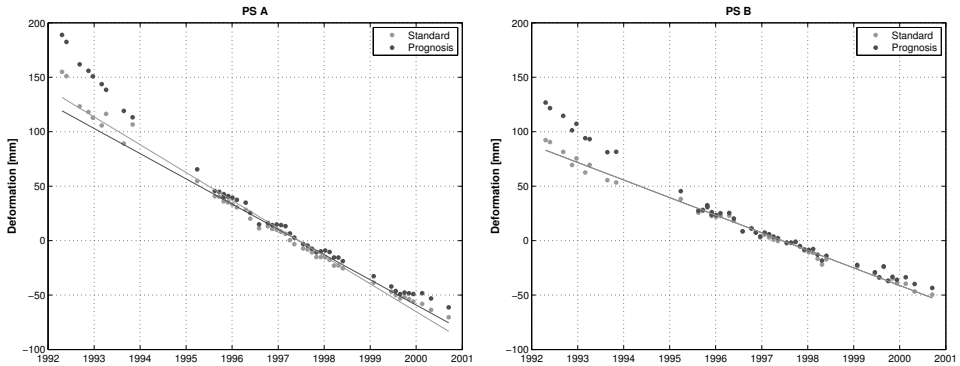


Figure 7.18: Approach 5. Deformation time series of two representative PS, see Figure 7.7, bottom-right, for the locations A and B. Both the result of the standard processing and applying the prognosis-based densification approach are shown. The solid lines represent the linear part of the model. For both PS an alternative solution compared to the standard approach is found. Since the solutions are obtained based on the variance factor indicating the goodness-of-fit to the data, these solutions are assumed to represent the true behavior best. Moreover, the results are equal to the time series obtained by the sequential testing approach.

Figure 7.18 show the deformation time series of points A and B. They are equal to the time series obtained by the sequential testing approach. Hence, the same decreasing deformation rate is observed. For PS B, they correspond to the same rates as found by the Deformation Phase Screen approach and in the earlier study by Bell et al. (2008b). However, regarding PS A, a higher deformation rate of -40 mm/y in the 1992-1996 period is estimated. Since these time series are obtained based on the variance factor indicating the goodness-of-fit to the data, they are believed to represent the true deformation behavior best. Hence, the prognosis-based densification approach is not only able to detect more PS, the reliability of the deformation time series in general also increased, despite an increase in the number of false detections. Additional quality indicators are required to remove these false detections from the dataset.

7.7 Area of Interest processing

7.7.1 Algorithm of Area of Interest processing

The approaches previously presented are all based on a set of pre-selected Persistent Scatterer Candidates (PSC) using amplitude information. Although amplitude information is a good proxy for phase stability (see Section 3.3), some PS may however not be pre-selected and are therefore not detected. The alternative, evaluation of all pixels within the data stack, will result in a large computational burden. As a compromise, an *Area of Interest* (AoI) can be selected, in which, after a standard approach to determine the first-order network, each pixel is evaluated in the densification step, see Section 5.4. By applying the side lobe detection algorithm (see Section 3.4) the pixels corresponding to side lobes (and sub-main lobes) are excluded from the selection. Because the side lobe detection algorithm also contains the selection of local amplitude maxima, the number of selected PSC is still considerably smaller compared to the full number of pixels, see

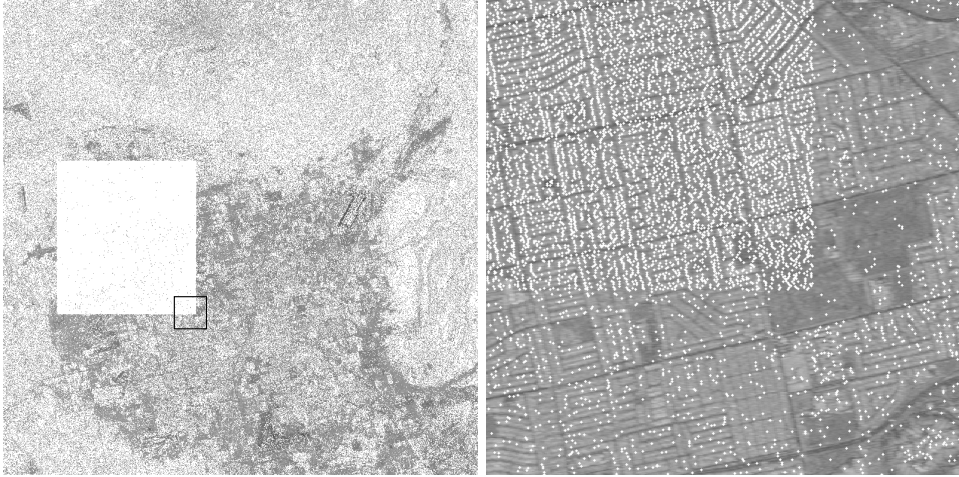


Figure 7.19: Approach 6. Selected PSC in case of an indicated Area of Interest. Left) Total test site, which clearly shows the rectangular Area of Interest with a much higher density of PSC. Right) Detailed view of the selected PSC for the region indicated by the black box in the figure on the left.

Figure 7.19. The Aol can either be rectangular, or of an arbitrary shape specified in a separate *mask* file. For example, a mask could be created which follows a certain rail track or a water defense structure, for which a detailed analysis is required.

7.7.2 Application of Area of Interest processing

The Area of Interest chosen for the Las Vegas test site is indicated with a white box in Figure 7.20A. The selected PSC are shown in Figure 7.19. The selection without a normalized amplitude dispersion threshold in the Area of Interest results in a significant increase in the density of PSC. In total $1.4N_{\text{PSCref}}$ PSC are selected in the whole test site using a normalized amplitude dispersion threshold of 0.45, as applied in the other approaches.

A linear deformation model is applied, both to construct the first order network as well as for the densification. As a result, the first order network is equal to the network obtained by the standard approach. Moreover, the common PS detected both in the Aol processing and the standard analysis show, as expected, the same estimates, see Figure 7.20 (bottom row). The same applies for the deformation time series, hence, the deformation time series of points A and B are equal to the series obtained by the standard approach. Therefore, the decreasing deformation rate as estimated by the sequential testing and prognosis approach is not observed.

The total number of detected PS is $1.17N_{\text{ref}}$, which is an increase of more than 60000 compared to the standard approach. More relevant in this case, the number of PS detected in the rectangular black box (which is part of the total Aol specified, see Figure 7.20A) increases to $2.98N_{\text{ref}}$, visible by comparing Figures 7.6 and 7.20, A and B.

As indicated in Section 7.2, to enable the comparison of the results by the various approaches, a standard threshold of 0.5 of the ensemble coherence estimator is applied to select the final set of PS. However, as discussed in Section 6.2, this global quality

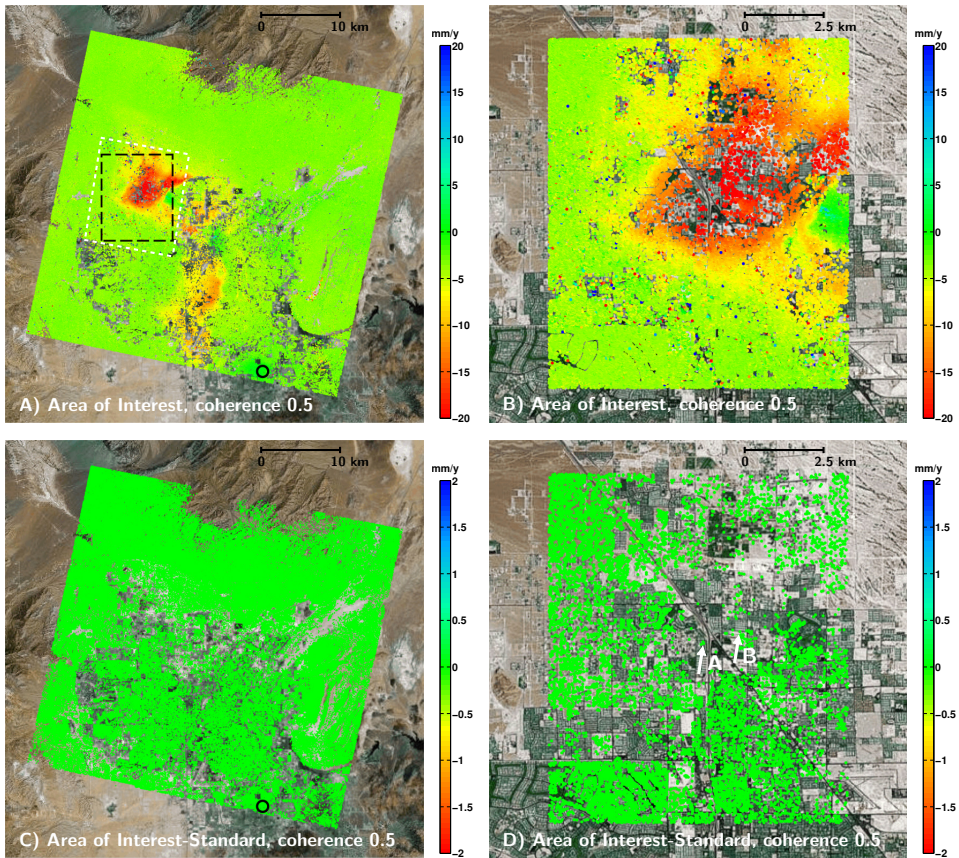


Figure 7.20: Approach 6. Top row) Linear deformation rates after applying the Area of Interest (Aol, white box) approach. The PS are selected based on an ensemble coherence threshold of 0.5, resulting in 426379 detected PS. The right column shows the detailed results within the black rectangular box in the figure on the top-left. Bottom row) Difference between the linear deformation rates of the common PS obtained by the standard approach and the Aol processing. Since in both cases only a linear deformation model is applied, the results of the common PS are the same.

indicator, which is defined with respect to the reference point, is not only showing the noise level of the measurements, but is also sensitive to model imperfections. Therefore, the use of local quality indicators may be beneficial to increase the number of detected PS, since they operate at shorter distances, making them less sensitive for the model used. Examples are shown in Figure 7.21. Figure 7.21A contains all the detected PS without any quality threshold. The result shows a large number of false detections. Hence, the testing scheme to detect inconsistencies in the phase ambiguities of multiple connecting arcs to a PSC is not sufficient for a reliable detection of PS. Apparently, often a consistent, but wrong, solution for multiple arcs is obtained. The top-right figure shows the set of PS after applying the standard global ensemble coherence threshold of 0.5 (same figure as shown in Figure 7.20). A large part of the false detections is removed. However, by comparing the top-left and top-right figure, it is observed that especially in the center of the subsidence bowl a large part of the PS showing a consistent signal is

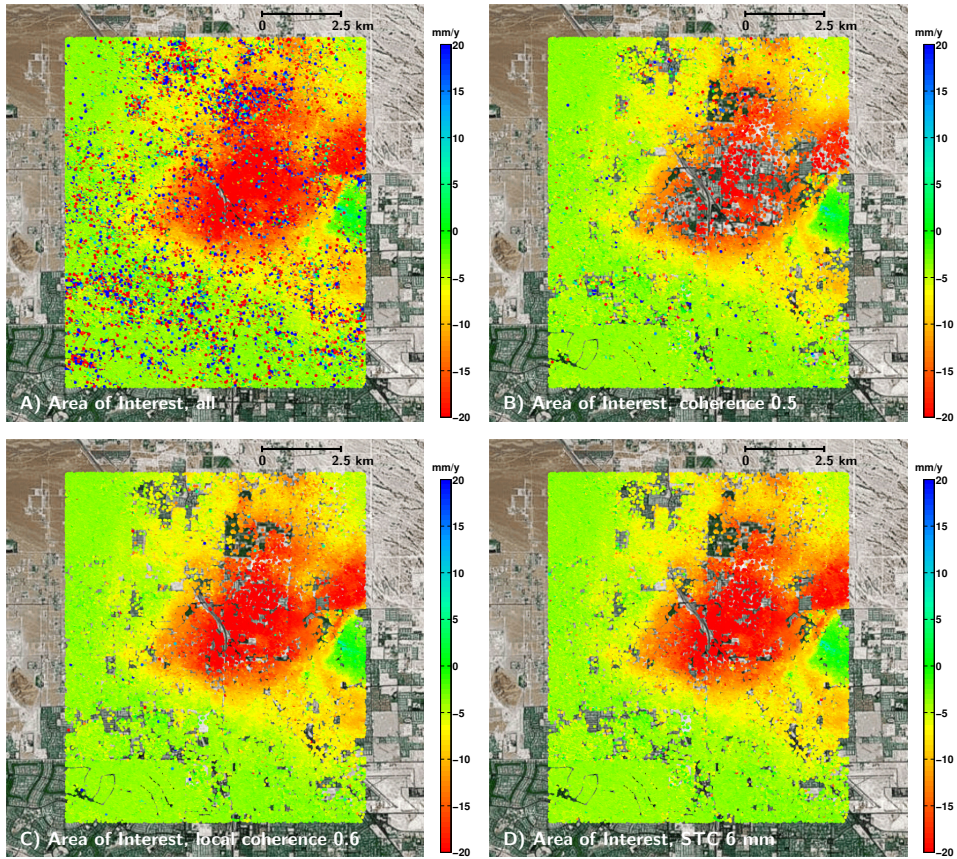


Figure 7.21: Approach 6. Comparison of detected PS in case of the Area of Interest approach after applying different global and local quality indicator thresholds. Top-left) Detected PS without application of a quality threshold. Top-right) Detected PS with a global ensemble coherence above 0.5. Bottom-left) Detected PS with a local ensemble coherence above 0.6. Bottom-right) Detected PS with a local determined spatio-temporal consistency (STC) below 6 mm. The local quality indicators (bottom row) are better able to preserve the PS in the center of the subsidence bowl.

removed. The threshold can be reduced, however, this would result in a strong increase in the number of false detections. Using a local ensemble coherence threshold of 0.6 (bottom-left) or a spatio-temporal consistency (STC) threshold of 6 mm (bottom-right), the signal in the center of the bowl is much better preserved. Moreover, the number of false detections is in both cases further reduced. Therefore, in general local quality indicators should be used for the detection of PS. Nevertheless, although the results in Figure 7.21 show a consistent distribution of PS, even in the subsidence bowl, the deformation time series do not show the decreasing deformation rate, which is expected to be closer to the true deformation behavior in the area. Hence, application of a linear deformation model only does not provide reliable results.

7.8 Time frame processing

7.8.1 Algorithm of time frame processing

Similar to a spatial selection of an Area of Interest, other specific analysis require a selection of radar acquisitions in the time domain, denoted as time frame processing. Normally all available radar acquisitions from a certain sensor and orbit are used for an analysis with DePSI. This, because with an increasing number of acquisitions, the various phase contributions such as deformation, height, and atmospheric signal delay, can better be separated. However, when an area is analyzed where construction works occurred during the acquisition time span, e.g., the construction of a new rail track or residential area, the full time span will not be coherent in that area. In such a situation, the time frame processing option can be applied (see, e.g., Arikan and Hanssen (2008)). Here, all available acquisitions are used to estimate the Atmospheric Phase Screen (APS), whereas the densification is based on a subset of interferograms covering the time span after the construction works, see module 6 in Figure 3.1. Hence, the surrounding areas are used to estimate the atmospheric signal, after which the atmosphere of the (relatively small) area with construction works is interpolated by least-squares prediction, see Section 5.3. Note that the master acquisition should be chosen within the selected time frame. If this is not the case, the random master phase contributions will bias the temporal ambiguity resolution, reducing the success rate of correct ambiguity resolution.

7.8.2 Application of time frame processing

The time frame processing is applied to the Las Vegas test site using a subset of 25 radar images acquired since January 1997 for the densification. Also here the Area of Interest as specified in Section 7.7 is applied. The deformation model is restricted to a linear deformation rate only. The results of the analysis are shown in Figure 7.22. In total $1.51N_{\text{ref}}$ PS are detected with a minimal coherence of 0.5. However, the figures on the top show, based on the large number of extreme values, a large number of false detections. Due to the relatively small number of acquisitions used, often an erroneous fit of the phase observations to a linear model is found. Because of the small size of the data stack, the ensemble coherence estimator is also less distinctive. Therefore, an increase of the ensemble coherence threshold to 0.7 is required to obtain a better selection of $0.96N_{\text{ref}}$ reliable PS. The result is shown in Figure 7.23B. As reference, the top-left figure shows the selected PS without quality threshold. The bottom row visualizes the results with a local ensemble coherence of 0.7 and a Spatio-Temporal Consistency (STC) of 4 mm, respectively. Note that these thresholds are also adjusted in comparison with the values used for the Area of Interest processing, to ensure a proper selection of reliable PS for this short time period.

The comparison of the time frame results with those of the standard approach, see bottom row in Figure 7.22, shows that the deformation rate in the center of the subsidence bowl is decreased for the short time frame at the end of the full acquisition period. This is in agreement with the earlier observation of a decrease in the deformation rate in the time series obtained by the sequential testing and prognosis approach. This is also visualized for points A and B in Figure 7.24.

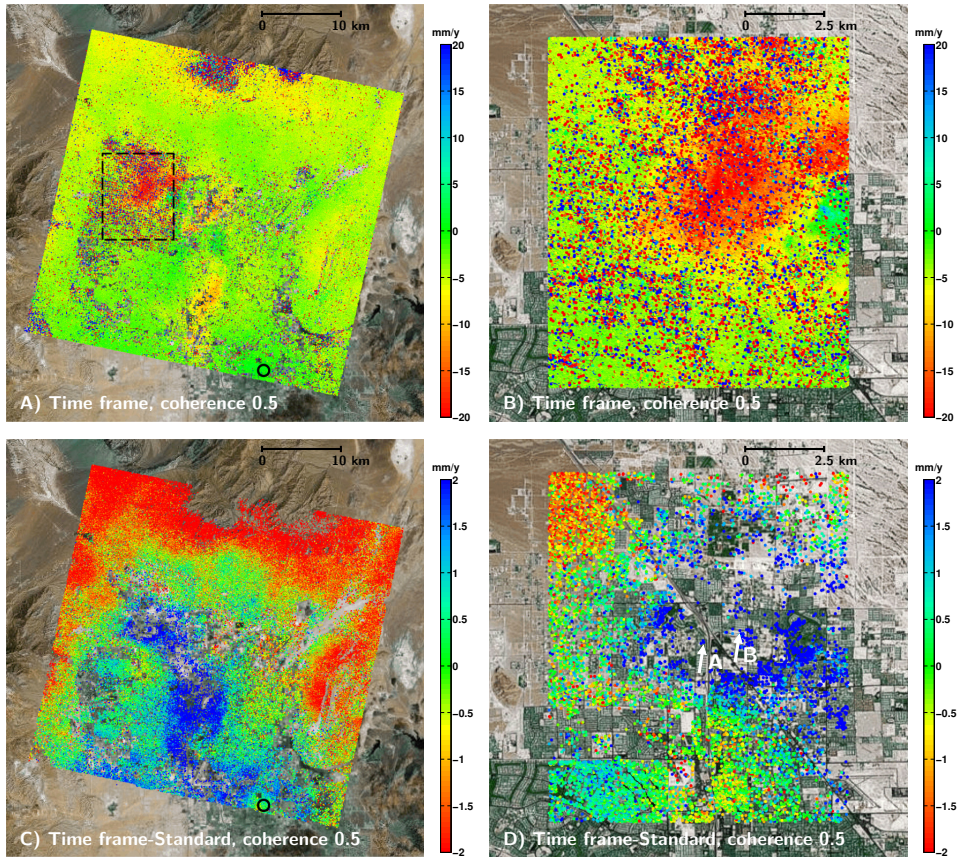


Figure 7.22: Approach 7. Top row) Linear deformation rates after applying the time frame processing approach. A subset of 25 images acquired between 1997 and 2000 are used for the final estimation of the deformation time series. The PS are selected based on an ensemble coherence threshold of 0.5, resulting in $1.51N_{ref}$ detected PS. The right column shows the detailed results within the rectangular box in the figures on the left. Bottom row) Difference between the linear deformation rates of the common PS obtained by the standard approach and the time frame processing. The difference shows a decrease in the deformation rate of the center of the subsidence bowl for the short time span, which is in correspondence with the decrease of deformation rate observed earlier using the sequential testing and prognosis-based approaches.

The objective of a time span processing is the measurement of the deformation of objects which are not coherent for the full time span. Although here a general example is used covering part of Las Vegas without any specific attention for construction works, some areas of detected PS are visible, which are not detected when observing the full time frame. Examples of two of these regions are indicated in Figure 7.23D, with a white circle. The hypothesis is that these are newly build areas, showing only coherence after 1996. For practical application of this processing approach, a-priori information regarding construction works is required. For a generic approach, automatic detection of change in coherence level is required. Such PS are often denoted as semi or temporary Persistent Scatterers (Basilico et al., 2004). This approach is however not implemented here.

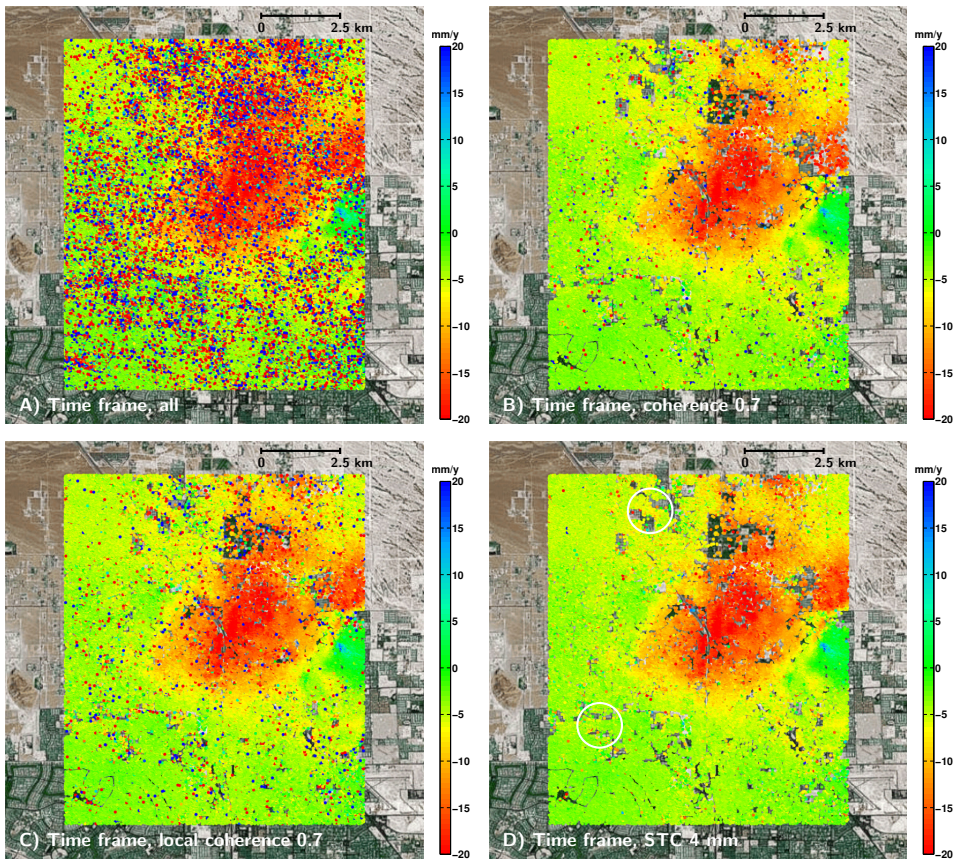


Figure 7.23: Approach 7. Comparison of detected PS in case of the time frame processing approach after applying different global and local quality indicator thresholds. Top-left) Detected PS without application of a quality threshold. Top-right) Detected PS with a global ensemble coherence above 0.7. Bottom-left) Detected PS with a local ensemble coherence above 0.7. Bottom-right) Detected PS with a local determined spatio-temporal consistency (STC) below 4 mm. Adjustment of the threshold values compared to the Area of Interest processing results is required due to the limited number of acquisitions used. The white circles indicate two areas with PS, which are not detected when analyzing the full acquisition time span (see Figure 7.21). Most likely these are newly build areas, showing only coherence after 1996.

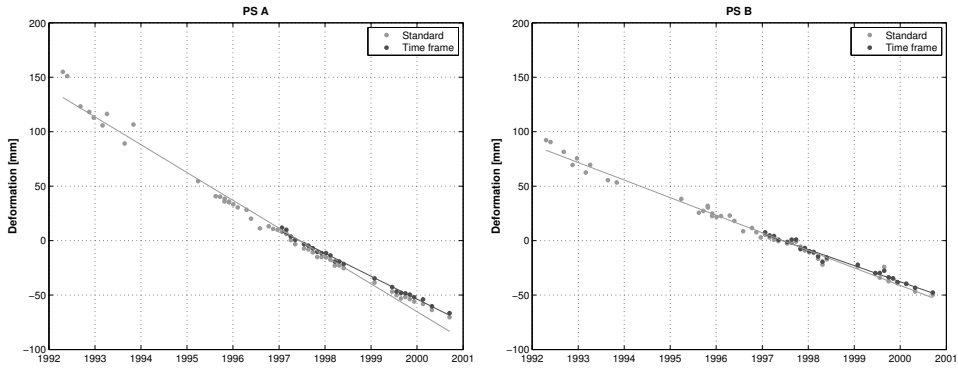


Figure 7.24: Approach 7. Deformation time series of two representative PS, see Figure 7.22, bottom-right, for the locations A and B. Both the result of the standard processing and applying the time frame approach are shown. The solid lines represent the linear deformation rates. For both PS a reduced deformation rate is observed for the short time span.

7.9 Summary and conclusions

The results of the seven different processing approaches presented in this chapter are summarized in Table 7.2 for the full region and Table 7.3 for the small rectangular area indicated in Figure 7.22. The tables contain the number of Persistent Scatterer Candidates (PSC) evaluated, the number of PS detected after the testing scheme based on the mode solution (see Section 5.4), and the number of PS detected after an additional ensemble coherence threshold. Moreover, the relative computation time with respect to the standard approach using a linear deformation model is given.

The relative computation times required by the extended deformation models (denoted as methods 2a and 2b in Tables 7.2 7.3) only show a slight increase with respect to the standard approach. This is a characteristic of the integer bootstrap estimator used to resolve the phase ambiguities. A similar small relative increase will apply for the integer least-squares (ILS) estimator, although the overall computation time for ILS is much larger compared to the bootstrap estimator, see also Table 7.2. However, the use of the ambiguity function would result in an enormous increase in the computation time due to a strongly growing solution space, see Section 4.7.

The estimation of a Deformation Phase Screen (DPS) causes a doubling of the time. This is directly related to the repetition of the densification step, after prediction of the DPS. The sequential testing scheme is much less efficient. Because a maximum of six different models is evaluated for each arc, the estimation time increases considerably. The same range of six models is considered in the PS density prognosis approach. However, unlike in the sequential approach, here in each iteration the ambiguity test is applied, based on the same model for all connecting arcs to a certain PSC. Use of the same model increases the consistency of the solutions considerably, with a strong reduction of the number of models to be evaluated as result. The computation time is therefore only 1.5 times longer compared to the standard approach. The increase of the computation time for the Area of Interest approach is directly related to the larger number of PSC to be evaluated. The Time frame approach requires on the other hand much less time due to a reduction of the number of acquisition used, and thereby the number of ambiguities

Table 7.2: Overview of number of detected PS using different approaches in the full Las Vegas test area. All values are given as a factor with respect to the results by the standard approach using the bootstrap estimator (absolute numbers given in brackets). Apart from the number of evaluated PSC and the number of detected PS, also the amount of PS after application of ensemble coherence thresholds is shown. In each analysis the same set of PSC is evaluated (only increased for the Area of Interest and Time frame processing), which is selected based on the normalized amplitude dispersion. Only for cases 1b and 1c integer least-squares and the ambiguity function are used instead as reference. Also the computation time factor with respect to the benchmark is given, which took 16.1 hours on the computing platform used.

#	Approach	Computation time factor	#PSC	#PS	Coherence threshold		
					0.5	0.6	0.7
1a	Standard, bootstrap	1.00	1.00	1.00	1.00	1.00	1.00
		(16.1 h)	(480625)	(422946)	(363058)	(281034)	(154941)
1b	Standard, ILS	10.52	1.00	1.04	1.03	1.01	0.99
1c	Standard, ambiguity function	0.82	1.00	1.08	1.07	1.04	1.02
2a	Periodic	1.02	1.00	0.94	0.98	1.01	1.05
2b	Periodic+cubic	1.05	1.00	0.65	0.76	0.94	1.29
3	Deformation Phase Screen	2.10	1.00	1.00	1.11	1.28	1.71
4	Sequential	5.68	1.00	0.83	0.96	1.21	1.61
5	Prognosis	1.50	1.00	1.04	1.16	1.29	1.56
6	Area of Interest	1.34	1.40	1.25	1.17	1.13	1.09
7	Time frame	0.43	1.40	1.36	1.51	1.68	2.25

to estimate.

The number of detected PS varies, not considering the Area of Interest and Time span results, from $0.76N_{\text{ref}}$ to $1.16N_{\text{ref}}$ for the full area, and between $0.93N_{\text{ref}}$ and $1.27N_{\text{ref}}$ for the small rectangular region when applying an ensemble coherence threshold of 0.5, see Tables 7.2 and 7.3. The smallest amount of PS is obtained using a Periodic+Cubic model for the full region, whereas the prognosis-based densification results in the largest set of detected PS. The tables also show the decrease in the number of PS with increasing coherence threshold. Since the use of extended deformation models reduces the influence of model imperfections on the coherence estimator, a relatively large amount of PS remain for the advanced approaches with increasing threshold.

The tables do however not show the reliability of the results. Visual analysis of the various figures in this chapter indicates that, assessed by the number of PS with extreme deformation rates, the number of false detections varies considerably between the approaches. The number of false detections is very limited when applying the standard approach or the DPS estimation, hence, when only a linear deformation model is applied in the ambiguity resolution. Most false detections are obtained by the Periodic+Cubic model and the sequential testing approach. The Periodic model and the prognosis-based densification approach give intermediate results. However, in this assessment also the total number of detected PS should be observed. For example, the standard approach outperforms the prognosis-based method regarding false detections, but the total number of PS is strongly increased with the advanced method. Moreover, the reliability of the deformation time series, that is, whether they describe the actual deformation

Table 7.3: Overview of number of detected PS using different approaches in the small area in Las Vegas indicated in Figure 7.22. All values are given as a factor with respect to the results by the standard approach using the bootstrap estimator (absolute numbers given in brackets). Apart from the number of evaluated PSC and the number of detected PS, also the amount of PS after application of ensemble coherence thresholds is shown. In each analysis the same set of PSC is evaluated (only increased for the Area of Interest and Time frame processing), which is selected based on the normalized amplitude dispersion. Only for cases 1b and 1c integer least-squares and the ambiguity function are used instead as reference. Also the computation time factor with respect to the benchmark is given, which took 16.1 hours on the computing platform used.

#	Approach	Computation time factor	#PSC	#PS	Coherence threshold		
					0.5	0.6	0.7
1a	Standard, bootstrap	1.00 (16.1 h)	1.00 (20929)	1.00 (17467)	1.00 (14274)	1.00 (11492)	1.00 (7544)
1b	Standard, ILS	10.52	1.00	1.05	1.06	1.03	1.01
1c	Standard, ambiguity function	0.82	1.00	1.11	1.07	1.03	1.01
2a	Periodic	1.02	1.00	0.93	1.01	1.05	1.10
2b	Periodic+cubic	1.05	1.00	0.76	0.93	1.13	1.37
3	Deformation Phase Screen	2.10	1.00	1.00	1.11	1.17	1.28
4	Sequential	5.68	1.00	0.89	1.09	1.34	1.61
5	Prognosis	1.50	1.00	1.09	1.27	1.38	1.50
6	Area of Interest	1.34	7.10	4.97	3.71	2.98	2.17
7	Time frame	0.43	7.10	6.51	7.27	6.92	6.91

behavior, should be considered. The figures throughout this chapter with deformation time series of points A and B indicate that a decaying deformation rate is observed when using the sequential testing, prognosis, or DPS approach. This effect is also observed by Bell et al. (2008b), where different subsequent periods are analyzed to detect the change in deformation rate. Application of the standard approach was not able to retrieve this deformation behavior.

In conclusion, the prognosis-based densification approach gives the best performance based on the number of detected PS, the reliability of the results, the relative low amount of false detections, and the computation time. Both the sequential testing approach and the prognosis-based method are able to retrieve the reducing deformation rate in the center of the subsidence bowl. However, regarding the number of false detections, the number of detected PS, and the computation time, the prognosis-based method outperforms the sequential testing scheme. This is mainly caused by the ambiguity test in each iteration with a certain deformation model, instead of after the iteration scheme, as is applied in the sequential approach. Hence, the use of the same deformation model for all connecting arcs to a certain PSC is recommended.

Apart from the prognosis and sequential approach, also the Deformation Phase Screen approach was able to retrieve part of the non-linear deformation signal in the subsidence bowl. Since in this approach only a linear deformation model was applied, also the ambiguity function could have been used for the temporal unwrapping. Hence, estimation of the DPS is a good alternative for algorithms which are restricted to the ambiguity function.

The use of extended deformation models for the full region not only results in less detected PS compared to the standard approach, also the number of false detections increases considerably. Hence, the higher degree of freedom in the ambiguity estimation

appears to result in a larger amount of inconsistent solutions for the connecting arcs of a certain PSC. Since the prognosis-based method using local deformation models resulted in an increase in the number of detected PS, it is shown that use of local deformation models is indeed beneficial.

Despite the tests on the estimated ambiguities, the results of all approaches show a certain degree of false detections. Hence, the ambiguity tests appear not to be sufficient to distinguish the true PS. In some cases, a consistent but wrong solution is obtained for the various arcs connecting a PSC. A further selection based on a threshold of a quality indicator, e.g., the coherence estimator or the Spatio-Temporal Consistency (STC), is therefore required to obtain the final selection of reliable PS. The results show that local quality indicators, such as the local coherence estimator and the STC, are less sensitive to model imperfections and therefore result in a better detection of PS.

In spite of the tests on the ambiguities and the use of additional quality indicators, still consistent solutions may be found with a sub-optimal deformation model, resulting in a wrong deformation time series. In this example of the Las Vegas test site the use of a linear deformation model resulted in detected PS in the center of the main subsidence bowl, which did not reflect the decreasing subsidence rate. Hence, interpretation of these results would have resulted in a wrong assessment of the past, and possibly prediction of future, deformation behavior of the area. Without the use of non-linear deformation models, this behavior would have remained undetected. In this specific dataset of ERS-1/2 radar images especially the 1993-1994 data gap is causing the range of alternative solutions found. Hence, in general the availability of a continuous dataset is desirable from a reliability perspective.

These conclusions are based on the results obtained by the integer bootstrap estimator. This estimator is chosen because the use of the ambiguity function is not possible due to the application of deformation models with multiple parameters, and the integer least-squares (ILS) estimator requires considerable more computation time. Although the performance of the bootstrap estimator is inferior to the integer least-squares estimator and the ambiguity function, it does enable the comparison of the various approaches, as is the objective of this chapter. Hence, it is assumed that equal conclusions would have been drawn based on results by the ILS estimator.

8.1 Conclusions

A new Persistent Scatterer Interferometry (PSI) algorithm is developed based on geodetic estimation and testing techniques. The algorithm is labeled as DePSI, the *Delft implementation of PSI*. DePSI is able to *detect* point scatterers with consistent reflection properties over time, for which the deformation time series can be *estimated* with sufficient reliability. Hence, the algorithm resolves a combined estimation and detection problem.

Various geodetic data analysis techniques are applied to estimate the deformation time series of the Persistent Scatterers (PS) from a set of radar images. The stochastic properties of the phase observations are estimated by least-squares variance component estimation (VCE). The phase ambiguities in the temporal domain are estimated by integer least-squares, integer bootstrapping, or the ambiguity function. A newly developed testing scheme based on the phase ambiguities is applied to detect and remove ambiguity errors and incoherent Persistent Scatterer Candidates (PSC). The Atmospheric Phase Screens are predicted by least-squares prediction. Due to the consistent framework of techniques, it is possible to propagate the errors, thereby obtaining a quality description of the results.

DePSI has been applied for various applications, such as subsidence due to gas extraction (Ketelaar, 2009), surface deformation due to mining (Perski et al., 2009; Caro Cuenca, 2012) and groundwater pumping (van Leijen and Hanssen, 2008; Osmanoglu et al., 2011; Cigna et al., 2012), the monitoring of water defense structures (Hanssen and van Leijen, 2008a,b; van Leijen et al., 2008), stability assessment of constructions (Perski et al., 2007; Chang and Hanssen, 2012), and atmospheric studies (Liu, 2012). Moreover, the algorithm is validated and certified by the European Space Agency (ESA) and the German Aerospace Center (DLR).

For the development of DePSI three main components were identified in the introduction: algorithm design, ambiguity resolution, and Persistent Scatterer detection. The conclusions in relation to these components are discussed below.

Algorithm design

The DePSI algorithm is characterized by a hierarchic structure of PS networks and an iterative approach to improve the stochastic model used for the estimations. The

hierarchical structure is based on first and higher-order networks of PS, comparable to the concept used for conventional geodetic measurement techniques. The first-order network forms the backbone of the analysis and aims to ensure the overall integrity of the full area analyzed, whereas the higher-order networks provide a further densification of the measurement points. The normalized amplitude dispersion is used as a proxy for coherence to pre-select the first and higher-order PSC. Hereby, the amount of data is strongly reduced and the hierarchy in the PSC is obtained.

An iterative scheme based on the first-order network is used to estimate and isolate the phase contribution due to error sources, i.e., satellite orbit inaccuracies and atmospheric delay. In each iteration the stochastic model of the corrected phase observations is updated by applying least-squares variance component estimation. The full coverage *Phase Screens* of the atmospheric signals are obtained by least-squares prediction.

Once the final first-order network is obtained, the deformation time series of the higher-order PSC are estimated and tested. After the final detected PS are georeferenced, the estimated deformation time series, together with their quality description, can be further analyzed and integrated with other geodetic measurements. The requirements for the georeferencing accuracy depend on the application, in combination with the spatial smoothness and extent of the deformation signal. When a high accuracy is desired, the sub-pixel position of point scatterers should be estimated, since it improves the geolocation accuracy with a factor three for typical satellite missions.

Ambiguity resolution

Each phase observation in the data stack has an unknown phase ambiguity. To estimate these ambiguities in the spatio-temporal domain, a two-step procedure is applied in DePSI. First, an estimation in the temporal domain is performed for each differential arc between two Persistent Scatterer Candidates. Three estimators are implemented and evaluated: integer least-squares (ILS), integer bootstrapping (IB), and the ambiguity function (AF). The ILS and AF estimator provide equivalent success rates for moderate deformation rates per arc. An advantage of the ambiguity function, together with the IB estimator, is the computation speed. However, a drawback of the ambiguity function estimator is that no additional deformation parameters can be inserted in the model without an unacceptable increase of the computational load. Hence, the estimation of for instance seasonal ground motion is not feasible. Using the ILS or IB estimator it is possible to add parameters without a significant increase of the computation time. However, the computational load of ILS increases significantly with an increasing number of images in the data stack. Therefore, the integer bootstrap estimator is a good alternative, although at the expense of performance.

The second step in the ambiguity resolution is a spatial integration of the estimated arcs based on a novel testing scheme to remove wrongly estimated arcs and inconsistent PSC. Hence, the phase stability determines the final selection of PS, instead of a pre-selection of points, as is often applied. Errors are therefore removed instead of distributed over the network. The testing is based on the integer ambiguities, instead of the real-valued parameters. This approach enables the use of varying deformation models in the temporal phase unwrapping, thereby ensuring a consistent network. Hence, models adapted to the local deformation behavior can be evaluated instead of a general model for the full area.

Persistent Scatterer detection

The objective of the algorithm is to detect the PS among the large amount of image pixels. To enable the detection based on the consistency of the phase observations, the deformation time series should be estimated. Experimental results show that the use of spatially local deformation models instead of a general model improves the PSI results. This conclusion is based on an increase in the number of detected PS, an increase in the reliability of the estimated deformation time series, and a decrease of the number of false detections. The assessment is based on the evaluation of seven different processing strategies for a test site in Las Vegas, which shows various deformation regimes. When only a linear deformation model is used, erroneous deformation time series are obtained in case of non-linear deformation behavior due to ambiguity errors. Hence, extended models with respect to the linear model should already be applied in the ambiguity resolution stage to obtain a reliable estimate of the time series. However, when applying an extended model to the full area, the number of detected PS reduces, whereas the number of false detections increase. This is caused by the higher degree of freedom in the mathematical model, leading to inconsistent solutions for the connecting arcs in the network. Therefore, extended deformation models should only be applied when required. When using these local models, an iterative scheme is used to select a sufficiently fitting model. Evaluation shows that the testing of the ambiguities should be performed in each iteration step, hence, when all connecting arcs to a certain PSC are resolved with the same model, instead of afterwards, when different models might be selected for the various arcs. This not only increases the number of detected PS, but also reduces the computation time considerably.

Furthermore, often a pre-selection of PSC based on amplitude information is made. The amplitude information is useful for the selection of the most consistent scatterers to construct the first order network. However, the results of the Las Vegas test site show that many PS appear to have a low amplitude consistency, which may be removed from the data beforehand when applying an amplitude based threshold. Therefore, all pixels showing a point scattering signature, e.g., based on a local maximum in the amplitude image, should be selected as PSC. In case the evaluation of this dense set of PSC is infeasible from a computational perspective, an iterative scheme based on PS density could be applied. When the number of selected PS in a certain area remains small compared to the number of PSC, this indicates that the deformation in this region could not be estimated with the deformation models used. Hence, regions with a lack of PS should be interpreted with extra care by the user of the PSI results.

Despite the thorough testing of the ambiguities, all processing strategies show a certain degree of falsely detected PS. A false detection is defined as a selected point which is either not coherent, or has, despite its coherence, an incorrectly estimated deformation time series. In this case the ambiguity tests appear not to be sufficient to distinguish the true PS. Apparently, in some cases, consistent but wrong solutions are obtained for the various connecting arcs to a PSC. Therefore, additional quality indicators on top of the testing scheme are required to obtain a final selection of PS. Ideally, a full variance-covariance matrix describing the stochastic relation between all PS and all estimated parameters is used. However, this is infeasible because of the large number of PS, resulting in an enormous full covariance matrix. Therefore, often quality indicators are used to describe the PS by a single parameter. Within DePSI various quality indicators are implemented, such as the ensemble coherence estimator,

the variance factor, and the newly developed Spatio-Temporal Consistency (STC). These quality indicators can either be evaluated global, i.e., with respect to the reference PS, or local. Application shows that local indicators perform better because they are less sensitive to model imperfections and therefore give a better assessment of the noise level in the deformation time series.

8.2 Contributions

The contributions of this research are:

- The design, implementation, validation, and description of the Delft Persistent Scatterer Interferometry (DePSI) software based on geodetic data analysis techniques.
- A theoretical comparison of existing radar interferometric time series analysis approaches (see Section 2.2).
- An analysis and performance comparison, both in success rate and computation time, of the ambiguity function, integer least-squares, and integer bootstrapping estimator for temporal ambiguity resolution (see Sections 4.5–4.7).
- The design and implementation of the concept of testing the phase ambiguities in the spatial domain to detect erroneous solutions and inconsistent PSC, both in the first-order network and in the densification (see Sections 5.1, 5.4). This approach enables the use of local deformation models.
- The design, implementation and evaluation of seven different processing approaches for PSI: the standard approach, extended deformation models, estimation of the Deformation Phase Screen (DPS), sequential testing of ambiguities, prognosis based densification, Area Of Interest (AOI) processing, and time frame processing (see Chapter 7).
- An analysis of the effect of side lobes and sub-main lobes on the estimated parameters and their geolocalization (see Section 3.4).
- An overview of local and global quality indicators, and a comparison of their performance (see Section 6.2, Chapter 7).
- A description of the geolocalization process and the associated errors (see Section 6.1).
- The co-design and implementation of the Spatio-Temporal Consistency (STC) as a new local quality measure (see Section 6.2).
- The design and co-implementation of the DEM-based coregistration algorithm in the DORIS software (Kampes and Usai, 1999; Kampes et al., 2003) (see Section 3.2.4).

8.3 Recommendations

The conclusions result in a number of recommendations for further research.

- It is desirable to enable the use of an arbitrary baseline configuration instead of a single master stack in DePSI (De Zan and Rocca, 2005; Ferretti et al., 2011). With a single master stack, the coherence of the interferometric phases obtained is not optimal since long baselines will exist. Interferometric combinations with shorter baselines, both in the temporal and perpendicular baseline domain, will reduce the noise and thereby increase the information content of the data. Furthermore, a redundant network can be created. Both the reduced noise and the redundancy will improve the correct estimation of the phase ambiguities. Moreover, flexibility in the baseline configuration will improve the possibilities to account for (seasonal) surface scattering effects, such as vegetation grow and snow cover. Furthermore, the number of detected pixels with a distributed scattering characteristic will increase, since the effect of temporal and geometric decorrelation is reduced.
- It is recommended to improve the use of amplitude information. At this stage the amplitude information is used to pre-select the Persistent Scatterer Candidates, both for the first-order network and the densification. It was already concluded that exclusion of PSC with low amplitude consistency results in the unnecessary mis-detection of PS. Nevertheless, the amplitude information can add useful information to the analysis process. Three applications can be considered. First, the amplitude consistency can be used to order the evaluation of the PSC in an iterative densification process, as is applied in the prognosis based densification approach. Alternatively, instead of only a distinction between first and second-order PSC, a further refinement in the classification can be made, thereby reducing the density of the subsequent networks and consequently the distance between nearby PSC. The shorter distance might be beneficial for the resolution of the ambiguities, thereby potentially increasing the number of detected PS. Second, the amplitude consistency forms an additional indication of phase stability, and can therefore be used in the final selection of PS. For instance a Bayesian classification can be used (Hooper, 2008). Third, the amplitude information can be used to identify blank spots in the PS distribution. As was concluded, the lack of PS in a certain region may be even more important information from a deformation perspective, compared to those regions where a relatively smooth deformation pattern can be resolved. A proper inclusion of this information in the final PS results is therefore recommended.
- It is desirable to extend DePSI for near real-time monitoring purposes. The current setup of DePSI is designed for an analysis of a fixed set of radar images. However, operational satellite missions will continuously deliver new acquisitions. With each new image the DePSI analysis can be repeated to obtain an update of the deformation time series. However, this is not optimal from a computational perspective, and may result in slightly different results compared to the previous time series due to the new information that is added by the new radar image. Although the most optimal solution is obtained, inconsistent solutions are undesirable from a practical perspective. Therefore, the capability to efficiently add a new radar acquisition to the image stack is required for monitoring purposes.

- It is recommended to increase the use of neighboring PSC in the analysis. Currently, DePSI resolves the phase ambiguities based on arcs between nearby PSC. Since each phase observation comes along with an unknown phase ambiguity, there is a lack of redundancy in the estimation problem. By using the phase information of multiple neighboring PSC the correlation of some phase contributors, such as deformation, can be used to improve the ambiguity resolution, at least in a first approximation (Hooper, 2008). Alternatively, neighboring pixels could be used in a multi-looking operation to reduce the noise level (Ferretti et al., 2011), thereby improving the ambiguity resolution.
- It would be an improvement to filter the atmospheric signal delay based on least-squares prediction (Liu, 2012) instead of based on a deterministic filter, such as a Gaussian kernel. By applying least-squares prediction, the stochastic properties of the phase observations are incorporated in the filter process. In principle for each PSC a unique covariance function can be applied. Hereby, a better estimate is obtained and the errors of the resulting time series can be propagated in a more consistent manner.
- It is desirable to speed-up the integer least-squares (ILS) estimator. The ILS estimator provides high success rates of correct ambiguity resolution, in combination with high flexibility in the number of model parameters to be used. However, the computation time is the limiting factor for application in large areas. Therefore, speed-up of the algorithm is desirable. Multiple approaches are proposed for GNSS applications, i.e., the Search and Shrink approach (Giorgi et al., 2008; Teunissen et al., 2010), the Expansion approach (Park and Teunissen, 2003; Buist, 2007), and the translation to a closest lattice point problem (Jazaeri et al., 2012). These approaches should be implemented and evaluated for PSI. Furthermore, apart from the class of integer estimators, containing ILS, two additional classes can be distinguished: the class of integer aperture (IA) estimators (Teunissen, 2003a) and the class of integer Equivariant (IE) estimators (Teunissen, 2003b). These classes of estimators are less strict compared to the integer estimator class, however, possess advantageous properties regarding validation and minimization criterion. Therefore, application and evaluation of these estimators for PSI is recommended.

Bibliography

- Adam, N., Kampes, B. M., and Eineder, M. (2004). Development of a scientific persistent scatterer system: Modifications for mixed ERS/ENVISAT time series. In *ENVISAT & ERS Symposium, Salzburg, Austria, 6–10 September, 2004*, page 9.
- Adam, N., Kampes, B. M., Eineder, M., Worawattanamateekul, J., and Kircher, M. (2003). The development of a scientific permanent scatterer system. In *ISPRS Workshop High Resolution Mapping from Space, Hannover, Germany, 2003*, page 6 pp.
- Amelung, F., Galloway, D. L., Bell, J. W., Zebker, H. A., and Lacznik, R. J. (1999). Sensing the ups and downs of Las Vegas: InSAR reveals structural control of land subsidence and aquifer-system deformation. *Geology*, 27(6):483–486.
- Amiri-Simkooei, A. (2007). *Least-Squares Variance Component Estimation; Theory and GPS Applications*. PhD thesis, Delft University of Technology.
- Arikan, M. and Hanssen, R. F. (2008). Structural deformation of the High-Speed Line (HSL) infrastructure in the Netherlands: observations using satellite radar interferometry. In *13th FIG International Symposium on Deformation Measurements and Analysis, Lisbon, Portugal, 12–15 May, 2008*, Lisbon, Portugal.
- Arikan, M., van Leijen, F., Guang, L., and Hanssen, R. (2008). Improved image alignment under the influence of elevation. In *Fifth International Workshop on ERS/Envisat SAR Interferometry, 'FRINGE07', Frascati, Italy, 26 Nov–30 Nov 2007*, page 4 pp.
- Baarda, W. (1968). *A testing procedure for use in geodetic networks*, volume 5 of *Publications on Geodesy*. Netherlands Geodetic Commission, Delft, 2 edition.
- Bähr, H. (2013). *Orbital Effects in Spaceborne Synthetic Aperture Radar Interferometry*. PhD thesis, Karlsruhe Institute of Technology.
- Bähr, H. and Hanssen, R. F. (2012). Reliable estimation of orbit errors in spaceborne SAR interferometry. the network approach. *Journal of Geodesy*, 86(12):1147–1164.
- Bamler, R. and Hartl, P. (1998). Synthetic aperture radar interferometry. *Inverse Problems*, 14:R1–R54.
- Bamler, R. and Schättler, B. (1993). SAR data acquisition and image formation. In Schreier, G., editor, *SAR Geocoding: data and systems*, pages 53–102. Wichmann Verlag, Karlsruhe.
- Basilico, M., Ferretti, A., Novali, F., Prati, C., and Rocca, F. (2004). Advances in permanent scatterer analysis: semi and temporary PS. In *European Conference on Synthetic Aperture Radar, Ulm, Germany, 25–27 May 2004*, pages 349–349.
- Bateson, L., Novali, F., and Cooksley, G. (2010). Terrafirma user guide; a guide to the use and understanding of Persistent Scatterer Interferometry in the detection and monitoring of terrain-motion. Technical report, GMES Terrafirma. European

- Space Agency TerraFirma report, ESRIN/Contract no. 19366/05/I- EC, version 8, 15 October 2010.
- Bell, J. W., Amelung, F., Ferretti, A., Bianchi, M., and Novali, F. (2008a). Monitoring aquifer-system response to groundwater pumping and artificial recharge. *First Break*, 26:51–57.
- Bell, J. W., Amelung, F., Ferretti, A., Bianchi, M., and Novali, F. (2008b). Permanent scatterer insar reveals seasonal and long-term aquifer-system response to groundwater pumping and artificial recharge. *Water Resources Research*, 44(W02407):18pp.
- Bell, J. W., Amelung, F., Ramelli, A. R., and Blewitt, G. (2002). Land subsidence in Las Vegas, Nevada, 1935–2000: New geodetic data show evolution, revised spatial patterns, and reduced rates. *Geoscience and Engineering Geoscience*, VIII(3):155–174.
- Bendat, J. S. and Piersol, A. G. (1986). *Random Data: Analysis and Measurement Procedures*. Wiley-Interscience, New York, 2 edition.
- Berardino, P., Fornaro, G., Lanari, R., and Sansosti, E. (2002). A new algorithm for surface deformation monitoring based on small baseline differential SAR interferograms. *IEEE Transactions on Geoscience and Remote Sensing*, 40(11):2375–2383.
- Bevis, M., Businger, S., Herring, T. A., Rocken, C., Anthes, R. A., and Ware, R. H. (1992). GPS meteorology: Remote sensing of atmospheric water vapor using the Global Positioning System. *Journal of Geophysical Research*, 97:15,787–15,801.
- Bianchi, M. (2003). Phase ambiguity estimation on permanent scatterers in SAR interferometry: the integer least-squares approach. Master's thesis, Politecnico di Milano/Delft University of Technology.
- Buist, P. J. (2007). The baseline constraint LAMBDA method for single epoch, single frequency attitude determination applications. In *Proceedings of ION GPS, Fort Worth, TX, US*, pages 2962–2973.
- Caro Cuenca, M. (2012). *Improving radar interferometry for monitoring fault-related surface deformation*. PhD thesis, Delft University of Technology, Delft, the Netherlands.
- Caro Cuenca, M., Hooper, A. J., and Hanssen, R. F. (2011). A new method for temporal phase unwrapping of persistent scatterers InSAR time series. *IEEE Transactions on Geoscience and Remote Sensing*, 49(11):4606–4615.
- Chang, L. and Hanssen, R. (2012). Near real-time, semi-recursive, deformation monitoring of infrastructure using satellite radar interferometry. In *International Geoscience and Remote Sensing Symposium, Munich, Germany, 22–27 July 2012*, pages 1876–1879.
- Chang, L. and Hanssen, R. (2014). Detection of cavity migration and sinkhole risk using radar interferometric time series. *Remote Sensing of Environment*. Submitted.
- Cigna, F., Osmanoglu, B., Cabral-Cano, E., Dixon, T. H., Avila-Olivera, J. A., Garduno-Monroy, V. H., DeMets, C., and Wdowinski, S. (2012). Monitoring land subsidence and its induced geological hazard with synthetic aperture radar interferometry: A case study in morelia, mexico. *Remote Sensing of Environment*, 117(-):146–161.
- Colesanti, C., Ferretti, A., Locatelli, R., and Savio, G. (2003a). Multi-platform permanent scatterers analysis: first results. In *Second GRSS/ISPRS Joint Workshop on "Data Fusion and Remote Sensing over Urban Areas", Berlin, Germany, 22–23 May*,

- 2003, pages 52–56.
- Colesanti, C., Ferretti, A., Novali, F., Prati, C., and Rocca, F. (2003b). SAR monitoring of progressive and seasonal ground deformation using the Permanent Scatterers Technique. *IEEE Transactions on Geoscience and Remote Sensing*, 41(7):1685–1701.
- Colesanti, C., Ferretti, A., Prati, C., Perissin, D., and Rocca, F. (2003c). ERS-ENVISAT Permanent Scatterers Interferometry. In *International Geoscience and Remote Sensing Symposium, Toulouse, France, 21–25 July 2003*, volume 2, pages 1130–1132.
- Colesanti, C., Ferretti, A., Prati, C., and Rocca, F. (2003d). Monitoring landslides and tectonic motions with the Permanent Scatterers Technique. *Engineering Geology*, 68:3–14.
- Costantini, M. (2003). A curvature based method for processing of multi-temporal SAR differential interferometric measurements. In *Third International Workshop on ERS SAR Interferometry, 'FRINGE03', Frascati, Italy, 1-5 Dec 2003*.
- Costantini, M. and Rosen, P. (1999). A generalized phase unwrapping approach for sparse data. In *International Geoscience and Remote Sensing Symposium, Hamburg, Germany, 28 June–2 July 1999*, pages cdrom, 3 pages.
- Crosetto, M., Monserrat, O., and Agudo, M. (2008). Validation of existing processing chains in terrafirma stage 2; process analysis report–part 2: IG inter-comparison. Technical report, Institut de Geomàtica, Spain. European Space Agency TerraFirma report, ESRIN contract No. 19366/05/I-E.
- Cumming, I. and Wong, F. (2005). *Digital Processing Of Synthetic Aperture Radar Data: Algorithms And Implementation*. Artech House Publishers, New York. ISBN 1580530583.
- De Zan, F. and Rocca, F. (2005). Coherent processing of long series of SAR images. In *International Geoscience and Remote Sensing Symposium, Seoul, Korea, 25–29 July 2005*.
- Eineder, M. (2003). Efficient simulation of SAR interferograms of large areas and of rugged terrain. *IEEE Transactions on Geoscience and Remote Sensing*, 41(6):1415–1427.
- Eineder, M. and Holzner, J. (1999). Phase unwrapping of low coherence differential interferograms. In *International Geoscience and Remote Sensing Symposium, Hamburg, Germany, 28 June–2 July 1999*, pages cdrom, 4 pages.
- Eineder, M., Minet, C., Steigenberger, P., Cong, X., and Fritz, T. (2011). Imaging geodesy — toward centimeter-level ranging accuracy with TerraSAR-X. *IEEE Transactions on Geoscience and Remote Sensing*, 49(2):661–671.
- Elachi, C. (1988). *Spaceborne radar remote sensing: applications and techniques*. Institute of Electrical and Electronics Engineers, New York.
- Elliott, J. L., Freymueller, J. T., and Rabus, B. (2007). Coseismic deformation of the 2002 Denali fault earthquake: Contributions from synthetic aperture radar range offsets. *Journal of Geophysical Research*, 112(B06421):19.
- Farr, T. G., Rosen, P. A., Caro, E., Crippen, R., Duren, R., Hensley, S., Kobrick, M., Paller, M., Rodriguez, E., Roth, L., Seal, D., Shaffer, S., Shimada, J., Umland, J., Werner, M., Oskin, M., Burbank, D., and Alsdorf, D. (2007). The shuttle radar topography mission. *Rev. Geophys.*, 45:33.

- Ferretti, A., Fumagalli, A., Novali, F., Prati, C., Rocca, F., and Rucci, A. (2011). A new algorithm for processing interferometric data-stacks: SqueeSAR. *IEEE Transactions on Geoscience and Remote Sensing*, 49(9):3460–3470.
- Ferretti, A., Perissin, D., Prati, C., and Rocca, F. (2005). On the physical nature of SAR permanent scatterers. In *URSI Commission F Symposium on Microwave Remote Sensing of the Earth, Oceans, Ice and Atmosphere, Ispra, Italy, 20–21 April, 2005*, page 6 pp.
- Ferretti, A., Prati, C., and Rocca, F. (2000). Nonlinear subsidence rate estimation using permanent scatterers in differential SAR interferometry. *IEEE Transactions on Geoscience and Remote Sensing*, 38(5):2202–2212.
- Ferretti, A., Prati, C., and Rocca, F. (2001). Permanent scatterers in SAR interferometry. *IEEE Transactions on Geoscience and Remote Sensing*, 39(1):8–20.
- Fornaro, G., Reale, D., and Serafino, F. (2009). Four-dimensional SAR imaging for height estimation and monitoring of single and double scatterers. *IEEE Transactions on Geoscience and Remote Sensing*, 47(1):224–237.
- Freeman, A. (1992). SAR calibration: An overview. *IEEE Transactions on Geoscience and Remote Sensing*, 30(6):1107–1121.
- Fruneau, B., Achache, J., and Delacourt, C. (1996). Observation and modelling of the Saint-Etienne-de-Tinée landslide. *Tectonophysics*, 265:181–190.
- Gabriel, A. K., Goldstein, R. M., and Zebker, H. A. (1989). Mapping small elevation changes over large areas: differential radar interferometry. *Journal of Geophysical Research*, 94(B7):9183–9191.
- Gatelli, F., Monti Guarnieri, A., Parizzi, F., Pasquali, P., Prati, C., and Rocca, F. (1994). The wavenumber shift in SAR interferometry. *IEEE Transactions on Geoscience and Remote Sensing*, 32(4):855–865.
- Ghiglia, D. C. and Pritt, M. D. (1998). *Two-dimensional phase unwrapping: theory, algorithms, and software*. John Wiley & Sons, Inc, New York.
- Giorgi, G., Teunissen, P. J. G., and Buist, P. J. (2008). A search and shrink approach for the baseline constrained LAMBDA: Experimental results. In *Proceedings of the International Symposium on GPS/GNSS 2008. A. Yasuda (Ed.), Tokyo University of Marine Science and Technology*, pages 797–806.
- Goldstein, R. M., Engelhardt, H., Kamp, B., and Frolich, R. M. (1993). Satellite radar interferometry for monitoring ice sheet motion: Application to an antarctic ice stream. *Science*, 262:1525–1530.
- Gray, A. L., Mattar, K. E., and Vachon, P. W. (1998). InSAR results from the RADARSAT Antarctic mapping mission data: estimation of data using a simple registration procedure. In *International Geoscience and Remote Sensing Symposium, Seattle, Washington, USA, 6–10 July 1998*, pages 1638–1640.
- Grebenitcharsky, R. and Hanssen, R. F. (2005). A matern class covariance function for modeling atmospheric delays in SAR interferometry. In *AGU Fall meeting, December 5–9, San Francisco, USA*.
- Hanssen, R. (2004). Stochastic modeling of time series radar interferometry. In *International Geoscience and Remote Sensing Symposium, Anchorage, Alaska, 20–24 September 2004*, pages cdrom, 4 pages.

- Hanssen, R. F. (2001). *Radar Interferometry: Data Interpretation and Error Analysis*. Kluwer Academic Publishers, Dordrecht.
- Hanssen, R. F. and van Leijen, F. J. (2008a). Monitoring water defense structures using radar interferometry. In *IEEE Radar Conference, Rome, Italy, 26–30 May 2008*, page 4.
- Hanssen, R. F. and van Leijen, F. J. (2008b). Water defense system monitoring using SAR interferometry. In *European Conference on Synthetic Aperture Radar, Friedrichshafen, Germany, 2–5 June 2008*, page 4.
- Hanssen, R. F., van Leijen, F. J., van Zwieten, G. J., Bremmer, C., Dortland, S., and Kleuskens, M. (2008). Validation of existing processing chains in terrafirma stage 2; product validation: Validation in the amsterdam and alkmaar area. Technical report, Delft University of Technology, The Netherlands; TNO, The Netherlands. European Space Agency TerraFirma report, ESRIN contract No. 19366/05/I-E.
- Hanssen, R. F., Teunissen, P. J. G., and Joosten, P. (2001). Phase ambiguity resolution for stacked radar interferometric data. In *International Symposium on Kinematic Systems in Geodesy, Geomatics and Navigation, Banff, Canada, 5–8 June 2001*, pages 317–320.
- Herring, T. A. (1992). Modeling atmospheric delays in the analysis of space geodetic data. In de Munck, J. C. and Spoelstra, T. A. T., editors, *Symposium on Refraction of transatmospheric signals in geodesy*, pages 157–164, Delft. Netherlands Geodetic Commission.
- de Heus, H. M., Joosten, P., Martens, M. H. F., and Verhoef, H. M. E. (1994). Geodetische deformatie analyse: 1d- deformatieanalyse uit waterpasnetwerken. Technical Report 5, Delft University of Technology, LGR Series, Delft.
- Hoffmann, J., Zebker, H. A., Galloway, D. L., and Amelung, F. (2001). Seasonal subsidence and rebound in Las Vegas Valley, Nevada, observed by synthetic aperture radar interferometry. *Water Resources Research*, 37(6):1551–1566.
- Hooper, A. (2006). *Persistent Scatterer Radar Interferometry for Crustal Deformation Studies and Modeling of Volcanic Deformation*. PhD thesis, Stanford University.
- Hooper, A. (2008). A multi-temporal InSAR method incorporating both persistent scatterer and small baseline approaches. *Geophysical Research Letters*, 35:L16302.
- Hooper, A. (2010). Statistical-cost approach to unwrapping the phase of InSAR time series. In *Advances in the Science and Applications of SAR interferometry, 'FRINGE09', Frascati, Italy, 30 Nov-4 Dec 2009*.
- Hooper, A., Segall, P., and Zebker, H. (2007). Persistent scatterer InSAR for crustal deformation analysis, with application to volcan alcedo, galapagos. *Journal of Geophysical Research*, 112.
- Hooper, A. and Zebker, H. (2007). Phase unwrapping in three dimensions with application to InSAR time series. *Journal of the Optical Society of America A.*, 24:2737–2747.
- Hooper, A., Zebker, H., Segall, P., and Kampes, B. (2004). A new method for measuring deformation on volcanoes and other non-urban areas using InSAR persistent scatterers. *Geophysical Research Letters*, 31:L23611, doi:10.1029/2004GL021737.
- Humme, A. (2007). Point density optimization for SAR interferometry; a study tested on salt mine areas. Master's thesis, Delft University of Technology.

- Jazaeri, S., Amiri-Simkooei, A. R., and Sharifi, M. A. (2012). Fast integer least-squares estimation for GNSS high-dimensional ambiguity resolution using lattice theory. *Journal of Geodesy*, 86:123–136.
- de Jonge, P. and Tiberius, C. (1996). The LAMBDA method for integer ambiguity estimation: implementation aspects. Technical Report 12, Delft University of Technology, LGR Series, Delft.
- Jonkman, N. F. (1998). *Integer GPS ambiguity estimation without the receiver-satellite geometry*. LGR Series, No. 18. Delft Geodetic Computing Centre.
- Joosten, P. (2000). Simulating the distribution of GPS ambiguities. *Physics and Chemistry of the Earth*, 25(9-11):687–692.
- Journel, A. G. and Huijbregts, C. J. (1978). *Mining Geostatistics*. Academic Press, London.
- Just, D. and Bamler, R. (1994). Phase statistics of interferograms with applications to synthetic aperture radar. *Applied Optics*, 33(20):4361–4368.
- Kampes, B. (1999). *Delft Object-Oriented Radar Interferometric Software: Users manual and Technical Documentation*. Delft University of Technology, Delft, 1.2 edition.
- Kampes, B. and Usai, S. (1999). Doris: the Delft Object-oriented Radar Interferometric Software. In *2nd International Symposium on Operationalization of Remote Sensing, Enschede, The Netherlands, 16–20 August, 1999*.
- Kampes, B. M. (2006). *Radar Interferometry: Persistent Scatterer Technique*. Springer, Dordrecht, The Netherlands.
- Kampes, B. M. and Adam, N. (2003). Velocity field retrieval from long term coherent points in radar interferometric stacks. In *International Geoscience and Remote Sensing Symposium, Toulouse, France, 21–25 July 2003*, pages cdrom, 4 pages.
- Kampes, B. M. and Adam, N. (2004). Deformation parameter inversion using permanent scatterers in interferogram time series. In *European Conference on Synthetic Aperture Radar, Ulm, Germany, 25–27 May 2004*, pages 341–344.
- Kampes, B. M. and Hanssen, R. F. (2004). Ambiguity resolution for permanent scatterer interferometry. *IEEE Transactions on Geoscience and Remote Sensing*, 42(11):2446–2453.
- Kampes, B. M., Hanssen, R. F., and Perski, Z. (2003). Radar interferometry with public domain tools. In *Third International Workshop on ERS SAR Interferometry, 'FRINGE03', Frascati, Italy, 1-5 Dec 2003*, page 6 pp.
- Kenselaar, F. and Quadvlieg, R. (2001). Trend-signal modelling of land subsidence. In *10th FIG International Symposium on Deformation Measurements, Orange, California, USA, 19–22 March, 2001*, pages 336–345.
- Ketelaar, G., van Leijen, F., Marinkovic, P., and Hanssen, R. (2007a). Multi-track PS-InSAR datum connection. In *International Geoscience and Remote Sensing Symposium, Barcelona, Spain, 23–27 July 2007*, page 4 pp.
- Ketelaar, G., van Leijen, F., Marinkovic, P., and Hanssen, R. (2007b). Multi-track PS-InSAR fusion. In *ESA ENVISAT Symposium, Montreux, Switzerland, 23–27 April 2007*, page Submitted xxx pp.
- Ketelaar, V. B. H. (2009). *Satellite Radar Interferometry: Subsidence Monitoring Tech-*

- niques*. Springer, Dordrecht, The Netherlands.
- Koch, K.-R. (1988). *Parameter estimation and hypothesis testing in linear models*. Springer-Verlag, New York.
- Kohlhase, A. O., Feigl, K. L., and Massonnet, D. (2003). Applying differential InSAR to orbital dynamics: a new approach for estimating ERS trajectories. *Journal of Geodesy*, 77(9):493–502.
- van der Kooij, M. (1997). Land subsidence measurements at the belridge oil fields from ers insar data. In *Third ERS Symposium on Space at the service of our Environment, Florence, Italy, 14–21 March, 1997*.
- Krige, D. G. (1951). A statistical approach to some mine valuation and allied problems on the Witwatersrand. Master's thesis, University of Witwatersrand.
- Lanari, R., Mora, O., Manunta, M., Mallorquí, J. J., Berardino, P., and Sansosti, U. (2004). A small-baseline approach for investigating deformations on full-resolution differential SAR interferograms. *IEEE Transactions on Geoscience and Remote Sensing*, 42(7):1377–1386.
- Laur, H., Bally, P., Meadows, P., Sanchez, J., Schaettler, B., Lopinto, E., and Esteban, D. (2002). Derivation of the backscattering coefficient σ^0 in ESA ERS SAR PRI products. Technical Report ES-TN-RS-PM-HL09, ESA. Issue 2, Rev. 5d.
- van Leijen, F. and Hanssen, R. (2004). Interferometric radar meteorology: resolving the acquisition ambiguity. In *CEOS SAR Workshop, Ulm Germany, 27–28 May 2004*, page 6.
- van Leijen, F. and Hanssen, R. (2008). Ground water management and its consequences in Delft, the Netherlands as observed by persistent scatterer interferometry. In *Fifth International Workshop on ERS/Envisat SAR Interferometry, 'FRINGE07', Frascati, Italy, 26 Nov–30 Nov 2007*, page 6 pp.
- van Leijen, F. J. and Hanssen, R. F. (2007a). Persistent scatterer density improvement using adaptive deformation models. In *International Geoscience and Remote Sensing Symposium, Barcelona, Spain, 23–27 July 2007*, page 4 pp.
- van Leijen, F. J. and Hanssen, R. F. (2007b). Persistent scatterer interferometry using adaptive deformation models. In *ESA ENVISAT Symposium, Montreux, Switzerland, 23–27 April 2007*, page pp.
- van Leijen, F. J., Hanssen, R. F., Marinkovic, P. S., and Kampes, B. M. (2006a). Spatio-temporal phase unwrapping using integer least-squares. In *Fourth International Workshop on ERS/Envisat SAR Interferometry, 'FRINGE05', Frascati, Italy, 28 Nov–2 Dec 2005*, page 6 pp.
- van Leijen, F. J., Humme, A. J. M., and Hanssen, R. F. (2008). Deformatie van de Hondsbosche en Pettemer zeewering geconstateerd met radarinterferometrie. In Barends, F., Dillingh, D., Hanssen, R., and van Onselen, K., editors, *Bodemdaling langs de Nederlandse kust. Case Hondsbosche en Pettemer Zeewering*, chapter 4.5, pages 151–169. IOS press, Amsterdam. in Dutch.
- van Leijen, F. J., Perski, Z., and Hanssen, R. F. (2006b). Error propagation and data quality assessment for ASAR persistent scatterer interferometry. In *European Conference on Synthetic Aperture Radar, Dresden, Germany, 16–18 May 2006*, page 6.
- Lillesand, T. M. and Kiefer, R. W. (1994). *Remote Sensing and Image Interpretation*.

- John Wiley & Sons, Inc., New York.
- Liu, S. (2012). *Satellite radar interferometry: estimation of atmospheric delay*. PhD thesis, Delft University of Technology, Delft, the Netherlands.
- Lombardini, F. (2005). Differential tomography: A new framework for SAR interferometry. *IEEE Transactions on Geoscience and Remote Sensing*, 43(1):37–44.
- Lutgens, F. K. and Tarbuck, E. J. (1986). *The Atmosphere: An Introduction to Meteorology*. Prentice-Hall, Inc, Englewood Cliffs, New Jersey, 3 edition.
- Marinkovic, P., Ketelaar, G., van Leijen, F., and Hanssen, R. (2008). InSAR quality control: Analysis of five years of corner reflector time series. In *Fifth International Workshop on ERS/Envisat SAR Interferometry, 'FRINGE07', Frascati, Italy, 26 Nov-30 Nov 2007*, page 8 pp.
- Marinkovic, P. and Larsen, Y. (2014). On the long term stability of ASAR LO frequency - empirical study of 10 years of data. *IEEE Transactions on Geoscience and Remote Sensing*. Submitted.
- Massonnet, D., Briole, P., and Arnaud, A. (1995). Deflation of Mount Etna monitored by spaceborne radar interferometry. *Nature*, 375:567–570.
- Massonnet, D., Rossi, M., Carmona, C., Adagna, F., Peltzer, G., Feigl, K., and Rabaute, T. (1993). The displacement field of the Landers earthquake mapped by radar interferometry. *Nature*, 364(8):138–142.
- Moore, E. H. (1920). On the reciprocal of the general algebraic matrix. *Bulletin of the American Mathematical Society*, 26(9):394–395.
- Mora, O., Mallorqui, J. J., and Broquetas, A. (2003). Linear and nonlinear terrain deformation maps from a reduced set of interferometric SAR images. *IEEE Transactions on Geoscience and Remote Sensing*, 41(10):2243–2253.
- Neyman, J. and Pearson, E. S. (1933). On the problem of the most efficient tests of statistical hypotheses. *Philosophic Transactions of the Royal Society London, Series A*, 231:289–337.
- Niell, A. E. (1996). Global mapping functions for the atmosphere delay at radio wavelengths. *Journal of Geophysical Research*, 101(B2):3227–3246.
- Nitti, D. O., Hanssen, R. F., Refice, A., Bovenga, F., Milillo, G., and Nutricato, R. (2008). Evaluation of DEM-assisted SAR coregistration. In *SPIE Europe Remote Sensing, Proceedings 15–18 September 2008, Cardiff, United Kingdom*, pages 1–14.
- Odijk, D. (2002). *Fast precise GPS positioning in the presence of ionospheric delays*. PhD thesis, Delft University of Technology.
- Osmanoglu, B., Dixon, T. H., Wdowinski, S., Cabral-Cano, E., and Jiang, Y. (2011). Mexico city subsidence observed with persistent scatterer InSAR. *International Journal of Applied Earth Observation and Geoinformation*, 13(1):1–12.
- Otten, M. and Dow, J. M. (2005). ENVISAT precise orbit determination. In *ENVISAT & ERS Symposium, Salzburg, Austria, 6–10 September, 2004*.
- Park, C. and Teunissen, P. J. G. (2003). A new carrier phase ambiguity estimation of GNSS attitude determination systems. In *Proceedings of the International GPS/GNSS Symposium, Tokyo, Japan*, pages –.
- Penrose, R. (1955). A generalized inverse for matrices. *Proceedings of the Cambridge*

- Philosophical Society*, 51:406–413.
- Pepe, A. and Lanari, R. (2006). On the extension of minimum cost flow algorithm for phase unwrapping of multitemporal differential SAR interferograms. *IEEE Transactions on Geoscience and Remote Sensing*, 44(9):2374–2383.
- Perissin, D. (2006). *SAR super-resolution and characterization of urban targets*. PhD thesis, Politecnico di Milano, Italy.
- Perissin, D., Ferretti, A., Piantanida, R., Piccagli, D., Prati, C., Rocca, F., Rucci, A., and de Zan, F. (2008). Repeat-pass SAR interferometry with partially coherent targets. In *Fifth International Workshop on ERS/Envisat SAR Interferometry, 'FRINGE07', Frascati, Italy, 26 Nov-30 Nov 2007*, page 6 pp.
- Perski, Z., Hanssen, R., Wojcik, A., and Wojciechowski, T. (2009). InSAR analysis of terrain deformation near the Wieliczka salt mine, Poland. *Engineering Geology*, 106(doi:10.1016/j.enggeo.2009.02.014):58–67.
- Perski, Z., van Leijen, F., and Hanssen, R. (2007). Applicability of PSInSAR for building hazard identification. study of the 29 January 2006 Katowice exhibition hall collapse and the 24 February 2006 Moscow Basmanny market collapse. In *ESA ENVISAT Symposium, Montreux, Switzerland, 23–27 April 2007*, page Submitted xxx pp.
- Rapp, R. H. (1997). Use of potential coefficient models for geoid undulation determinations using a spherical harmonic representation of the height anomaly/geoid undulation difference. *Journal of Geodesy*, 71(5):282–289.
- Reigber, A. and Moreira, A. (2000). First demonstration of airborne SAR tomography using multibaseline L-band data. *IEEE Transactions on Geoscience and Remote Sensing*, 38(5):2142–2152.
- Rosen, P., Hensley, S., Joughin, I. R., Li, F. K., Madsen, S., Rodríguez, E., and Goldstein, R. (2000). Synthetic aperture radar interferometry. *Proceedings of the IEEE*, 88(3):333–382.
- Samiei-Esfahany, S. (2008). Improving persistent scatterer interferometry for deformation monitoring; (case study on the Gardanne mining site). Master's thesis, Delft University of Technology.
- Samiei-Esfahany, S., van Leijen, F. J., Marinkovic, P., Ketelaar, G., and Hanssen, R. F. (2008). Lessons learned from PSIC4: Improving PSI results for a constrained test site. In *Fifth International Workshop on ERS/Envisat SAR Interferometry, 'FRINGE07', Frascati, Italy, 26 Nov-30 Nov 2007*, page 7 pp.
- Sandwell, D. T. and Price, E. J. (1998). Phase gradient approach to stacking interferograms. *Journal of Geophysical Research*, 103(B12):30183–30204.
- Sansosti, E., Berardino, P., Manunta, M., Serafino, F., and Fornaro, G. (2006). Geometrical SAR image registration. *IEEE Transactions on Geoscience and Remote Sensing*, 44(10):2861–2870.
- Scharroo, R. and Visser, P. (1998). Precise orbit determination and gravity field improvement for the ERS satellites. *Journal of Geophysical Research*, 103(C4):8113–8127.
- Schmidt, D. A. and Bürgmann, R. (2003). Time-dependent land uplift and subsidence in the Santa Clara valley, California, from a large interferometric synthetic aperture radar data set. *Journal of Geophysical Research*, 108(B9):doi:10.1029/2002JB002267.

- Schwäbisch, M. (1995). *Die SAR-Interferometrie zur Erzeugung digitaler Geländemodelle*. PhD thesis, Stuttgart University.
- Small, D., Werner, C., and Nüesch, D. (1993). Baseline modelling for ERS-1 SAR interferometry. In *International Geoscience and Remote Sensing Symposium, Tokyo, Japan, 18–21 August 1993*, pages 1204–1206.
- Teunissen, P. J. G. (1988). *Towards a Least-Squares Framework for Adjusting and Testing of both Functional and Stochastic Models*, volume 26 of *Mathematical Geodesy and Positioning series*.
- Teunissen, P. J. G. (1990). Quality control in integrated navigation systems. *IEEE Aerospace and Electronic Systems Magazine*, 5(7):35–41.
- Teunissen, P. J. G. (1993). Least-squares estimation of the integer GPS ambiguities. In *Invited Lecture, Section IV Theory and Methodology, IAG General Meeting, Beijing, China, august 1993*. Also in: Delft Geodetic Computing Centre, LGR Series, No. 6, 1994.
- Teunissen, P. J. G. (1994). Least-squares estimation of the integer GPS ambiguities. In *Publications and annual report 1993*, number 6 in LGR-Series, pages 59–74. Delft geodetic computing centre.
- Teunissen, P. J. G. (1997). A canonical theory for short GPS baselines. part IV: Precision versus reliability. *Journal of Geodesy*, 71:513–525.
- Teunissen, P. J. G. (1998). Success probability of integer GPS ambiguity rounding and bootstrapping. *Journal of Geodesy*, 72:606–612.
- Teunissen, P. J. G. (1999a). An optimality property of the integer least-squares estimator. *Journal of Geodesy*, 73:587–593.
- Teunissen, P. J. G. (1999b). A theorem on maximizing the probability of correct integer estimation. *Artificial Satellites*, 34(1):3–9.
- Teunissen, P. J. G. (2000a). *Adjustment theory; an introduction*. Delft University Press, Delft, 1 edition.
- Teunissen, P. J. G. (2000b). *Testing theory; an introduction*. Delft University Press, Delft, 1 edition.
- Teunissen, P. J. G. (2003a). Integer aperture GNSS ambiguity resolution. *Artificial Satellites*, 38(3):79–88.
- Teunissen, P. J. G. (2003b). Theory of integer equivariant estimation with application to GNSS. *Journal of Geodesy*, 77:402–410.
- Teunissen, P. J. G. (2007). Least-squares prediction in linear models with integer unknowns. *Journal of Geodesy*, 81:565–579.
- Teunissen, P. J. G. and Amiri-Simkooei, A. R. (2008). Least-squares variance component estimation. *Journal of Geodesy*, 82:65–82.
- Teunissen, P. J. G., Giorgi, G., and Buist, P. J. (2010). Testing of a new single-frequency GNSS carrier-phase compass method: Land, ship and aircraft experiments. *GPS Solutions*, 15:15–28.
- Teunissen, P. J. G. and Kleusberg, A., editors (1998). *GPS for geodesy*. Springer-Verlag, 2 edition.
- Teunissen, P. J. G. and Odijk, D. (1997). Ambiguity dilution of precision: concept and

- application. In *In: proc. ION-97, 16-19 September, Kansas City, USA, pp. 891-899.*
- Teunissen, P. J. G., Simons, D. G., and Tiberius, C. C. J. M. (2005). *Probability and observation theory.* Delft Institute of Earth Observation and Space Systems (DEOS), Delft University of Technology, The Netherlands.
- Tienstra, J. M. (1956). *Theory of the adjustment of normally distributed observations.* Argus, Amsterdam.
- Usai, S. (1997). The use of man-made features for long time scale insar. In *International Geoscience and Remote Sensing Symposium, Singapore, 3-8 Aug 1997*, pages 1542–1544.
- Usai, S. (2001). *A New Approach for Long Term Monitoring of Deformations by Differential SAR Interferometry.* PhD thesis, Delft University of Technology.
- Usai, S. (2003). A least squares database approach for SAR interferometric data. *IEEE Transactions on Geoscience and Remote Sensing*, 41(4):753–760.
- Usai, S. and Hanssen, R. (1997). Long time scale INSAR by means of high coherence features. In *Third ERS Symposium—Space at the Service of our Environment, Florence, Italy, 17–21 March 1997*, pages 225–228.
- Verhoef, H. M. E. (1997). Geodetische deformatie analyse. Lecture notes, Delft University of Technology, Faculty of Geodetic Engineering, in Dutch.
- Wright, T., Parsons, B., and Fielding, E. (2001). Measurement of interseismic strain accumulation across the North Anatolian Fault by satellite radar interferometry. *Geophysical Research Letters*, 28(10):2117–2120.
- Wright, T. J., Parsons, B., England, P. C., and Fielding, E. J. (2004). InSAR observations of low slip rates on the major faults of western Tibet. *Science*, 305:236–239.
- Yoon, Y., Eineder, M., Yague-Martinez, N., and Montenbruck, O. (2009). TerraSAR-X precise trajectory estimation and quality assessment. *IEEE Transactions on Geoscience and Remote Sensing*, 47(6):1859–1868.
- Zebker, H. A. and Goldstein, R. M. (1986). Topographic mapping from interferometric synthetic aperture radar observations. *Journal of Geophysical Research*, 91(B5):4993–4999.
- Zebker, H. A., Rosen, P. A., and Hensley, S. (1997). Atmospheric effects in interferometric synthetic aperture radar surface deformation and topographic maps. *Journal of Geophysical Research*, 102(B4):7547–7563.
- Zebker, H. A. and Villasenor, J. (1992). Decorrelation in interferometric radar echoes. *IEEE Transactions on Geoscience and Remote Sensing*, 30(5):950–959.
- Zhu, X. and Bamler, R. (2010). Tomographic SAR inversion by L1 norm regularization—The compressive sensing approach. *IEEE Transactions on Geoscience and Remote Sensing*, 48(10):3839–3846.

Geodetic measurements, such as interferometric radar observations, are stochastic quantities. Errors, which can be both random (noise) and systematic (bias), affect the measurements and prevent a straightforward transformation of the measurements into the parameters of interest. During the last century, Delft University of Technology developed a systematic and rigorous methodology to solve this problem in an optimal way. The methodology basically consists of two steps: estimation and testing, see Sections A.1 and A.2. Within the same framework, related techniques are developed: prediction (Section A.3), least-squares variance component estimation (Section A.4), and integer least-squares (Section A.5)¹.

A.1 Estimation

A geodetic problem is normally specified by a mathematical model. The general form of the mathematical model is denoted by the Gauss-Markov model

$$E\{\underline{y}\} = Ax \quad ; \quad D\{\underline{y}\} = Q_y, \quad (\text{A.1})$$

where the first part is the functional model and the second part the stochastic model. The *design matrix* A describes the functional relation between the measurements \underline{y} and the unknowns x . The underline denotes the stochasticity of the measurements. The stochastic properties of the measurements are specified by the variance matrix Q_y , which is constructed based on a priori knowledge or is derived from the data.

To estimate an optimal solution, the following minimization problem is solved

$$\min_x \|\underline{y} - Ax\|_{Q_y}^2, \quad (\text{A.2})$$

where $\|\cdot\|_Q^2 = (\cdot)^T Q^{-1}(\cdot)$. Hence, the solution that is obtained minimizes the difference between the observations and the model in a least-squares sense. Linear least-squares estimators that have optimal properties in the sense that they are unbiased and have minimum variance are called Best Linear Unbiased Estimators (BLUE). For normally distributed data, the BLUE estimator is equal to the Maximum Likelihood (ML) estimator (Teunissen, 2000a).

¹Part of this appendix was published in the report:
Hanssen, R. F., van Leijen, F., Ketelaar, G., Marinkovic, P. S., and Gehlot, S. (2005). PSIC4: PSI-processing over a validation test site. applicability report. Technical report, Delft University of Technology, Delft. European Space Agency Study report ESA Contract Nr. 18707/04/I-LG.

The estimator for the unknowns $\hat{\underline{x}}$, the adjusted observations $\hat{\underline{y}}$ and the residues $\hat{\underline{e}}$ are calculated by

$$\hat{\underline{x}} = (A^T Q_y^{-1} A)^{-1} A^T Q_y^{-1} \underline{y}, \quad (\text{A.3})$$

$$\hat{\underline{y}} = A \hat{\underline{x}}, \quad (\text{A.4})$$

$$\hat{\underline{e}} = \underline{y} - \hat{\underline{y}}, \quad (\text{A.5})$$

where $\{\cdot\}^T$ denotes the transpose. Optimal estimators are obtained on the condition that the number of unknowns n is smaller than the number of observations m and that the design matrix is of full rank. If the last two conditions are not fulfilled, the system of equations is rank defect and no unique solution can be determined. More information about geodetic data adjustment can be found in (Teunissen, 2000a; Koch, 1988).

The quality of the stochastic variables is characterized by the *precision* and the *reliability*. The precision describes the variability of the observables and the estimators of the unknown parameters. The precision is quantified by their variance matrix. If the observations have a normal distribution and provided a linear relation between the observations and the unknowns (Eq. (A.1)), the estimates are normally distributed as well. The variance matrices are obtained by applying the error propagation laws, which results in

$$Q_{\hat{\underline{x}}} = (A^T Q_y^{-1} A)^{-1}, \quad (\text{A.6})$$

$$Q_{\hat{\underline{y}}} = A Q_{\hat{\underline{x}}} A^T, \quad (\text{A.7})$$

$$Q_{\hat{\underline{e}}} = Q_y - Q_{\hat{\underline{y}}}. \quad (\text{A.8})$$

The reliability describes the sensitivity of the estimators for model errors. The reliability is ensured by testing, which is discussed in the next section. Precision and reliability are independent components of the quality description. A high precision of the observables does not imply a reliable estimation of the unknown parameters and vice versa. Precision and reliability together describe the *accuracy*.

A.2 Testing and quality control

Once estimates for the unknown parameters and their variance matrix are obtained, the validity of the mathematical model is tested. That is, the model is tested for errors in the observations \underline{y} , in the design matrix A and in the variance matrix Q_y .

Testing is performed by subsequent comparison of two hypotheses: the *null hypothesis* H_0 and the *alternative hypothesis* H_a , see Figure A.1. The null hypothesis describes the situation that there are no errors in the model, whereas the alternative hypothesis assumes that there is a certain error. Symbolically the hypotheses can be denoted as

$$H_0 : E\{\underline{y}\} = Ax \quad ; \quad D\{\underline{y}\} = Q_y, \quad (\text{A.9})$$

$$H_a : E\{\underline{y}\} = Ax + C_q \nabla \quad ; \quad D\{\underline{y}\} = Q_y, \quad (\text{A.10})$$

where ∇ holds q additional unknown parameters and C_q describes the functional relation of these parameters with the observation vector \underline{y} .

Acceptance or rejection of H_0 is based on the test statistic \underline{T}_q (Teunissen, 2000b)

$$\underline{T}_q = \hat{\underline{e}}_0^T Q_y^{-1} \hat{\underline{e}}_0 - \hat{\underline{e}}_a^T Q_y^{-1} \hat{\underline{e}}_a, \quad (\text{A.11})$$

$$= \hat{\underline{e}}_0^T Q_y^{-1} C_q (C_q^T Q_y^{-1} Q_{\hat{\underline{e}}_0} Q_y^{-1} C_q)^{-1} C_q^T Q_y^{-1} \hat{\underline{e}}_0. \quad (\text{A.12})$$

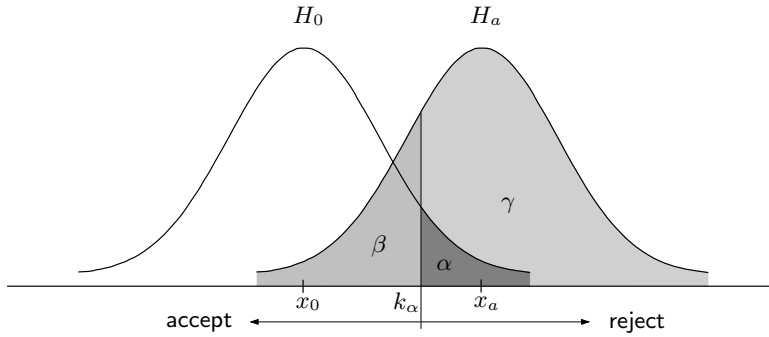


Figure A.1: The concept of hypotheses testing. The null hypothesis H_0 is compared to an alternative hypothesis H_a . The test statistic \underline{T}_q in relation to the critical value k_α determines whether the null hypothesis is accepted or rejected. The critical value is based on the chosen level of significance α . The α represents the probability of incorrect rejection of H_0 , known as a Type-I error. The opposite error, incorrect acceptance of H_0 , is denoted as a Type-II error. The probability of this error is indicated by β . Often, the power of the test $\gamma = 1 - \beta$ is used, i.e., the probability that H_0 is correctly rejected.

The test statistic has a χ^2 -distribution with q degrees of freedom

$$\begin{aligned} H_0 &: \underline{T}_q \sim \chi^2(q, 0), \\ H_a &: \underline{T}_q \sim \chi^2(q, \lambda), \end{aligned} \tag{A.13}$$

where λ is the non-centrality parameter

$$\lambda = \nabla^T C_q^T Q_y^{-1} Q_{\hat{e}_0} Q_y^{-1} C_q \nabla. \tag{A.14}$$

A critical value k_α is used to determine whether the H_0 should be rejected

$$\text{reject } H_0 \text{ if } \underline{T}_q > k_\alpha. \tag{A.15}$$

The critical value is determined from the χ^2 -distribution with q degrees of freedom by choosing a level of significance α , see Figure A.1. The relation between α and k_α is denoted by

$$\alpha(q) = \int_{k_\alpha}^{\infty} P(\chi^2|q, 0) d\chi^2, \tag{A.16}$$

where $P(\cdot)$ is the probability density distribution. The α represents the probability of incorrect rejection of H_0 and should be as low as possible. Typical values for α are within the range 0.001-0.05. Such an incorrect rejection of H_0 is known as a *Type-I error*. The opposite error, incorrect acceptance of H_0 is denoted as a *Type-II error*. The probability of a Type-II error is equal to β , as indicated in Figure A.1. In geodesy, instead of β often the *power of the test* $\gamma = 1 - \beta$ is used, i.e., the probability that H_0 is correctly rejected. The power of the test is a function of α, q and λ

$$\gamma(\alpha, q, \lambda) = \int_{k_\alpha}^{\infty} P(\chi^2|q, \lambda) d\chi^2. \tag{A.17}$$

A typical applied value of γ is 0.8 (Teunissen, 2000b). However, when tests of different dimensions are compared, a value of 0.5 should be applied, see Section A.2.2.

To reduce the probability of the two types of errors, both α and β should be as small as possible, ideally zero. However, if α is chosen smaller, β increases, and vice versa, see Figure A.1. To define a test that copes with this paradox, the Neyman-Pearson principle is applied (Neyman and Pearson, 1933). This principle states that from all tests with the same probability of Type-I errors, the one for which the chance of Type-II errors is as small as possible should be used. The test statistic \underline{T}_q is a consequence of this principle (Teunissen, 2000b).

The practical implementation of testing is based on an iterative scheme known as the Detection, Identification and Adaption (DIA) procedure (Teunissen, 2000b). First, H_0 is tested to detect whether there are any errors in the model. In case of rejection of H_0 , the source of the most significant error is identified, followed by adaption of the model to account for the error. This three-step procedure is repeated until H_0 is accepted.

A.2.1 Detection

In the detection step the null hypothesis is tested by the *Overall Model Test* (OMT). Here, no assumptions about specific kind of errors are made and the number of errors is taken equal as the redundancy, hence the degrees of freedom $q = m - n$, where m is the number of observations and n is the number of unknowns. As a consequence, the redundancy of the model under H_a is zero, which implies that the residues $\hat{\underline{e}}_a$ are zero as well. Therefore the test statistic Eq. (A.11) reduces to

$$\underline{T}_{q=m-n} = \hat{\underline{e}}_0^T Q_y^{-1} \hat{\underline{e}}_0. \quad (\text{A.18})$$

In case H_0 is rejected, the next step is the identification of the most significant error.

A.2.2 Identification

Identification of the most significant error is based on the testing of alternative hypothesis H_a . The most common applied H_a is a test on outliers in the observations. This one-dimensional test ($q = 1$) is also known as the *w-test*. In this case the C_q -matrix for a certain observation has the form

$$C_{q=1} = [0 \quad \cdots \quad 0 \quad 1 \quad 0 \quad \cdots \quad 0]^T. \quad (\text{A.19})$$

The test is repeated for each observation. The observation with the highest test statistic (above k_α) is the most significant error. In case the observations \underline{y} are uncorrelated, hence Q_y is a diagonal matrix, the test statistic for the i -th observation simplifies to

$$\underline{T}_{q=1} = \frac{\hat{\underline{e}}_{0i}^2}{\sigma_{\hat{\underline{e}}_i}^2}. \quad (\text{A.20})$$

Apart from the one-dimensional tests also higher order H_a can be applied, e.g., to test the correctness of coordinates of points. If more than one alternative hypothesis is tested against H_0 , e.g., the OMT and the *w-test*, inconsistencies in the testing can occur due to the overlap of the different tests. For example, an inconsistency occurs when the OMT is accepted, while a *w-test* leads to rejection of an observation. To minimize the chance of inconsistencies, the *B-method* of testing is applied (Baarda, 1968; Teunissen, 2000b).

The B-method ensures that an equivalent error at different dimensions, indicated with an equal non-centrality parameter $\lambda_q = \lambda_0$ for all q , can be detected with equal probability $\gamma_q = \gamma_0$. Since the level of significance α is dependent on λ , γ and q , this results in a different α for each test. In practice, the set of parameters is initialized by choosing α_1 for the one-dimensional test, together with the general power of the test γ_0 . de Heus et al. (1994); Kamps (2006) show that it is essential to set $\gamma_0 = 0.5$ to ensure that the most significant alternative hypothesis among tests of different dimensions is identified. Once α_1 and γ_0 are set, the corresponding λ_0 is computed, followed by the α_q per test, using the relation

$$\lambda_0 = \lambda(\alpha_1, 1, \gamma_0) = \lambda(\alpha_q, q, \gamma_0). \quad (\text{A.21})$$

Based on α_q , the critical value k_{α_q} can now be computed for each dimension. Actual comparison of the different tests is only possible based on the *test quotient*, i.e., the test statistic normalized by the critical value,

$$\underline{T}_q / k_{\alpha_q} \begin{cases} > 1, & \text{reject } H_0, \\ \leq 1, & \text{accept } H_0. \end{cases} \quad (\text{A.22})$$

From all test quotients larger than one, the highest identifies the most significant error. This error is adapted.

A.2.3 Adaption

Once the most significant error is identified, the error is removed from the functional model. For example, in case of the one-dimensional test on the observations, the corresponding observation is removed from the observation vector \underline{y} and the design matrix A is adapted. After adaption the DIA procedure is repeated until the OMT is accepted.

A.3 Prediction

A related technique to least-squares estimation is least-squares prediction. Whereas in case of estimation a deterministic parameter vector x is guessed based on an observed vector \underline{y} , in case of prediction the same vector \underline{y} is used to guess an unobserved random vector \underline{y}_0 . An example is the prediction of the temperature at a certain location based on temperature observations at a number of meteorological stations.

Assume that the mathematical model can be denoted by the so-called trend-signal-noise model

$$\underline{y} = Ax + \underline{s} + \underline{n}, \quad D\{\underline{y}\} = Q_y = Q_s + Q_n, \quad (\text{A.23})$$

where, apart from the familiar terms A and x , \underline{s} is a signal with a certain temporal and/or spatial correlation described by the covariance matrix Q_s and \underline{n} is uncorrelated noise, characterized in Q_n .

The mathematical model for the prediction of observations \underline{y}_0 is

$$\underline{y}_0 = A_0x + \underline{s}_0 + \underline{n}_0, \quad D\{\underline{y}_0\} = Q_{y_0} = Q_{s_0} + Q_{n_0}, \quad (\text{A.24})$$

where the parameters have similar meaning as above.

Both mathematical models are combined in the following system of equations (Teunissen, 2007)

$$\begin{bmatrix} \underline{y} \\ \underline{s} \\ \underline{n} \\ \underline{y}_0 \\ \underline{s}_0 \\ \underline{n}_0 \end{bmatrix} = \begin{bmatrix} A \\ 0 \\ 0 \\ A_0 \\ 0 \\ 0 \end{bmatrix} x + \begin{bmatrix} \underline{s} + \underline{n} \\ \underline{s} \\ \underline{n} \\ \underline{s}_0 + \underline{n}_0 \\ \underline{s}_0 \\ \underline{n}_0 \end{bmatrix}, \quad (\text{A.25})$$

with

$$D \begin{Bmatrix} \underline{y} \\ \underline{s} \\ \underline{n} \\ \underline{y}_0 \\ \underline{s}_0 \\ \underline{n}_0 \end{Bmatrix} = \begin{bmatrix} Q_s + Q_n & Q_s & Q_n & Q_{ss_0} & Q_{ss_0} & 0 \\ Q_s & Q_s & 0 & Q_{ss_0} & Q_{ss_0} & 0 \\ Q_n & 0 & Q_n & 0 & 0 & 0 \\ Q_{s_0s} & Q_{s_0s} & 0 & Q_{s_0} + Q_{n_0} & Q_{s_0} & Q_{n_0} \\ Q_{s_0s} & Q_{s_0s} & 0 & Q_{s_0} & Q_{s_0} & 0 \\ 0 & 0 & 0 & Q_{n_0} & 0 & Q_{n_0} \end{bmatrix}, \quad (\text{A.26})$$

The estimators and predictors are

$$\begin{aligned} \hat{\underline{x}} &= (A^T Q_y^{-1} A)^{-1} A^T Q_y^{-1} \underline{y}, \\ \hat{\underline{y}} &= A \hat{\underline{x}}, \\ \hat{\underline{s}} &= Q_s Q_y^{-1} (\underline{y} - A \hat{\underline{x}}), \\ \hat{\underline{n}} &= Q_n Q_y^{-1} (\underline{y} - A \hat{\underline{x}}), \\ \hat{\underline{y}}_0 &= A_0 \hat{\underline{x}} + Q_{s_0s} Q_y^{-1} (\underline{y} - A \hat{\underline{x}}), \\ \hat{\underline{s}}_0 &= Q_{s_0s} Q_y^{-1} (\underline{y} - A \hat{\underline{x}}), \\ \hat{\underline{n}}_0 &= 0, \end{aligned} \quad (\text{A.27})$$

where

$$Q_y = Q_s + Q_n. \quad (\text{A.28})$$

The prediction error is defined as

$$\hat{\underline{\epsilon}}_0 = \underline{y}_0 - \hat{\underline{y}}_0, \quad (\text{A.29})$$

with corresponding variance matrix of the prediction error

$$Q_{\hat{\underline{\epsilon}}_0} = Q_{y_0} - Q_{s_0s} Q_y^{-1} Q_{ss_0} + (A_0 - Q_{s_0s} Q_y^{-1} A) Q_{\hat{\underline{x}}} (A_0 - Q_{s_0s} Q_y^{-1} A)^T. \quad (\text{A.30})$$

Equivalent to the Best Linear Unbiased properties for the estimators (BLUE), it can be shown that the predictors have minimum mean squared prediction error, are linear, and unbiased (Teunissen et al., 2005). These predictors are denoted as Best Linear Unbiased Predictors (BLUP). BLUP is equivalent to Kriging (Kriging, 1951). In case the mean is estimated, hence A, A_0 are vectors of ones, the BLUP estimator is equal to Ordinary Kriging. In case also an additional trend is modeled in A and A_0 , the BLUP estimator will result in the same solution as obtained by Universal Kriging.

A.4 Least-squares Variance Component Estimation (VCE)

Besides unknown parameters in the functional part of the mathematical model (Eq. A.1), the stochastic part may also contain unknown elements. Using a parameterization of the stochastic model, the statistical properties of the data can be estimated as well. Here, least-squares Variance Component Estimation (VCE) is applied (Teunissen, 1988; Teunissen and Amiri-Simkooei, 2008).

The mathematical model (Eq. A.1) is re-written to

$$E\{\underline{y}\} = A\underline{x} \quad ; \quad D\{\underline{y}\} = Q_y = Q_0 + \sum_{v=1}^V \sigma_v Q_v, \quad (\text{A.31})$$

where Q_0 is the known part of the covariance matrix, σ_v are the unknown (co-)variance components and Q_v are the cofactor matrices, which are assumed known. The least-squares estimator of the (co-)variance components is

$$\hat{\underline{\sigma}} = N^{-1}\underline{r}, \quad (\text{A.32})$$

where N is a square ($V \times V$) matrix and \underline{r} a ($V \times 1$) vector. The elements of N and \underline{r} are (Amiri-Simkooei, 2007)

$$\begin{aligned} N_{vw} &= \frac{1}{2} \text{tr}(Q_v Q_y^{-1} P_A^\perp Q_w Q_y^{-1} P_A^\perp), \\ \underline{r}_v &= \frac{1}{2} \underline{y}^T Q_y^{-1} P_A^\perp Q_v Q_y^{-1} P_A^\perp \underline{y} - \frac{1}{2} \text{tr}(Q_v Q_y^{-1} P_A^\perp Q_0 Q_y^{-1} P_A^\perp), \\ &= \frac{1}{2} \underline{e}^T Q_y^{-1} Q_v Q_y^{-1} \underline{e} - \frac{1}{2} \text{tr}(Q_v Q_y^{-1} P_A^\perp Q_0 Q_y^{-1} P_A^\perp), \end{aligned} \quad (\text{A.33})$$

where $\text{tr}(\cdot)$ indicates the trace of a matrix, i.e., the sum of the diagonal elements, $P_A^\perp = I - A(A^T Q_y^{-1} A)^{-1} A^T Q_y^{-1}$ is the least-squares orthogonal projector and \underline{e} are the residuals. Since Q_y is part of the estimator itself, the solution is obtained by iteration, starting with a covariance matrix based on a-priori knowledge or an identity matrix. The inverse of the normal matrix N gives the covariance matrix of the covariance component estimates

$$Q_{\hat{\underline{\sigma}}} = N^{-1}. \quad (\text{A.34})$$

To estimate the (co-)variance components the system of equations Eq. A.31 must have a large redundancy and the number of (co-)variance components should be limited. The precision increases with increasing redundancy. Both values for variances and covariances can be estimated. Positive values for the variance components are however not guaranteed. Negative variance factors are an indication of a badly chosen (co-)variance model or insufficient redundancy.

A.5 Integer least-squares

The integer least-squares (ILS) technique was introduced by Teunissen (1993) as a solution to the ambiguity problem in Global Navigation Satellite Systems (GNSS) measurements. However, the technique is applicable for all problems encountering a combination of real and integer unknown parameters, as is the case in radar interferometry.

The general integer least-squares problem can be formulated with the extended Gauss-Markov model

$$E\{\underline{y}\} = Aa + Bb, \quad y \in \mathbb{R}, a \in \mathbb{Z}, b \in \mathbb{R}; \quad D\{\underline{y}\} = Q_y, \quad (\text{A.35})$$

where \underline{y} denotes the vector of phase observations, a is the vector of unknown integer valued ambiguities and b represents the unknown real valued parameters. The *design matrices* A and B describe the functional relation between the observations and the unknowns. The dispersion of the phase observations is expressed by the variance matrix Q_y .

The optimal estimates of the unknown parameters in a least-squares sense (L_2 -norm) are obtained by solving the minimization problem

$$\min_{a,b} \|y - Aa - Bb\|_{Q_y}^2, \quad y \in \mathbb{R}, a \in \mathbb{Z}, b \in \mathbb{R}; \quad D\{y\} = Q_y, \quad (\text{A.36})$$

where $\|\cdot\|_Q^2 = (\cdot)^T Q^{-1}(\cdot)$. To account for the integer constraint $a \in \mathbb{Z}$, the function to be minimized can be orthogonally decomposed into the sum-of-squares (Teunissen and Kleusberg, 1998)

$$\|y - Aa - Bb\|_{Q_y}^2 = \underbrace{\|\hat{e}\|_{Q_y}^2}_1 + \underbrace{\|\hat{a} - a\|_{Q_a}^2}_2 + \underbrace{\|\hat{b}_{|a} - b\|_{Q_{b|a}}^2}_3. \quad (\text{A.37})$$

Hence, the original minimization problem is transformed into three individual problems. The solutions to these problems are referred to as the *float solution*, *ambiguity resolution* and the *fixed solution*, which are estimated in a three-step procedure (Teunissen, 1993).

Float solution

The float solution is obtained by disregarding the integer nature of the ambiguities a . Hence, real valued estimates for the ambiguities and the parameters of interest are estimated by solving the standard least-squares problem

$$\min_{a,b} \|y - Aa - Bb\|_{Q_y}^2, \quad y \in \mathbb{R}, a \in \mathbb{R}, b \in \mathbb{R}; \quad D\{y\} = Q_y. \quad (\text{A.38})$$

The solution and the accompanying covariance matrix is denoted as

$$\begin{bmatrix} \hat{a} \\ \hat{b} \end{bmatrix}; \quad \begin{bmatrix} Q_{\hat{a}} & Q_{\hat{a}\hat{b}} \\ Q_{\hat{b}\hat{a}} & Q_{\hat{b}} \end{bmatrix}. \quad (\text{A.39})$$

An example of the probability density function for the ambiguity float solution \hat{a} in case of two ambiguities is shown in Figure A.2, Left.

Ambiguity resolution

Once the float solution is obtained, the float ambiguities \hat{a} are used to resolve the corresponding integer ambiguity estimates \check{a} . This step requires a mapping $S: \mathbb{R} \mapsto \mathbb{Z}$, such that

$$\check{a} = S(\hat{a}). \quad (\text{A.40})$$

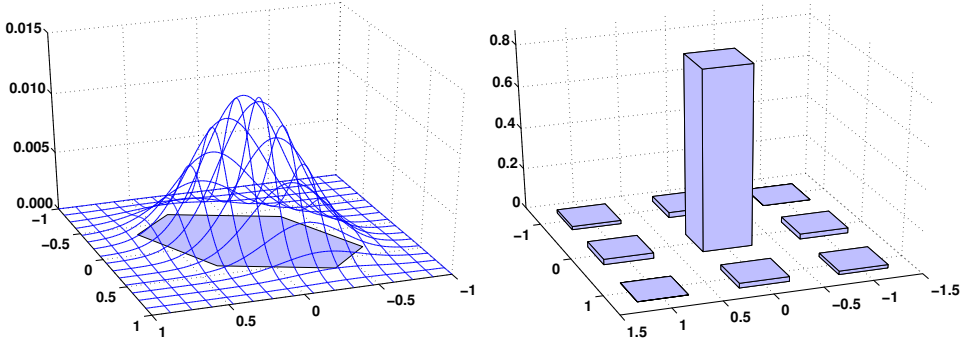


Figure A.2: Left) Example of the float ambiguity PDF in 2D. Right) Example of the integer ambiguity PMF in 2D. Figures are taken from Joosten (2000).

Because of the discrete nature of \check{a} , this is a many-to-one map. In other words, different real-valued ambiguity vectors \hat{a} will be mapped to the same integer vector \check{a} . Hence, a subset $S_z \subset \mathbb{R}$ can be assigned to each integer vector $z \in \mathbb{Z}$

$$S_z = \{x \in \mathbb{R} \mid z = S(x)\}, \quad z \in \mathbb{Z}. \quad (\text{A.41})$$

This subset is referred to as the *pull-in region* of z (Jonkman, 1998). It is the region in which all ambiguity float solutions are pulled to the same fixed solution. Using the pull-in regions, an explicit expression for the corresponding integer ambiguity estimator can be given

$$\check{a} = \sum_{z \in \mathbb{Z}} z s_z(\hat{a}), \quad \text{with the indicator function } s_z(\hat{a}) = \begin{cases} 1 & \text{if } \hat{a} \in S_z, \\ 0 & \text{otherwise.} \end{cases} \quad (\text{A.42})$$

The pull-in regions define the integer estimator completely. Many forms of pull-in regions can be constructed, however, not all of them are *admissible*. To be admissible, the pull-in region of an integer estimator should fulfill the following criteria (Teunissen, 1999a)

$$\begin{aligned} \bigcup_{z \in \mathbb{Z}} S_z &= \mathbb{R} \quad \text{no gaps,} \\ S_{z_1} \cap S_{z_2} &= \emptyset \quad \forall z_1, z_2 \in \mathbb{Z}, z_1 \neq z_2 \quad \text{no overlap,} \\ S_z &= z + S_0 \quad \forall z \in \mathbb{Z} \quad \text{integer remove-restore.} \end{aligned} \quad (\text{A.43})$$

Hence, there should be no gaps, ensuring that every float ambiguity vector can be assigned to an integer solution. Moreover, there should be no overlap, ensuring that there are not multiple integer solutions for a certain float solution. And last, the pull-in regions are translated copies of each other, enabling translations with an integer amount z while preserving the solution. Three admissible integer estimators are *integer rounding*, *integer bootstrapping* and *integer least-squares* (Teunissen, 1999a). These estimators are discussed in Section A.5.1.

Fixed solution

The estimated integer ambiguities \check{a} are used to correct the float estimates of the parameters of interest \check{b} . The resulting fixed solution is obtained by

$$\hat{b}_{|a} \doteq \check{b} = \hat{b} - Q_{\hat{b}\hat{a}} Q_{\hat{a}}^{-1} (\hat{a} - \check{a}). \quad (\text{A.44})$$

The variance matrix of this estimator is (Teunissen, 1999b)

$$Q_{\check{b}} = Q_{\hat{b}} - Q_{\hat{b}\hat{a}} Q_{\hat{a}}^{-1} Q_{\hat{a}\hat{b}} + Q_{\hat{b}\hat{a}} Q_{\hat{a}}^{-1} Q_{\check{a}} Q_{\hat{a}}^{-1} Q_{\hat{a}\hat{b}}, \quad (\text{A.45})$$

where

$$Q_{\check{a}} = \sum_{z \in \mathbb{Z}} (z - a)(z - a)^T P(\check{a} = z). \quad (\text{A.46})$$

Hence, the variance of the fixed solution is not only dependent on the variance of the float solution, but also on the chance of success in the ambiguity resolution. This chance of success is denoted by the *success rate* $P(\check{a} = z)$ (see further Section A.5.2). Because of its discrete nature, the fixed ambiguities \check{a} have a probability mass function (PMF) (see Figure A.2, Right). As a consequence, the fixed solution \check{b} has a multi-modal probability density function.

A.5.1 Admissible integer estimators

Three integer estimators which fulfill the criteria introduced by Eq. (A.43) are the integer rounding, integer bootstrapping, integer least-squares estimator. To illustrate these estimators, the float ambiguity solution, consisting of a vector with estimates and corresponding covariance matrix, is written as

$$\hat{a} = \begin{bmatrix} \hat{a}_1 \\ \hat{a}_2 \\ \vdots \\ \hat{a}_q \end{bmatrix}; \quad Q_{\hat{a}} = \begin{bmatrix} \sigma_{\hat{a}_1}^2 & \sigma_{\hat{a}_1 \hat{a}_2} & \cdots & \sigma_{\hat{a}_1 \hat{a}_q} \\ \sigma_{\hat{a}_2 \hat{a}_1} & \sigma_{\hat{a}_2}^2 & \cdots & \sigma_{\hat{a}_2 \hat{a}_q} \\ \vdots & \vdots & \ddots & \vdots \\ \sigma_{\hat{a}_q \hat{a}_1} & \sigma_{\hat{a}_q \hat{a}_2} & \cdots & \sigma_{\hat{a}_q}^2 \end{bmatrix}. \quad (\text{A.47})$$

Integer rounding

The simplest integer estimator is rounding of entries of the float ambiguity solution to their nearest integer values. The integer estimator \check{a}_R is

$$\check{a}_R = \begin{bmatrix} \check{a}_{R,1} \\ \check{a}_{R,2} \\ \vdots \\ \check{a}_{R,q} \end{bmatrix} = \begin{bmatrix} [\hat{a}_1] \\ [\hat{a}_2] \\ \vdots \\ [\hat{a}_q] \end{bmatrix}, \quad (\text{A.48})$$

where $[\cdot]$ denotes the rounding to the nearest integer operator. Since each component of the real-valued ambiguity vector is rounded to its nearest integer, the absolute value of the maximum difference between the float and fixed solution is $1/2$. Therefore, the pull-in region for integer rounding in \mathbb{R} is an q -dimensional cube with sides of length one.

Even though the rounding technique is an admissible estimator, it does not take the ambiguity correlation into account, and therefore, does not satisfy the minimization criteria formulated by means of Eq. (A.37). Exception is the case when there is no correlation between the float solutions, i.e., when the covariance matrix $Q_{\hat{a}}$ is a *diagonal matrix*.

Integer bootstrapping (sequential conditional rounding)

An integer estimator which takes *some* of the correlation between the float ambiguities into account, is the so-called integer bootstrapping estimator, also known as the *sequential conditional rounding* estimator. The integer solution is computed in a sequential order. The first ambiguity (\hat{a}_1) is simply rounded to its nearest integer. After that, the real-valued estimates of the remaining ambiguities are corrected by means of their correlation with the first ambiguity. In a next step, the second (corrected) ambiguity is rounded to its nearest integer, and so on. The bootstrap estimator \check{a}_B can be expressed by (Teunissen, 1998)

$$\check{a}_B = \begin{bmatrix} \check{a}_{B,1} \\ \check{a}_{B,2} \\ \vdots \\ \check{a}_{B,q} \end{bmatrix} = \begin{bmatrix} [\hat{a}_1] \\ [\hat{a}_2 - \sigma_{\hat{a}_2\hat{a}_1} \sigma_{\hat{a}_1}^{-2} (\hat{a}_1 - \check{a}_{B,1})] \\ \vdots \\ [\hat{a}_q - \sum_{i=1}^{q-1} \sigma_{\hat{a}_q\hat{a}_i|I} \sigma_{\hat{a}_i|I}^{-2} (\hat{a}_i|I - \check{a}_{B,i})] \end{bmatrix}, \quad (\text{A.49})$$

where $I = 1, \dots, i-1$. Since the integer solution depends on the order of the ambiguities, the sequence should start with the most precise float ambiguity. The real-valued sequential least-squares solution can be obtained by means of the triangular decomposition of the covariance matrix of the ambiguities $Q_{\hat{a}} = LDL^T$, where L denotes a unit lower triangular matrix with entries

$$l_{j,i} = \sigma_{\hat{a}_j\hat{a}_i|I} \sigma_{\hat{a}_i|I}^{-2}, \quad (\text{A.50})$$

and D a diagonal matrix with the conditional variances $\sigma_{\hat{a}_i|I}^2$. Although the integer bootstrapping technique is an admissible integer estimator and takes some of the ambiguity correlation into account, like in the case of the rounding the solution does in general not satisfy the minimization criterion as formulated in Eq. (A.37).

Integer least-squares (ILS)

The integer least-squares estimator is the only estimator which is fully based on the minimization criterion in Eq. (A.37)

$$\min_{a \in \mathbb{Z}} (\hat{a} - a)^T Q_{\hat{a}}^{-1} (\hat{a} - a). \quad (\text{A.51})$$

Due to the variance matrix $Q_{\hat{a}}$, the integer least-squares estimator takes all the correlation between the ambiguities into account. In contrast to rounding and bootstrapping, the integer least-squares solution \check{a}_{LS} is at shortest distance to the float solution, in the metric of the variance matrix $Q_{\hat{a}}$.

Unfortunately, this minimization problem cannot be solved directly. A discrete search in the solution space is necessary to find the optimal solution (Teunissen, 1993). In order

to avoid a search through the complete space of integers \mathbb{Z} , it is possible to identify a smaller search space that still contains the integer least-squares solution. This ambiguity search space, i.e., a hyper-ellipsoid centered at \hat{a} of which its shape is defined by the variance matrix $Q_{\hat{a}}$, is bounded by

$$(\hat{a} - a)^T Q_{\hat{a}}^{-1} (\hat{a} - a) \leq \chi^2, \quad (\text{A.52})$$

where the factor χ^2 is a positive constant. This constant should be chosen sufficiently large, i.e., that the search space contains at least one integer vector. A convenient strategy to find a suitable value for χ^2 is by using the integer bootstrap solution

$$\chi^2 = (\hat{a} - \check{a}_B)^T Q_{\hat{a}}^{-1} (\hat{a} - \check{a}_B). \quad (\text{A.53})$$

Hence, a χ^2 is found which at least contains one integer solution (the bootstrap solution) and is assumed to be small enough to strongly reduce the search space. Once the size of the search space is set, the actual discrete search can be performed. In de Jonge and Tiberius (1996) an efficient search procedure is described.

However, due to the often high correlation between the ambiguities, the search space becomes very elongated. As a result, the discrete search becomes highly inefficient and slow in terms of computation time. To reduce the search time, the LAMBDA method was introduced.

LAMBDA method

To reduce the correlation between the ambiguities, a decorrelating transformation is performed. This procedure, together with the integer least-squares technique, forms the LAMBDA method (Least-squares AMBiguity Decorrelation Adjustment method), (Teunissen, 1993). By means of the decorrelation transformation the ambiguity search space is transformed to a shape as similar as possible to a hyper-sphere, e.g., as if $Q_{\hat{a}}$ were a diagonal matrix (that is, ambiguities are uncorrelated). A complete decorrelation is however not possible, since in that case the integer nature of the solution would be lost.

The transformation is denoted by

$$\hat{z} = Z^T \hat{a}, \quad Q_{\hat{z}} = Z^T Q_{\hat{a}} Z. \quad (\text{A.54})$$

The matrix Z must have integer entries and must be volume preserving (i.e., $|Z| = \pm 1$) to be an *admissible transformation matrix* (Teunissen, 1993). Moreover, it can be shown (see for example Teunissen (1994)), that in spite of the decorrelating transformation, the minimization constraint is satisfied

$$(\hat{z} - z)^T Q_{\hat{z}}^{-1} (\hat{z} - z) = (\hat{a} - a)^T Q_{\hat{a}}^{-1} (\hat{a} - a). \quad (\text{A.55})$$

Just as in case of the original ambiguities, the discrete search for the integer solution can now be performed. The size of the search space can be determined based on the bootstrap solution of the decorrelated ambiguities. Once the optimal solution \check{z} is found, the solution of the original ambiguities \check{a}' can be retrieved by

$$\check{a}' = Z^{-T} \check{z}. \quad (\text{A.56})$$

Note that the solution obtained with or without decorrelation of the ambiguities is the same, i.e., $\check{a}' = \check{a}$. This is however not necessarily the case for the bootstrap solutions \check{a}'_B and \check{a}_B .

To summarize, the integer least-squares technique provides the optimal solution. Applying the LAMBDA method, the optimal solution is found in a computationally effective way due to the decorrelation of the ambiguities.

A.5.2 On the quality of the solutions: Success rate

In order to judge the correctness of the solution the probability of *correct integer ambiguity estimation* can be computed, defined as the *success rate* $P(\check{a} = a)$. Note that the ambiguity success rate can be computed without collecting real data at all, hence purely based on the functional and stochastic assumptions in the mathematical model.

In (Teunissen, 1999a) it is shown that the integer least-squares (ILS) technique maximizes the success rate

$$P(\check{a}_{LS} = a) \geq P(\check{a}_X = a), \quad (\text{A.57})$$

where X stands for any other arbitrary integer estimator.

Due to the complicated geometry of the ILS pull-in regions, the numerical computation of the ILS success rate $P(\check{a}_{LS} = a)$ is difficult. A lower bound of this probability is given by the success rate of the bootstrapped integer estimator (Teunissen, 1998), i.e.,

$$P(\check{a}_{LS} = a) \geq P(\check{a}_B = a) = \prod_{i=1}^n \left(2\Phi\left(\frac{1}{2\sigma_{i|I}}\right) - 1 \right), \quad (\text{A.58})$$

where $\sigma_{i|I}$ are the conditional variances and $\Phi(x)$ is defined as

$$\Phi(x) = \int_{-\infty}^x \frac{1}{\sqrt{2\pi}} \exp\left(-\frac{1}{2}v^2\right) dv. \quad (\text{A.59})$$

An upper bound of the ILS success rate can be computed using the *ADOP* (Ambiguity Dilution Of Precision, see (Teunissen, 1997)). The upper bound is (Teunissen, 1998)

$$P(\check{a}_{LS} = a) \leq P\left(\chi^2(n, 0) \leq \frac{c_n}{ADOP^2}\right), \quad (\text{A.60})$$

with $c_n = \left(\frac{n}{2}\Gamma\left(\frac{n}{2}\right)\right)^{\frac{2}{n}} / \pi$. Here, Γ is the Gamma function and $\chi^2(n, 0)$ is a variable with a central Chi-square distribution. The *ADOP* [cycles], which is defined as the *geometric mean* of the conditional covariances $\sigma_{i|I}$, is

$$ADOP = \sqrt{\det Q_{\check{a}}^{-1}}^{\frac{1}{n}}. \quad (\text{A.61})$$

The *ADOP* is a scalar representation of the quality of the ambiguity resolution.

B

Adopted PSI terminology

To clearly describe and annotate the processing flow of the Delft implementation of Persistent Scatterer Interferometry (DePSI) a specific terminology is adopted. The rationale behind the terminology is described here.

The DePSI terminology is based on a similar approach as applied in conventional geodetic networks, using first-order and second (or higher)-order points. The first-order points are more thoroughly tested than the second-order points. The first-order points form a first-order network, which is used for the estimation of phase screens, such as the atmospheric and orbital phase screens. The second order points are referred relative to this first-order network—which is considered to be correctly unwrapped—and serve as a densification of the PS distribution. As a consequence of this setup, errors in the first-order network will propagate undetected in the second-order network. Iterative approaches and additional testing should be applied to prevent this.

While establishing a network, different phases can be distinguished, i.e., (a) the initial classification of points based on certain characteristics, after which the point is considered a candidate for testing, or a 'Candidate' for short, and (b) the testing of these candidate points based on their phase behavior. If a point is not rejected during the testing procedure, it is not a candidate anymore. This convention is summarized in Table B.1. The scheme can be extended to higher-order levels, in the limit to the 'level infinite', at which all pixels in an image are considered.

There is a class (set) of points which is coherent, but which is erroneously not identified as such. This can be due to two causes:

1. these points do not satisfy the criteria to become candidates, hence, their phase behavior is simply not evaluated, or
2. these points are identified as candidates, but during the testing procedure, they are falsely rejected as PS.

These points are referred to as Type-1 errors or Type-1 error points (falsely rejected as PS or PSC), or as undetected PS.

Lower-order PS candidates are a subset of higher-order PS candidates, i.e., the set of PSC2 (second-order PS candidates) also contains the PSC1 (first-order PS candidates). Hence, rejected PSC1 are tested again in the second-order network and possibly accepted

Table B.1: Conventions in DePSI terminology.

	Initial selection (leading to PS 'Candidates')		After testing	
	Pixel/network	Abbreviation	Pixel/network	Abbreviation
General	<i>PS Candidate</i>	PSC	<i>PS</i>	PS
First-order	<i>First-order PS Candidate or first-order candidate network</i>	PSC1	<i>First-order PS or first-order network</i>	PS1
Second-order (densification)	<i>Second-order PS Candidate or second-order candidate network</i>	PSC2	<i>Second-order PS or second-order network</i>	PS2
Third-order	<i>Third-order PS Candidate or third-order candidate network</i>	PSC3
...	...			
Infinite-order	All Pixels	PSC ∞		

as PS2. Note that this subset construction is not applicable for the detected PS, i.e., PS1 and PS2 cannot contain the same points.

Algorithm implementation

The DePSI algorithm is implemented in Matlab[®]. The main script guides the complete processing flow, which is illustrated in Figure 3.1. Here, nine main modules can be distinguished, see also Section 3.1:

1. Initialization.
2. Persistent Scatterer Candidates (PSC) selection.
3. Network construction.
4. Trend estimation (optional).
5. Atmosphere estimation.
6. Interferogram selection (optional).
7. Densification.
8. Deformation modeling (optional).
9. Output generation.

The algorithm is initialized based on two input files. The first file contains the specification of the interferometric data stack, including filenames, acquisition dates, baselines and image crop parameters. In the second input file the processing flow is specified by defining the processing steps to apply and setting various parameters based on a-priori information about the area of interest and the expected deformation signal. By changing this input file a certain step can be re-run based on different parameter settings to improve the result.

After each processing step a result file is adapted with a summary of the processing results and the associated processing time. Furthermore, a series of figures is created of the most important intermediate results, which supports the interpretation of the final results. All (created) processing variables are saved to a single Matlab[®] .mat file, whereas the large data volumes are stored in binary format.

Within the input file with parameters also the maximum usable amount of internal memory can be specified. Based on the allocated memory, the processing in each step

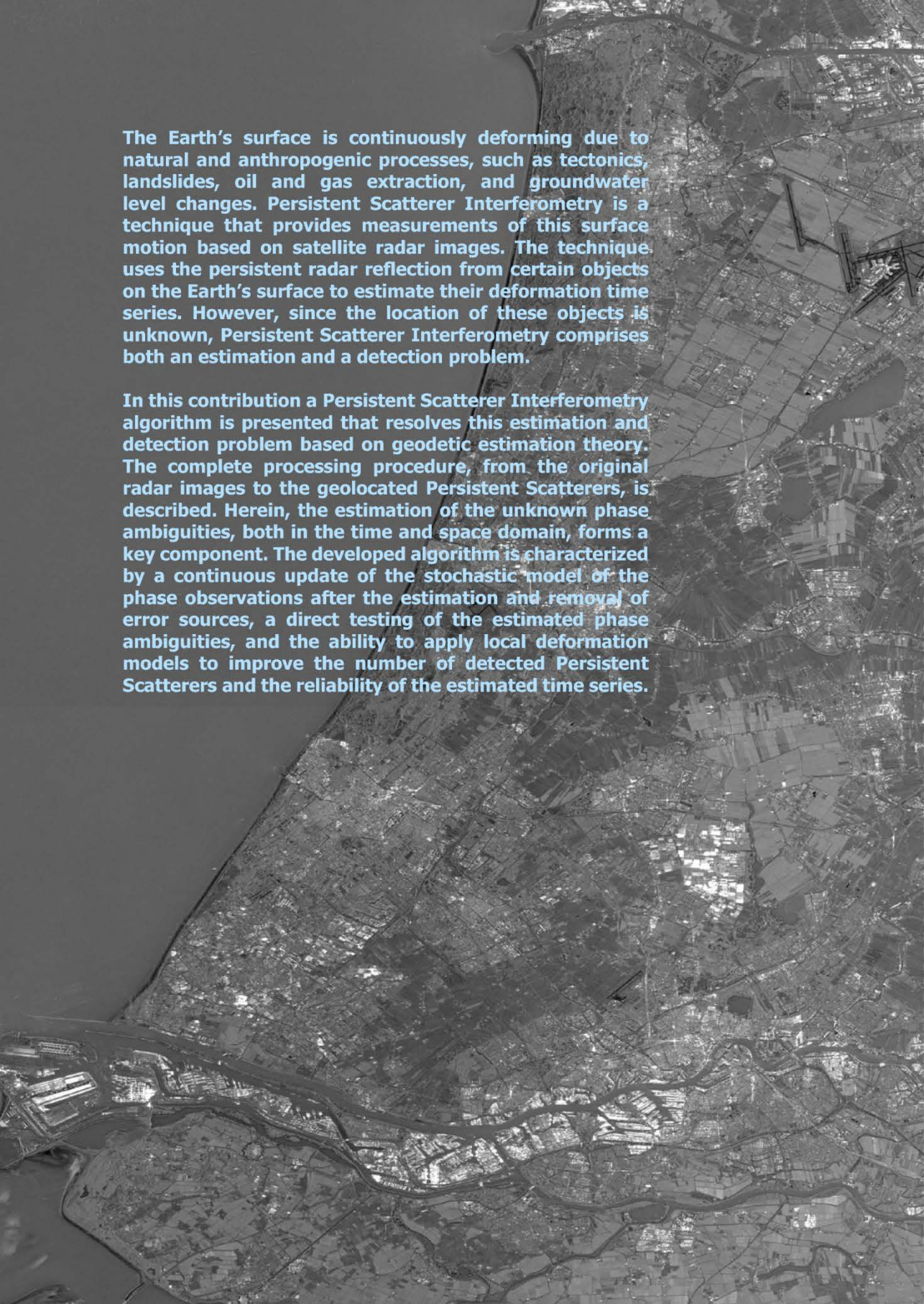
is divided in buffers. Hereby, the inversion of the first-order network is the most complicated part of the algorithm. However, by using a partitioned model, also this step can be performed within a certain memory buffer. The use of buffers enables the possibility to run DePSI on machines with various memory capacity, i.e., local desktops with 1 or 2 GB of internal memory and dedicated servers. Moreover, a parallelization of the processing is possible.

The final results of the algorithm are stored in binary files as well as comma-separated value files (.csv), which can be used to visualize the data in a Geographic Information System (GIS), or to integrate the measurements with other geodetic observations.

Curriculum Vitae

I, Frederik Johannes van Leijen, was born on July 24, 1977, in Woerden, the Netherlands. In 1995, after secondary school, I started studying Geodetic Engineering at the Delft University of Technology. During my studies, in 1998-1999, I was a board member of the Landmeetkundig Gezelschap Snellius, the student union associated with the Geodetic Engineering track. In 2000 I went four months to Cape Town, South Africa, for a traineeship at the University of Cape Town, working on the simulation of satellite radar images. I obtained my MSc degree in 2002 based on a thesis regarding the stochastic modeling of the tropospheric delay of microwave signals.

After a year of traveling around the world, I started my PhD project in 2003. During my PhD I had the opportunity to work on various related projects, such as the Persistent Scatterer Interferometry Codes Cross-Comparison And Certification (PSIC4) and Terrafirma projects of the European Space Agency (ESA). In 2006 I worked four months at the Rosenstiel School of Marine and Atmospheric Science, University of Miami, USA, as a Fulbright Scholar. In 2007 I co-founded Hansje Brinker, a Delft University of Technology spin-off company that provides satellite radar interferometry based services. In 2013, after being five years at Hansje Brinker, I returned to Delft University of Technology as a researcher in geodesy and remote sensing.

The background of the page is a grayscale aerial satellite radar image. It shows a coastal urban area with a river winding through it. The image is characterized by a grid-like pattern of buildings and streets, with some areas appearing brighter than others, likely due to the radar's interaction with the terrain and structures. The river is visible as a dark, winding line, and a large body of water is on the left side of the image.

The Earth's surface is continuously deforming due to natural and anthropogenic processes, such as tectonics, landslides, oil and gas extraction, and groundwater level changes. Persistent Scatterer Interferometry is a technique that provides measurements of this surface motion based on satellite radar images. The technique uses the persistent radar reflection from certain objects on the Earth's surface to estimate their deformation time series. However, since the location of these objects is unknown, Persistent Scatterer Interferometry comprises both an estimation and a detection problem.

In this contribution a Persistent Scatterer Interferometry algorithm is presented that resolves this estimation and detection problem based on geodetic estimation theory. The complete processing procedure, from the original radar images to the geolocated Persistent Scatterers, is described. Herein, the estimation of the unknown phase ambiguities, both in the time and space domain, forms a key component. The developed algorithm is characterized by a continuous update of the stochastic model of the phase observations after the estimation and removal of error sources, a direct testing of the estimated phase ambiguities, and the ability to apply local deformation models to improve the number of detected Persistent Scatterers and the reliability of the estimated time series.